Universidad de Valencia

Departamento de Física Teórica

On Implications of Modified Gravity Models of Dark Energy

Tesis doctoral

Zahara Gironés Delgado-Ureña

Directores de tesis:

Dr. Olga Mena Requejo

Dr. Carlos Peña Garay

Valencia, 2014.

A mi familia.

Cuando emprendas tu viaje a Ítaca
pide que el camino sea largo,
lleno de aventuras, lleno de experiencias.
No temas a los lestrigones ni a los cíclopes
ni al colérico Poseidón,
seres tales jamás hallarás en tu camino,
si tu pensar es elevado, si selecta
es la emoción que toca tu espíritu y tu cuerpo.
Ni a los lestrigones ni a los cíclopes
ni al salvaje Poseidón encontrarás,
si no los llevas dentro de tu alma,
si no los yergue tu alma ante ti.
Pide que el camino sea largo.
Que muchas sean las mañanas de verano
en que llegues -con qué placer y alegría!-
a puertos nunca vistos antes.
Detente en los emporios de Fenicia
y hazte con hermosas mercancías,
nácar y coral, ámbar y ébano
y toda suerte de perfumes sensuales,
cuantos más abundantes perfumes sensuales puedas.
Ve a muchas ciudades egipcias
a aprender, a aprender de sus sabios.
Ten siempre a Itaca en tu mente.
Llegar allí es tu destino.
Mas no apresures nunca el viaje.
Mejor que dure muchos años
y atracar, viejo ya, en la isla,
enriquecido de cuanto ganaste en el camino
sin aguantar a que Ítaca te enriquezca.
Ítaca te brindó tan hermoso viaje.
Sin ella no habrías emprendido el camino.
Pero no tiene ya nada que darte.
Aunque la halles pobre, Ítaca no te ha engañado.
Así, sabio como te has vuelto, con tanta experiencia,
entenderás ya qué significan las ítacas.

C. P. Cavafis

Contents

Chapter 1

Introducción

1.1   Motivación

La cosmología moderna tiene como objetivo modelizar la dimámica y la estructura a gran escala del universo, así como su origen y su destino. La formulación de la teoría de la Relatividad General (RG) de Einstein, en 1915, dio lugar al nacimiento de la cosmología como una ciencia cuantitativa. Poco después, la RG fue verificada empíricamente por primera vez a través de dos de sus predicciones más relevantes: la precesión del perihelio de Mercurio y la deflección de la luz alrededor del Sol. Según ésta, la energía y el momento de la materia son las fuentes del campo gravitatorio y, a gran escala, determinan la geometría del universo. En particular, Einstein estudió soluciones de las ecuaciones de campo de la RG para una distribución homogénea de materia, como modelo de la estructura a gran escala del universo. Pronto descubrió que su teoría, en su forma más simple, no admitía como solución un universo estático, en su lugar predecía un universo en expansión o en contracción. Por el contrario, las observaciones indicaban que las estrellas se movían a velocidades muy pequeñas, lo cual sugería un universo estacionario. Con el objetivo de permitir soluciones estacionarias, Einstein tuvo que introducir en sus ecuaciones de campo lo que se llamó la *constante cosmológica*. La dinámica de un universo isótropo y homogéneo, según la RG, fue estudiada posteriormente de forma más sistemática por Alexander Friedmann en 1922, quien de nuevo encontró soluciones de un universo en expansión o en contracción. En paralelo, Edwin Hubble descubrió la existencia de galaxias fuera de la Via Láctea, la cual se creía hasta entonces que comprendía todo el universo. Las observaciones posteriores de Hubble revelaron, en 1929, que la velocidad de recesión de las galaxias aumenta con su distancia a la Tierra, indicando que el universo está en expansión. En consecuencia Einstein eliminó la constante cosmológica de las ecuaciones de campo, lamentando su hipótesis *ad hoc* de un universo estático. Sin embargo, de acuerdo con la teoría cuántica de campos, la constante cosmológica emerge de forma natural como la densidad de energía de vacío; debido al principio de incertidumbre cuántico, la energía

del estado fundamental de todos los campos de materia no es cero, y contribuye a la densidad de energía de vacío, actuando como una constante cosmológica para el campo gravitatorio. Como resultado, eliminar la constante cosmológica de la ecuaciones de campo necesitaría una justificación teórica.

En 1998 se dio un gran punto de inflexión cuando las observaciones de las Supernovas del tipo Ia (SN Ia) relevaron, por primera vez, una tendencia muy reciente en la expansión del universo: a un redshift de $z < 1$ el universo comenzó a expandirse de forma acelerada. Esta observación ha sido corroborada posteriormente por otras observaciones cosmológicas independientes: el fondo cósmico de microondas (Cosmic Microwave Background, CMB), la estructura a gran escala del universo (Large Scale Structure, LSS), las oscilaciones acústicas bariónicas (Baryonic Acoustic Oscillations, BAO) y la estimación de la edad del universo. La naturaleza fundamental de dicha aceleración es aún desconocida y constituye uno de los mayores problemas por resolver en el campo de la cosmología. La geometría del espacio-tiempo está determinada por la densidad de materia-energía que contiene el universo. Sin embargo, según los modelos cosmológicos actuales, basados en las ecuaciones de campo de Einstein, la interacción gravitatoria de la densidad de materia-energía estándar es atractiva, en consecuencia sólo puede decelerar la expansión. Por consiguiente, en el marco de la RG, se atribuye la aceleración de la expansión a una densidad de energía de vacío con presión negativa. Dicha energía de vacío actúa como "anti-gravedad" a nivel efectivo, y se le ha dado el nombre de energía oscura. Las observaciones de la expansión del universo requieren que la componente energía oscura represente aproximadamente un 70% de la densidad de energía total en el universo. El 30% restante se atribuye a materia; un 25% de materia oscura y tan sólo un 5% representa la materia ordinaria. Además la densidad de energía de la energía oscura parece ser constante, jugando el papel de una constante cosmológica en las ecuaciones de campo de Einstein. Este hecho, respaldado por las observaciones más precisas durante los últimos quince años, ha conducido al modelo estándar cosmológico actual, en el cual la aceleración de la expansión del universo es debida a una constante cosmológica positiva, cuya densidad de energía está dominando actualmente la expansión. Esto es lo que se llama el modelo Λ Cold Dark Matter (ΛCDM).

Naturalmente, la densidad constante de energía de vacío observada, se atribuyó a la energía del estado fundamental de los campos de materia. Sin embargo, las estimaciones teóricas de dicho punto-cero de energía basadas en la teoría cuántica de campos, dan como resultado un valor de la constante cosmológica que es muchos órdenes de magnitud mayor que el valor necesario para satisfacer las observaciones de la aceleración de la expansión del universo; esta discrepancia, o el extremado ajuste de precisión que es necesario para evitar el problema, se llama el *problema de la constante cosmológica*. Otra cuestión fundamental emerge del hecho de que el valor de la densidad de energía de vacío y el valor de la densidad de materia tienen el mismo orden de magnitud en el momento presente de la historia expansiva del universo; en principio, estas dos cantidades no están correlacionadas. Esto es lo que se llama el *problema de la coincidencia.*

Además no hay evidencia que indique que la energía de vacío haya sido constante durante la historia pasada del universo, cuando la radiación o la materia eran las componentes dominantes, ni siquiera se sabe con certeza si es realmente constante en el presente. La naturaleza real de la energía oscura, y por tanto la causa subyacente de la aceleración de la expansión del universo, es todavía una cuestión fundamental sin resolver que constituye uno de los mayores problemas abiertos en cosmología, y sugiere que existe nueva física ausente en nuestro paradigma cosmológico actual.

Con el objetivo de entender la naturaleza fundamental de la aceleración de la expansión del universo, se han propuesto muchas teorías alternativas a la teoría de la RG con una constante cosmológica. Una de estas alternativas es remplazar la constante cosmológica por un campo escalar dinámico, llamado *quintaesencia*, que varía en el espacio y en el tiempo, acercándose lentamente a su estado fundamental. Sin embargo, los modelos de quintaesencia no son mejores que el escenario de la constante cosmológica en lo que refiere a solucionar el problema del ajuste de precisión; estos modelos no son capaces de explicar el diminuto valor del potencial en su estado fundamental (por ejemplo, a través de un principio de simetría), el cual juega el papel de la constante cosmológica. Una alternativa más atractiva es modificar la gravedad misma. Este tipo de modificaciones de las ecuaciones de gravedad de Einstein, no son inesperadas en una descripción efectiva 4-dimensional de teorías de altas energías con dimensiones extra. Se han estudiado diferentes teorías de *gravedad modificada* con el objetivo de explicar el fenómeno de la aceleración cosmológica. Algunos modelos propuestos de gravedad modificada involucran dimensiones espaciales extra, mientras que otros modifican la acción de Hilbert-Einstein, *e.g.*, teorías con derivadas superiores, teorías scalar-tensor, etc. En particular, los modelos de gravedad modificada $f(R)$ introducen modificaciones en el sector gravitatorio de las ecuaciones de campo de RG; mientras la densidad Lagrangiana en la acción de Hilbert-Einstein viene dada por la curvatura escalar R, en dichos modelos de gravedad modificada la densidad Lagrangiana se generaliza, reemplazándola por una función no lineal de la curvatura escalar, esto es $f(R)$. Los modelos $f(R)$ son modelos fenomenológicos particularmente simples cuyo análisis permite la búsqueda de pequeñas desviaciones respecto al modelo estandar cosmológico, ΛCDM. Aunque estas modificaciones de gravedad, en principio, no resuelven el problema de la constante cosmológica, tienen el propósito de iluminar nuestra interpretación del fenómeno de la energía oscura.

1.2   Objetivos de esta Tesis

En los últimos años, las teorías de gravedad modificada $f(R)$ han sido consideradas como una posible explicación de la aceleración de la expansión del universo. Tipos específicos de modelos $f(R)$ han sido propuestos y estudiados en la literatura. Para que dichos modelos sean cosmológicamente viables, deben ser capaces de reproducir las predicciones de RG a pequeñas escalas (*e.g.* en el sistema solar) y a su vez ser capaces

de reproducir la aceleración de la expansión del universo a escalas cosmológicas. Por tanto, a un nivel efectivo, los modelos $f(R)$ contienen pequeñas correcciones de la acción de Hilbert-Einstein. El objetivo de esta tesis es analizar modelos de gravedad modificada $f(R)$ fenomenológicos y su viabilidad empírica a escalas cosmológias y del sistema solar comparándolos con las restricciones observacionales que deben satisfacer.

Comenzamos esta tesis introduciendo el modelo estándar cosmológico y describiendo las observaciones que indican que la expansión del universo esta actualmente en una fase de aceleración. A continuación, en el Capítulo 3, hacemos una descripción de los modelos $f(R)$ de gravedad modificada como una posible alternativa que explique el fenómeno de la energía oscura. En este punto derivamos las ecuaciones de Friedmann modificadas, las cuales describen la dinámica de la expansión de un universo homogéneo. A continuación llevamos a cabo un análisis de perturbaciones lineales, el cual describe la evolución de pequeñas inhomogeneidades y el crecimiento de estructura en comologías $f(R)$. Finalizamos el Capítulo 3 con una discusión general de las condiciones que los modelos $f(R)$ deben satisfacer para no violar las restricciones impuestas por los tests del sistema solar.

En el Capítulo 4 describimos una metodología basada en la teoría de sistemas dinámicos, mediante la cual se obtiene una clasificación cualitativa los modelos $f(R)$ según su viabilidad cosmológica en un universo homogéneo; en este punto hacemos una síntesis de las condiciones necesarias para que modelos $f(R)$ específicos puedan reproducir una historia de la expansión aceptable de acuerdo con las observaciones. En la segunda parte de este Capítulo, cinco tipos diferentes de modelos $f(R)$ cualitativamente aceptables son analizados acorde a dicha metodología.

Considerando estos cinco tipos de modelos, en el Capítulo 5 llevamos a cabo un análisis cuantitativo que incluye además el análisis perturbativo de inhomogeneidades cosmológicas a orden lineal. Para ello confrontamos la historia expansiva del universo y la formación del crecimiento de estructura con datos experimentales de distintas fuentes. Concretamente, confrontamos la historia expansiva de estos modelos $f(R)$ con datos de SN Ia, medidas del *shift parameter* del CMB, medidas del *acoustic parameter* de las BAO, y datos del parámetro de Hubble derivados de la edad de las galaxias. Además ajustamos también el crecimiento de estructura lineal descrito por dicho modelos $f(R)$ a la información derivada de las observaciones de las distorsiones espaciales debidas al *redshift*. Con este análisis, demostramos que la combinación de datos basados en la medida de distancias cosmológicas con datos del crecimiento lineal de estructura, constituye una metodología robusta para descartar la viabilidad cosmológica de modelos $f(R)$.

Finalmente, los tipos de modelos que resultan ser consistentes con todos los datos cosmológicos utilizados en esta tesis, son analizados en el límite de campo-débil y velocidades pequeñas, para la región de parámetros en la cual los modelos han resultado ser viables a escalas cosmológicas. Utilizando este análisis, determinamos qué modelos son compatibles con las ajustadas restricciones impuestas por los tests del sistema solar.

Introduction

1.3   Motivation

Modern cosmology aims to model the large scale structure and dynamics of the universe, and its origin and fate. It was born as a quantitative science after the advent of Einstein's theory of General Relativity (GR) in 1915. Soon after, GR found its first empirical verification in its successful prediction of two solar system phenomena: the perihelion precession of Mercury and the deflection of light by the Sun. Since then, GR has become an essential tool in the study of astrophysical and cosmological phenomena. According to GR, the energy and momentum of matter are the source of the gravitational field, and at large scales determine the geometry of the universe. In particular, Einstein studied solutions of the GR field equations for a homogeneous distribution of matter, as a model of the large scale structure of the universe. He discovered soon that his theory, in its simplest form, does not support a static universe, but instead predicts an expanding or a contracting one. By contrast, the small velocities of the stars observed at that time suggested that the universe is stationary. In order to allow for a steady-state solution, Einstein had to add what came to be called the *cosmological constant* to the field equations of GR. The dynamics of a homogeneous and isotropic universe according to GR was subsequently studied more systematically by Alexander Friedmann in 1922, again finding expanding or contracting solutions. In parallel, Edwin Hubble discovered the existence of galaxies outside of the Milky Way, which until then was believed to comprise the entire universe. His subsequent observations showed, in 1929, that the recessional velocity of galaxies increases with their distance from the earth, implying that the universe is expanding. In consequence, Einstein dropped the cosmological constant from the field equations, famously regretting his *ad hoc* hypothesis of the universe being static as his "greatest blunder." However, from a quantum field theory perspective, the cosmological constant in fact arises naturally as the energy density of the vacuum; due to the quantum uncertainty principle, the ground state energy of all matter fields is nonzero, and contributes to the vacuum energy density, acting like a cosmological constant for the gravitational field. Thus dropping the cosmological constant from the field equations turned out to beg a theoretical justification. Nevertheless, until the 1990's the standard cosmological paradigm was described by a homogeneous and isotropic matter-dominated expanding universe,

with no cosmological constant.

A great turnover happened in 1998 when observations of type Ia Supernovae (SN Ia) revealed for the first time a very recent trend in the expansion of the universe: at a redshift $z < 1$ the expansion of the universe started accelerating. This observation has been subsequently corroborated by other independent cosmological observations: the Cosmic Microwave Background (CMB), the Large Scale Structure (LLS), the Baryonic Acoustic Oscillations (BAO) and the estimated age of the universe. The fundamental nature of such acceleration remains unknown and constitutes one of the major problems to be solved in cosmology. The geometry of spacetime is determined by the energy content of the universe. But according to the current cosmological models, based on Einstein's field equations, the gravitational interaction of the standard matter-energy density components is attractive, and can only slow down the expansion. Thus, in the GR framework, a vacuum energy density component with negative pressure, is thought to be responsible for the accelerated expansion. Such vacuum energy, which effectively acts as "anti-gravity", has been called *dark energy*. Observations of the universe's expansion require the dark energy component to account for about 70% of the total energy density in the universe. The remaining 30% is accounted for by matter; a $\sim 25\%$ accounted for by a dark matter component and only about 5% accounted for by ordinary matter. Furthermore, the energy density of the dark energy component appears to be constant, playing the role of a cosmological constant in Einstein's field equations. This fact, supported by the most accurate observations over the past fifteen years, have led to the current standard cosmological model, in which the accelerated expansion is due to a positive cosmological constant, whose corresponding energy density is currently dominating the expansion history. This is the so-called Λ Cold Dark Matter (ΛCDM) model.

Naturally, the observed constant vacuum energy density was attributed to the ground state energy of matter fields. However, reasonable estimates from quantum field theory of this zero-point energy, yield values of the cosmological constant which are many orders of magnitude larger than the value necessary to account for the observed acceleration of the universe; this discrepancy, or the extreme fine-tuning which is necessary to avoid it, is referred to as the *cosmological constant problem*. Another fundamental question arises from the fact that the present value of the vacuum energy density is of the same order of magnitude as the present matter energy density; whereas in principle there is no correlation between these two quantities. This is the so-called *coincidence problem.* Furthermore, there is no evidence indicating that the vacuum energy has been constant over the past history of the universe, when radiation or matter where the dominant components, nor even if it is really constant at the present. Thus, the true nature of the dark energy component, and hence the underlying cause of the accelerated expansion of the universe, is still an unsettled fundamental question which constitutes a major open problem in cosmology, suggesting that there is new physics missing from our standard cosmological paradigm.

With the aim of understanding the fundamental nature of the accelerated expan-

sion, many alternative theories to GR with a cosmological constant have been proposed. One set of alternatives replace the cosmological constant with a dynamic cosmic scalar field, the so-called *quintessence*, that varies with time and space, slowly approaching its ground state. However, quintessence models are no better than the cosmological constant scenario in avoiding the fine-tuning problem; they do not provide an explanation (*e.g.* via a symmetry principle) for the tiny value of the potential at its ground state, which plays the role of an effective cosmological constant. A more attractive alternative is to modify gravity itself. Modifications of Einstein's gravitational field equations are not unexpected from an effective 4-dimensional description of higher dimensional theories in high-energy physics. Various *modified gravity* theories have been studied in the context of the accelerated cosmic expansion. Some proposed modified gravity models involve extra spatial dimensions, while others modify the Hilbert-Einstein action, *e.g.*, to higher derivative theories, scalar-tensor theories, etc. In particular, $f(R)$ models modify GR by generalizing the Hilbert-Einstein action, replacing the scalar curvature R in its Lagrangian density with a nonlinear function of it. $f(R)$ models are particularly simple phenomenological models which allow to search for small deviations from the ΛCDM scenario. Although these modifications of gravity, in principle, do not solve the cosmological constant problem, they intend to shed light in the interpretation of the dark energy phenomenon.

1.4 Goals of this thesis

In recent years, $f(R)$ modified gravity theories have been considered as a possible explanation of the accelerated expansion of the universe. Some specific types of $f(R)$ models have been proposed and studied in the literature. In order to be cosmologically viable, these models must reproduce the GR expectations at small scales (*e.g.* in the solar system) while giving rise to accelerated expansion at large, cosmic scales. Effectively, viable $f(R)$ models contain small corrections to the Hilbert-Einstein action. In this thesis, the goal is to analyze phenomenological $f(R)$ modified gravity models and their empirical viability against cosmological and solar system constraints.

We begin this thesis by introducing the standard cosmological framework and describing the observations which indicate that the expansion of the universe is currently in an accelerated phase. Then in Chapter 3 we introduce the $f(R)$ modified gravity models as a possible alternative to explain the dark energy phenomenon. We derive the modified Friedmann equations, governing the expansion of the homogeneous universe, as well as the linear perturbation analysis describing the evolution of small inhomogeneities. We also give a general discussion of the conditions under which $f(R)$ models would not violate the constraints imposed by solar system tests.

In Chapter 4, we describe a dynamical systems approach which allows to classify $f(R)$ models according to their qualitative cosmological viability in a homogeneous universe; we summarize under which conditions particular $f(R)$ models can reproduce

an acceptable expansion history according to observations. Five different types of $f(R)$ models are shown to have a qualitatively acceptable expansion history.

Considering these five types of models, in Chapter 5 we perform a quantitative analysis which includes the perturbative analysis of cosmic inhomogeneities up to the linear order; here we confront the models' expansion history and the growth of structure formation with various experimental datasets. Specifically, we confront the expansion history of these $f(R)$ models with SN Ia data, measurements on the CMB shift parameter, BAO acoustic parameter measurements, and data on the Hubble parameter derived from galaxy ages. We furthermore fit the linear growth of structure in these $f(R)$ models to the growth information derived from observations of redshift space distortions. We show that the combination of geometrical probes with data on the linear growth of structure constitutes a robust approach to rule out $f(R)$ models.

Finally, for the types of models which result to be consistent with all the cosmological datasets exploited in this thesis, we analyze their slow-motion, weak-field limits in the parameter ranges in which they are viable at cosmological scales. Using this analysis we determine which models are compatible with the tight constraints imposed by solar system tests.

Chapter 2

The Standard Cosmological Paradigm

In this chapter we review the standard cosmological model and the observational evidence revealing that the universe is currently in an accelerated expansion phase. We start by describing Einstein's field equations and their solutions for a Friedmann-Robertson-Walker metric. At large scales, matter is approximated as a perfect homogeneous fluid, leading to the Friedmann equations for a homogeneous universe. We introduce the definitions of the cosmological parameters and the cosmic distances, which we will use in the following chapters. We describe the standard paradigm of the growth of structure formation and derive the growth of structure equation in GR. We then describe the observations supporting the recent acceleration of the universe's expansion. We finish this chapter by describing the cosmological constant problem.

2.1   Einstein Equations and The Homogenous Universe

2.1.1   Einstein Equations

The theory of General Relativity describes spacetime as a four-dimensional manifold with a geometry characterized by the metric $g_{\mu\nu}$. Einstein's equations are derived from a generally covariant action, which remains invariant under general coordinate transformations $x^\mu \to x'^\mu(x^\nu)$. The Ricci scalar curvature is the only nontrivial scalar which is constructed from the metric, and depends on, at most, second order derivatives of the metric. Using the Ricci scalar as the Lagrangian density leads to the Einstein-Hilbert action, which is given by

$$S_{\mathrm{G}} = \frac{1}{\kappa^2} \int d^4x \sqrt{-g} R \,, \tag{2.1}$$

where $\kappa^2 = 8\pi G$, and G is the Newton's gravitational constant. The action of the closed system containing both, the spacetime metric and the matter fields, is obtained by adding to Eq. (2.1) the action for the matter, $S_{\mathrm{M}} = \int dx^4 \sqrt{-g}\mathcal{L}_{\mathrm{M}}$. Here, $\mathcal{L}_{\mathrm{M}}$ is the matter Lagrangian density, which depends on the matter fields that are not of gravitational nature. Considering infinitesimal variations of $S_{\mathrm{G}} + S_{\mathrm{M}}$ with respect to arbitrary variations of the gravitational field, $\delta g_{\mu\nu}$, yields

$$\frac{1}{\kappa^2}(R_{\mu\nu} - \frac{1}{2}g_{\mu\nu}R) = -\frac{2}{\sqrt{-g}}\frac{\delta(\sqrt{-g}\mathcal{L}_{\mathrm{M}})}{\delta g_{\mu\nu}} \equiv T_{\mu\nu}\,, \qquad (2.2)$$

which leads to Einstein's equations:

$$G_{\mu\nu} \equiv R_{\mu\nu} - \frac{1}{2}g_{\mu\nu}R = \kappa^2\,T_{\mu\nu}. \qquad (2.3)$$

Here, $T_{\mu\nu} \equiv -\frac{2}{\sqrt{-g}}\frac{\delta(\sqrt{-g}\mathcal{L}_{\mathrm{M}})}{\delta g_{\mu\nu}}$ denotes the energy-momentum tensor of all matter fields. The field equations Eqs. (2.3), reflect the fundamental idea that the matter energy content of the universe determines its geometry. The metric tensor is covariantly constant, $g^{\alpha\beta}_{;\mu} = 0$ (where $;\mu$ denotes the covariant derivative). With this property, it can be proved that the Einstein and the energy momentum tensors, $G^{\mu\nu}$ and $T^{\mu\nu}$ respectively, satisfy the Bianchi identities

$$G^{\mu\nu}_{;\nu} = 0\,; \qquad (2.4)$$

$$T^{\mu\nu}_{;\nu} = 0\,, \qquad (2.5)$$

and Eq. (2.5) generalizes the energy conservation law in curved spacetimes.

2.1.2 Friedmann-Robertson-Walker Geometry

Einstein equations are, in general, complicated non-linear equations; only few analytic solutions are known in the presence of strong symmetry constraints. The deepest galaxy catalogs show that, at large scales (beyond 1000 Mpc), the universe is, in good approximation, homogeneous and isotropic. Thus, by imposing these symmetries, we derive the evolution equations at large scales. The most general metric satisfying homogeneity and isotropy is the Friedmann-Robertson-Walker (FRW) metric, which in terms of the invariant geodesic distance $ds^2 = g_{\mu\nu}dx^\mu dx^\nu$ in four dimensions, is given by

$$ds^2 = -dt^2 + a^2(t)\left[\frac{dr^2}{1 - k\,r^2} + r^2(d\theta^2 + \sin^2\theta\,d\phi^2)\right]\,, \qquad (2.6)$$

where $a(t)$ is the scale factor and k is the spatial curvature of the universe, which takes the values $k = 0$ or ± 1. Here, the coordinates r, θ and ϕ are spherical coordinates referred to as comoving coordinates. The worldline of an observer which is at rest in these coordinates (*i.e.*, with time independent r, θ and ϕ) is a geodesic of the metric

Eq. (2.6). Hence, such "comoving" objects or observers are freely falling. The temporal coordinate, t, measures the proper time of comoving observers. It is customary to parametrize the radial coordinate, r, as

$$r = f_k(\chi) \equiv \begin{cases} \sin\chi\,, & k = +1\,, \\ \chi\,, & k = 0\,, \\ \sinh\chi\,, & k = -1\,. \end{cases} \tag{2.7}$$

after which the metric Eq. (2.6) becomes

$$ds^2 = -dt^2 + a^2(t)\left[d\chi^2 + f_k^2(\chi)(d\theta^2 + \sin^2\theta d\phi^2)\right]\,. \tag{2.8}$$

The spatial part of the metric Eq. (2.8), characterizes the geometry of the constant t spatial sections of spacetime, and is that of a homogenous, isotropic 3-dimensional space of constant curvature. The constant k determines the sign of this curvature; for $k = 0$ the space is flat. In the case of positive curvature ($k = +1$), the values of χ are bounded above by π; the spatial part of the metric is that of a 3-sphere whose radius, $i.e.$, the physical size of the universe, is proportional to the scale factor $a(t)$. For this reason, the $k = +1$ universe is referred to as closed. In the negative curvature ($k = -1$) and flat ($k = 0$) cases, χ is unbounded and the universe is infinite. These are referred to as open and flat universes, respectively. As light geodesics on these different geometries behave differently, these alternatives could in principle be distinguished observationally. The only dynamic feature of the metric Eq. (2.8) is $a(t)$, referred to as the scale factor. It represents the time evolution of all physical distances. Depending on its dynamics, we will have different possible outcomes for the evolution of the universe. The universe may expand forever, recollapse, or approach an asymptotic state. Einstein's field equations, Eq. (2.3), allow to determine the dynamics of the scale factor if the matter content of the universe is specified. We will consider this in Sec. 2.1.3.

Hubble's Law and Redshifts

In 1929, E. Hubble [1] observed that the spectral lines of the chemical elements in the galaxies were shifted towards higher wavelengths with respect to those obtained in the laboratory. Based on the classical Doppler effect, he concluded that the galaxies are receding from us with an average speed proportional to their distance. To see this in the FRW spacetime, consider a comoving object ($i.e.$, one with fixed spatial coordinates as defined in Eq. (2.8)) at radial coordinate χ. It can be easily shown that radial paths ($dt = d\theta = d\phi = 0$) are geodesics of Eq. (2.8). Therefore, the length of the radial path connecting the origin ($\chi = 0$) to the comoving object at χ, gives its distance, $d(t)$, from the comoving observer at the origin. The path length can be calculated by integrating ds along this path using Eq. (2.8), yielding $d(t) = a(t)\chi$. Differentiating this expression with respect to time leads to

$$\dot{d} = H(t)d\,, \tag{2.9}$$

where

$$H(t) \equiv \frac{\dot{a}}{a}, \tag{2.10}$$

is the Hubble parameter. Here (and hereinafter), $\dot{} \equiv d/dt$. The galaxies that we can observe are *close* enough in time that $H(t)$ is approximately constant, since the scale factor, $a(t)$, varies slowly. Under this approximation, Eq. (2.9) leads to the Hubble's law: the recession speed of an object, $\dot{d}$, is in good approximation proportional to its distance from us. Theoretically, however, $H(t)$ evolves with time.

In the context of the curved FRW geometry, the redshift of galaxies is caused by the expansion of space itself. Based on the properties of null geodesics (worldlines of photons) in the comoving frame, the redshift z (the relative change in wavelengths) is related to the ratio of scale factors at the emission and observation times, t_{emitted} and t_{obs} respectively. This is,

$$z \equiv \frac{\lambda_{\mathrm{obs}} - \lambda_{\mathrm{emitted}}}{\lambda_{\mathrm{emitted}}} = \frac{a(t_{\mathrm{obs}})}{a(t_{\mathrm{emitted}})} - 1, \tag{2.11}$$

where $\lambda_{\mathrm{emitted}}$ and λ_{obs} are the emitted and observed wavelengths respectively. Commonly, the scale factor at the current era is denoted by $a(t_{obs}) \equiv a_0$, (we will use this notation for any other quantity) and we can rewrite Eq. (2.11) as

$$\frac{a(t_{\mathrm{emitted}})}{a_0} = \frac{1}{1+z}. \tag{2.12}$$

The redshift increases with distance (*i.e.*, looking towards the past), being $z = 0$ today. For small distances, the redshift is proportional to the distance of an object d, via the Hubble's parameter value today H_0, this is $z = H_0 d$.

The latest measurements on H_0 come from the Planck collaboration [2] measurements of the Cosmic Microwave Background (CMB; see Sec. 2.3.1 and Sec. 2.4.3), resulting in

$$H_0 = 100 \, h \,\, \mathrm{km} \,\, \mathrm{sec}^{-1} \,\, \mathrm{Mpc}^{-1}, \tag{2.13}$$
$$h = 0.673 \pm 0.012 \,.$$

As we will discuss in Sec. 2.4.3, Eq. (2.13) is in tension with other recent direct measurements on H_0. From the value of H_0 in Eq. (2.13), the Hubble length and the age of the universe can be estimated from

$$c \, H_0^{-1} = 3000 \, h^{-1} \,\, \mathrm{Mpc} \,; \tag{2.14}$$
$$H_0^{-1} = 9.773 \, h^{-1} \,\, \mathrm{Gyr} \,, \tag{2.15}$$

respectively.

2.1.3 Friedmann Equations and Cosmological Parameters

In the FRW spacetime, the Ricci tensor and the scalar curvature are given by

$$R_0^0 = \frac{3\ddot{a}}{a}, \tag{2.16}$$

$$R_j^i = \left(\frac{\ddot{a}}{a} + \frac{2\dot{a}^2}{a^2} + \frac{2k}{a^2}\right)\delta_j^i, \tag{2.17}$$

$$R = 6\left(\frac{\ddot{a}}{a} + \frac{\dot{a}^2}{a^2} + \frac{k}{a^2}\right). \tag{2.18}$$

At large scales, matter can be approximated as a perfect fluid, which is characterized by its pressure, p, energy density, ρ, and four-velocity field, u^μ (with $u_\mu u^\mu = -1$). For such a fluid, the energy-momentum tensor takes the simple general form

$$T^\mu_{\ \nu} = (p + \rho)\,u^\mu u_\nu + p\,\delta^\mu_\nu, \tag{2.19}$$

where p and ρ are the total pressure and energy density respectively, obtained by summing over the contribution of all forms of matter that fill the universe at the corresponding time. Under the assumption of spatial homogeneity and isotropy, p and ρ can only depend on time. In comoving coordinates, $u^\mu = (1, 0, 0, 0)$, and Eq. (2.19) becomes

$$T^\mu_{\ \nu} = \text{Diag}(-\rho(t),\ p(t),\ p(t),\ p(t)). \tag{2.20}$$

With Eqs. (2.16)-(2.18) and Eq. (2.20), Einstein's equations, Eq. (2.3), lead to

$$\left(\frac{\dot{a}}{a}\right)^2 + \frac{k}{a^2} = \frac{8\pi G}{3}\,\rho\,; \tag{2.21}$$

$$\frac{\ddot{a}}{a} = -\frac{4\pi G}{3}\,(\rho + 3p)\,, \tag{2.22}$$

where Eq. (2.21) is the Friedmann equation, derived from the 0-0 component of Eq. (2.3), and Eq. (2.22) is the acceleration equation, derived from the trace of Eq. (2.3). On the other hand, the conservation of energy-momentum, Eq. (2.5), gives the continuity equation in the FRW spacetime

$$\dot{\rho} + 3\frac{\dot{a}}{a}(p + \rho) = 0\,. \tag{2.23}$$

However, notice that Eq. (2.23) can be derived from Eq. (2.21) and Eq. (2.22), and only two of Eqs. (2.23), (2.21) and (2.22) are independent. Equations (2.21)-(2.22) show explicitly that the energy density and pressure of the matter components characterize the geometry and the dynamics of spacetime.

Cosmic Evolution of a Barotropic Perfect Fluid

In order to find explicit solutions of Eqs. (2.23), an equation of state relating the pressure and the density of the fluid is needed. Considering a barotropic fluid, *i.e.*, its pressure is only a function of its density $p = p(\rho)$, we further assume that p is linearly proportional to ρ,

$$w \equiv \frac{p}{\rho}\,, \tag{2.24}$$

where w is the equation of state parameter (under this approximation, the speed of sound is constant). The sum of Eqs. (2.21) and (2.22) yields $3H^2 + 2\dot{H} = -8\pi G p$, and substituting this together with Eq. (2.21) in Eq. (2.24), leads to the expression of w in terms of the Hubble parameter,

$$w = -1 - \frac{2\dot{H}}{3H^2}\,. \tag{2.25}$$

Different matter components have different equation of state parameters, w_i. We further assume a negligible energy exchange between different components. Under this approximation, the continuity equation, Eq. (2.23), for each component becomes

$$\frac{\dot{\rho}_i}{\rho_i} = -3(1 + w_i)\frac{\dot{a}}{a}\,. \tag{2.26}$$

Integrating Eq. (2.26) yields $\rho_i \propto a^{-3(1+w_i)}$. Summing over the contribution of all components involved in the evolution of the universe lead to the time evolution of the total energy density

$$\begin{aligned} \rho &= \sum_i \rho_i(t_0)(a/a_0)^{-3(1+w_i)}, & \text{(2.27)} \\ &= \sum_i \rho_i(t_0)(1+z)^{3(1+w_i)}, & \text{(2.28)} \end{aligned}$$

where $\rho_i(t_0)$ is the present value of the energy density of the i-th component. We have used the definition of the redshift, Eq. (2.12), to write Eq. (2.28).

There are three specific types of barotropic perfect fluids which describe the different matter-energy components involved in the evolution of the universe; these are characterized by their equation of state parameter:

- **Radiation**, for which $w_R = \frac{1}{3}$. This type of fluid describes relativistic particles (with temperatures much larger than their mass). From Eq. (2.26), the energy density of radiation decays as $\rho_R \propto a^{-4}$ with the expansion of the universe. With this, we can integrate Eq. (2.21) obtaining that, in a flat universe, the expansion of the universe scales with time as $a \propto t^{1/2}$ during radiation domination.

20

- **Matter**, for which $w_M = 0$. This type of fluid describes nonrelativistic particles (with temperatures much smaller than their mass). The energy density of matter decays as $\rho_M \propto a^{-3}$ as the universe expands and, from Eq. (2.21), $a \propto t^{2/3}$ in a flat universe during matter domination.

- **Vacuum energy**. If we neglect the dynamical nature of the (not yet known) mechanism giving rise to the vacuum energy, we can replace it with a cosmological constant, Λ. This constant can effectively be considered a form of matter with an equation of state parameter $w_\Lambda = -1$. From Eq. (2.26), the corresponding energy density remains constant as the universe expands, in this case the scale factor grows exponentially with time.

From Eq. (2.22), whether the expansion of the universe is accelerating ($\ddot{a} > 0$) or decelerating ($\ddot{a} < 0$) depends on the sign of $\rho + 3p$. Matter and radiation can only decelerate the expansion as for them the term $\rho + 3p$ is always positive; this corresponds to the familiar notion that gravity is attractive and hence the gravitation of matter can only slow down the expansion. Vacuum energy, on the other hand, can lead to cosmic acceleration, given that $p = -\rho$, and $\rho + 3p$ can be negative. An accelerating universe implies that the total density and pressure should satisfy $p < -\rho/3$.

Cosmological Parameters

According to the Friedmann equation Eq. (2.21), the sign of the spatial curvature, k, is determined by the balance between the total energy density ρ and what is referred to as the critical density, defined as

$$\rho_c \equiv \frac{3H^2}{8\pi G}, \tag{2.29}$$

which corresponds to the energy density yielding a flat universe ($k = 0$). The current value of the critical density, $\rho_c(t_0)$, can be obtained by using the present measured expansion rate H_0 (Eq. (2.13)),

$$
\begin{aligned}
\rho_c(t_0) \equiv \frac{3H_0^2}{8\pi G} &= 1.88\, h^2\, 10^{-29} \text{ g/cm}^3 \\
&= 2.77\, h^{-1}\, 10^{11}\ M_\odot/(h^{-1}\,\text{Mpc})^3 \\
&= 11.26\, h^2 \text{ protons/m}^3,
\end{aligned} \tag{2.30}
$$

where $M_\odot = 1.989 \times 10^{33}$ g is the solar mass. Equation (2.30) characterizes a very dilute fluid.

The dimensionless density parameters for each species of matter are defined in terms of the critical density as

$$\Omega_i(t) \equiv \frac{\rho_i(t)}{\rho_c(t)}, \tag{2.31}$$

and

$$\Omega_i \equiv \frac{\rho_i(t_0)}{\rho_c(t_0)}, \tag{2.32}$$

at present. From Eq. (2.21),

$$\sum_i \Omega_i - 1 = \frac{k}{(a_0 H_0)^2}, \tag{2.33}$$

The quantity on the right hand side of Eq. (2.33), which determines the spatial curvature, is formally defined as

$$\Omega_k = -\frac{k}{(a_0 H_0)^2}, \tag{2.34}$$

and, considering all species described above, Eq. (2.33) becomes

$$\Omega_R + \Omega_M + \Omega_\Lambda + \Omega_k = 1. \tag{2.35}$$

By substituting Eq. (2.27) into Eq. (2.21) and using the definition Eq. (2.31), we can write the expansion rate, $H(t)$, in terms of the density parameters, Ω_i, of all components,

$$H^2(t) = H_0^2 \left[\Omega_R \left(\frac{a_0}{a(t)} \right)^4 + \Omega_M \left(\frac{a_0}{a(t)} \right)^3 + \Omega_\Lambda + \Omega_k \left(\frac{a_0}{a(t)} \right)^2 \right], \tag{2.36}$$

which can be also written in terms of the redshift, z, by using Eq. (2.12),

$$H^2(z) = H_0^2 \left[\Omega_k (1+z)^2 + \sum_i \Omega_i (1+z)^{3(1+w_i)} \right]. \tag{2.37}$$

The density of photons from the CMB (see Sec. 2.3.1 and Sec. 2.4.3), given by $\rho_{\mathrm{CMB}} = \pi^2 k^4 T_{\mathrm{CMB}}^4 / (15 \hbar^3 c^3) = 4.5 \times 10^{-34}$ g/cm^3, leads to a radiation component today $\Omega_R(\mathrm{CMB}) = 2.4 \times 10^{-5}$ h^{-2} *. Thus, the contribution of radiation to the total energy density of the universe at present can be safely neglected compared to that of non-relativistic matter and vacuum energy.

In Sec. 2.4 we will discuss the current observations which indicate that the universe is approximately flat and that the cosmic expansion is accelerating. According to these observations, about 68% of the total energy density corresponds to a vacuum energy component with negative pressure which accelerates the expansion, almost 27% of the total energy density corresponds to a dark matter component and only 5% corresponds to ordinary matter. The vacuum energy density, so-called *dark energy*, appears to be constant, such that acquires a greater importance as the universe expands. These observations have led to the establishment of the current standard cosmological model,

---

*Massless neutrinos contribute with a quantity of the same order.

the so-called Λ-Cold Dark Matter (ΛCDM) model which is based on six parameters: the physical baryon density, the physical dark matter density, the dark energy density, the scalar spectral index, the curvature fluctuation amplitude and the reionization optical depth (see [3] for more details). In Sec. 2.4 we will see that, according to observations, in the ΛCDM model $\Omega_k \approx 0$, $\Omega_M \approx 0.3$ and $\Omega_\Lambda = 1 - \Omega_M$.

2.2 Cosmic Distances

A particularly useful theoretical notion of cosmological distance is the comoving distance, which factors out the expansion of the universe, giving a distance which does not change in time due to the expansion of space. Consider two comoving observers (*i.e.*, with fixed comoving coordinates), their comoving distance is defined as the length of the spacelike geodesic connecting both observers at the same cosmological time t, divided by the scale factor at that time, $a(t)$. In the coordinate system of Eq. (2.8) centered on one of the observers, the comoving distance is simply given by the fixed χ-coordinate of the other comoving observer. Light follows null geodesics, which in particular satisfy $ds^2 = 0$, and from Eq. (2.8), light worldlines are given by $ds^2 = -dt^2 + a(t)^2(t)\,d\chi^2 = 0$. Solving for $d\chi$, we obtain $d\chi = dt/a(t)$. We can evaluate the comoving distance between both comoving observers by integrating this relation. If light is emitted by a source at redshift z and reaches an observer situated at $z = 0$, the comoving distance can be written as

$$d_c = \int_{t_e}^{t_0} \frac{1}{a(t)} dt = \frac{1}{a_0} \int_0^z \frac{dz'}{H(z')}. \tag{2.38}$$

The comoving distance is, however, not directly measured by observational probes. In order to discuss the observational constraints on the parameters of the FRW universe, we thus need to introduce various different definitions of cosmic distances. There are several ways of probing distances in an expanding universe, leading to different definitions of cosmic distances.

2.2.1 Luminosity Distance

The luminosity distance is defined in terms of the luminosity of a stellar object. In Minkowski spacetime, the energy flux, $\mathcal{F}$, of a source at a distance d, is related to its absolute luminosity, L_s (amount of energy emitted per unit time), through $\mathcal{F} = L_s/(4\pi d^2)$. In an expanding universe this becomes,

$$d_L^2 \equiv \frac{L_s}{4\pi\mathcal{F}}, \tag{2.39}$$

where d_L is the luminosity distance. Consider a luminous object located at a coordinate distance χ_s from an observer at $\chi = 0$. The object emits an energy ΔE_1 in a time

interval Δt_1, and the energy that reaches the sphere with radius χ_s is ΔE_0. The luminosities are given by

$$L_0 = \frac{\Delta E_0}{\Delta t_0} \,, \quad L_s = \frac{\Delta E_1}{\Delta t_1} \,, \tag{2.40}$$

at χ_0 and χ_s respectively. Since $\Delta E_0 \propto \nu_0$ and $\Delta E_1 \propto \nu_1$, and $c = \nu_0 \lambda_0 = \nu_1 \lambda_1$, where ν_0 (ν_1) and λ_0 (λ_1) are the the frequency and wavelengths at $\chi = \chi_0$ ($\chi = \chi_s$) respectively, taking into account that $\nu_0 \Delta t_0 = \nu_1 \Delta t_1$, we can write the relation

$$\frac{\lambda_0}{\lambda_1} = \frac{\nu_1}{\nu_0} = \frac{\Delta t_0}{\Delta t_1} = \frac{\Delta E_1}{\Delta E_0} = 1 + z \,, \tag{2.41}$$

where we have used Eq. (2.11). Combining Eq. (2.40) and Eq. (2.41),

$$L_s = L_0 (1 + z)^2 \,. \tag{2.42}$$

On the other hand, from the metric Eq. (2.8), the area of the sphere with radius χ_s (at $t = t_0$), is given by $S = 4\pi (a_0 f_K(\chi_s))^2$, and the observed energy flux is

$$\mathcal{F} = \frac{L_0}{4\pi (a_0 f_K(\chi_s))^2} \,. \tag{2.43}$$

Substituting Eq. (2.42) and Eq. (2.43) in Eq. (2.39), we obtain the luminosity distance in an expanding universe

$$d_L = a_0 f_K(\chi_s)(1 + z) \,. \tag{2.44}$$

In a flat FRW background $f_K(\chi_s) = \chi_s$, and Eq. (2.44) becomes $d_L = a_0 \chi_s (1 + z)$. Using Eq. (2.38) with $d_c = \chi_s$,

$$d_L = (1 + z) \int_0^z \frac{dz'}{H(z')} \,, \tag{2.45}$$

which can be written in terms of the density parameters and the equation of state of each component by using Eq. (2.37),

$$d_L = \frac{(1 + z)}{H_0} \int_0^z \frac{dz'}{\sqrt{\sum_i \Omega_i (1 + z')^{3(1+w_i)}}} \tag{2.46}$$

Equation (2.45) can be inverted to express the Hubble parameter, $H(z)$, in terms of the luminosity distance $d_L(z)$,

$$H(z) = \left\{ \frac{d}{dz} \left(\frac{d_L(z)}{1 + z} \right) \right\}^{-1} \,. \tag{2.47}$$

Equation (2.47) allows to infer the expansion rate of the universe from luminosity distance measurements.

24

2.2.2 Angular Diameter Distance

The angular diameter distance is the distance to an object of actual size Δx seen under an angle $\Delta \theta$, that is

$$d_A = \frac{\Delta x}{\Delta \theta}. \tag{2.48}$$

Consider a source located at a coordinate distance χ_s from an observer at $\chi = 0$. Using the metric Eq. (2.8), the size of the source, Δx (lying on the surface of a sphere of radius χ_s), at the time t_1 is given by

$$\Delta x = a(t_1) f_K(\chi_s) \Delta \theta. \tag{2.49}$$

Substituting Eq. (2.49) in Eq. (2.48) and using Eq. (2.12), the angular diameter distance becomes

$$d_A = a(t_1) f_K(\chi) = \frac{a_0}{1+z} f_K(\chi), \tag{2.50}$$

and

$$d_A = \frac{a_0}{1+z} \chi. \tag{2.51}$$

in a flat universe (for which $f_K(\chi) = \chi$). In the following chapters we will use the standard definition $a_0 \equiv 1$.

2.3 Gravitational Instability: The Origin of Inhomogeneities

2.3.1 The Early Universe

The observations of the CMB (see Sec. 2.4.3) and the cosmological redshift (described in Sec. 2.1.2), have made the inflationary Big Bang theory [4–6] the standard model of the earliest eras of the universe. According to the inflationary model, an exponential expansion took place between 10^{-36} and 10^{-32} seconds after the big bang singularity. The inflationary period can account for the observed large-scale homogeneity of the universe. During this period, microscopic quantum fluctuations led to small macroscopic inhomogeneities in the smooth energy density distribution of the universe contents. These small inhomogeneities are the seeds of the formation of structures like our own galaxy. From 10^{-10} seconds to today, the history of the universe is based on well understood laws of particle physics and classical gravity, with the important exception of the accelerated expansion at late times, whose fundamental nature remains to be understood.

According to the standard cosmological model, in the first moments after inflation, the universe was extremely hot and dense. The temperature dropped as the universe expanded; below ~ 100 GeV the symmetry between the electromagnetic and the weak

forces was broken. The resulting photon-baryon fluid was in equilibrium in this epoch. Around $T \sim 0.1$ MeV the strong interaction became important and protons and neutrons combined into the light elements (H, He, Li) during the Big Bang Nucleosynthesis (~ 200 s). The abundances of H, He and Li are one of the most successful predictions of the Big Bang theory. The matter and radiation densities were equal around the time corresponding to $T \sim 1$ eV (roughly 10^{11} s after Big Bang). Charged matter particles and photons were strongly coupled in the plasma and fluctuations in the density propagated as cosmic 'sound waves.' Around $T \sim 0.1$ eV (380,000 yrs after the Big Bang), the universe had cooled down to the point that protons and electrons combined into neutral hydrogen atoms in the so-called recombination epoch, that corresponds to a redshift $z \sim 1100$. Before this time, the universe was effectively opaque to radiation (mainly due to the interaction of photons with free electrons via Compton scattering). After recombination the universe became transparent to photons and they have been freely traveling in all possible directions since their last scattering, forming the free-streaming CMB (see Sec. 2.4.3). 13.9 billion years later these photons give us today the earliest picture of the universe. The precise isotropy in the observed CMB temperature (see Sec. 2.4.3) implies that the universe was very homogeneous and isotropic at the time of recombination, with extremely small density differences across the universe. Nonetheless the anisotropies in the CMB temperature, although just a few parts per million at that time [7], provide evidence for small inhomogeneities in the primordial matter density. The latter played a crucial role in the structure formation, providing the seeds for the growth of the very nonlinear structures like galaxies and their clusters which we observe today. The disparity between the smooth photon distribution and the clumpy distribution of matter today is due to radiation pressure. The small matter density fluctuations grow due to gravitational instability to form the large scale structures observed in the late universe, but pressure prevents the clustering of photons. Thus, even though both inhomogeneities have the same origin, they appear very different today. A competition between the background pressure and the universal attraction of gravity determines the details of the growth of structure. During radiation domination the growth was slow; clustering became more efficient as matter started dominating the background density and pressure dropped to zero. Inhomogeneities at small scales became large first, and formed gravitationally bound objects, like stars and galaxies, which decoupled from the background expansion. These small-scale structures merged into larger structures such as galaxy clusters and superclusters which formed more slowly. Finally, at $z < 1$, a negative pressure dark energy component came to dominate the universe. The background spacetime started accelerating, leading to an eventual cessation in the growth of structure.

2.3.2 Linear Cosmological Perturbations

Inhomogeneities in the matter energy density distribution induce perturbations in the metric; in this thesis we consider only linear perturbations. Scalar modes exhibit

gravitational instability and their dynamics leads to the growth of structure formation in the universe. We restrict ourselves to a spatially flat universe, well in agreement with present observations [2]. Throughout this thesis we work in the Newtonian gauge, in which the metric of a flat FRW universe with small perturbations can be written as [8–10]

$$ds^2 = -(1 + 2\Psi)dt^2 + a(t)^2(1 - 2\Phi)\delta_{ij}dx^i dx^j \,. \tag{2.52}$$

Einstein's field equations (Eq. (2.3)) become

$$G^\mu_\nu + \delta G^\mu_\nu = \kappa^2(T^\mu_\nu + \delta T^\mu_\nu) \,, \tag{2.53}$$

where the background tensors, G^μ_ν and T^μ_ν, are defined by Eqs. (2.3) and (2.19) respectively. With the metric Eq. (2.52), the background solution of Eq. (2.53) is given by Eqs. (2.21)-(2.22) and the linearized Einstein's field equations, $\delta G^\mu_\nu = \kappa^2 \delta T^\mu_\nu$, read

$$-\nabla^2\Phi + 3a^2 H(\dot\Phi + H\Psi) = 4\pi G a^2 \delta T^0_0 \,; \tag{2.54}$$

$$-a(\dot\Phi + H\Psi)_{,i} = 4\pi G a^2 \delta T^0_i \,; \tag{2.55}$$

$$\left[a^2\ddot\Phi + a^2 H(3\dot\Phi + \dot\Psi) + a^2(2\dot H + 3H^2)\Psi + \frac{1}{2}\nabla^2(\Psi - \Phi)\right]\delta_{ij}$$
$$+ \frac{1}{2}(\Phi - \Psi)_{,ij} = 4\pi G a^2 \delta T^i_j \,, \tag{2.56}$$

and $\delta G^0_i = -\delta G^i_0$. Decomposition of Eq. (2.56) into its trace and traceless parts yields

$$a^2\ddot\Phi + a^2 H(3\dot\Phi + \dot\Psi) + a^2(2\dot H + 3H^2)\Psi + \frac{1}{3}\nabla^2(\Psi - \Phi) = \frac{4\pi G}{3}a^2 \delta T^i_i \,; \tag{2.57}$$

$$(\Phi - \Psi)_{,ij} = 8\pi G a^2 \delta T^i_j \,, \quad i \neq j \,. \tag{2.58}$$

The linearized stress-energy tensor of a perfect fluid in the Newtonian gauge read

$$\delta T^0_0 \;=\; -\delta\rho \,; \tag{2.59}$$
$$\delta T^0_i \;=\; -\delta T^i_0 = -(\rho + p)v_{,i} \,; \tag{2.60}$$
$$\delta T^i_j \;=\; \delta p \delta^i_j \,, \tag{2.61}$$

where v is the velocity of perturbations. Equation (2.58) together with Eq. (2.61) lead to [†]

$$(\Phi - \Psi)_{,ij} = 0 \,, \quad i \neq j \,. \tag{2.62}$$

Since Ψ and Φ are the metric perturbations, the only consistent solution of Eq. (2.62) is $\Psi = \Phi$ [‡], remaining only one degree of freedom in the scalar metric perturbation.

[†] Equation (2.62) is only valid for perfect fluids, it is proportional to spatial derivatives of the anisotropic stress tensor (or anisotropic pressure) otherwise.

[‡] Since the spatial average of a perturbation is always zero, the equality of gradients of two perturbations means the equality of those perturbations themselves.

This solution together with Eqs. (2.54)-(2.55)-(2.57) and using Eqs. (2.59)-(2.60)-(2.61) yields

$$\nabla^2\Psi - 3a^2 H(\dot{\Psi} + H\Psi) = 4\pi G a^2 \delta\rho\,; \qquad (2.63)$$

$$a(\dot{\Psi} + H\Psi)_{,i} = 4\pi G a^2 (\rho + p) v_{,i}\,; \qquad (2.64)$$

$$a^2\ddot{\Psi} + 4a^2 H\dot{\Psi} + a^2(2\dot{H} + 3H^2)\Psi = 4\pi G a^2 \delta p\,. \qquad (2.65)$$

In a non-expanding universe, in which $H = 0$, Eq. (2.63) becomes exactly the usual Poisson equation for the gravitational potential. In the case of an expanding universe, time derivatives can be neglected with respect to spatial derivatives at sub-horizon scales and the second and third terms of the left hand side of Eq. (2.63) can be neglected with respect to the first term. Thus, Eq. (2.63) generalizes the Poisson equation and supports the interpretation of Ψ as the relativistic generalization of the Newtonian gravitational potential.

In this thesis we are interested in the expansion history of the universe at late times, at which the accelerated expansion begins to dominate. At such low redshifts ($z < 1$), the radiation component can be neglected, as we have discussed at the end of Sec. 2.1.3. Furthermore we consider the scenario in which the accelerated expansion arises due to modifications of the gravitational sector instead of due to a vacuum energy component. Thus, we are only interested in pressureless matter perturbations as the source of metric perturbations. In Fourier space, the conservation equation Eq. (2.5) at first order in perturbations leads to the adiabatic conservation equations

$$\dot{\delta} = 3\dot{\Phi} - \theta\,; \qquad (2.66)$$

$$\dot{\theta} = -H\theta + \left(\frac{k}{a}\right)^2 \Psi\,, \qquad (2.67)$$

where θ is the velocity divergence. A combination of Eqs. (2.66) and (2.67) leads to

$$\ddot{\delta} + H\dot{\delta} = 3\ddot{\Phi} + 3H\dot{\Phi} - \frac{k^2}{a^2}\Psi\,. \qquad (2.68)$$

Again, neglecting the time derivatives of the potentials with respect to its spatial derivatives at sub-horizon scales, and using Eq. (2.63) in Fourier space ($k^2\Psi = -4\pi G a^2 \delta\rho$), Eq. (2.68) leads to the growth factor equation

$$\ddot{\delta} + H\dot{\delta} - 4\pi G \delta\rho = 0\,. \qquad (2.69)$$

Equation (2.69) shows that the dynamics of the growth of structure in GR is independent of the scale. As we shall see in the next chapter, this is not the case in the modified gravity theories that we consider.

2.4 Observational Evidence of the Accelerated Expansion

As we have previously stated, cosmological observations indicate that the expansion of the universe is currently accelerating. A minute vacuum energy component with negative pressure, known as dark energy, is believed to be the acceleration's underlying mechanism. The existence of dark energy is supported by many observations and is, by cosmological standards, a very late-time phenomenon in the history of the universe, starting at redshift $z < 1$. The acceleration of the expansion was first observed in 1998, when two groups independently measured the luminosity of Supernovae Type Ia (SN Ia) [11, 12]. In the following we review the most relevant observations indicating that the universe is in an accelerating phase; in each case, we point out how current cosmological models lacking a dark energy component are unable to account for the observation.

2.4.1 Supernovae Ia Measurements of Cosmic Acceleration

The Supernovae (SN) are classified according to their spectral characteristics and the most useful in cosmology are those called Type Ia. The SN Ia is the final state of the evolution of a stellar binary system composed of a standard star (sustained by thermal energy) and a compact star, typically a white dwarf (a carbon star which burned up its nuclear fuel and counteracts gravity by the degeneracy pressure of electrons, due to Pauli's principle repulsion). The compact star has a much larger mass than the standard star. When the latter reaches the state of a red giant, the compact star begins accruing its gases through gravitational interaction. The mass of the white dwarf becomes large enough to reach the temperature to create a thermonuclear explosion which can reach the luminosity of an entire galaxy. The crucial feature of such explosions is that they occur when the compact star passes the same universal mass limit, the Chandrasekhar limit [13] ($\sim 1.4 M_\odot$). As a consequence, the intrinsic luminosity of the phenomena is always the same. Assuming that SN Ia are formed in the same way independently of their location in the universe, they must have a common absolute magnitude independent of the redshift. This feature makes SN Ia ideal *standard candles*. The absolute magnitude, M, of the source is related to the logarithm of the luminosity, and its apparent magnitude, m, is related to the logarithm of the flux. Both are related to the luminosity distance, d_L (see Eq. (2.39)), by the distance moduli

$$\mu = m - M = 5 \log_{10}\left(\frac{d_L}{Mpc}\right) + 25 \ , \tag{2.70}$$

where the numerical factors come from astrophysical conventions in the definitions of m and M. The luminosity distance can be derived from Eq. (2.70) once the relative magnitude is measured. The redshift of the source can be obtained simply by spectroscopic measurements and the Hubble parameter can be inferred from Eq. (2.47).
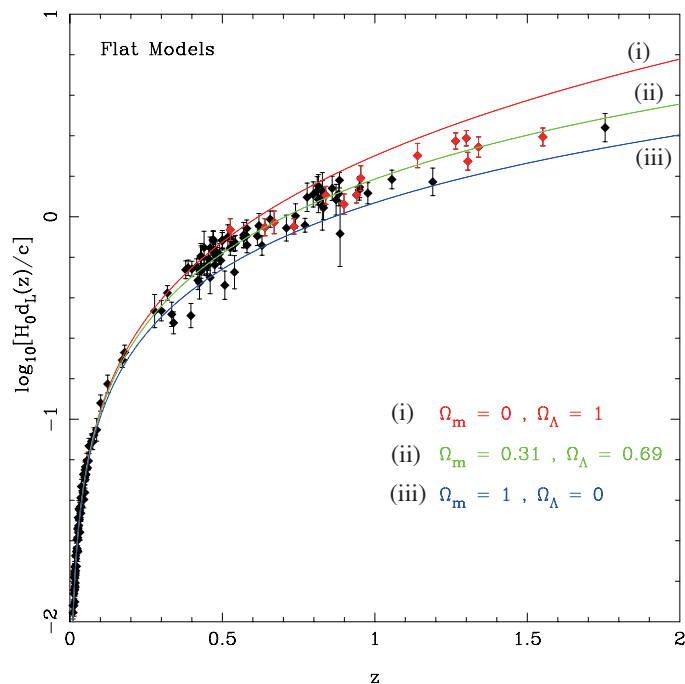
Figure 1: The luminosity distance $H_0 d_L$ versus the redshift z for a flat cosmological model. The black points come from the "Gold" data sets by Riess *et al.* [14], whereas the red points show the data from HST. The three curves show the theoretical values of $H_0 d_L$ for (i) $\Omega_M = 0$, $\Omega_\Lambda = 1$, (ii) $\Omega_M = 0.31$, $\Omega_\Lambda = 0.69$ and (iii) $\Omega_M = 1$, $\Omega_\Lambda = 0$. Extracted from Ref. [15].

Up to 1998, Perlmutter *et al.* [Supernova Cosmology Project (SCP)] discovered 42 SN Ia in the redshift range $z = 0.18\text{-}0.83$ [12], whereas Riess *et al.* [High-z Supernova Search Team (HSST)] had found 14 SN Ia in the range $z = 0.16\text{-}0.62$ and 34 nearby SN Ia [11]. In 2004 Riess *et al.* [14] reported the measurement of 16 high-redshift SN Ia with redshift $z > 1.25$ with the Hubble Space Telescope (HST). By including the 170 previously known SN Ia data points, and assuming a flat universe ($\Omega_M + \Omega_\Lambda = 1$), they showed that, at $z \sim 0.3$, the universe exhibited a transition from deceleration to acceleration at $> 99\ \%$ confidence level (CL). The best-fit value of the matter energy density was found to be $\Omega_M = 0.29^{+0.05}_{-0.03}$, showing that a dark energy density component with an equation of state parameter $w \approx -1$, must be present and has to be roughly the 70% of the total energy density of the universe. Figure 1 depicts the observational values of the luminosity distance, d_L, versus redshift, z, together with the theoretical curves derived from Eq. (2.46). This shows that the data can not be fitted by a matter dominated universe without a dark energy component ($\Omega_M = 1$).

2.4.2   Age of the Universe

When comparing the age of a matter dominated universe, t_0, with the age of the oldest stellar populations, t_s, another evidence for the existence of the accelerated expansion emerges. Obviously, $t_0 > t_s$ is required. However, this condition is not satisfied by the t_0 estimated for a flat cosmological model only sourced by non-relativistic matter and radiation, with no vacuum energy. As we shall see, the presence of a vacuum energy can resolve this discrepancy.

Different research groups have estimated the age of the oldest stars with different methods. One group, Jimenez *et al.* [16] estimated the age of globular clusters in the Milky Way to be $t_1 = 13.5 \pm 2$ Gyr. Richer *et al.* [17] and Hansen *et al.* [18] obtained $t_1 = 12.7 \pm 0.7$ Gyr to be the age of the globular cluster $M4$. Thus, the age of the universe is constrained and must to satisfy the lower bound, $t_0 > 11 - 12$ Gyr.

The inverse of the Hubble parameter gives an estimate of the age of the universe. From Eqs. (2.13) and (2.12), we obtain the relation $dt = -dz / \left[(1 + z) H \right]$, and the age of the universe can be inferred from its integral,

$$t_0 = \int_0^\infty \frac{dz}{(1 + z) H(z)}. \tag{2.71}$$

Equation (2.71) can be solved by using Eq. (2.37), given the values of the density parameters, Ω_i, of all species in the universe and the space curvature k. The radiation dominated period is negligible compared to the matter dominated epoch (*i.e.*, the contribution to the integral coming from the region $z \geq 1000$ is much smaller than the value of the total integral). Thus, is a good approximation to neglecting the contribution of Ω_R. In a flat universe, $\Omega_k = 0$, filled with non-relativistic matter ($w_M = 0$) and without a vacuum energy component, $\Omega_\Lambda = 0$, Eq. (2.35) leads to $\Omega_M = 1$; in this case Eq. (2.71) has the simple solution $t_0 = 2/(3H_0)$. From Eq. (2.13) and Eq. (2.15), this gives $t_0 \sim 9.7$ Gyr , which is inconsistent with the stellar age bound, $t_0 > 11 - 12$ Gyr. If we consider a non-flat universe with arbitrary curvature, k, again without a vacuum energy component, filled with non-relativistic matter, Eq. (2.35) leads to $\Omega_k = 1 - \Omega_M$. This, together with Eq. (2.37), gives the solution to Eq. (2.71),

$$t_0 = \frac{1}{H_0} \frac{1}{1 - \Omega_M} \left[1 + \frac{\Omega_M}{2\sqrt{1 - \Omega_M}} \ln \left(\frac{1 - \sqrt{1 - \Omega_M}}{1 + \sqrt{1 - \Omega_M}} \right) \right]. \tag{2.72}$$

In the limit of $\Omega_k \to 1$ ($\Omega_M \to 0$), Eq. (2.72) approaches the value $t_0 = 1/H_0 = 13$ Gyr; this shows that in an open universe model, $\Omega_k > 0$, it is possible to increase the model's prediction of the cosmic age (as the matter density decreases, it would take longer for gravitational interactions to slow down the expansion rate to its present value). However, the spatial curvature is constrained by CMB (see Sec. 2.4.3) observations [2,7] to be much smaller than unity and $\Omega_k = \Omega_M - 1 << 1$. With this constraint, Ω_k cannot be large enough to bring the cosmic age up to the lower bound, $t_0 > 11 - 12$ Gyr. When considering a flat universe with a vacuum energy component given by a cosmological
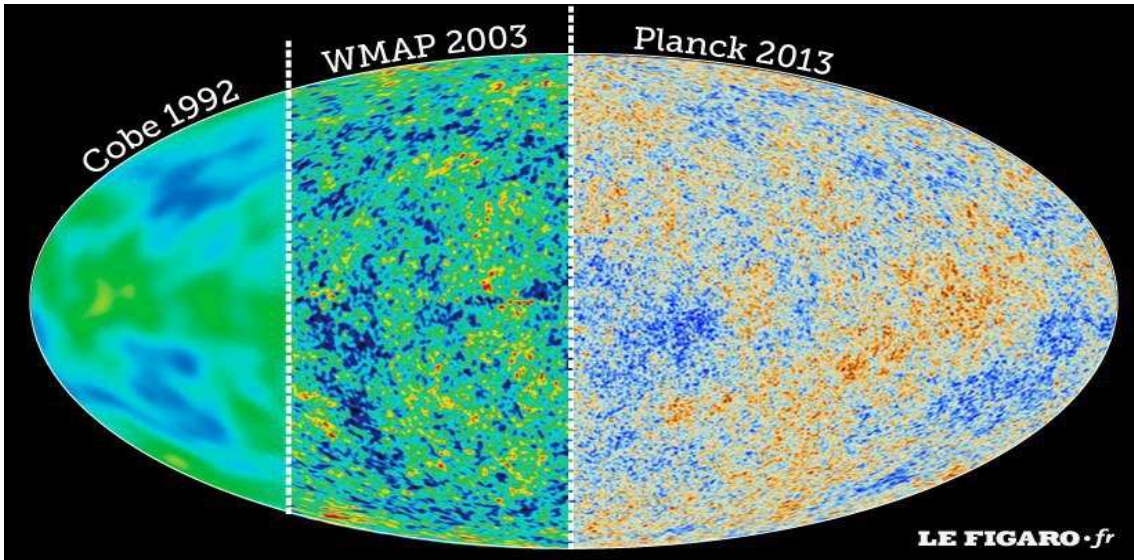
Figure 2: Map of the CMB temperature fluctuations from COBE, WMAP and Planck data. The average temperature is 2.725 K and the colors represent the tiny temperature fluctuations. Red regions are warmer and blue regions are colder.

constant, Ω_Λ, Eq. (2.35) yields $\Omega_\Lambda = 1 - \Omega_M$, and the solution to Eq. (2.71) is given by

$$t_0 = \frac{2}{3H_0\sqrt{1-\Omega_M}} \ln\left(\frac{1+\sqrt{1-\Omega_M}}{\sqrt{\Omega_M}}\right). \tag{2.73}$$

In this case, $t_0 \rightarrow 2/3H_0$ when $\Omega_M \rightarrow 1$ and $t_0 \rightarrow \infty$ when $\Omega_M \rightarrow 0$. The age of the universe increases as Ω_M decreases. For $\Omega_M = 0.3$ ($\Omega_\Lambda = 0.7$), Eq. (2.73) leads to $t_0 = 0.964H_0^{-1}$, and using Eqs. (2.13) and (2.15), $t_0 = 13.9\,\mathrm{Gyr}$, which satisfies the constraint $t_0 > 11\text{-}12\,\mathrm{Gyr}$, coming from the oldest stellar populations. The best fit value of the age of the universe coming from Planck [2] measurements results in $t_0 = 13.813 \pm 0.058$ Gyr, assuming a ΛCDM model.

2.4.3 Cosmic Microwave Background

The CMB was accidentally discovered by A. Penzias and R. Wilson in 1965 [19], opening a window to the universe when it was only about 4×10^5 years old. The photons forming the CMB have been redshifted, and today we observe the CMB to have a perfect blackbody spectrum peaking in the microwaves, with a nearly isotropic temperature $T \simeq 2.73$ K, with small relative deviations $\delta T/T \lesssim 10^{-5}$ [20]. These small temperature fluctuations were first detected by the Cosmic Bakground Explorer (COBE) satellite in 1992 [21]. Since then many other experiments have measured these anisotropies on different angular scales, providing a wealth of new cosmological data which has led to the current standard cosmological model. From 2003 until 2013 the Wilkinson

32

Microwave Anisotropy Probe (WMAP) [22, 23], has provided the most accurate measurements, revealing information on the most fundamental questions, such as the age of the universe, its spatial geometry and the density of its matter contents. WMAP data strongly support the current theory of structure formation, arising from gravitational instabilities and the inflationary Big Bang theory. In 2013 the Planck mission [24] released more accurate measurements of CMB anisotropies than WMAP, leading to an improvement in the constraints on the cosmological parameters and to a robust proof of the standard cosmological model. Figure 2 shows a map of the CMB temperature anisotropies comparing the resolution since the anisotropies were first measured until 2013.

The great uniformity on the photon distribution allows for a linear perturbation approach to analyze the CMB temperature anisotropies. If the fluctuations are gaussian, the multiple moments of the temperature field are fully characterized by their temperature power spectrum, C_ℓ, for different spherical harmonics ℓ; the values of C_ℓ for different ℓ's are statistically independent, hence prediction and analyses are conveniently performed in harmonic space. On small sections of the sky, where the curvature can be neglected, the spherical harmonic analysis becomes ordinary Fourier analysis in two dimensions, with ℓ effectively the Fourier wavenumber; large multipole moments (large ℓ's) correspond to small angular scales, $\ell \sim 2\pi/\theta$ (with $\ell \sim 10^2$ representing the scale of one angular degree). Under this approximation, the temperature power spectrum becomes $(\delta T/T)_\ell^2 \equiv \ell\,(1+\ell)\,C_\ell/2\pi$ (power per logarithmic interval in wavenumber for $\ell \gg 1$). The crucial feature of the acoustic peaks is that, they only exist because all modes of a particular wavelength are in phase everywhere in the universe. Given that all the photons that reach us started their journey at the time of recombination, the temporal phase is a constant and the pattern of hot and cold temperature produced by each mode is originated in their spatial dependency. The contribution from a given mode peaks as $\ell \sim kD_{LSS}$ where D_{LSS} (LSS denotes Last Scattering Surface) is the distance that the photon has travelled towards the observer after its last scattering. In this scenario, the universe is filled with standing waves, all modes of a given wavenumber are in phase and there is perfect coherence. Each mode ℓ receives contributions preferentially from Fourier modes of a particular wavelength and the phase of their oscillation gets mapped into the power we observe at a particular ℓ.

Figure 3 shows the temperature anisotropies from Planck data [24] together with the best fit to the standard cosmological model. Observations on small and intermediate angular scales agree extremely well with the ΛCDM model predictions. However the fluctuations detected on large angular scales on the sky (between 90 and six degrees) are about 10 per cent weaker than the best fit of the ΛCDM model to Planck data. This anomaly in the CMB pattern remains to be understood, indicating that, besides the great improvement in our understanding of the universe, there are still fundamental aspects of the standard cosmological model under question marks. The specific features of the CMB temperature power spectrum provide information on combinations of fundamental cosmological parameters, the shape of its peaks is mainly sensitive to the
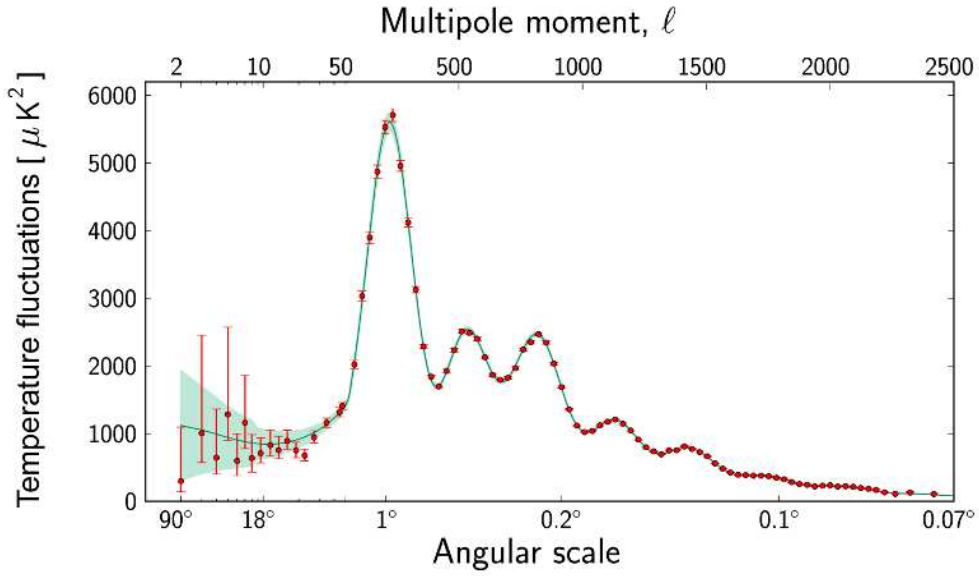
Figure 3: The CMB temperature power spectrum $(\delta T/T)_\ell^2 \equiv \ell\,(1+\ell)\,C_\ell/2\pi$ versus the multiple ℓ and the angular size θ. The red dots are the Planck data and the green curve represents the best fit of the ΛCDM model. The pale green area around the curve shows the predictions of all the variations of the standard model that best agree with the data (the cosmic variance). Extracted from ESA and the Planck Collaboration [2].
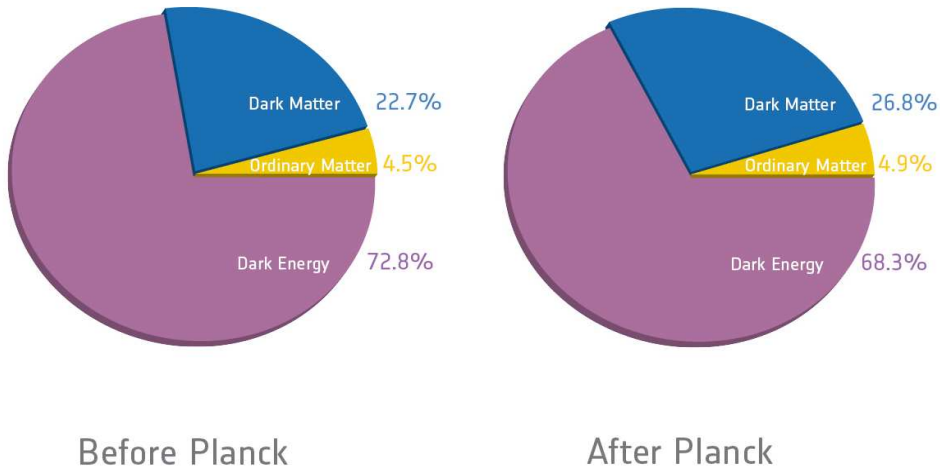
Figure 4: Matter contents of universe before and after Planck.

value of $\Omega_b h^2$ (where Ω_b is the density parameter for baryons), $\Omega_M h^2$, and to the scalar spectral index of primordial density fluctuations, n_s. From these measurements, the cosmological parameters estimated by Planck [2] for the ΛCDM model are significantly different from the values previously estimated by other experiments. In particular, Planck data leads to a weaker cosmological constant (by 2%), more baryons (by 0.3%), and more cold dark matter (by 5%) (see Fig. 4). The parameter estimates lead to a value of the Hubble constant, $H_0 = 67.3 \pm 1.2 \, (\mathrm{km \, s^{-1} \, Mpc^{-1}})$, and a value of the matter density, $\Omega_M = 0.315 \pm 0.017$. These values are in tension with other recent direct measurements of H_0, such as the one obtained by the Hubble Space Telescope (HST) [25] (which gives $H_0 = 74.3 \pm 1.5$ km sec^{-1} Mpc^{-1}). However they are in excellent agreement with current Baryonic Acoustic Oscillations (BAO; see Sec. 2.4.5) measurements when considering their estimate of the Hubble constant. The tension between different data sets remains to be understood. Planck data are also consistent with spatial flatness. Using CMB and BAO data, the dark energy equation of state is constrained by Planck to be $w = -1.13^{+0.13}_{-0,10}$.

2.4.4 Large Scale Structure

According to the standard paradigm, cosmic structures grow from small matter density perturbations in the early universe due to gravitational instabilities. Overdensities are characterized through the density contrast,

$$\delta\left(t, \vec{x}\right) = \frac{\rho\left(t, \vec{x}\right) - \bar{\rho}\left(t\right)}{\bar{\rho}\left(t\right)}, \qquad (2.74)$$

which quantifies the change in the energy density, $\rho\left(t, \vec{x}\right)$, with respect to the background density, $\bar{\rho}\left(t\right)$. From a statistical approach, matter overdensities and other related quantities are elements of an ensemble, its evolution encodes the large scale

structures's dynamics. Initial density perturbations in the early universe are represented as Gaussian random variables with an initial matter power spectrum given by the Fourier transform of the $\delta(t, \vec{x})$ two-point correlation function,

$$P(k)(2\pi)^3 \delta_D(\vec{k} - \vec{k'}) = \langle \delta(\vec{k}) \delta^*(\vec{k'}) \rangle. \tag{2.75}$$

Clustering has an effect at late times turning the density contrast non Gaussian. When the density contrast is small, at large scales, a linear perturbation approach is sufficient to study its evolution, in this case each Fourier mode $\delta_k(t)$ grows independently. At small scales linear theory breaks down and an analytical approach becomes very complicated, the computations of these modes are mainly based on numerical results. The large scale structures of the universe began to be formed after matter-radiation equality a_{eq}, when the supported pressure due to photons becomes smaller than the gravitational attraction due to the non relativistic matter component. Since non-relativistic matter has a negligible pressure relative to its energy density, the gravitational attraction becomes stronger and objects in the universe start to form. The matter-radiation equality fixes the position of the peak in the matter power spectrum, see Fig. 5; the wavenumber k_{eq} corresponds to the one that entered the Hubble radius at the radiation-matter equality (*i.e.*, $k_{eq} = a_{eq}H(a_{eq})$) and it characterizes the transition between "large scale" and "small scale" modes.

The observations of large scale structures such as galaxy clustering, provide another independent observational test for the existence of dark energy. Although the galaxy power spectrum by itself does not provide tight bounds on the vacuum energy density parameter Ω_Λ, observations of large scale structure must be consistent with the existence of dark energy [26, 27]. Figure 5 shows the matter power spectrum for two different flat cosmologies: ΛCDM with $\Omega_M = 0.289$ and CDM with $\Omega_M = 1$ (left panel), computed with the Code for Anisotropies in the Microwave Background (CAMB) [28]. The position of the peak in the matter power spectrum, $P_m(k)$, is shifted toward larger scales (smaller k) in the presence of a vacuum energy component; the scale of the position of this peak can be used as a probe of dark energy. The right panel shows the galaxy power spectrum of the Luminous Red Galaxy (LRG) and main galaxy samples of the SDSS experiment [29]. The position of the peaks are around $0.01h$ Mpc $< k < 0.02h$ Mpc indicating that the ΛCDM model is favored over the CDM one without a cosmological constant.

2.4.5 Baryon Acoustic Oscillations

The acoustic phenomenon was first predicted by J. Peebles and J. Yu [31], and R. Sunyaev and Y. Zeldovich [32]. According to the standard cosmological model, before recombination all matter components are confined inside regions of overdensity perturbations originated during inflation. Photons are tightly couple to baryons, forming a primordial plasma that interacts gravitationally with the dark matter overdensity in the region. However the photon pressure counteracts the gravitational attraction
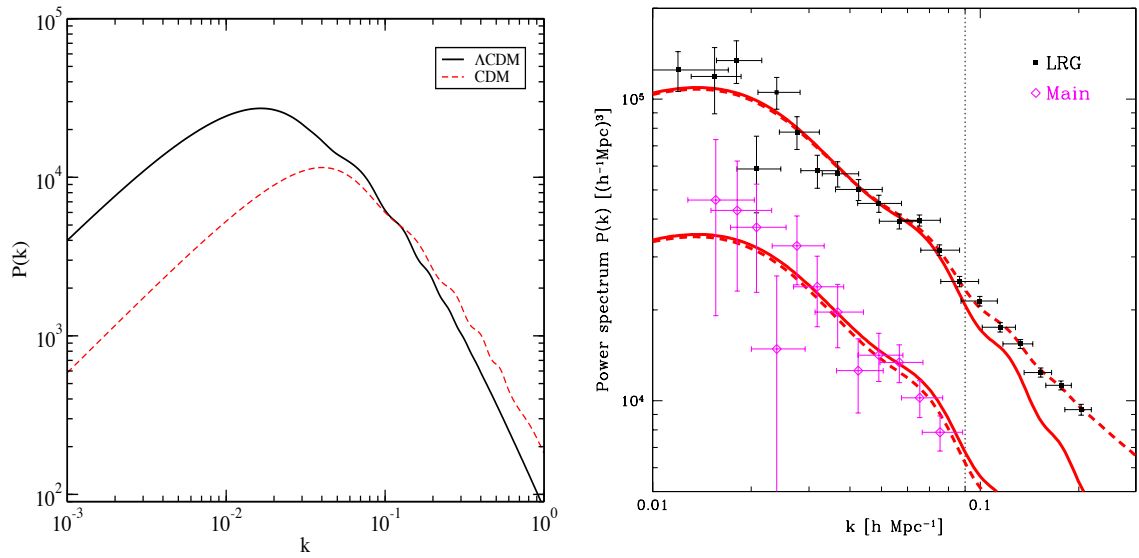
Figure 5: In the left panel, the matter power spectrum for a flat ΛCDM model with $\Omega_M = 0.289$ (solid line) and for a CDM model with $\Omega_M = 1$ (dashed line) computed with CAMB [30]. In the right panel, the measured matter power spectrum with error bars for the full luminous red galaxy sample (LRG) and the main galaxy sample from SDSS. The solid curves show the linearized distribution prediction by ΛCDM. The dashed curves include the non-linear correction to the matter power spectrum. Figure extracted from [29].

and as a result spherical sound waves are produced in the plasma. Since neutrinos are not coupled to the rest of the matter, they start to diffuse out of the sound wave. The CDM distribution is significantly 'smoothed' due to the gravitational interaction with the outward-traveling baryon-photon perturbation. After recombination photons begin to diffuse out of the sound wave, baryons are released from the photon pressure and the sound speed drops radically. The slow motion of the baryonic shell continues down to $z \sim 200$ (the so-called drag epoch) [33]. After that redshift baryons decouple from the photons completely and start falling back onto the central CDM density mean, which has grown significantly since the matter-radiation equality. The baryonic density is not completely negligible, its gravitational interaction with the CDM component appears as a small density enhancement in the final matter density profile at the distance corresponding to the size of the sound horizon at the end of the drag epoch. As a consequence, the effects of the acoustic oscillations remain imprinted in the spatial distribution of baryons and CDM.

In this scenario, the acoustic peaks in the temperature power spectrum of the CMB are predicted to be present also in the clusters of galaxies as a series of weak fluctuations as a function of scale. An enhancement in the two-point correlation function of $\delta(t, \vec{x})$ is expected at the separation corresponding to the sound horizon, given by the comoving distance that a sound wave can travel before recombination. This relatively narrow peaks in the correlation function of the density contrast, leads to an oscillating behavior in the matter power spectrum, usually called *wiggles* [34–36], which encodes precious information on the expansion rate of the universe. At a given redshift, the comoving size of an object along the line of sight $\lambda_{\parallel}$, is related to the observed size of the object Δz, through the Hubble parameter $H(z)$, and the comoving size of the object in the transverse direction $\lambda_{\perp}$, is related to the observed size $\Delta\theta$, through the angular diameter distance d_A. When the true scales, $\lambda_{\parallel}$ and $\lambda_{\perp}$, are known, measurements on the observed dimensions, Δz (deep in space) and $\Delta\theta$ (wide in angle), give estimates on $H(z)$, d_A, and information on the cosmological parameters can be extracted. Thus, the position of the *wiggles* in the matter power spectrum serves as a *standard ruler* [37, 38] and measurements of the corresponding scale at low redshifts provide information on the magnitude of the acceleration of the universe's expansion. The physical length scale of the acoustic oscillations depends on the sound horizon at the recombination epoch, which is given by the baryon and matter densities. These densities are measured with excellent accuracy from the relative heights of the acoustic peaks in the temperature power spectrum of the CMB. Comparing high precision measurements of the acoustic peaks in the galaxy power spectrum with the temperature power spectrum of the CMB, provides spectacular confirmation of the standard cosmological model of the growth of structure formation.

The detection of the acoustic signature imprinted in the correlation of matter distribution requires the survey of large sky volumes ($1h^{-3}\mathrm{Gpc}^3$) since the signal is about 10% contrast in the matter power spectrum. A clear signal of Baryonic Acoustic Oscillations (BAO) was first detected by the galaxy surveys 2dFGRS [39] and SDSS [40]. BAO
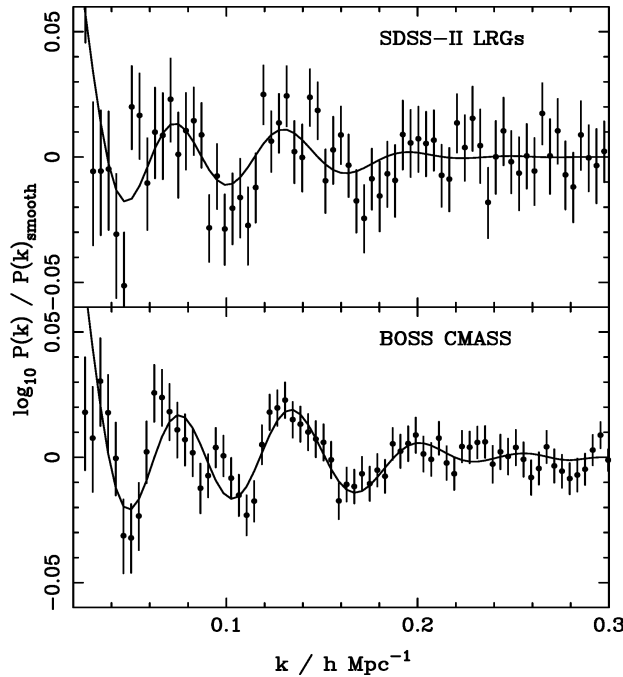
Figure 6: The lower panel shows the BAO signature in the matter power spectrum measured from BOSS data (the CMASS catalogue comprehend the high redshift galaxies of BOSS, $0.43 < z < 0.7$) (with 1σ errors). The upper panel shows the BAO signature from the SDSS-II LRG data (with 1σ errors). Solid curves depict the best-fit models. Figure extracted from [41].

measurements have been greatly improved over the last years by the last generation surveys; the acoustic features have been already detected at a significance of 7σ [41, 42] in the matter power spectrum. We shall summarize the recent data in Sec. 5.1.4. Figure 6 shows the BAO signal in the matter power spectrum from the Baryon Oscillation Spectroscopic Survey (BOSS) [43], part of SDSS-III [44] (lower panel), compared with the one computed from SDSS-II LRG data [45, 46] (upper panel).

2.5   The Cosmological Constant Problem

The cosmological constant, Λ, was introduced for the first time by Einstein in 1917 [47]: when applying GR to cosmology, he found the first cosmological solution of a consistent theory of gravity. He introduced this term only for the purpose of making possible a quasi-static distribution of matter, as required by the fact of the small velocities of the stars observed at that time. Twelve years later, Hubble announced the observed recession of galaxies and the term was dropped from Einstein's equations as it was no longer required. However, from the point of view of particle physics, the cosmological constant arises naturally as an energy density of the vacuum and unfortunately it was

not so simple to drop it from the equations because, anything that contributes to the energy density of the vacuum acts just like a cosmological constant, as it was well discussed by Weinberg in 1989 [48]. But the energy scale of Λ, if originated from the vacuum energy density, it should be much larger than the energy scale of the present Hubble parameter H_0. This is the cosmological constant problem and was well known before the observed accelerated expansion in 1998. However, after this discovery, the problem has been extensibly studied from many different perspectives since the cosmological constant is the simplest candidate for the dark energy phenomenon given that it is characterized by a constant energy density in spacetime and its parameter of the state equation is simply $w = -1$. Moreover it is a simple term to be added in the Lagrangian, it appears as a constant added to R. But there are two fundamental questions to be solve in this regard, namely *the fine tuning problem* and *the coincidence problem.*

Consider the action of the gravity sector S_G in Eq. (2.1) with a cosmological constant,

$$ S_G = \frac{1}{\kappa^2} \int dx^4 \sqrt{-g}(R - 2\Lambda) \,, \tag{2.76} $$

the field equations become

$$ R_{\mu\nu} - \frac{1}{2}g_{\mu\nu}R + \Lambda g_{\mu\nu} = \kappa^2 T_{\mu\nu} \,. \tag{2.77} $$

Since the metric $g^{\mu\nu}$ is constant with respect to covariant derivatives ($g^{\mu\nu}_{;\alpha} = 0$), there is a freedom to add a term $\Lambda g_{\mu\nu}$ in Einstein's field equations and preserve covariance (the cosmological term is, in four dimensions, the only possible generally covariant term to be added when no higher than second order derivatives of the metric are allowed). Thus, Eqs. (2.4) and (2.5) hold. By taking the trace of Eq. (2.77), we find that $-R + 4\Lambda = \kappa^2 T$. Combining this relation with Eq. (2.77), we obtain

$$ R_{\mu\nu} - \Lambda g_{\mu\nu} = \kappa^2 \left(T_{\mu\nu} - \frac{1}{2}T g_{\mu\nu} \right) \,. \tag{2.78} $$

Considering Newtonian gravity with a metric $g_{\mu\nu} = \eta_{\mu\nu} + h_{\mu\nu}$, where $h_{\mu\nu}$ is the perturbation around the Minkowski metric $\eta_{\mu\nu}$, we can neglect the time-variation and rotational effect of the metric and g_{00} is given by $g_{00} = -1 - 2\Psi$. With these approximations we can write R_{00} in terms of the gravitational potential Ψ, as $R_{00} \simeq -(1/2)\Delta h_{00} = \Delta\Psi$. In the relativistic limit with $|p| \ll \rho$, we can take the approximation $T_{00} \simeq -T \simeq \rho$, and the 00 component of Eq. (2.78) is

$$ \Delta\Psi = 4\pi G\rho - \Lambda \,, \tag{2.79} $$

which means that to reproduce the Poisson equation in Newtonian gravity, it is required that either $\Lambda = 0$ or $\Lambda << 4\pi G\rho$. The cosmological constant becomes important on very large scales given that Λ has dimensions of $[\text{Length}]^{-2}$ and the scale corresponding to the cosmological constant needs to be much larger than the scale of stellar objects

at which Newtonian gravity is well tested. In the FRW background, the modified Friedmann Eqs. (2.21) and (2.22) become

$$H^2 = \frac{8\pi G}{3}\rho - \frac{k}{a^2} + \frac{\Lambda}{3} \,, \tag{2.80}$$

$$\frac{\ddot{a}}{a} = -\frac{4\pi G}{3}\left(\rho + 3p\right) + \frac{\Lambda}{3} \,. \tag{2.81}$$

Equation (2.81) clearly shows that Λ acts as a repulsive effect against gravity. From Eq. (2.80), in order to have a late-time phase of accelerated expansion, Λ must be of the same order of the square of the Hubble parameter today

$$\Lambda \approx H_0^2 = (2.13h \times 10^{-42}\,\text{GeV})^2 \,. \tag{2.82}$$

which corresponds to an energy density

$$\rho_\Lambda = \frac{\Lambda m_{\text{pl}}^2}{8\pi} \approx 10^{-47}\,\text{GeV}^4 \,. \tag{2.83}$$

where $m_{\text{pl}} = 1.22 \times 10^{19}$ GeV is the Planck mass. On the other hand, the vacuum energy density evaluated by the sum of zero-point energies of quantum fields with mass m and k momentum is

$$\rho_{\text{vac}} = \frac{1}{2}\int_0^\infty \frac{d^3\mathbf{k}}{(2\pi)^3}\sqrt{k^2 + m^2} = \frac{1}{4\pi^2}\int_0^\infty dk\,k^2\sqrt{k^2 + m^2} \,.$$

This integral shows an ultraviolet divergence, $\rho_{\text{vac}} \propto k^4$, but we expect quantum field theory to be valid up to some cut-off scale k_{max} for which the integral (2.84) is finite

$$\rho_{\text{vac}} \approx \frac{k_{\text{max}}^4}{16\pi^2} \,. \tag{2.84}$$

We expect General Relativity to hold to just below the Planck scale, m_{pl} and if we chose $k_{\text{max}} = m_{\text{pl}}$, the vacuum energy density will be

$$\rho_{\text{vac}} \approx \frac{k_{\text{pl}}^4}{16\pi^2} \simeq 10^{74}\text{GeV}^4. \tag{2.85}$$

The ratio between the theoretical and the observed value of the cosmological constant is

$$\frac{\rho_{\text{vac,th}}}{\rho_{\text{vac,ob}}} = \frac{10^{74}\text{GeV}^4}{10^{-47}\text{GeV}^4} = 10^{121}. \tag{2.86}$$

The theoretical value is then about 121 orders of magnitude larger than the observed value. This ratio can be reduced by assuming a different cutoff scale, but even if we take an energy scale of QCD for k_{max}, we obtain $\rho_{\text{vac}} \approx 10^{-3}\,\text{GeV}^4$ which is still much larger than ρ_Λ. Given that the approach of throwing away the vacuum energy is ad hoc, attempts to cancel the vacuum energy by introducing counter terms have been

done. However this requires a fine-tuning to adjust ρ_Λ to the present energy density of the universe. This is *the fine tuning problem*. It is still an open question whether or not the zero point energy in field theory is realistic. Supersymmetry provides a solution of the zero point energy. In exact supersymmetry there is an equal number of fermionic and bosonic degrees of freedom for a given value of the mass m [49,50], each of them contributing to the zero point energy with an opposite sign, such that the net contribution to the vacuum energy is cancelled. It is in this sense that supersymmetric theories do not admit a non-zero cosmological constant. But supersymmetry must be broken today, as we do not live in a supersymmetric vacuum state and the vacuum energy will be non-zero. For a viable supersymmetric scenario, the supersymmetry breaking scale should be around $M_{\text{SUSY}} \sim 10^3 \, \text{GeV}$. This will reduce the ratio approximately by 60 orders of magnitude but it is still far away from the observed value of Λ. Therefore a cosmological constant originated from a vacuum energy density, suffers from a serious fine-tuning problem. This open question have lead many authors to try many different approaches to the issue of explaining the dark energy phenomenon via a cosmological constant. A big number of attempts to solve this problem includes: adjustment mechanisms [51], anthropic considerations [52–55], quantum gravity [56,57], degenerate vacua [58], higher dimensional gravity [59,60], string theory [61,62] and vacuum fluctuations of the energy density [63].

A second fundamental question arises from the fact that at present, the value of the vacuum energy density is comparable with the current matter energy density; in other words, why the value of Ω_Λ differs from the value of Ω_M only by a factor of 2 or 3? In principle, these two quantities are not correlated. To appreciate this, note that the evolution (or redshift dependence) of ρ_M and ρ_Λ are very different. Taking into account that $w_M = 0$ and $w_\Lambda = -1$, we have $\rho_M(z) = \rho_M(z = 0)(1 + z)^3$, while ρ_Λ remains constant and independent of z. This result means that at earlier times (higher redshifts) the constant vacuum energy density was negligible compared to the densities of other forms of energy and matter. However, at sufficiently late times the matter density would eventually dilute as the universe expands; the constant vacuum energy cause the expansion to accelerate at such late times. But it is surprising that the dark matter and dark energy contributions to the energy budget of the universe have a similar magnitude at the precise era of the cosmic history in which we live. This is referred to as the "why now?" or the *coincidence problem*. More quantitatively, we can compute the redshift at which the matter density and the vacuum energy density were equal in the expansion history, *i.e.*, $\rho_M(z) = \rho_\Lambda$. Using Eq. (2.28), and taking into account that $w_M = 0$ and $w_\Lambda = -1$, we obtain $\rho_M(t_0)(1 + z)^3 = \rho_\Lambda$, which in terms of the cosmological parameters leads to (see Eq. (2.32)))

$$z_{(\rho_M = \rho_\Lambda)} = \left(\frac{\Omega_\Lambda}{\Omega_M} \right)^{1/3} - 1. \tag{2.87}$$

Considering the best fit value of Ω_M resulting from the Planck collaboration, $\Omega_M = 0.315$, and taking into account that $\Omega_\Lambda = 1 - \Omega_M$ at present, Eq. (2.87) leads to a

redshift $z_{(\rho_M = \rho_\Lambda)} \approx 0.296$ which is very recent in the expansion history (notice that $z = 1100$ at the time of recombination and $z = 0$ today).

With the aim of understanding the fundamental nature of the accelerated expansion, many alternatives to the cosmological constant have been proposed. In the following, we shall focus on a particular alternative in which the gravitational sector is modified, that is, the Hilbert-Einstein action is generalized by replacing the scalar curvature R in its Lagrangian density with a non-linear function of it. The study of such modifications of gravity is the goal of this thesis.

Chapter 3

$f(R)$ Models as the Physics of Dark Energy

In the previous chapter we have reviewed the standard cosmological model and the most recent observations supporting that the expansion of the universe is currently in an accelerated phase. In this chapter we introduce the $f(R)$ modified gravity theories as an alternative to the standard cosmological model to describe the late time accelerated expansion of the universe. We begin by motivating the $f(R)$ framework. We then introduce the $f(R)$ field equations in the Jordan frame, in which matter fields remain minimally coupled to the GR metric; in this frame the conservation equations for the different matter components remain the same as GR. We continue with a brief description of the scalar-tensor representation of the $f(R)$ theories; their relation with the Brans-Dicke theory as well as the conformal transformation between the Jordan frame and the Einstein Frame *. We obtain the cosmological evolution equations of the background and the dynamical equations of linear perturbations. We use the latter to study the growth of structure formation, which will be crucial in the analysis of the different $f(R)$ models, as we will see in Chapter 4. We also introduce the specific $f(R)$ functions that we study in the next chapters by giving examples of numerical solutions to the expansion history and the growth of structure for cosmologically viable parameter values. Finally we explore the weak field limit of $f(R)$ theories.

3.1   Motivation

Understanding the origin of the observed accelerated expansion in the universe's late epoch is a keystone for understanding the universe's dynamics. The standard GR framework together with the standard matter-energy density components cannot account for such accelerated expansion and the conclusion that arises from the obser-

---

*In the Einstein frame the matter Lagrangian is not minimally coupled to the GR metric; the metric is not the physical metric in this frame and matter fields do not fall along geodesics.

vations is that the increasing expansion rate reveals new physics missing from our standard cosmological paradigm. We have discussed in the previous chapter that the most economical description of the cosmological data attributes the negative-pressure dark energy component to a cosmological constant in Einstein's equations, giving rise to the standard ΛCDM model. However many fundamental questions arise when considering a cosmological constant in our picture of the universe: is it really constant? has it been constant during the whole past history of the universe? if so, is it another fundamental constant in our physics framework? why is it so small compared to the predicted vacuum energy from quantum field theory? In the attempt to understand the fundamental nature of the accelerated expansion, the simplest alternative to the ΛCDM model introduces a new dynamical scalar degree of freedom mediating the gravitational interaction. It is this extra scalar field that behaves as an "anti-gravity" component at large scales. Attributing the late time accelerated expansion of the universe to the dynamics of a scalar field has been extensively proposed in the literature through different approaches. For instance, in the so-called *quintessence* models, the dynamical scalar is introduced in the standard GR framework as an extra field in the matter-energy sector. In this case the gravitational sector of Einstein's field equations remain unmodified, while the scalar field contributes to the matter sector and the corresponding conservation equations. Alternatively, the new scalar degree of freedom can be introduced as a modification of the gravitational sector, as is the case of the $f(R)$ gravity models. In this case, new terms appear in the gravitational field equations, while the conservation equations remain the same as in GR.

The simplest way of modifying the gravitational sector in GR is by adding a correction to the Einstein-Hilbert action, a general function $f(R)$ of the Ricci scalar. The modification of the gravitational sector in Einstein's equations at very large distances (or small curvatures) is not unexpected from an effective 4-dimensional description of higher dimensional theories. For instance string theory requires quantum corrections at small scales, therefore it is not unreasonable to consider geometrical corrections at large scales, considering GR an effective theory at intermediate scales, as it has been tested with great accuracy. Many specific forms of $f(R)$ parametric functions have been proposed in the literature, which should be treated as toy-models from a more fundamental perspective. However, the phenomenological study of viable $f(R)$ functions, opens a simple and unique window to test and understand which type of corrections to the Hilbert-Einstein action can account for the observed dynamics of the universe.

3.2 Actions and Field Equations

In the following we introduce the $f(R)$ field equations which we will use in the analyses of following chapters. We work under the metric formalism and we formulate the dynamical equations in the Jordan frame. However in this section we add a brief de-

scription of the formal equivalence between $f(R)$ theories and scalar-tensor theories, in particular with the Brans-Dicke theory. We also formulate the relevant $f(R)$ equations in the Einstein frame in order to clarify the identification of the scalar field in the Jordan frame, this will be particularly useful for understanding the phenomenological aspects of $f(R)$ models in the slow motion, weak field limit.

In the Jordan frame, the action of $f(R)$ modified gravity is obtained by adding a general function $f(R)$ of the Ricci scalar R to the usual Hilbert-Einstein Lagrangian, and the action takes the form

$$S_{\mathrm{JF}} = \frac{1}{2\kappa^2} \int d^4x \sqrt{-g} \, [R + f(R)] + \int d^4x \, \mathcal{L}_{\mathrm{M}}[\psi_i, g_{\mu\nu}] \,, \qquad (3.1)$$

Note that the gravitational constant G (in $\kappa^2 = 8\pi G$) in this theory is typically not the Newton's gravitational constant (see Eq. (3.44) bellow). The matter Lagrangian, $\mathcal{L}_{\mathrm{M}}$, is minimally coupled and therefore the matter fields, ψ_i, fall along geodesics of the metric $g_{\mu\nu}$. The field equations obtained from varying the action Eq. (3.1) with respect to $g_{\mu\nu}$ are

$$(1 + f_R)R_{\mu\nu} - \frac{g_{\mu\nu}}{2}(R + f - 2\Box f_R) - \nabla_\mu \nabla_\nu f_R = \kappa^2 \, T_{\mu\nu} \,, \qquad (3.2)$$

where $f_R \equiv \partial f / \partial R$. Equation (3.2) gives a set of equations which are fourth order in $g_{\mu\nu}$. We assume matter to behave as a perfect fluid as in GR, with an energy-momentum tensor

$$T_{\mu\nu} = (\rho + p)u_\mu u_\nu + p g_{\mu\nu} \,, \qquad (3.3)$$

where u^μ is the fluid rest-frame four-velocity, ρ is the energy density and p is the pressure as we have explained in the previous chapter. Note that in the Jordan frame, because the metric is the same as in GR (minimally coupled to matter), the stress-energy tensor and its conservation laws remain the same as in GR.

3.2.1 Scalar-Tensor Representation

The idea of a scalar field mediating the gravitational interaction has been considered since long ago in cosmology, these are the so called scalar-tensor theories and $f(R)$ theories are a subclass of them. To see this, let us consider the following action with a new field χ,

$$S = \frac{1}{2\kappa^2} \int \mathrm{d}^4x \sqrt{-g} \, [\chi + f(\chi) + (1 + f_\chi)(R - \chi)] + \int \mathrm{d}^4x \mathcal{L}_M(\psi_i, g_{\mu\nu}) \,, \qquad (3.4)$$

where $f_\chi \equiv \partial f / \partial \chi$. Varying this action with respect to χ, we obtain

$$f_{\chi\chi}(R - \chi) = 0 \,. \qquad (3.5)$$

If $f_{\chi\chi}(\chi) \neq 0$, the field equation for χ is given simply by $\chi = R$ and the action Eq. (3.4) becomes identical to the action Eq. (3.1). A particularly well-known scalar-tensor theory is the Brans-Dicke (BD) theory of gravitation [64], a metric theory which

was proposed by Robert H. Dicke and Carl H. Brans in 1961 as an alternative to GR. It was shown [65,66] that $f(R)$ theories in the metric formalism can be reformulated in the form of a BD theory with an effective scalar field potential. To see this, we define

$$\varphi \equiv 1 + f_\chi \,, \tag{3.6}$$

and the action (3.4) can be rewritten as

$$S = \int \mathrm{d}^4 x \sqrt{-g} \left[\frac{1}{2\kappa^2} \varphi R - U(\varphi) \right] + \int \mathrm{d}^4 x \mathcal{L}_M(\psi_i, g_{\mu\nu}) \,, \tag{3.7}$$

where $U(\varphi)$ is the φ potential given by

$$U(\varphi) = \frac{\chi \varphi - (\chi + f(\chi))}{2\kappa^2} \,, \tag{3.8}$$

where $\chi = \chi(\varphi)$. The BD action with a potential $U(\varphi)$ is given by [64]

$$S_{\mathrm{BD}} = \int \mathrm{d}^4 x \sqrt{-g} \left[\frac{1}{2} \varphi R - \frac{\omega_{\mathrm{BD}}}{2\varphi} (\nabla \varphi)^2 - U(\varphi) \right] + \int \mathrm{d}^4 x \mathcal{L}_M(\psi_i, g_{\mu\nu}) \,, \tag{3.9}$$

where ω_{BD} is the BD parameter, which is constant and dimensionless [†], and $(\nabla \varphi)^2 \equiv g^{\mu\nu} \partial_\mu \varphi \partial_\nu \varphi$ is the kinetic term of the scalar field. Thus, the Newton's constant is promoted to a scalar field in BD theories. Comparing Eq. (3.7) with Eq. (3.9), it follows that $f(R)$ theory in the metric formalism is equivalent to BD theory with the parameter $\omega_{\mathrm{BD}} = 0$ (with units $\kappa^2 = 1$) [‡]. Since the BD action contains a dimensionless parameter, GR has been always consider a simpler theory than the BD one which could account for observations.

Mapping the field equations Eqs. (3.2) to the Einstein frame will be useful for understanding certain features of $f(R)$ models. In the Einstein frame Eqs. (3.2) can be recast as a system of second order differential equations in $g_{\mu\nu}$ with an extra dynamical equation for the scalar field and an extra term in the conservation equations as we will next see. Consider the conformal transformation

$$1 + f_R = \exp\left(-2\kappa\beta\phi\right), \tag{3.10}$$

where ϕ is the extra scalar degree of freedom in the Einstein frame, $\beta = \sqrt{1/6}$, and

$$g_{\mu\nu} = e^{2\kappa\beta\phi} \bar{g}_{\mu\nu}, \tag{3.11}$$

where $\bar{g}_{\mu\nu}$ is the metric in the Einstein frame and $\bar{R}$ is the scalar curvature of $\bar{g}_{\mu\nu}$. In the Einstein frame the action becomes

$$S_{\mathrm{EF}} = \int \mathrm{d}^4 x \sqrt{-\bar{g}} \left(\frac{1}{2\kappa^2} \bar{R} - \frac{1}{2} \bar{g}^{\mu\nu} \bar{\nabla}_\mu \phi \bar{\nabla}_\nu \phi - V(\phi) \right) +$$
$$+ \int \mathrm{d}^4 x \, \mathcal{L}_{\mathrm{M}}(\psi_i, e^{2\kappa\beta\phi} \bar{g}_{\mu\nu}), \tag{3.12}$$

[†]In general, for scalar-tensor theories, $\omega \equiv \omega(\varphi)$.

[‡]In [67], T. Chiba suggested that the BD theory with $w_{BD} = 0$ is ruled out by solar system tests. However, there are certain conditions under which this is not the case. See the last paragraph of Sec. 3.4.1.

where the potential $V(\phi)$ is given by

$$V(\phi) = \frac{1}{2\kappa^2} \frac{Rf_R - f}{(1 + f_R)^2}, \tag{3.13}$$

which is completely determined by the original form of the action (3.1). Notice that in the Einstein frame matter fields are not minimally coupled to the GR metric $g_{\mu\nu}$ and they do not fall along geodesics. Varying the action Eq. (3.12) with respect to $\bar{g}_{\mu\nu}$ the field equations become

$$\bar{R}_{\mu\nu} - \frac{1}{2}\bar{R}\bar{g}_{\mu\nu} = \kappa^2 \bar{\nabla}_\mu \phi \bar{\nabla}_\nu \phi - \kappa^2 \bar{g}_{\mu\nu} \left[\frac{1}{2}(\bar{\nabla}\phi)^2 + V(\phi) \right] + \kappa^2 \bar{T}_{\mu\nu} \tag{3.14}$$

$$\bar{\Box}\phi = V'(\phi) - \kappa\beta\bar{T}, \tag{3.15}$$

where the covariant derivatives $\bar{\nabla}_\mu$, obey the relation $\bar{\nabla}_\mu \bar{g}_{\mu\nu} = 0$ and $\bar{T}_{\mu\nu} = e^{2\kappa\beta\phi}T_{\mu\nu}$, thus $\bar{T} = \bar{g}^{\mu\nu}\bar{T}_{\mu\nu} = e^{4\kappa\beta\phi}g^{\mu\nu}T_{\mu\nu}$. For non-relativistic matter, $g^{\mu\nu}T_{\mu\nu} = -\rho$, but we can write Eq. (3.15) in terms of the energy density $\bar{\rho} = \rho e^{3\kappa\beta\phi}$, which is conserved in the Einstein frame [68]. The right hand side of Eq. (3.15) shows that the dynamics of ϕ depends on an effective potential

$$V_{eff}(\phi) \equiv V(\phi) + \bar{\rho}e^{\kappa\beta\phi}. \tag{3.16}$$

The minimum of the effective potential is given by

$$V'(\phi_{min}) + \kappa^2\beta^2\bar{\rho}e^{\kappa\beta\phi_{min}} = 0, \tag{3.17}$$

where ϕ_{min} is the value of the field at the minimum. The curvature of the potential, typically interpreted as the *mass* squared of the scalar field, is given by the inverse squared of the field's Compton wavelength, λ_ϕ, at ϕ_{min} as

$$m^2_{\phi_{min}} \equiv \lambda^{-2}_{\phi_{min}} = V''(\phi_{min}) + \kappa\beta\bar{\rho}e^{\kappa\beta\phi_{min}}. \tag{3.18}$$

In the last section of this chapter we will see that, by linearizing Eq. (3.15), static solutions give a field's potential with a Yukawa profile, $\delta\phi \sim e^{-r/\lambda_\phi}/r$, with an interaction range given by the field's Compton wavelength, λ_ϕ.

We can recast the terms depending on ϕ in Eq. (3.14) in the form of an energy momentum tensor of the scalar field such that

$$\bar{R}_{\mu\nu} - \frac{1}{2}\bar{g}_{\mu\nu}\bar{R} = \kappa^2(\bar{T}_{\mu\nu} + T^\phi_{\mu\nu}), \tag{3.19}$$

where

$$T^\phi_{\mu\nu} = \bar{\nabla}_\mu \phi \bar{\nabla}_\nu \phi - \bar{g}_{\mu\nu} \left[\frac{1}{2}(\bar{\nabla}\phi)^2 + V(\phi) \right]. \tag{3.20}$$

As we mentioned above, in the Einstein frame $\bar{\nabla}_\mu \bar{T}_{\mu\nu} \neq 0$, while the conservation equation becomes

$$\bar{\nabla}_\mu \bar{T}^\mu{}_\nu = \kappa\beta\bar{T}\bar{\nabla}_\nu\phi. \tag{3.21}$$

The $f(R)$ modified gravity equations in the Einstein frame, Eq. (3.14), become of the same form as in GR with an extra energy density component, ϕ. This fact will let us use the intuition we have acquired by studying GR for understanding some aspects of $f(R)$ theories. The metric in the Einstein frame is not the physical metric, *i.e.*, matter fields do not fall along geodesics, as it is implied by the gradients in ϕ in Eq. (3.21), instead will feel an effective 'fifth' force mediated by the new energy density component ϕ, with an interaction range given by the field's Compton wavelength. However all physical observables must be independent of the choice of frame.

Since we perform all our analysis in the Jordan frame, we introduce the scalar-tensor formulation in the Jordan frame, in which f_R plays the role of the additional scalar degree of freedom, becoming the analog to the scalar field ϕ in the Einstein frame. The equation of motion of f_R in the Jordan frame is given by the trace of Eq. (3.2) yielding

$$3\Box f_R - R - 2f + Rf_R = -\kappa^2(\rho - 3p)\,. \tag{3.22}$$

which can be recast in the form

$$\Box f_R = V'_{eff}(f_R)\,, \tag{3.23}$$

with the effective potential

$$V'_{eff}(f_R) \equiv \frac{1}{3}\left[R + 2f - Rf_R - \kappa^2(\rho - 3p)\right]\,, \tag{3.24}$$

which has an extremum at

$$R + 2f - Rf_R = \kappa^2(\rho - 3p)\,. \tag{3.25}$$

with curvature given by

$$\lambda_{f_R}^{-2} = V''_{eff}(f_R) = \frac{1}{3}\left(\frac{1 + f_R}{f_{RR}} - R\right)\,, \tag{3.26}$$

where λ_{f_R} is the Compton wavelength of f_R.

3.3 Cosmological Evolution

Given the $f(R)$ field equations, we obtain in this section the equations of the cosmological evolution in a flat FRW universe. In Sec. 3.3.1 we obtain the modified Friedmann equations and in Sec. 3.3.2 we obtain the dynamical equations of cosmological perturbations.

3.3.1 Background Evolution Equations

We take the metric of the form of a flat FRW background $ds^2 = -dt^2 + a(t)^2 \sum_{i=1}^{3}(dx^i)^2$, and the modified Friedmann equation becomes

$$H^2 + \frac{1}{6}f - (H^2 + \dot{H})f_R + H\dot{f}_R = \frac{\kappa^2}{3}\rho\,, \qquad (3.27)$$

the acceleration equation becomes

$$H^2 + \dot{H} + \frac{1}{6}f - H^2 f_R + \frac{1}{2}\ddot{f}_R = -\frac{\kappa^2}{6}(\rho + 3p)\,, \qquad (3.28)$$

and the scalar curvature satisfies $R = 6(2H^2 + \dot{H})$. Equations (3.27) and (3.28) are the analog of Eqs. (2.21) and (2.22) respectively in a $f(R)$ universe. The late time accelerated expansion arises from the terms that depend on $f(R)$ in the left hand side of Eqs. (3.27) and (3.28), therefore we just consider matter and radiation as sources in the right hand side when using Eq. (2.27). However, it is useful to recast the terms that accelerate the expansion in an effective equation of state of a dark energy component by following the same procedure in which we obtained Eq. (2.25) in the previous chapter. By summing up Eqs. (3.27) and (3.28) we obtain

$$3H^2 + 2\dot{H} + \frac{1}{2}f - (3H^2 + \dot{H})f_R + H\dot{f}_R + \ddot{f}_R = -\kappa^2 p\,, \qquad (3.29)$$

and from Eq. (3.27) and Eq. (3.29) we can write

$$3H^2 = \kappa^2(\rho + \rho_{DE})\,, \qquad (3.30)$$
$$-3H^2 - 2\dot{H} = \kappa^2(p + p_{DE})\,, \qquad (3.31)$$

where we have defined

$$\rho_{DE} \equiv \frac{1}{\kappa^2}\left(-\frac{1}{2}f + 3(H^2 + \dot{H})f_R - 3H\dot{f}_R\right)\,, \qquad (3.32)$$

$$p_{DE} \equiv \frac{1}{\kappa^2}\left(\frac{1}{2}f - (3H^2 + \dot{H})f_R + H\dot{f}_R + \ddot{f}_R\right)\,, \qquad (3.33)$$

$$w_{DE} = \frac{p_{DE}}{\rho_{DE}} = -1 + \frac{2\dot{H}f_R + 4H\dot{f}_R + \ddot{f}_R}{-\frac{1}{2}f + 3(H^2 + \dot{H})f_R - 3H\dot{f}_R}\,. \qquad (3.34)$$

Expansion History of Specific $f(R)$ Models

Equation (3.27) gives the evolution of a flat FRW background under a generic $f(R)$ cosmology. In the next chapter we study the conditions under which $f(R)$ models are cosmologically viable. In the last chapter of this thesis we shall show how a combination

Type of model	Type 1	Type 2	Type 3	Type 4	Type 5
H_0 (km/s/Mpc)	69.9	67.5	69.6	69.6	67.9

Table 3.1: H_0 values for the models Eqs. (3.35)-(3.39) resulting from the numerical integration of Eq. (3.40) with the choice of parameters shown in Fig. 7.

of different observational tests constitute a powerful tool to rule out, or either constrain, specific types of $f(R)$ models, even when they are, in principle, cosmologically viable. The specific type of models we study in the next chapters are

$$\text{Type 1}: f(R) = R^p \left[\log(\alpha R)\right]^q - R, \tag{3.35}$$

$$\text{Type 2}: f(R) = R^p \exp(q/R) - R, \tag{3.36}$$

$$\text{Type 3}: f(R) = \alpha R^n, \tag{3.37}$$

$$\text{Type 4}: f(R) = \alpha R^2 - \Lambda, \tag{3.38}$$

$$\text{Type 5}: f(R) = -M^2 c_1 (R/M^2)^n / (1 + c_2 (R/M^2)^n), \tag{3.39}$$

which have been proposed in the literature as cosmologically viable models [69–71]. The values of the free parameters in each of these models determine whether or not they can reproduce the cosmological observations described in the previous chapter. The allowed parameter regions by cosmological data will be analyzed in the next chapters. As a graphical example in this section we compute the Hubble expansion rate of the specific $f(R)$ models, Eqs. (3.35)-(3.39), for given parameter values. For convenience, in the numerical integration, we rewrite Eq. (3.27) as

$$H^2 + \frac{1}{6}f - (H^2 + aHH')f_R + aH^2 f'_R = H_0^2 \Omega_M a^{-3} \tag{3.40}$$

where $' \equiv d/da$ and the scalar curvature satisfies $R = 6(2H^2 + aHH')$. We neglect radiation and consider the total CDM energy density, ρ_m as the source, which we have written in terms of the cosmological parameters. Accordingly to a recent fit to cosmological data [2], we fix the present dark matter energy density to $\Omega_M = 0.315 \pm 0.017$ and $H_0 = 67.3 \pm 1.2$ km/s/Mpc. We integrate numerically Eq. (3.40) for the five different type of $f(R)$ models and the results for the Hubble parameter $H(a)$ in the five different cases are shown in Fig. 7. The ranges of the free parameters have been chosen to obtain a value of the Hubble parameter today, H_0, within a 1-σ range from the value obtained by Planck observations, $H_0 = 67.3 \pm 1.2$ km/s/Mpc. The H_0 values for these choice of parameters are shown in Tab. 3.1. The parameters are expressed in terms of $\bar{H}_0$, being $\bar{H}_0 = 67.3$ km/s/Mpc. For comparison, we also show the Hubble rate predicted by the ΛCDM model which, as we have discussed in Sec. 2.1.3, describes a a flat universe ($\Omega_k = 0$) with a cosmological constant, Λ. For the ΛCDM model, the Hubble parameter is given by Eq. (2.36), which, neglecting radiation ($\Omega_R = 0$), leads to $H(a) = H_0 \sqrt{\Omega_M a^{-3} + (1 - \Omega_M)}$ (with $H_0 = 67.3$ km/s/Mpc and $\Omega_M = 0.315$).
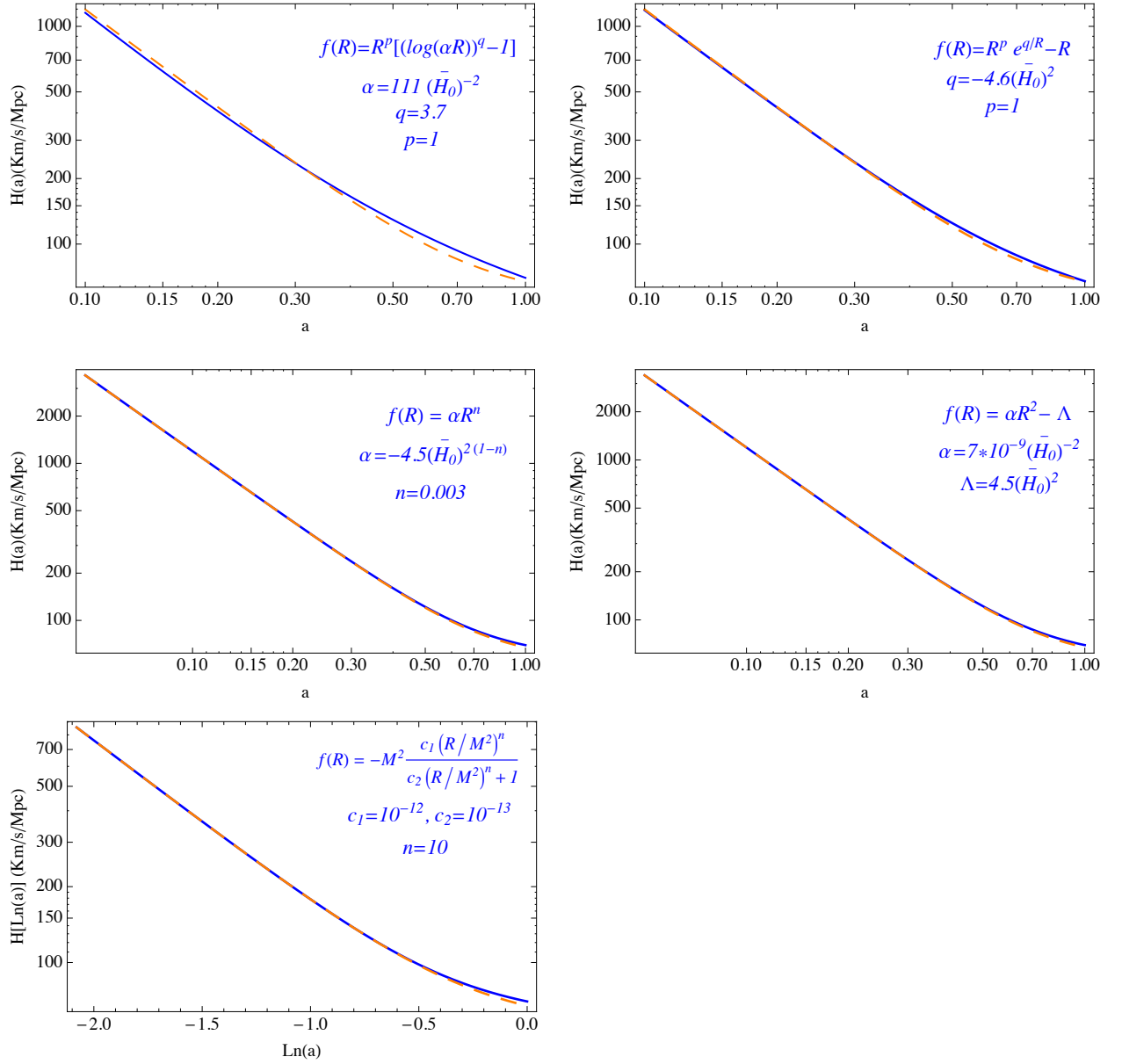
Figure 7: **Expansion history of various** $f(R)$ **models**. Hubble rate versus the scale factor for the $f(R)$ models Eqs. (3.35)-(3.39) (blue solid line). The parameters were chosen so to have an acceptable expansion history, and they are expressed in terms of $\bar{H}_0$, being $\bar{H}_0 = 67.3$ km/s/Mpc. We add the $H(a)$ curve of the standard ΛCDM model for comparison (orange dashed line).

3.3.2 Dynamics of Linear Perturbations

In this section we introduce the dynamics of linear scalar perturbations in $f(R)$ theories in the Jordan frame. We consider scalar linear perturbations around a flat FRW

background in the Newtonian gauge given by the metric Eq. (2.52). In the Jordan frame the conservation equations for the CDM component have the same form as in GR, these are given at first order in perturbations by Eqs. (2.66) and (2.67). For subhorizon modes, in which time derivatives are negligible compared with spatial derivatives, the linearized $0-0$ and $i-j$ $(i \neq j)$ components of the Einstein equations read

$$2 \left(\frac{k}{a}\right)^2 \left[\Phi(1+f_R) - f_{RR}\left(\frac{k}{a}\right)^2 (\Psi - 2\Phi)\right] = -8\pi G \rho \, \delta \; ;$$

$$\Psi = \left(\frac{1-2Q}{1-Q}\right)\Phi \; , \qquad (3.41)$$

where ρ is the CDM energy density and we have neglected the radiation contribution. The factor Q is defined as

$$Q(k,a) \equiv -2 \left(\frac{k}{a}\right)^2 \frac{f_{RR}}{1+f_R} \; . \qquad (3.42)$$

By substituting the equation for the $i-j$ component into the one for the $0-0$ component we obtain the modified Poisson equation

$$\Phi = \frac{-8\pi G}{\left(\frac{k}{a}\right)^2 (1+f_R)} \left(\frac{1-Q}{2-3Q}\right) \delta\rho \; , \qquad (3.43)$$

which can be rewritten as

$$\Phi = -4\pi G_{eff} \left(\frac{a}{k}\right)^2 \delta\rho \; , \quad G_{eff} = \frac{2}{(1+f_R)}\left(\frac{1-Q}{2-3Q}\right) \qquad (3.44)$$

and reduces to the standard Poisson equation when $f_R = 0$. The growth factor equation is obtained by combining Eqs. (2.66), (3.41) and Eq. (3.43) (see also Ref. [72]) as

$$\ddot{\delta} + 2H\dot{\delta} - \frac{1}{(1+f_R)}\left(\frac{1-2Q}{2-3Q}\right)\kappa^2\rho\delta = 0 \; , \qquad (3.45)$$

where $\dot{} \equiv d/dt$ and δ is normalized such that $\delta \rightarrow a$ when $a \rightarrow 0$. The factor $Q(k,a)$, given by Eq. (3.42), recasts the scale dependence of the linear growth factor in $f(R)$ models. In general relativity $Q(k,a) = 0$ and the linear growth factor is scale independent. The fact that the dynamics of matter inhomogeneities in $f(R)$ modified gravity models depends on the scale is a crucial feature which makes them potentially distinguishable from the ΛCDM model.

Growth of Structure of specific models

As an example, we solve numerically Eq. (3.45) for the same models introduced in the previous section, as well as for the same values of the free parameters, by using the
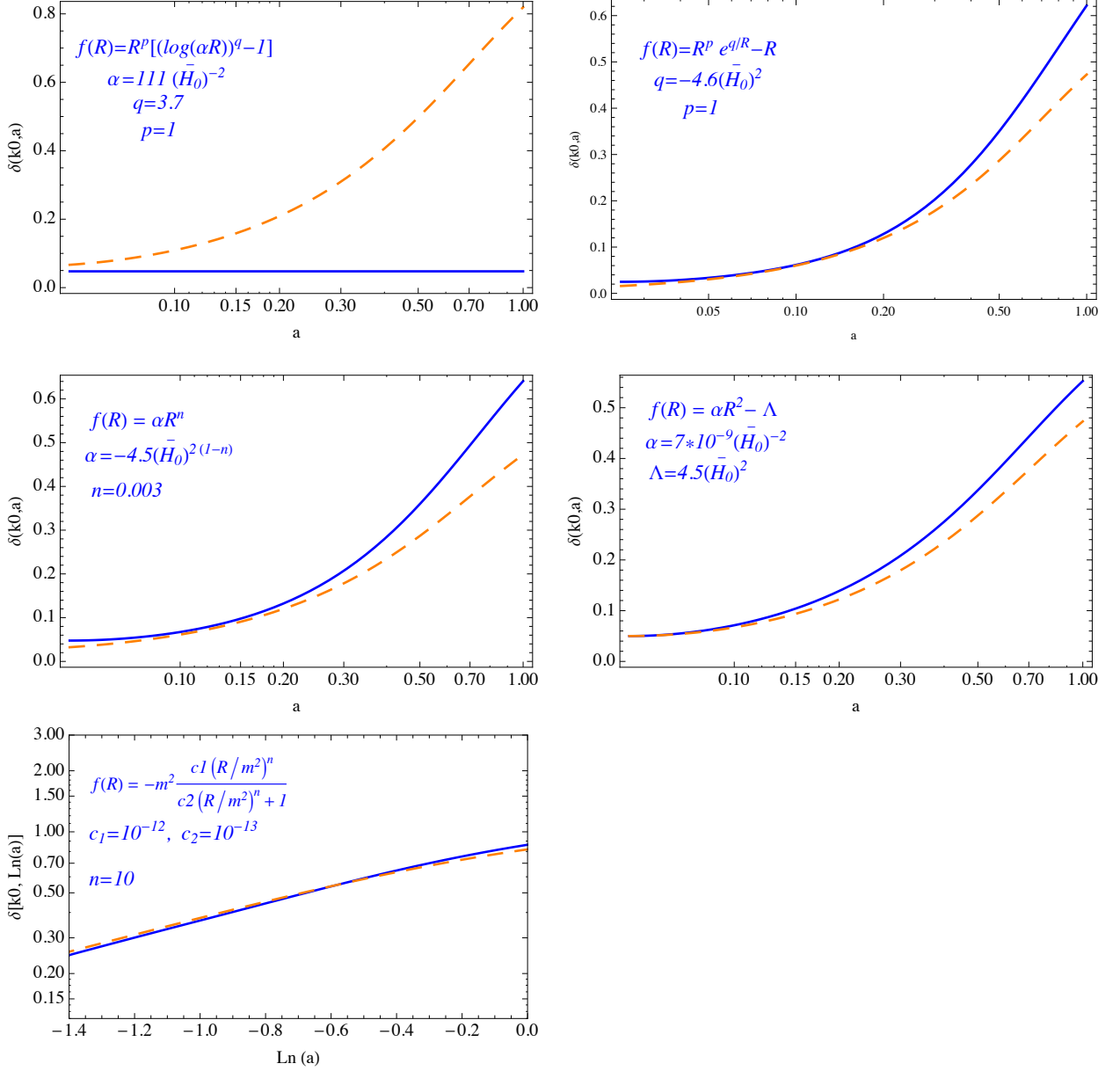
Figure 8: **Linear growth factor of various $f(R)$ models versus the scale factor**. Solid curves represent the linear growth factor δ as a function of a, for a fixed value of the scale $k_0 = 0.1h/\text{Mpc}$, of models Eqs. (3.35)-(3.39). The parameters were chosen so to have an acceptable expansion history. The dashed line represents δ for the ΛCDM model.

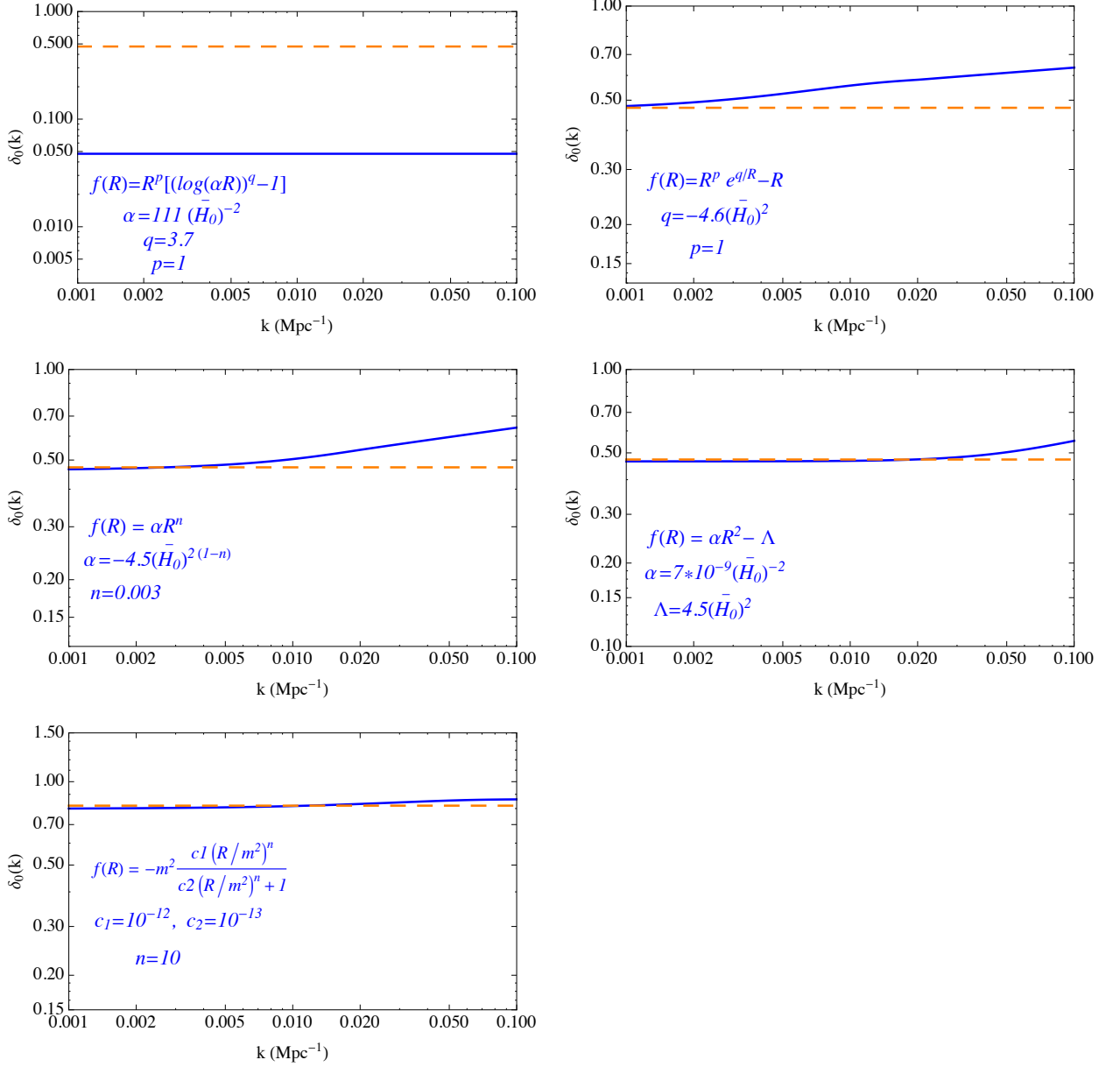numerical results of their expansion history obtained from integrating Eq. (3.40). For

Figure 9: **Scale dependence of the linear growth factor of various $f(R)$ models**. Solid curves represent the present ($a_0 = 1$) linear growth factor δ as a function of the scale, k, of models Eqs. (3.35)-(3.39). The parameters were chosen to have an acceptable expansion history. The dashed line is the linear growth factor of the ΛCDM model, which is scale independent.

convenience we integrate Eq. (3.45) rewritten as a function of the scale factor

$$\delta'' + \left(\frac{3}{a} + \frac{H'}{H}\right)\delta' - \frac{1}{(1+f_R)}\left(\frac{1-2Q}{2-3Q}\right)\frac{3\Omega_M(a)}{a^2\left(H/H_0\right)^2}\delta = 0 \ . \qquad (3.46)$$

In Fig. 8 we show the evolution of the matter overdensity $\delta(k, a)$ as a function of the scale factor a by fixing the scale to $k_0 = 0.1h/\text{Mpc}$ for the models of Eqs. (3.35)-(3.39). In Fig. 9 we show the scale dependence of the linear growth factor by plotting the present value $(a = 1)$ of the matter overdensity $\delta_0(k)$ versus k for the same models. In both figures we also plot the same curve for a ΛCDM universe for comparison. Notice that for the choice of parameters that leads to an acceptable expansion history, the linear growth of matter perturbations for the logarithmic model given by Eq. (3.35), is highly suppressed with respect to the growth in a universe with a cosmological constant (see the upper left panel of Figs. (8) and (9)). For the other four $f(R)$ models the growth is very close to the ΛCDM growth at large scales. However, it shows a k dependence as k increases, due to a larger $Q(k, a)$ factor.

3.4 Slow-motion weak-field limit

In the previous section we have shown some examples of cosmologically viable $f(R)$ models. We have seen that, for some value of the parameters, these models can reproduce an expansion history and an evolution of cosmological perturbations close to the ΛCDM model. Viable $f(R)$ models must show a correct cosmological evolution according to observations. In addition, a consistent $f(R)$ model must be compatible with the observational constraints at solar system scales, where GR is well tested. As we have mentioned, in the last chapter we will test models Eqs. (3.35)-(3.39) against experimental data. For those models that are allowed by cosmological observations, we shall also check whether they pass solar system tests within the parameter range constrained by cosmological observations. To this end we introduce in this chapter the weak field limit of $f(R)$ models. In the next sections we follow the criteria presented by W. Hu and I. Sawicki in [70].

3.4.1 Isotropic static space-times in the weak field limit

We are interested in testing $f(R)$ models at solar system scales, at which velocities are small (compare to c) and the gravitational field is weak. A general form of an isotropic space-time metric around a spherically symmetric source is given by

$$ds^2 = -[1 - 2\mathcal{A}(r) + 2\mathcal{B}(r)]\text{d}t^2 + [1 + 2\mathcal{A}(r)](\text{d}r^2 + r^2\text{d}\Omega) \,. \tag{3.47}$$

Since in the solar system the space-time is close to Minkowski, $|\mathcal{A}(r)| \ll 1$ and $|\mathcal{B}(r)| \ll 1$ near a source such as the Sun. This is the so called post-Newtonian limit, in which GR has been tested to a great accuracy and constitutes the physically relevant regime to test models against solar system data. In this regime it becomes particularly simple, and sufficiently accurate, to compare different metric theories with each other, and with experimental constraints, since in this limit the space-time metrics predicted by most metric theories have the same structure. In the GR limit, $\mathcal{B}(r) \rightarrow 0$, so that

deviations from GR are characterized by $\mathcal{B}(r)$. Since deviations from GR are highly suppressed at solar system scales, $|\mathcal{B}(r)| \ll |\mathcal{A}(r)|$ is required to pass solar system tests, or equivalently $|\gamma - 1| \ll 1$ where

$$\gamma(r) - 1 \equiv \frac{\mathcal{B}(r)}{\mathcal{A}(r) - \mathcal{B}(r)}. \tag{3.48}$$

The parameter γ is the most relevant one in the Parametrized Post-Newtonian (PPN) formalism[§] and it measures *how much* space-time curvature is induced by a unit mass relative to GR, for which $\gamma = 1$. Constraints in γ provide the strongest test of scalar-tensor theories.

Using the definition of the Ricci tensor and the time-time component of the modified Einstein equations, Eq. (3.2), combined with

$$3\nabla^2 f_R - R - 2f + Rf_R = -\kappa^2 \rho, \tag{3.49}$$

which is Eq. (3.22) in the static limit for non-relativistic matter, we find that the sources of $\mathcal{A}$ and $\mathcal{B}$ are

$$\nabla^2(\mathcal{A} + \mathcal{B}) = -\frac{1}{2}R, \tag{3.50}$$

$$\nabla^2 \mathcal{B} = -\frac{1}{4}\left(\frac{-4\kappa^2\rho + 4R + 5f_R R - f}{3(1 + f_R)}\right), \tag{3.51}$$

where $f(R)$ is given by the solution of Eq. (3.49). Close to the source $|f_R| \ll 1$ and $|f/R| \ll 1$, and from Eq. (3.51) the Poisson equation for the potentials $\mathcal{A}$ and $\mathcal{B}$ becomes

$$\nabla^2 \mathcal{A} \approx -\frac{1}{2}\kappa^2\rho + \frac{1}{6}\left(\kappa^2\rho - R\right), \tag{3.52}$$

$$\nabla^2 \mathcal{B} \approx \frac{1}{3}\left(\kappa^2\rho - R\right). \tag{3.53}$$

Equation (3.53) shows that the source of the potential $\mathcal{B}$ is the deviation of the scalar curvature R from $\kappa^2\rho$, its GR value. On the other hand, the trace Eq. (3.22) in the static limit when $|f_R| \ll 1$ and $|f/R| \ll 1$, becomes

$$\nabla^2 f_R \approx \frac{1}{3}\left(R - \kappa^2\rho\right). \tag{3.54}$$

[§]The PPN formalism is the most common framework to test metric theories of gravitation at solar system scales. In the slow motion, weak field limit, in which velocities and potentials are small (*i.e.*, $\Psi, v^2/c^2 \sim \epsilon^2 \ll 1$), the metric can be written as an expansion about the Minkowski metric in terms of dimensionless gravitational potentials. A consistent post-Newtonian expansion requires corrections of g_{00} through $O(\epsilon^2)$, g_{0i} through $O(\epsilon^{3/2})$ and g_{ij} through $O(\epsilon)$ [73]. Such an expansion in different metric theories only differs in the numerical values of the coefficients of the metric potentials, thus the PPN formalism turns these coefficients into parameters whose values depend on the metric theory of gravity. In general, for a fluid description of matter and allowing for generic Poisson-like potentials, the PPN formalism requires ten parameters for a complete description.

From Eqs. (3.53) and (3.54), $\nabla^2\mathcal{B} = -\nabla^2 f_R$. Imposing boundary conditions such that $\mathcal{B}$ is finite at the center of the source ($r = 0$) and that it vanishes at large radii while the field converges to some value $f_R(r) \to f_{R\infty}$, a solution for the field, f_R, gives the potential $\mathcal{B}$,

$$\mathcal{B}(r) = -[f_R(r) - f_{R\infty}] \equiv -\Delta f_R(r) \,. \tag{3.55}$$

The source of $\mathcal{B}$, Eq. (3.53), can be quantified as an enclosed effective mass given by

$$M_{\text{eff}} \equiv 4\pi \int (\rho - R/\kappa^2) r^2 \mathrm{d}r \,. \tag{3.56}$$

Beyond a certain radius $R \approx \kappa^2\rho$, to a good approximation, and in those regions the contribution of $\kappa^2\rho - R$ to the integral, Eq. (3.56), can be neglected, yielding

$$\mathcal{B}(r) = -\Delta f_R(r) \approx \frac{2GM_{\text{eff}}}{3r} \,. \tag{3.57}$$

On the other hand, using Eq. (3.52),

$$\mathcal{A}(r) \approx -\frac{GM_{\text{tot}}}{r} + \frac{GM_{\text{eff}}}{3r} \,, \tag{3.58}$$

where

$$M_{\text{tot}} \equiv 4\pi \int_0^\infty \rho r^2 dr, \tag{3.59}$$

is defined as the total mass of the system. Substituting Eqs. (3.57) and (3.58) in the definition Eq. (3.48), the deviation from the GR metric can be expressed in terms if the parameter γ as

$$\gamma - 1 \approx -\frac{2M_{\text{eff}}}{3M_{\text{tot}} + M_{\text{eff}}} \,. \tag{3.60}$$

By comparing M_{eff} with M_{tot} we can appreciate two limiting cases in Eq. (3.60) depending on whether the field gradients are large or small. To see this consider Eq. (3.54), where two asymptotic regimes of local solutions to this equation are present: 1) when the field gradients are small, $\nabla^2 f_R \ll \kappa^2\rho \Rightarrow R \approx \kappa^2\rho$, which we refer to as the high curvature regime (with the curvature as in GR). In this situation $\mathcal{B}$ is negligible compared to the source and $M_{\text{eff}} \ll M_{\text{tot}}$, thus in this limit the deviation of the metric from the GR one is given by $\gamma - 1 = -2M_{\text{eff}}/3M_{\text{tot}}$. 2) When the field gradients are large, $\nabla^2 f_R \approx -\kappa^2\rho \Rightarrow R \ll \kappa^2\rho$, which we refer to as the low curvature regime. In this case, from Eq. (3.56) follows that $M_{\text{eff}} = M_{\text{tot}}$ and in this limit the deviation from GR becomes $\gamma - 1 = -1/2$.

Equation (3.54) is in general nonlinear. In the special case in which the density is constant *everywhere*, $\bar{\rho}$, by symmetry the scalar field is also space-independent, we denote its constant value by $\bar{f}_R$. In this case the l.h.s of Eq. (3.54) vanishes, and the solution is given by $R[\bar{f}_R] = \kappa^2\bar{\rho}$. Interpreting the r.h.s. of Eq. (3.54) as the derivative of the f_R effective potential as in Eq. (3.23), the field's homogeneity leads

to the field being at the minimum of its potential, which is given by Eq. (3.25) under the approximation $|f/R \ll 1|$ and $|f_R \ll 1|$ for non-relativistic matter. For local test of $f(R)$ models we are of course interested in non-trivial space-dependent solutions; in particular in spherically symmetric solutions in the solar system. First, it is useful to consider situations in which the density, and hence the scalar field, deviate only slightly from a constant homogenous background. Then Eq. (3.54) can be linearized in the deviations $\delta\rho \equiv \rho - \bar{\rho}$ and $\delta f_R \equiv f_R - \bar{f}_R$ and we obtain the *linear* equation

$$\nabla^2 \delta f_R = \lambda_{f_R}^{-2} \delta f_R - \frac{1}{3}\kappa^2 \delta\rho. \tag{3.61}$$

where

$$\lambda_{f_R}^{-2} = \frac{R'[\bar{f}_R]}{3}, \tag{3.62}$$

since $R' = 1/f_{RR}$ (by inverting $f_R(R)$), we can rewrite Eq. (3.62) as

$$\lambda_{f_R}^2 = 3 f_{RR}\Big|_{\bar{f}_R}, \tag{3.63}$$

with λ_{f_R} the field's Compton wavelength set by the background field value [¶]. Notice that Eq. (3.63) implies that $f_{RR} > 0$ is required for stability [74]. The Green's function for Eq. (3.61), *i.e.*, the solution for a point source $\rho(\mathbf{x}) = \delta(\mathbf{x})$ at the origin, is the Yukawa potential $\delta f_R(r) \propto e^{-r/\lambda_{f_R}}/r$, implying an effective "fifth force" mediated by the scalar field with an interaction range given by its Compton wavelength. The relevant solutions in the solar system are far from this linear regime. However Eq. (3.63) plays an important role in solar system tests. Crucially, due to the nonlinearity of the original equation Eq. (3.54), the Compton wavelength depends on the background solution $\bar{f}_R$ which itself depends on the background density $\bar{\rho}$. We will show below that this is a key feature which triggers a *chameleon* behavior, allowing some $f(R)$ models to evade solar system constraints.

The tightest constrain on γ comes from the Doppler tracking of the Cassini space-craft [75]. By measuring the time delay of light on its way to Saturn, it measured $\gamma - 1 = (2.1 \pm 2.3) \times 10^{-5}$. Weaker constraints are given by light deflection measurements, $\gamma - 1 \sim 10^{-4}$ [76], and the observed perihelion shift of Mercury's orbit, $\gamma - 1 \sim 10^{-3}$ [77]. In the BD theory given by Eq. (3.9), $\gamma = (1 + \omega_{BD})/(2 + \omega_{BD})$ and the rest of the PPN parameters take the same value as in GR [64]. From the results of the Cassini experiment $\omega_{BD} > 40000$. Since $f(R)$ gravity models are equivalent to the BD theory with $\omega_{BD} = 0$, it was first suggested in [67] that all $f(R)$ models are incompatible with solar system constraints. Since then, whether $f(R)$ models can survive solar system tests has been a long theme of discussion [67, 78–84].

But as we have seen above, in the situation in which $M_{\text{eff}} \ll M_{\text{tot}}$, $-2M_{\text{eff}}/3M_{\text{tot}} \ll 1$ and $\gamma \approx 1$. In the following we discuss under which conditions such situation arises.

[¶]Equation (3.63) is Eq. (3.26) under the approximation $|f_R| \ll 1$, and since $f_{RR} \sim f_R/R$, $|f_R/R| \ll 1/R$, leading to $|f_{RR}| \ll 1/R$.

3.4.2 Compton Condition

In $f(R)$ theories, high density does not necessarily correspond to high curvature [74]. A sufficient condition for the high curvature solution is that the field gradients are small at all radii, then $R \approx \kappa^2\rho$ gives the solution for R everywhere. However for self-consistency is necessary that field gradients implied by this high curvature solution, $f(R = \kappa^2\rho)$, are small compared to local density gradients. To justify that the Laplacian of the field is indeed negligible at high density regions, consider

$$\nabla^2 f_R = f_{RRR}\left(\frac{\partial R}{\partial x_i}\right)^2 + f_{RR}\frac{\partial^2 R}{\partial x_i^2}\,, \tag{3.64}$$

evaluated with $R \approx \kappa^2\rho$. This must be

$$f_{RRR}\mid_{R=\kappa^2\rho}\kappa^4\left(\frac{\partial\rho}{\partial x_i}\right)^2 + f_{RR}\mid_{R=\kappa^2\rho}\kappa^2\frac{\partial^2\rho}{\partial x_i^2} \ll \kappa^2\rho\,, \tag{3.65}$$

which yields the conditions $\parallel$

$$1) \quad f_{RR}\mid_{R=\kappa^2\rho}\frac{\partial^2\rho}{\partial x_i^2} \ll \rho\,, \tag{3.66}$$

$$2) \quad f_{RRR}\mid_{R=\kappa^2\rho}\kappa^2\left(\frac{\partial\rho}{\partial x_i}\right)^2 \ll \rho. \tag{3.67}$$

By taking $f_{RRR} \sim f_{RR}/R$, we can rewrite the expression given by Eq. (3.67) as

$$f_{RR}^{1/2}\mid_{R=\kappa^2\rho}\partial_i\rho \ll \rho\,. \tag{3.68}$$

More intuitively, we can write $\partial_i\rho \sim \rho/L$, where L is the scale at which the density changes, substituting this in Eq. (3.68) and using Eqs. (3.63)

$$\lambda_{f_R} \sim f_{RR}^{1/2}\mid_{R=\kappa^2\rho} \ll L\,, \tag{3.69}$$

which gives the Compton condition. That is, if the Compton wavelength of the field is much smaller than the length scale of changes in the density of the source, then high density correspond to high curvature. In this situation, as we have discussed above, $M_{\text{eff}} \ll M_{\text{tot}}$ and $\gamma - 1 = -2M_{\text{eff}}/3M_{\text{tot}}$. If the Compton condition is satisfied at all radii, the high curvature solution is also satisfied at all radii and deviations from GR are highly suppressed. As we have seen in Eq. (3.23) (or equivalently in Eq. (3.15) in the Einstein frame), the dynamics of the scalar field is governed by the effective potential given by Eq. (3.24), which explicitly depends on the matter density. The source induces changes in the field with a Yukawa profile and when the Compton condition is satisfied, such changes are highly suppressed on scales larger than the Compton wavelength.

$\parallel$Equations (3.67)-(3.68) correspond to Eq.(49) of [70].

In summary, the Compton condition is what self-consistently justifies the approximate high-curvature solution $R \approx \kappa^2 \rho$ for Eq. (3.54). Under such condition the field is everywhere approximately at the minimum of the potential, even though the density is not strictly speaking constant but it changes slowly, *i.e.*, on length scales much larger than the local Compton's wavelength set by the local value of the density. Note that, if it holds with good accuracy it is sufficient to make the model pass the solar system test, because it assures that the "source" in the r.h.s. of Eq. (3.54) is everywhere small and hence $\mathcal{B}$, which satisfies the same equation (and a zero boundary condition at infinity), will be small compared to $\mathcal{A}$, yielding a small $|\gamma - 1|$.

The scale at which density changes, L, is related to k in Eq. (3.42) as $L \sim k^{-1}$. Thus, since $Q \sim k^2$, $\lambda_{f_R}^2 Q \sim \lambda_{f_R}^2 / L^2$. When the Compton condition is satisfied and $L \gg \lambda_{f_R}$, $Q \ll 1$ and the growth of structure equation (3.45), reduces to the ΛCDM one, which is scale independent. As we saw, $Q(k, a)$ recasts the dependence on the scale of the growth of structure, Eq. (3.45), in $f(R)$ models.

3.4.3 Thin Shell Condition

As we have mentioned in the previous section, the matter density induces changes in the field with a Yukawa profile. If such changes are not suppressed on scales larger than the Compton wavelength, the approximate high curvature solution, $R \approx \kappa^2 \rho$ does not give the solution for R everywhere: the Compton condition is not everywhere satisfied and at some radius there is a transition to the regime in which field gradients are not small compared to the matter density, the low curvature regime. However, if the dependence of the field's Compton wavelength on the matter density is very strong, there is a possible situation in which the Compton condition is locally satisfied in the bulk of the source, while not being satisfied just in a thin-shell at the boundary of the source, small enough to evade solar system constraints. This is the so-called thin-shell condition, also known as the Chameleon mechanism. More concretely, if the source $\kappa^2 \rho - R$ is non-negligible only in a thin-shell on the boundary of the Sun that is small enough to pass the Cassini mission constraint, the thin-shell condition will be satisfied. In this situation, the Compton wavelength outside the Sun (set by the background galactic density) does not need to be much smaller than the scales on which the density changes (e.g. the Sun's radius), indeed it can be very large.

In order to see what is self-consistently required to justify the thin-shell condition, let us write $f_R(r) = \varphi(r) + \varphi_g$, where the constant $\varphi_g = f_R^g$ is the boundary condition at $r \to \infty$ set by the galactic density via $R[f_R^g] = \kappa^2 \rho_g$; thus $\varphi(r)$ satisfies the boundary condition $\varphi \to 0$ as $r \to \infty$. We can then rewrite Eq. (3.54), as

$$\nabla^2 \varphi = -\frac{\kappa^2}{3}(\rho - \kappa^{-2}R[\varphi + \varphi_g]), \qquad (3.70)$$

which can be cast as a set of two integral equations as follows

$$M(r) = 4\pi \int_0^r \left(\rho(\tilde{r}) - \kappa^{-2} R[\varphi(\tilde{r}) + \varphi_g] \right) \tilde{r}^2 d\tilde{r} \, ; \tag{3.71}$$

$$\varphi(r) = \frac{\kappa^2}{3} \int_r^\infty \frac{M(\tilde{r})}{4\pi\tilde{r}^2} d\tilde{r} = \frac{2G}{3} \int_r^\infty \frac{M(\tilde{r})}{\tilde{r}^2} d\tilde{r} \, , \tag{3.72}$$

where the second equation is obtained by integrating $-\nabla\varphi = \frac{M(r)}{r^2}$ using Gauss's law, and imposing the boundary condition $\varphi(r = \infty) = 0$. Now let us assume that well inside the Sun the high-curvature solution, $R \approx \kappa^2\rho_\odot$, holds, so that the integrand in Eq. (3.71) is zero. Thus, $M(r) \approx 0$ for $r < r_\odot - \Delta r$, where Δr is the width of the thin-shell in which the actual solution starts deviating from the high-curvature solution. Furthermore, if $\Delta r \ll r_\odot$, $M(r)$ will have a sharp rise from 0, for $r < r_\odot - \Delta r$, to a nonzero value $M(r_\odot^+)$ just outside the Sun's radius. Assuming that the contribution of $\rho_g - \kappa^{-2} R$ to $M(r)$ for $r > r_\odot$ is negligible compared to the contribution of the thin-shell of $r \in [r_\odot - \Delta r, r_\odot]$, we can approximate $M(r_\odot^+)$ with $M(\infty) = M_{\text{eff}}$. The result is that $M(r)$ is a function that is zero for $r < r_\odot - \Delta r$ and rises sharply within the thin-shell, almost like a step-function, to $M(\infty) = M_{\text{eff}}$ just outside the Sun's radius. With such a profile for $M(r)$, from Eq. (3.72) we obtain that

$$\varphi(r) = \frac{2GM_{\text{eff}}}{3} \int_{\max(r,r_\odot)}^\infty \frac{d\tilde{r}}{\tilde{r}^2} = \frac{2GM_{\text{eff}}}{3\max(r,r_\odot)}. \tag{3.73}$$

In particular, well within the Sun, $r < r_\odot - \Delta r$, and given the definition of φ,

$$f_{_R}(r) - f_{_R}^g = \frac{2GM_{\text{eff}}}{3r_\odot}. \tag{3.74}$$

On the other hand, the high-curvature solution, which we assumed valid well inside the Sun, states that in the same range $f_{_R}(r) = f_{_R}^\odot$, where $f_{_R}^\odot$ is determined by solving $R[f_{_R}^\odot] = \kappa^2\rho_\odot$, where we have written $R[f_{_R}]$, because in order to solve this equation in general for the scalar field $f_{_R}$, we need to express R as function of $f_{_R}$ by inverting the relation $f_{_R}(R)$. Combining this with Eq. (3.74) we obtain

$$f_{_R}^\odot - f_{_R}^g = \frac{2GM_{\text{eff}}}{3r_\odot}. \tag{3.75}$$

Since $-\mathcal{B}$ can be identified with φ given that it satisfies the same equation and the same boundary condition at infinity, from Eq. (3.73) we have

$$\mathcal{B}(r) = -\frac{2GM_{\text{eff}}}{3r} \quad , \qquad (r > r_\odot) \, , \tag{3.76}$$

which is equivalent to Eq. (3.57). As we have discussed after Eq. (3.60), to pass the Cassini mission constraint, $\mathcal{B}(r_\odot) \ll \mathcal{A}(r_\odot)$, or equivalently $2M_{\text{eff}}/3 \ll M_{\text{tot}}$. Thus, using Eq. (3.75) we can thus rephrase the thin-shell condition in terms of M_{tot} as

$$f_{_R}^\odot - f_{_R}^g \ll \frac{GM_{\text{tot}}}{r_\odot}. \tag{3.77}$$

By substituting Eq. (3.60) (for $M_{\text{eff}} \ll M_{\text{tot}}$) in Eq. (3.76), we can express the thin-shell condition, Eq. (3.77), in terms of the parameter γ as

$$f_R^{\odot} - f_R^g \approx (\gamma - 1)\frac{GM_{\text{tot}}}{r_{\odot}} \, . \tag{3.78}$$

Since $M_{\text{tot}} \approx M_{\odot}$, we can rewrite Eq. (3.78) in terms of the Newtonian potential of the Sun, $\Phi_{\odot} = GM_{\odot}/r_{\odot}$, as

$$f_R^{\odot} - f_R^g \approx (\gamma - 1)\Phi_{\odot} \tag{3.79}$$

Notice that there is no need to find the full solution for φ or f_R to verify Eq. (3.78). The thin-shell condition for a given $f(R)$ model, can be verified given the Newtonian potential of the Sun, $\Phi_{\odot} = GM_{\odot}/r_{\odot} = 2.12 \times 10^{-6}$ and the galactic mass density. Given the Cassini constrain, $\gamma - 1 = (2.1 \pm 2.3) \times 10^{-5}$, Eq. (3.79) implies that

$$\mid f_R^{\odot} - f_R^g \mid \approx \mid f_R^g \mid < 4.9 \times 10^{-11} \, . \tag{3.80}$$

In Sec. 5.6, we shall explore this condition for the models which do not satisfy the Compton condition.

In the next chapter we describe the general conditions under which particular $f(R)$ models describe viable cosmological histories, based on the qualitative features of the observed expansion history of the universe.

Chapter 4

Cosmological Viability of $f(R)$ Models

Any cosmologically viable $f(R)$ model must respect the cosmological constraints imposed by qualitative features of the observed expansion history of the universe, as discussed in Chapter 1. In particular, a viable $f(R)$ model should allow for a cosmological expansion history which starts from an era dominated by radiation leading to a matter dominated epoch, long enough to give rise to structure formation, ending in the current accelerated expansion era. A study of the general conditions under which a $f(R)$ theory allows for such a expansion history in a spatially flat, homogeneous and isotropic spacetime, have been proposed in [69]. In this chapter, we follow the analysis of [69] to study the particular $f(R)$ models previously introduced. In Sec. 4.1 we present the dynamical systems approach and describe the general conditions under which a $f(R)$ model is cosmologically viable. In Sec. 4.2 we perform this analysis on specific families of $f(R)$ models which in principle are able to produce viable cosmological histories.

4.1   General Conditions

In this section we present the dynamical system approach proposed by [69] which encloses the dynamics of the modified Friedmann equations presented in the previous chapter. This system has two crucial properties. In first place, the only dependence on the specific $f(R)$ model under study is encoded in only one function, namely $m(r)$. In second place, the fixed points of this dynamical system can be identified with the different epochs of the expansion history of the universe through the value of the observable cosmological parameters (Ω_i and w_{eff}) at each of the fixed points. As we will see, the stability of the fixed points depends on the function $m(r)$. This feature allows to generalize the conditions under which a general $m(r)$ function (*i.e.*, a general $f(R)$ model) can reproduce a viable cosmological history according to observations.

Throughout this chapter we consider well-behaved and smooth $f(R)$ functions. It is also important to consider functions for which $1 + f_R > 0$ everywhere to maintain a positive effective gravitational constant under linear perturbations (see Eq. (3.44)) [*].

4.1.1 Evolution of the Homogeneous Universe in $f(R)$ Cosmology

The modified Friedmann equations, Eqs. (3.27)–(3.28), can be rewritten in the form of an autonomous system of first order differential equations. Following [69], we can introduce the dimensionless variables

$$x_1 \equiv -\frac{\dot{f}_R}{H(1 + f_R)}, \tag{4.1}$$

$$x_2 \equiv -\frac{R + f}{6H^2(1 + f_R)}, \tag{4.2}$$

$$x_3 \equiv \frac{R}{6H^2} = \frac{\dot{H}}{H^2} + 2, \tag{4.3}$$

$$x_4 \equiv \frac{\kappa^2 \rho_{\rm rad}}{3H^2(1 + f_R)}. \tag{4.4}$$

From Eq. (3.27) and the definitions Eqs. (4.1)–(4.4) we obtain the algebraic relation

$$\Omega_M(t) \equiv \frac{\kappa^2 \rho_M}{3H^2(1 + f_R)} = 1 - x_1 - x_2 - x_3 - x_4. \tag{4.5}$$

In a similar way we can also define [†]

$$\Omega_R(t) \equiv x_4, \tag{4.6}$$

$$\Omega_{DE}(t) \equiv x_1 + x_2 + x_3, \tag{4.7}$$

By taking the derivatives of Eqs. (4.1)–(4.4) with respect to $\ln a$, and using Eq. (3.28) and the conservation law Eq. (2.26) for $\rho_{\rm rad}$, we obtain the following four-dimensional dynamical system:

$$\frac{d\mathbf{x}}{d \ln a} = \boldsymbol{v}(\mathbf{x}), \tag{4.8}$$

---

[*]It may happen that this condition is violated in some range of $f_R(R)$ but not in the real trajectory *i.e.*, $f_R(R(t))$.

[†]Equation (4.5) is reminiscent of Eq. (2.33) (which followed from the first Friedman equation Eq. (2.21) for $f(R) = R - 2\Lambda$) obeyed by the dimensionless density parameters defined in Eq. (2.31). Indeed, the x_i variables are chosen to mimic and generalize the various dimensionless density parameters of ΛCDM cosmology in a general $f(R)$ model. The formulation of the dynamics in terms of such parameters facilitates the study of epochs in which the total energy density is dominated by one form of matter.

where $\mathbf{x} \equiv (x_1, x_2, x_3, x_4)$ and the components of the vector field $\boldsymbol{v}(\mathbf{x})$ are given by

$$v_1(\mathbf{x}) = -1 - x_3 - 3x_2 + x_1^2 - x_1 x_3 + x_4, \tag{4.9}$$

$$v_2(\mathbf{x}) = \frac{x_1 x_3}{m(R)} - x_2(2x_3 - 4 - x_1), \tag{4.10}$$

$$v_3(\mathbf{x}) = -\frac{x_1 x_3}{m(R)} - 2x_3(x_3 - 2), \tag{4.11}$$

$$v_4(\mathbf{x}) = -2x_3 x_4 + x_1 x_4. \tag{4.12}$$

The only dependence of this system on the specific $f(R)$ model is through $m(R)$, defined as

$$m(R) \equiv \frac{R f_{RR}}{1 + f_R}, \tag{4.13}$$

which depends only on the instantaneous value of R. However, in order to write the system Eqs. (4.8)–(4.12) as an explicitly closed system, we have to rewrite $m(R)$ as a function of x_i. To this end, notice from the definitions Eqs. (4.2)–(4.3) that the ratio x_3/x_2 is also only a function of R. Thus if we define

$$r \equiv \frac{x_3}{x_2} = -\frac{R(1 + f_R)}{R + f}, \tag{4.14}$$

we can in principle invert this relation for any given $f(R)$ model, to express R as a function of $r = x_3/x_2$, and then substitute the obtained $R(r)$ in Eq. (4.13) to obtain the function $m(r) \equiv m(R(r))$ [‡]. From now on we understand the $m(R)$ in Eqs. (4.10)–(4.11) to be given in this way, *i.e.*, as a function of $r = x_3/x_2$.

Finally, note that from the definition Eq. (4.3), x_3 is closely related to the effective equation of state parameter, w_{eff}, defined in Eq. (2.25). Namely,

$$w_{eff} = -\frac{1}{3}(2x_3 - 1). \tag{4.15}$$

As we mentioned in the introduction to this chapter, a viable $f(R)$ model should allow for a cosmological history that, according to observations, initiates at a radiation dominated epoch that leads to a matter dominated era, long enough to allow for structure formation, and finally enters in the current accelerated expansion era. Following the discussion after Eq. (2.28), at each of these epochs, the universe expands at different time rates. During radiation domination the expansion of the universe is characterized by $a \propto t^{1/2}$ (associated to $w_{eff} = w_R = 1/3$), while during matter domination expands as $a \propto t^{2/3}$ for $w_{eff} = w_M = 0$, finally at the accelerated expansion era, the universe scales as $a \propto e^{Ht}$ (de Sitter solution), provided that $w_{eff} = w_{DE} = -1$. The crucial feature in this analysis is that these three different epochs are dominated by a single

---

[‡]In some cases $r(R)$ is not invertible and is not possible to find $m(r)$. In other cases $R(r)$ has more than one root and $m(r)$ becomes a multi-branched function, in which case the system of Eqs. (4.8)–(4.12) must be solved for each branch separately.

form of energy density where w_{eff} is more or less constant over time. According to Eq. (4.15), these are eras with an approximately constant x_3. However, in a coupled system such as (4.8)–(4.13), such a situation can generically be achieved only if the solution passes close to a fixed point, such that *all* x_i's are approximately constant. For all these reasons in the next section we will classify all fixed points of Eq. (4.8) and study their stability properties.

4.1.2 Fixed Points and Their Stability

In the first analysis, the qualitative dynamics of the autonomous system Eqs. (4.8)–(4.12) is captured by the study of its fixed points and their stability. For a general $f(R)$, eight fixed points $F_{1,2,3,4,5,6,7,8}$ arise when setting $dx_i/d\ln a = 0$ in Eqs. (4.8)–(4.12). These are recast in Tab. 4.1.2. At a first look, an important feature to realize is that not all the fixed points depend on the model *i.e.*, on $m(r)$. In particular, F_1, F_3, F_5, F_7 and F_8 exist for any given $f(R)$ model [§], while F_2, F_4 and F_6 depend on the specific value of $m(r)$.

In Tab. 4.1.2 are also recast the values of Ω_R, Ω_M and w_{eff} of each fixed point. As we can see, only trajectories passing close to F_1 and F_2 will reproduce a radiation era, as for the rest of the points $\Omega_R = 0$. F_1 is always a standard radiation point as it has $w_{eff} = 1/3$, while for F_2, $w_{eff} = 1/3$ only when $m_2 \simeq 0$; hereinafter m_i denotes $m(r)$ at F_i. A standard matter era can only arise from trajectories passing close to F_3 and F_4 since these are the only ones with $\Omega_M \neq 0$. However, they should also satisfy $w_{eff} \approx 0$ which, from Tab. 4.1.2, only happens for F_4 when $m_4 \simeq 0$; for F_3 the effective equation of state is always $w_{eff} = 1/3$, giving rise to a non-standard evolution with $a \propto t^{1/2}$ and yielding a non-desirable matter era. The accelerated expansion would be possible for trajectories ending at F_5 which provides $w_{eff} = -1$, or either F_6 depending on the value of m_6. F_6 can provide accelerated expansion when m_6 satisfies the condition for acceleration, $w_{eff} < -1/3$, which happens in the regions $m_6 < -(1 + \sqrt{3})/2$, $-1/2 < m_6 < 0$ and $m_6 > (\sqrt{3}-1)/2$. In principle F_4 and F_2 could also give rise to an accelerated expansion epoch when $m_4 > 1/2$ or $m_4 < -1$, and $m_2 \to \infty$, respectively. However, they yield a saddle point or an unstable node which means that the universe would not remain in an accelerated state. Finally, F_7 and F_8 do not have the properties

---

[§] It should be noted that F_3 and F_7 are generically, but not always, legitimate fixed points. As is seen from Tab. 4.1.2 and Eqs. (4.10)–(4.11), for these to be fixed points the necessary condition is that the ratio x_3/m vanishes. However, given that $x_2 = x_3 = 0$ for both points, r and also $m = m(r)$ are indeterminate at both points. Thus for F_3 and F_7 to be fixed points we must have $\lim_{x_{2,3}\to 0} \frac{x_3}{m} = 0$, which assuming H^2 does not diverge, is equivalent to having

$$\frac{1 + f_R}{f_{RR}} \to 0, \tag{4.16}$$

when $R \to 0$ and $\frac{R+f}{1+f_R} \to 0$. This turns out to hold for most $f(R)$ models of interest, but is not guaranteed in general and must be verified case by case.

P	(x_1, x_2, x_3, x_4)	Ω_R	Ω_M	w_{eff}
F_1	$(0, 0, 0, 1)$	1	0	$1/3$
F_2	$\left(\frac{4m}{1+m}, -\frac{2m}{(1+m)^2}, \frac{2m}{1+m}, \frac{1-2m-5m^2}{(1+m)^2}\right)$	$\frac{1-2m-5m^2}{(1+m)^2}$	0	$\frac{1-3m}{3+3m}$
F_3	$(-1, 0, 0, 0)$	0	2	$1/3$
F_4	$\left(\frac{3m}{1+m}, -\frac{1+4m}{2(1+m)^2}, \frac{1+4m}{2(1+m)}, 0\right)$	0	$1 - \frac{m(7+10m)}{2(1+m)^2}$	$-\frac{m}{1+m}$
F_5	$(0, -1, 2, 0)$	0	0	-1
F_6	$\left(\frac{2(1-m)}{1+2m}, \frac{1-4m}{m(1+2m)}, -\frac{(1-4m)(1+m)}{m(1+2m)}, 0\right)$	0	0	$\frac{2-5m-6m^2}{3m(1+2m)}$
F_7	$(1, 0, 0, 0)$	0	0	$1/3$
F_8	$(-4, 5, 0, 0)$	0	0	$1/3$

Table 4.1: Fixed points of the autonomous system Eqs. (4.8)–(4.12). Ω_R, Ω_M and w_{eff} are given by Eq. (4.6), Eq. (4.5) and Eq. (4.15), respectively.

to reproduce either radiation, matter nor accelerated eras (F_7 is a particular case of F_6 when $m = 1/4$, F_8 has similar properties and it is also a particular case of F_6 for $m = -1$).

As we mentioned above, only the points F_2, F_4 and F_6 depend on the specific $f(R)$ model through $m(r)$. Importantly, in the system of Eqs. (4.8)–(4.12), $m(r)$ is a function of x_3/x_2. However, the putative fixed points in Tab. 4.1.2 where found by replacing the function $m(x_3/x_2)$ with a parameter m; thus these putative fixed point solutions for x_i yield true fixed points of Eqs. (4.8)–(4.12) only if they further satisfy the equation $m = m(r) = m(x_3/x_2)$. From Tab. 4.1.2 we see that for F_2, F_4 and F_6 (the only points that depend parametrically on m), we have $\frac{x_3}{x_2} = -(m+1)$, or $m = -\frac{x_3}{x_2} - 1$. Thus the points F_2, F_4 and F_6 exist as true fixed points of Eqs. (4.8)–(4.12) only for values of $m(r)$ corresponding to the roots of the equation

$$m(r) = -r - 1. \tag{4.17}$$

Geometrically, to every root, r_i, of Eq. (4.17), there corresponds a 3D subspace of the phase space satisfying $x_3 = r_i x_2$, and on each such subspace we have a F_2, a F_4 and a F_6. Therefore the exact number of fixed points depends on the number of roots of Eq. (4.17), which in turn depends on the specific $f(R)$ model. An important fact arises by the inspection of the dynamics of r. By the chain rule and $\frac{dt}{d\ln a} = H^{-1}$ we have

$$\frac{dr}{d\ln a} = \frac{dr}{dR}\frac{\frac{dR}{dt}}{H}, \tag{4.18}$$

while from the definitions Eqs. (4.13) and (4.14) we can write $\frac{dr}{dR}$ in terms of r and $m(r)$

$$\frac{dr}{dR} = -(m(r) + r + 1)\frac{r}{R}. \tag{4.19}$$

69

Thus, clearly when r is a root of Eq. (4.17) $dr/dR = 0$, and from Eq. (4.18), it follows that $dr/d\ln a = 0$ (as long as $\dot{R}/HR$ is not divergent). This shows that the subspaces corresponding to the roots of Eq. (4.17) cannot be crossed by any cosmological trajectory. That is, a trajectory starting at a point between two subspaces corresponding to two adjacent roots of Eq. (4.17), will always remain between them.

Going back to the discussion of the expansion history, a possible one consistent with observations, would be given by any trajectory which starts at either F_1 or the F_2 corresponding to a root of Eq. (4.17) with $m_2 \approx 0$ (which we will call $F_2^{(0)}$), then passes close to the F_4 corresponding to a root of Eq. (4.17) with $m_4 \approx 0$ (which we will call $F_4^{(0)}$), and finally lands on either F_5 or one of the F_6 points. To reconstruct such trajectories, the fixed points giving rise to the radiation and matter epochs need to be saddle points, the trajectory should be close to these fixed points long enough to generate the observed expansion history and then depart to the next epoch. Assuming that the universe will keep accelerating, we need the final accelerated stage, given by either F_5 or F_6, to be a stable attractor.

Stability analysis for fixed points

The stability of the fixed points can be easily studied by linearizing the system around each fixed point. In the following we summarize the stability properties of the relevant fixed points:

1. Radiation dominated saddle points

    - F_1: the eigenvalues of this point are $4, 4, 1, -1$, which means F_1 is a saddle point.

    - F_2: in this case the eigenvalues are given by

    $$ 1 \quad , \quad \frac{m_2 - 1 \pm \sqrt{81m_2^2 + 30m_2 - 15}}{2(1 + m_2)} \quad , \quad 4(m_2' + 1) \, , \qquad (4.20) $$

    where $m' = dm/dr$. In the limit $m_2 \to 0$, the two eigenvalues in the middle of expression (4.20) are complex with negative real parts, therefore F_2 in that limit, which we denoted as $F_2^{(0)}$ and we will refer to it as the radiation fixed point, is a saddle point independently of the value of m_2'. It is worth noting that when $m_2 \approx 0$, one can see from Tab. 4.1.2 that F_1 coincides with $F_2^{(0)}$, and it is not necessary to consider F_1 separately.

2. Matter dominated saddle point

    - F_4: as we have mentioned before, a standard matter era, *i.e.*, scaling as $a \propto t^{2/3}$ and with $\Omega_M = 1$, can only be provided by the F_4 corresponding to a root of Eq. (4.17) with $m_4 \simeq 0$, which we denote as $F_4^{(0)}$ and we will

refer to it as the matter fixed point. According to Eq. (4.17) the necessary condition for the existence of $F_4^{(0)}$ is

$$m_4(r = -1) \approx 0. \tag{4.21}$$

In the limit $|m_4| \ll 1$, its eigenvalues reduce to

$$-1 \quad , \quad -\frac{3}{4} \pm \sqrt{-\frac{1}{m_4}} \quad , \quad 3(1 + m_4'). \tag{4.22}$$

When $F_4^{(0)}$ is approached from $m_4 \to 0^+$, two of the eigenvalues are complex with negative real parts and very large imaginary parts. Provided $m_4' > -1$, in this case $F_4^{(0)}$ is a saddle point with very fast but damped oscillations. This situation allows for trajectories to evolve through a standard matter era and then depart to another fixed point corresponding to the desired current acceleration era. If instead $F_4^{(0)}$ is approached from $m_4 \to 0^-$, the eigenvalues remain real, but diverge. Therefore the point will be extremely unstable in one direction and trajectories will not be able to remain long enough around the $F_4^{(0)}$ to generate a long enough matter era. Therefore Eq. (4.21) and

$$m_4 > 0 \quad , \quad m_4' > -1, \tag{4.23}$$

are the conditions for the existence of a saddle point matter era with damped oscillations which would be cosmologically acceptable.

3. Accelerated expansion attractors

- F_5: the eigenvalues of F_5 are

$$-4 \quad , \quad -3 \quad , \quad -\frac{3}{2} \pm \frac{\sqrt{25 - 16/m_5}}{2}, \tag{4.24}$$

with $m_5 = m(r = -2)$. Thus, F_5 is a stable point when $0 < m_5 < 1$ and otherwise is a saddle point. Given that $w_{eff} = -1$, F_5 corresponds to the de Sitter solution.

- F_6: an accelerated expansion only occurs if $w_{eff} < -1/3$, which constrains m_6 to three different ranges of interest given by $m_6 < -(1+\sqrt{3})/2$, $-1/2 < m_6 < 0$ and $m_6 > (\sqrt{3}-1)/2$. These are shown in Fig. 10. The eigenvalues of F_6 are

$$-4 + \frac{1}{m_6} \, , -\frac{8m_6^2 + 3m_6 - 2}{m_6(2m_6 + 1)} \, , -\frac{10m_6^2 + 4m_6 - 2}{m_6(2m_6 + 1)} \, , -\frac{2(m_6^2 - 1)(m_6' + 1)}{m_6(2m_6 + 1)}, \tag{4.25}$$

meaning that the stability of F_6 depends on both m_6 and m_6'. We can distinguish four different regions where F_6 is stable and accelerated:
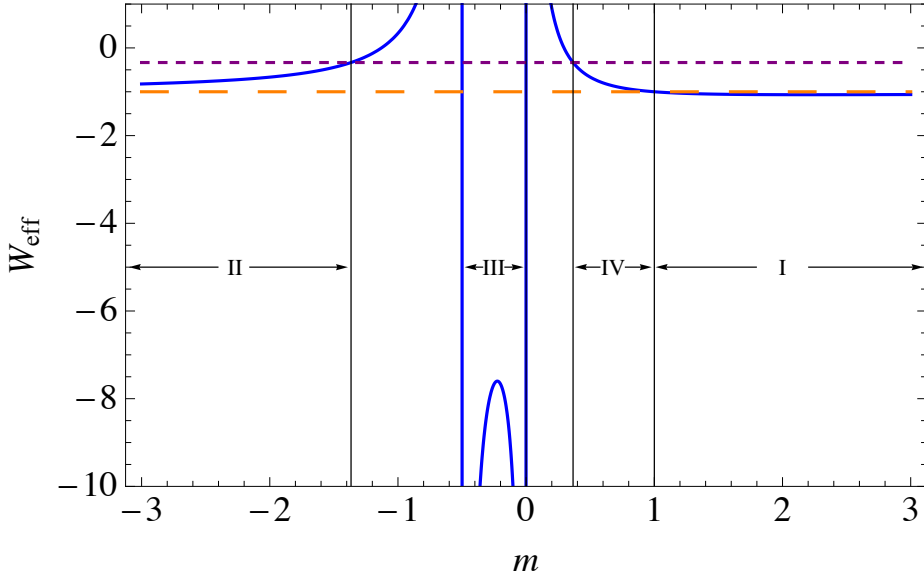
71

Figure 10: w_{eff} versus m for the F_6 fixed point (blue line). The dashed purple line represents $w_{eff} = -1/3$ and the orange line represents $w_{eff} = -1$. In the regions I, II and III, F_6 is stable and accelerated when $m'_6 > -1$, while in the region IV it is stable when $m'_6 < -1$.

Region I: when $m'_6 > -1$ and $m_6 \geq 1$.
In this region $-1.07 < w_{eff} \leq -1$. In the limits $m_6 \to 1$ and $m_6 \to +\infty$, $w_{eff} \to -1$ in which case F_6 corresponds to the de Sitter solution.

Region II: when $m'_6 > -1$ and $m_6 < -(1 + \sqrt{3})/2$.
In this region $w_{\text{eff}} > -1$. In the limit $m_6 \to -\infty$, $w_{eff} \to -1$ and F_6 corresponds again to the de Sitter solution.

Region III: when $m'_6 > -1$ and $-1/2 < m_6 < 0$.
In this region $w_{eff} < -7.6$, range which is completely ruled out by observations.

Region IV: when $m'_6 < -1$ and $(\sqrt{3} - 1)/2 < m_6 < 1$.
In this region $w_{eff} > -1$.

4.1.3   Cosmologically Viable Trajectories

The possibility for the correct transitions between different cosmological epochs, translates into the possibility of transitions between the corresponding fixed points. As we have shown, this imposes certain conditions on the stability properties of these fixed

points. In the following we recast all these conditions into properties of the $m(r)$ curve, Eq. (4.17), and its behavior in the (r, m) plane.

The fixed points F_2, F_4 and F_6 (see Tab. 4.1.2), only exist for roots of Eq. (4.17). In terms of the (r, m) plane, these roots correspond to intersections of the $m(r)$ curve with the line $m = -r - 1$. We call this line the *critical line*, following Ref. [69]. According to the discussion after Eq. (4.19), a transition between any two of these fixed points is possible only if the $m(r)$ curve directly connects the corresponding roots of Eq. (4.17) without intersecting the critical line in between, or if the two fixed points correspond to the same root.

We consider now the different fixed points and transitions. For a given $m(r)$, Eq. (4.21) gives the necessary condition for the existence of the matter fixed point, $F_4^{(0)}$. Thus, the matter fixed point, when it exists, corresponds to an intersection of $m(r)$ and the critical line close to the coordinates $(-1, 0)$ in the (r, m) plane. We call this root of Eq. (4.17) the 0-root. The existence of this root also guarantees the existence of the radiation saddle fixed point, $F_2^{(0)}$. Since $F_2^{(0)}$ belongs to the same subspace as the matter fixed point, this automatically allows for the cosmological trajectory to start at the radiation fixed point and depart to the matter fixed point. Therefore in the following we will focus on the conditions under which a transition from the standard matter fixed point to one of the final accelerated attractors is possible. Firstly, for such a transition to be possible, $F_4^{(0)}$ must be a saddle point. Equation (4.23) translates this into a condition on $m(r)$. The 0-root can be approached from $m \to 0^+$ or from $m \to 0^-$. However, as we have discussed in the previous section, in the latter case the matter era is highly unstable and likely very short-lived. Therefore, the $m(r)$ curve must intersect the critical line above $(r, m) = (-1, 0)$. The other condition following from Eq. (4.23) is that the $m(r)$ curve must intersect the critical line with a slope $m_4' > -1$.

There are two possible candidates for the accelerated expansion, F_5 and F_6, which we will consider in turn.

Transition to F_5 on the de Sitter line

F_5 is at coordinates $(-2, m(r = -2))$ and is stable and accelerated when $0 < m(r = -2) < 1$. Thus, a transition to a desirable de Sitter phase given by F_5 is possible if the $m(r)$ curve intersects the vertical line segment connecting $(-2, 0)$ and $(-2, 1)$, without intersecting the critical line in between. We call the described line segment the de Sitter-line.

Transition to F_6 in regions I, II or IV

F_6 is stable and accelerated only if the corresponding root of Eq. (4.17) is in one of the four different regions I, II, III and IV. However in region III we have $w_{eff} < -7.6$ and we will not consider it since such a range of w_{eff} is completely ruled out by observations. As we mentioned above, a transition from the matter

fixed point to the accelerated fixed point is possible if the $m(r)$ curve, after leaving the 0-root, intersects immediately the critical line again in one of these four regions. For the first two cases, I or II, stability furthermore requires $m_6' > -1$. Given that we have also required $m' > -1$ at the 0-root, this situation requires $m(r)$ to be either a multivalued function or to be singular at a finite r.[¶] Otherwise the only possibility is for the $m(r)$ curve to be asymptotically convergent on the critical line at $r \to \pm\infty$ with a slope $m_6' = -1$.

On the other hand, if F_6 is in region IV, the $m(r)$ curve must intersect the critical line with $m_6' < -1$, for the F_6 to be stable. In this case, it is possible for the $m(r)$ curve to leave the 0-root going leftwards, and cross the critical line again in region IV from below, without any crossings in between.

Figure 11 illustrates the (r, m) plane with all these regions of stability. In short, we shall see that the possible intersections of the $m(r)$ curve with the critical line or the de Sitter-line capture crucial information about the viability of the model [‖].

This analytical study, summarized in terms of the behavior of the $m(r)$ curve, is a very useful *prior* analysis of the viability of any type of $f(R)$ models. However, to perform a full study, a numerical analysis is still mandatory, to ensure that initial conditions will lead from the radiation point to the desired matter point $F_4^{(0)}$ and they are not attracted by F_3 (which yields to a non-standard matter era).

4.2   Specific Types of Viable $f(R)$ Models

In the previous section we have described a straightforward methodology that recasts the general conditions under which $f(R)$ models are cosmologically viable. In this section we use this method to analyze specific families of $f(R)$ models. In each case we start by calculating the corresponding $m(r)$ function and analyzing its specific properties in the (r, m) plane. As we will shortly show, these properties allow to constrain the values of the free parameters of the corresponding type of model. We also give the numerical results of the cosmological parameters in each case by solving the system Eqs. (4.8)–(4.12) and choosing initial conditions close to the fixed point that gives rise to a radiation era. We add some graphical examples of possible trajectories in the vector field of the system (in these cases we have neglected radiation for simplicity).

[¶]As we have mentioned in the introduction to this section, we are assuming $1 + df/dR > 0$ and f to be smooth with all its derivatives. Under these conditions, $m(r)$ is a single valued and non-singular function given that $r(R)$ (Eq. (4.14)) is a monotonic function and is not possible to connect the region close to $m = 0^+$ with any of the regions I or II.

[‖]We should also note that the non-standard matter era fixed point F_3, when it exists (see the footnote before Eq. (4.17)), is either a saddle point or a stable node. Only by choosing appropriate initial conditions, is it possible to avoid trajectories entering in F_3, which would result in a non-standard matter era.
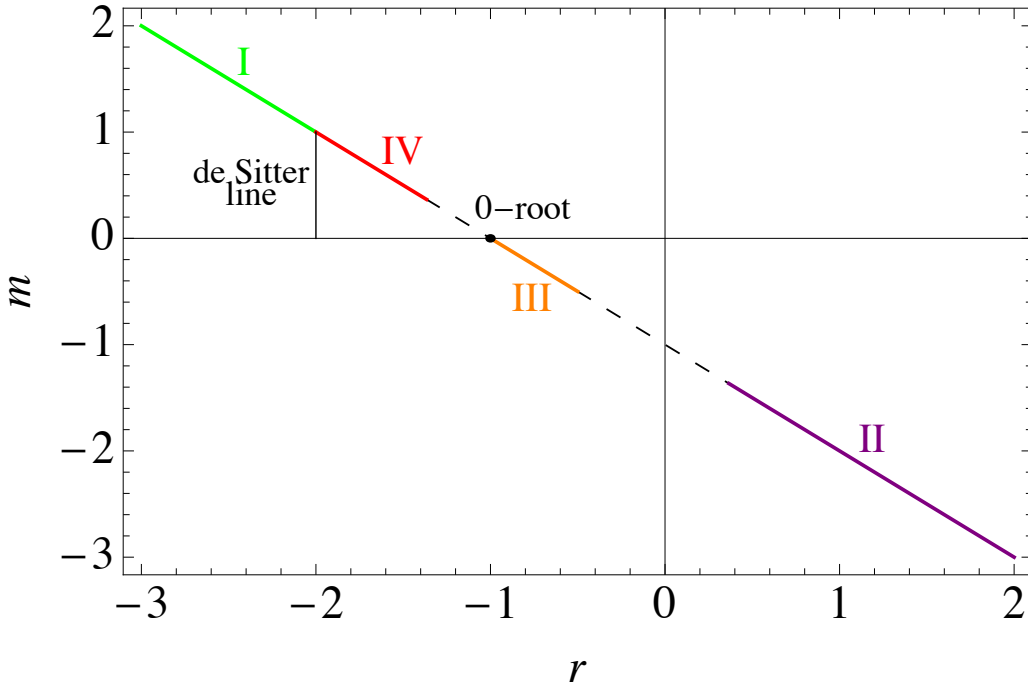
Figure 11: The critical line $m(r) = -r - 1$ in the (r, m) plane. The matter fixed point, $F_4^{(0)}$ lies at the 0-root at $(-1, 0)$, the de Sitter fixed point F_5, belongs to the grey line going from $(-2, 0)$ to $(-2, 1)$ (the de Sitter-line). The accelerated attractor F_6, is stable in the colored regions. In regions I, II and III F_6 is stable if $m_6' > -1$ and in region IV it is stable if $m_6' < -1$.

The ΛCDM model, $f(R) = R - 2\Lambda$, corresponds to $m = 0$ at all times, therefore satisfies the conditions required for the existence of a matter era, $m \simeq 0$, matched with the final attractor of the de Sitter point, $m(r = -2) = 0$. This means that deviations from the line $m = 0$ characterize other viable models under study. In the following, we reproduce the analysis of four $f(R)$ models, which were studied in [69] and classified as cosmologically viable, together with the $f(R)$ model proposed by W. Hu and I. Sawicki in [70] (see also [71]).

4.2.1   Type 1

We call type 1 to the family of models of the form

$$f(R) = R^p \left[\log(\alpha R)\right]^q - R \,, \tag{4.26}$$

as we have introduced in the previous chapter. This family is characterized by three free parameters, p, q and α. From Eq. (4.13) and Eq. (4.14) we obtain

$$m(r) = \frac{(p + r)^2}{qr} - 1 - r \quad ; \quad m'(r) = -1 + \frac{r^2 - p^2}{qr^2} \,. \tag{4.27}$$
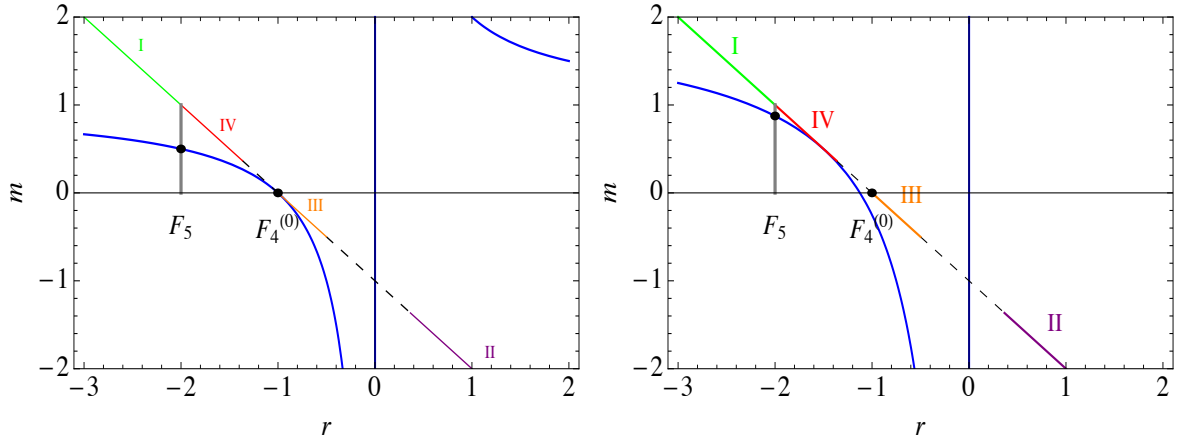
Figure 12: **The $m(r)$ curve of the type 1 models**. The left panel shows that the function $m(r)$ of models given by Eq. (4.26) passes close to $(r, m) = (-1, 0)$ when $p = q = 1$. On the right panel, the curve $m(r)$ with $q = 1$ and $p = 1.5$ shows that, if $p \neq 1$ then the model does not pass close to $(r, m) = (-1, 0)$ and a standard matter era is absent.

Notice that $m(r)$ does not depend on α. Following the conditions given by Eqs. (4.21)-(4.23) discussed in the previous section, from Eq. (4.27) a standard matter era only exist if $p = 1$ given that $m(r = -1) = -(p - 1)^2/q$. When $p = 1$, $m'(r = -1) = -1$, and $F_4^{(0)}$ then becomes a marginally stable point. In this case the linearization breaks down, however we need $m \approx 0^+$ and $m'(r) > -1$ for $F_4^{(0)}$ to be saddle point, these conditions are given when $r < -1$ for $q > 0$. F_5 is stable only if $0 \leq 1 - 1/(2q) \leq 1$ for $r = -2$, which also requires $q > 0$. This is actually the only possibility to have a late time acceleration given that, although F_6 is also stable in region I for $q > 0$, the function $m(r)$ (Eq. (4.27)) for $p = 1$ is $m(r) < -r - 1$ when $r < -1$ and therefore in this case $m(r)$ does not pass through F_6 in region I. The existence of $F_2^{(0)}$ is also guaranteed when $p = 1$. In Fig. 12 is represented the function $m(r)$ for this model. Summarizing, models given by Eq. (4.26) are cosmologically viable when the power indexes are constrained to be $p = 1$ and $q > 0$. The only possible trajectories that give rise to observationally acceptable trajectories are those starting at $F_2^{(0)}$, then passing close to $F_4^{(0)}$ and then landing in F_5.

A numerical approach is possible by solving the ordinary differential equation given by the system of Eqs. (4.8)–(4.12) for type 1 models, Eq. (4.26). Given initial conditions for x_i, we can find possible trajectories in the phase space that will give different expansion histories. As a graphical example, we plot in Fig. 13 a two dimensional section of the three dimensional space (x_1, x_2, x_3) (in this case we have neglected radiation for simplicity), where we show the vector field and one possible trajectory as an example. We can see the damped oscillations around the matter dominated fixed point $F_4^{(0)}$
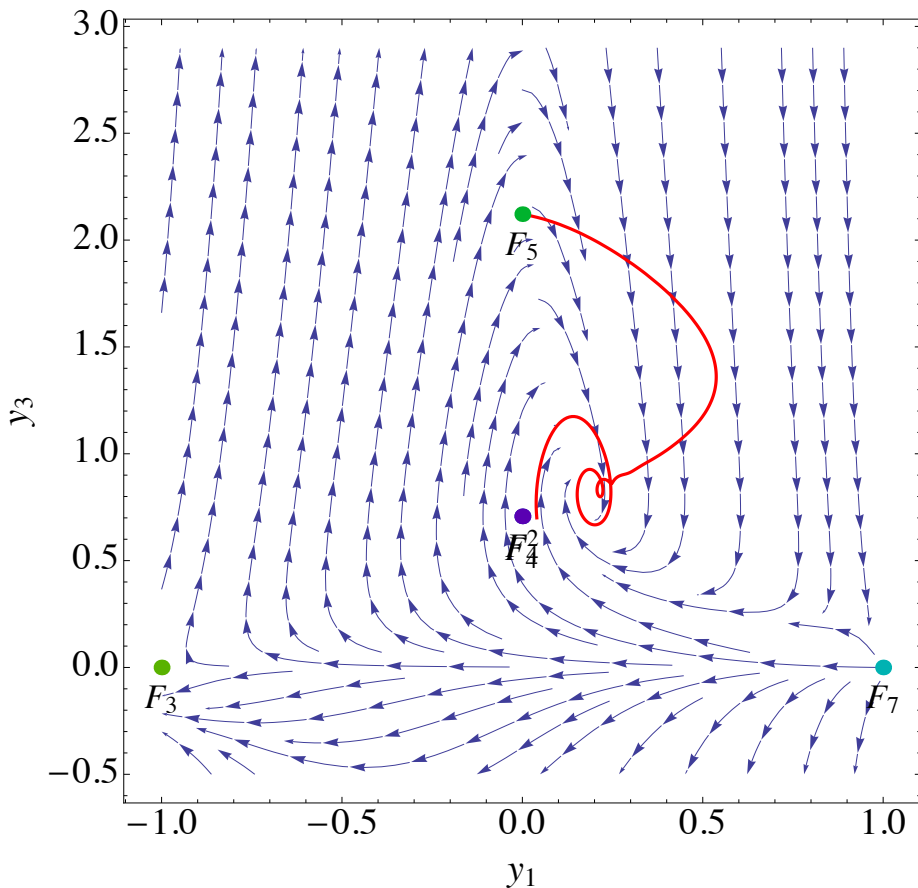
Figure 13: **Vector field and a trajectory of the type 1 models**. The vector field around the F_4 and F_5 fixed points given by the system Eq. (4.8)–(4.12) for models of type 1, see Eq. (4.26), with $p = 1$ and $q = 2.3$. The red curve shows one possible cosmologically viable trajectory. By neglecting radiation for simplicity, initial conditions are chosen to be close to the matter fixed point $F_4^{(0)}$ $((x_1, x_2, x_3) = (0.04, -0.48, 0.51))$; the dynamics shows damped oscillations around the matter fixed point before the trajectory lands in the stable attractor F_5. The axes (y_1, y_3) represents a rotation of the subspace $(x1, x3)$.

before the trajectory departures to the accelerated attractor F_5, as expected from the analytical discussion. In Fig. 14 we show an example of the cosmic evolution of model Eq. (4.26) with $p = 1$ and $q = 0.65$. The left figure shows the evolution of the different components involved in the expansion history of the model, the yellow line represents the radiation density component (Eq. (4.6)), the purple line the matter density component (Eq. (4.5)) and the red line the dark energy density component (Eq. (4.7)). The radiation era ends at $z \sim 10^3$ and at present $\Omega_{DE} \approx 0.7$, $\Omega_M \approx 0.3$ and $\Omega_R \approx 10^{-4}$, however in this case the matter era is shorter than in a ΛCDM universe. In the right figure the blue line represents the effective equation of state, w_{eff} given by Eq. (4.15),
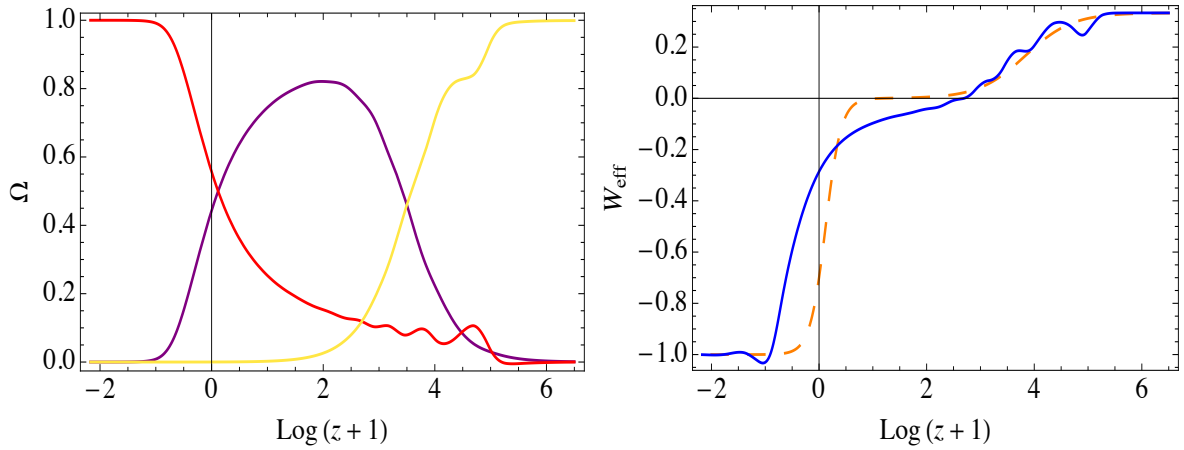
Figure 14: **Cosmic evolution of type 1 models**. The cosmic evolution of the model given by Eq. (4.26) with $p = 1$ and $q = 0.68$. The left panel shows the cosmic evolution of the different matter-energy components; the yellow line represents Ω_R, the purple line represents Ω_M and the red line represents Ω_{DE}. The right panel shows w_{eff} predicted by this model (blue) together with w_{eff} for the ΛCDM model (orange dashed) with parameters $\Omega_M = 0.3$, $\Omega_R \approx 10^{-4}$ (notice that w_{eff} is not the dark energy equation of state, which is $w = -1$ for the ΛCDM model). The initial conditions are $(x_1, x_2, x_3, x_4) = (10^{-10}, -10^{-7}, 1.019 \cdot 10^{-7}, 0.999)$ at redshift $z = 3.15 \cdot 10^6$.

were we can be appreciate the absent plateau at $w_{eff} \approx 0$ showing a non-standard matter era. The orange line is the w_{eff} of the ΛCDM model, for comparison.

4.2.2 Type 2

The family of exponential models, type 2

$$f(R) = R^p \ \exp(q/R) - R, \tag{4.28}$$

is characterized by two free parameters, p and q. Equation (4.13) and Eq. (4.14) give the curve

$$m(r) = -\frac{p + r(r + 2)}{r} \quad ; \quad m'(r) = -1 + \frac{p}{r^2}, \tag{4.29}$$

which is independent of the parameter q. In Fig .15 we show the function $m(r)$ for this model. The condition for the existence of a radiation and matter eras, $m(r = -1) = p - 1 \approx 0$, is satisfied when $p = 1$. The curve approaches zero from the positive side given that $m(r < 0) = -(r+1)^2/r > 0$ and also $m'(r = -1) = 0$ and $m'(r < -1) > -1$, which turns $F_4^{(0)}$ into a saddle point. On the other hand $m(r = -2) = 1/2$ therefore F_5 is stable, making possible the late acceleration through this point. Furthermore F_6 is stable in region I and in principle it would be possible the transition from $F_4^{(0)}$ to F_6, however the trajectory would be trapped by the attractor F_5 before getting to the stable region of F_6.
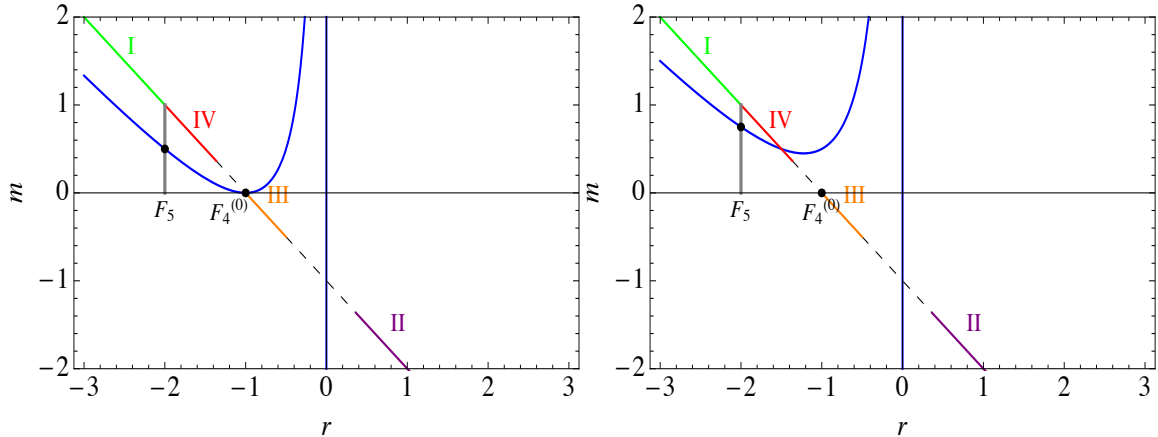
78

Figure 15: **The $m(r)$ curve of the type 2 models**. The function $m(r)$ of the models given by Eq. (4.28) with $p = 1$ (left panel) connects the matter fixed point with the de-Sitter line and, in principle, a viable expansion history can be reproduced in this case. If instead $p = 1.5$ (right panel) the $m(r)$ curve does not pass close to $(-1, 0)$ in the (r, m) plane and the matter era is absent.

From the numerical analysis of the system Eq. (4.8)–(4.12), for the model Eq. (4.28) with $p = 1$, we obtain the vector field in the subspace (x_1, x_2, x_3) (with $x_4 = 0$). In Fig. 16 we show a two dimensional section of this subspace together with one possible trajectory (red line) for which we have chosen initial conditions close to the matter fixed point F_4. As expected from the analytical discussion, the trajectory lands in the de Sitter fixed point F_5. Given initial conditions, Fig. 17 shows an example of the cosmic evolution of the radiation, matter and dark energy density components (left figure) and the resulting w_{eff} (right figure). This example does not have an acceptable cosmology, it is unphysical since it gives a negative dark energy density.

4.2.3 Type 3

The power law family

$$f(R) = \alpha R^n \, , \qquad (4.30)$$

is characterized by two free parameters, n and α. From Eqs. (4.13) and (4.14) we obtain in this case

$$m(r) = n \left(1 + \frac{1}{r} \right) \quad ; \quad m'(r) = -\frac{n}{r^2}, \qquad (4.31)$$

which does not depend on α. In Fig. 18 we show the function $m(r)$ for this model. In this case, $m(r = -1) = 0$ which guarantees the existence of $F_4^{(0)}$, however its stability and also the existence and stability of the fixed points F_5 and F_6, depends on the
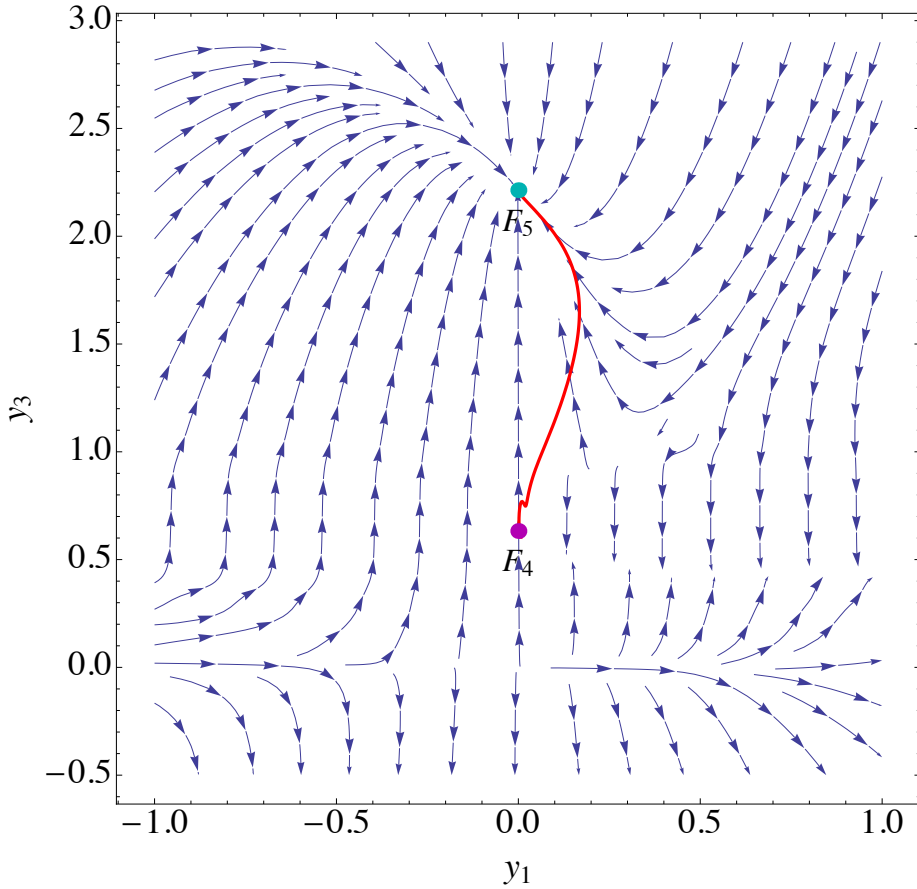
Figure 16: **Vector field and a trajectory of the type 2 models**. The vector field given by the system Eq. (4.8)–(4.12) for the model Eq. (4.28) with $p = 1$. The axes (y_1, y_3) represent a rotation of the two dimensional section (x_1, x_3) of the subspace (x_1, x_2, x_3). The red line shows one possible trajectory with initial conditions close to $F_4^{(0)}$ $((x_1, x_2, x_3) = (0.01, -0.49, 0.51))$, which lands in F_5.

value of n and on the sign of α as we discuss next. Solving Eq. (4.17) together with Eq. (4.31), we find two roots r_i which are $r_a = -1$ and $r_b = -n$, giving $m_a = 0$, $m_b = n - 1$, $m_a' = -n$ and $m_b' = -1/n$. These roots give two F_2, two F_4 and two F_6 which are

$$F_{2a} = F_2^{(0)} : (0, 0, 0, 1) \ , \quad \Omega_M = 0 \ , \quad w_{eff} = \frac{1}{3} \ ; \tag{4.32}$$

$$F_{2b} : \left(-\frac{4(n-1)}{n}, -\frac{2(n-1)}{n^2}, \frac{2(n-1)}{n}, -\frac{5n^2 - 8n + 2}{n^2} \right) \ ,$$

$$\Omega_M = 0 \ , \quad w_{eff} = -1 + \frac{4}{3n} \ ; \tag{4.33}$$

80
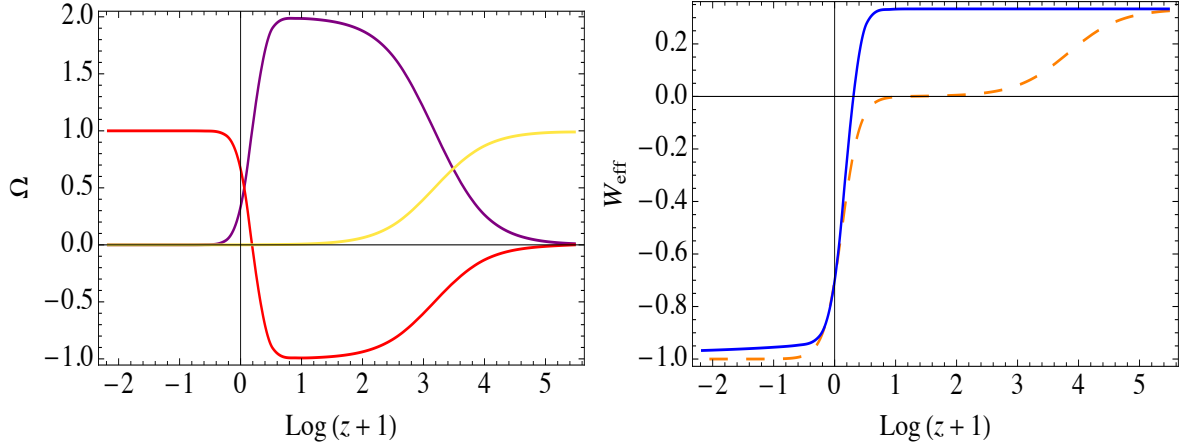
Figure 17: **Cosmic evolution of type 2 models**. Cosmic evolution for the model given by Eq. (4.28) with $p = 1$ and initial conditions $(x_1, x_2, x_3, x_4) = (0, 2.13 \cdot 10^{-20}, 5.33 \cdot 10^{-21}, 0.99)$ at redshift $z = 3 \cdot 10^5$. The left panel shows the evolution of Ω_R (yellow), Ω_M (purple) and Ω_{DE} (red). The right panel shows w_{eff} (blue) for this model together with w_{eff} for the ΛCDM model (orange dashed) with parameters $\Omega_M = 0.3$, $\Omega_R \approx 10^{-4}$. Notice that the dark energy density is negative and therefore the model is unphysical.
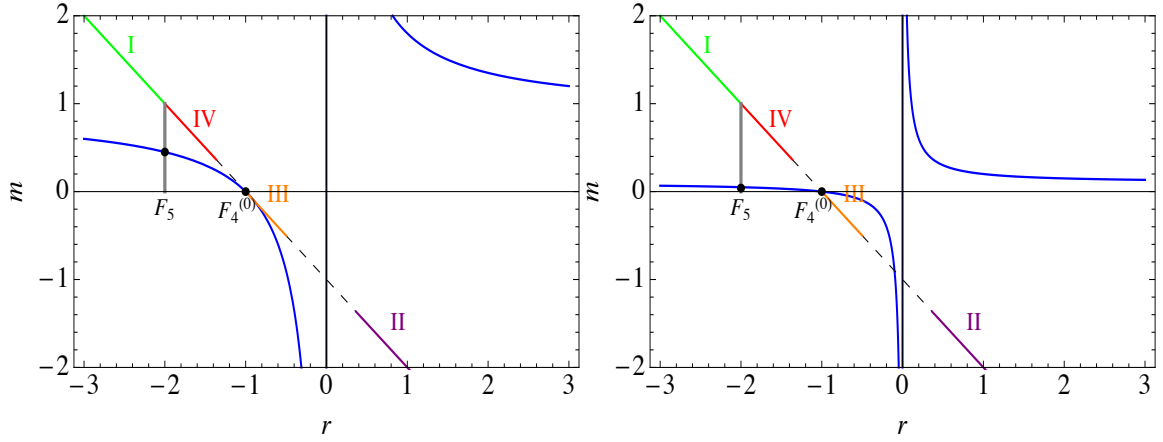
Figure 18: **The $m(r)$ curve of the type 3 models**. The $m(r)$ function of the model of Eq. (4.30) with $n = 0.9$ (left panel) and with $n = 0.1$ (right panel), in both cases the curve connects the 0-root with the de Sitter line.

$$F_{4a} = F_4^{(0)} : \left(0, -\frac{1}{2}, \frac{1}{2}, 0\right) , \quad \Omega_M = 1 , \quad w_{eff} = 0 ; \tag{4.34}$$

$$F_{4b} : \left(-\frac{3(n-1)}{n}, -\frac{4n-3}{2n^2}, \frac{4n-3}{2n}, 0\right) ,$$

$$\Omega_M = -\frac{8n^2 - 13n + 3}{2n^2} , \quad w_{eff} = -1 + \frac{1}{n} ; \tag{4.35}$$

81

$$F_{6a} \longrightarrow \infty \tag{4.36}$$

$$F_{6b} : \left(-\frac{2(n-2)}{2n-1}, -\frac{4n-5}{(2n-1)(n-1)}, \frac{n(4n-5)}{(2n-1)(n-1)}, 0 \right) \ ,$$

$$\Omega_M = 0 \ , \quad w_{eff} = \frac{-6n^2 + 7n + 1}{6n^2 - 9n + 3} \ . \tag{4.37}$$

From Eq. (4.31) we see that $m'(r = -1) = -n$, if $n > 1$ then $m'(r = -1) < -1$ and $F_4^{(0)}$ becomes a stable fixed point, making impossible the final acceleration phase. Therefore, to have a late time accelerated attractor we need $n < 1$, but depending on whether $n < 0$ or $0 < n < 1$ this model shows different behaviors.

- $0 < n < 1$: In this case the conditions for the stability of $F_4^{(0)}$, $m(r = -1) \approx 0$ and $m'(r = -1) > -1$ are satisfied depending on whether the trajectories approximate to zero from the positive or from the negative side. In order to understand this we shall look at the function $m(R)$ given by Eq. (4.13) which for this type of models is given by

$$m(R) = \frac{n(n-1)\alpha R^{n-1}}{1 + n\alpha R^{n-1}}. \tag{4.38}$$

  For m to be close to zero, the curvature must be $R \to \infty$. If $\alpha > 0$, $m \approx 0^-$ and two of the eigenvalues diverge, turning $F_4^{(0)}$ into an unstable point. If $\alpha < 0$, $m \approx 0^+$ and $F_4^{(0)}$ is a saddle point, giving the damped oscillations previously discussed. F_5 is stable given that $m(-2) = n/2$ and in this case $0 < n/2 < 1/2$. In fact, trajectories reaching F_5 after oscillating around $F_4^{(0)}$ are the only possible viable trajectories because F_6 is unstable in this case, given that for $m'_a > -1$, there is no connection with either I, II or III, and for $m'_b < -1$, there is no connection with the region IV.

- $n < 0$: In this case, if $\alpha < 0$, m approaches zero from the negative side and $F_4^{(0)}$ becomes unstable. Therefore we would need $\alpha > 0$, for m to approach zero from the positive side, $m'(r = -1) = -n > 0$ giving rise to a saddle point with damped oscillations. However it is not possible to end in any of the accelerated points. On one hand F_5 is unstable because $m(r = -2) = n/2 < 0$, on the other hand F_6 is stable in the region II, since $m'_b > -1$ and m_b comprehends the region $m_b < -(1 + \sqrt{3})$, but it is not possible to connect $F_4^{(0)}$ with region II as we have explained in the previous section.

Therefore this family of models can describe a viable expansion history only when $\alpha < 0$ and $0 < n < 1$.

From the numerical analysis we show in Fig. 19 the vector field in a two dimensional section of the three dimensional space (x_1, x_2, x_3) (again neglecting radiation) for $n = 0.9$. By choosing initial conditions close to the matter fixed point F_4, a possible
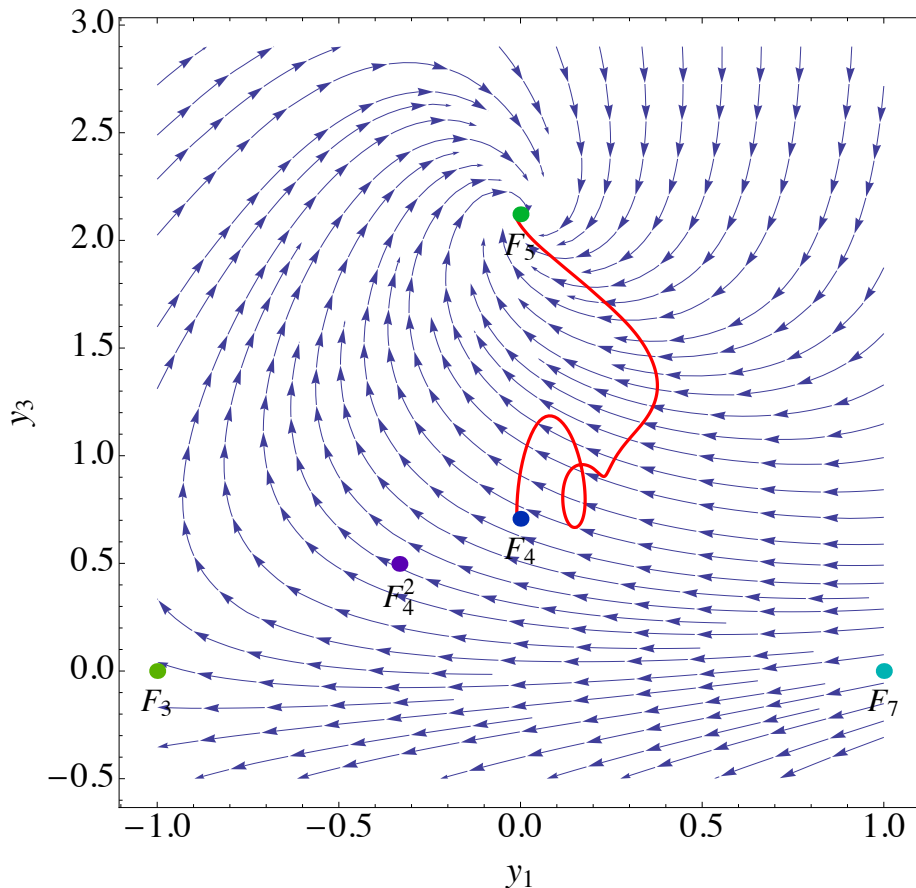
Figure 19: **Vector field and a trajectory of the type 3 models**. The vector field given by the system Eqs. (4.8)–(4.12) for the model Eq. (4.30) with $n = 0.9$. The axes (y_1, y_3) is a rotation of the two dimensional section (x_1, x_3) of the subspace (x_1, x_2, x_3). The red curve shows a cosmologically viable trajectory (neglecting radiation) with initial conditions close to $F_4^{(0)}$ and landing in F_5.

trajectory (red line), exhibits the damped oscillations around the matter era landing in the the accelerated fixed point F_5, expected from the analytical analysis. For the chosen initial conditions at the radiation era and $n = 0.97$, we show in Fig. 20 the cosmological evolution of the different components and the resulting equation of state of the system. Again we observe in this example a too short matter era leading to an absent matter plateau in the equation of state.

4.2.4 Type 4

In this family,

$$f(R) = \alpha R^2 - \Lambda \,, \tag{4.39}$$

83
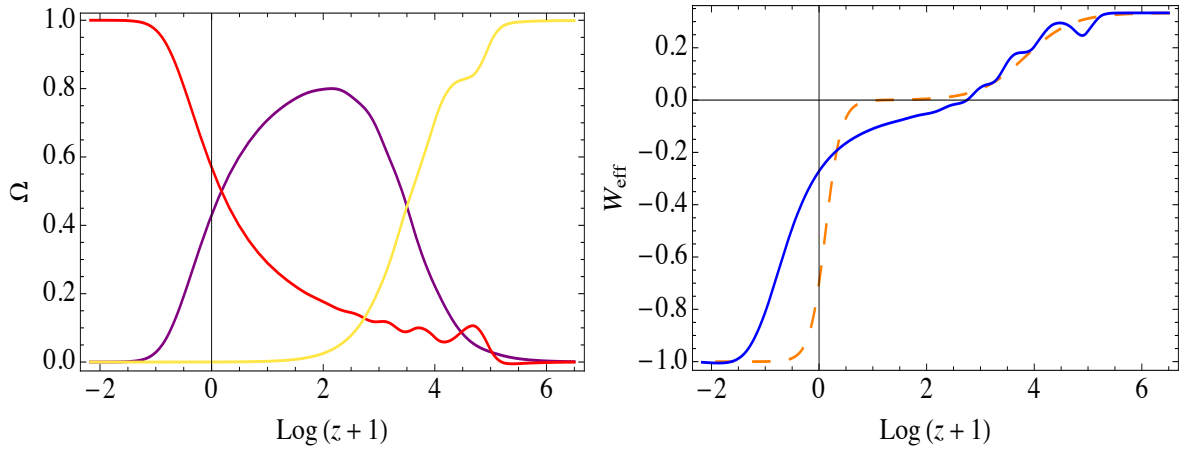
Figure 20: **Cosmic evolution of type 3 models**. Cosmic evolution for the model of Eq. (4.30) with $n = 0.982$ and initial conditions $(x_1, x_2, x_3, x_4) = (10^{-4}, -10^{-7}, 1.019 \cdot 10^{-7}, 0.999)$ at redshift $z = 3 \cdot 10^6$. On the left panel, the evolution of Ω_R (yellow), Ω_M (purple) and Ω_{DE} (red). On the right panel, the blue line represents the w_{eff} of the model while the orange dashed line represents w_{eff} for the ΛCDM model with parameters $\Omega_{M0} = 0.3$, $\Omega_{R0} \approx 10^{-4}$.

we have two free parameters, α and Λ. If $\alpha \to 0$, then $f(R) \to \Lambda$, which represents the standard ΛCDM model and implies that this family of models must be allowed in some range of the parameters. Notice that the ΛCDM action contains the term $R - 2\overline{\Lambda}$, therefore Λ in this family is twice the usual cosmological constant $\overline{\Lambda}$. From Eq. (4.13) and Eq. (4.14) in we obtain the curves

$$m(r)_\pm = \frac{-r - 1 \pm \sqrt{(r+1)^2 + 4\beta r(r+2)}}{1 \pm \sqrt{(r+1)^2 + 4\beta r(r+2)}}, \tag{4.40}$$

where we have called $\beta = \alpha\Lambda$ and we assume $\alpha, \Lambda > 0$. In this case $m(r)_\pm$ is a two-branched function (we call the positive and negative branch to $m(r)_+$ and $m(r)_-$ respectively according to the sign of the square root). However we can show that the different branches can be studied separately. We have discussed after Eq. (4.19) that subspaces corresponding to the roots of $m = -r - 1$ are invariant hyper-surfaces of the dynamical system $(x_1, ..., x_4)$, and they cannot be crossed by any cosmological trajectory. In a similar way we can realize that at points where the tangent to the curve becomes vertical, $\frac{dr}{dR} = 0$ and $\frac{dr}{d\ln a} = 0$, which means that switching points between different branches cannot be crossed either, therefore the different branches can be studied one at a time, as if we had different $f(R)$ models **.

** Note that we cannot state the opposite: not at all points where $\frac{dr}{dR} = 0$, the curve becomes instantaneously vertical, given that $\frac{dm}{dR}$ could also be zero.

84

Solving Eq. (4.17) together with $m(r)_+$, we find three roots r_i

$$r_{1,2} = -\frac{4\beta + 1 \pm 2\sqrt{\beta(4\beta + 1)}}{4\beta + 1} \quad , \quad r_3 = -2, \tag{4.41}$$

which give

$$m_{1,2} = \pm\frac{2\beta}{\sqrt{\beta(4\beta + 1)}} \quad , \quad m_3 = 1, \tag{4.42}$$

and a different F_2, F_4 and F_6 for each of these values of m. The three F_4 fixed points are given by

$$F_{4a,4b} : \left(\frac{6\beta}{2\beta \pm \sqrt{\beta(4\beta + 1)}}, \frac{\beta(4\beta + 1) \pm 8\beta\sqrt{\beta(4\beta + 1)}}{2(\sqrt{\beta(4\beta + 1)} \pm 2\beta)^2}, \frac{8\beta \pm \sqrt{\beta(4\beta + 1)}}{4\beta \pm 2\sqrt{\beta(4\beta + 1)}}, 0 \right);$$

$$\Omega_M = \frac{\beta\left(1 - 12\beta \pm 3\sqrt{\beta(4\beta + 1)}\right)}{(\sqrt{\beta(4\beta + 1)} \mp 2\beta)^2} \quad , \quad w_{eff} = 4\beta \mp 2\sqrt{\beta(4\beta + 1)}; \tag{4.43}$$

$$F_{4c} : \left(\frac{3}{2}, -\frac{5}{8}, \frac{5}{4}, 0 \right) \quad , \quad \Omega_M = -\frac{9}{8} \quad , \quad w_{eff} = -\frac{1}{2} \tag{4.44}$$

For F_{4c}, $\Omega_M < 0$, giving an unphysical fixed point. For $F_{4a,4b}$, in the limit $\beta = \alpha\Lambda << 1$, $\Omega_M \approx 1$ and $w_{eff} \approx \mp 2\sqrt{\beta}$, which gives an approximated matter era. In this limit, a standard matter era exist either for $\alpha \to 0$ or for $\Lambda \to 0$ which shows the degeneracy between these two parameters. However, the model becomes ΛCDM only in the limit $\alpha \to 0$. In the limit $\beta << 1$, F_6 is not a stable attractor, on the other hand F_5 is always a stable attractor since $m(r = -2) = 1$ is satisfied for any value of β. Therefore, in the limit $\beta << 1$ these models are cosmologically viable, otherwise $m(r)$ becomes singular around $F_4^{(0)}$ and there is no possible matter era. In Fig. 21 we show the function $m(r)$ of this model for $\beta = 5 \cdot 10^{-4}$ and for $\beta = 10^{-2}$.

The branch with the negative sign of the square root in Eq. (4.40), $m(r)_-$, together with Eq. (4.17), gives the same two roots $r_{1,2}$ in Eq. (4.41) ($m(r)_-$ becomes singular for $r_3 = -2$). Given that the root r_3 gave an unphysical matter fixed point for the positive branch $m(r)_+$ of Eq. (4.41), in this family of models, the same result is obtained in the analysis of the branch $m(r)_-$.

Solving numerically the system of Eqs. (4.8)–(4.12), we obtain Fig. 22, where it is shown the vector field in a two dimensional section of the three dimensional space (x_1, x_2, x_3) (again neglecting radiation). The red curve is a cosmologically viable trajectory of this model starting close to one of the matter fixed points and landing in one of the accelerated attractor (F_5^3) with a less oscillating behavior than the type 1 and 3 examples. Fig. 23 shows the effective equation of state for low redshifts for fixed values of the parameters reproducing a curve close to the one obtain for the ΛCDM model.
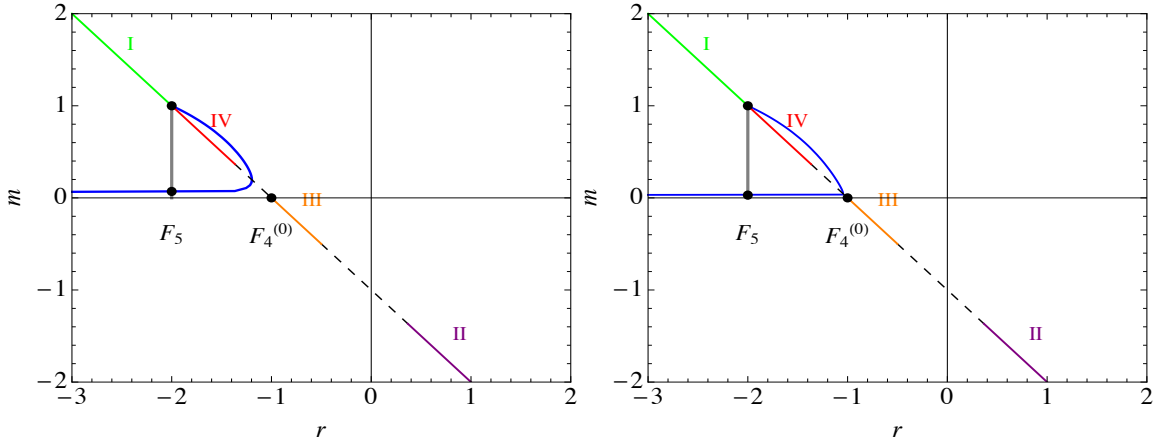
Figure 21: **The $m(r)$ curve of the type 4 models**. The $m(r)$ function given by the model Eq. (4.39) with $\beta = 10^{-2}$ (left panel) and with $\beta = 5 \cdot 10^{-4}$ (right panel). As β decreases the curve passes close to the 0-root.

4.2.5 Type 5

The following family of models

$$f(R) = -M^2 \frac{c_1 (\frac{R}{M^2})^n}{1 + c_2 (\frac{R}{M^2})^n}, \tag{4.45}$$

was proposed by W. Hu and I. Sawicki in [70], herein after we may refer to this family as the HS class of models. The mass scale M^2 is in principle a free parameter of the model, but following [70], for convenience, we fix it to be $M^2 = \kappa^2 \bar{\rho}_0 / 3$, where $\bar{\rho}_0 = \bar{\rho}(a = 1)$ is the average matter density today (for the numerical values of which we take the estimate based on the best-fit parameters of the standard ΛCDM); thus the model contains three dimensionless free parameters, c_1, c_2 and $n > 0$. The type of models given by Eq. (4.45) does not explicitly contain a cosmological constant. However, in the high curvature regime, under the approximation

$$|c_2|(R/M^2)^n \gg 1\,, \tag{4.46}$$

the model given by Eq. (4.45) can be expanded as

$$f(R) \simeq -M^2 \frac{c_1}{c_2} + M^2 \frac{c_1}{c_2^2} \left(\frac{M^2}{R} \right)^n\,, \tag{4.47}$$

and in the limit $c_1/c_2^2 \to 0$ at fixed c_1/c_2, Eq. (4.47) becomes a cosmological constant. Therefore, we expect that the amplitude c_1/c_2^2 and n in the second term of Eq. (4.47) modulate small deviations from ΛCDM.
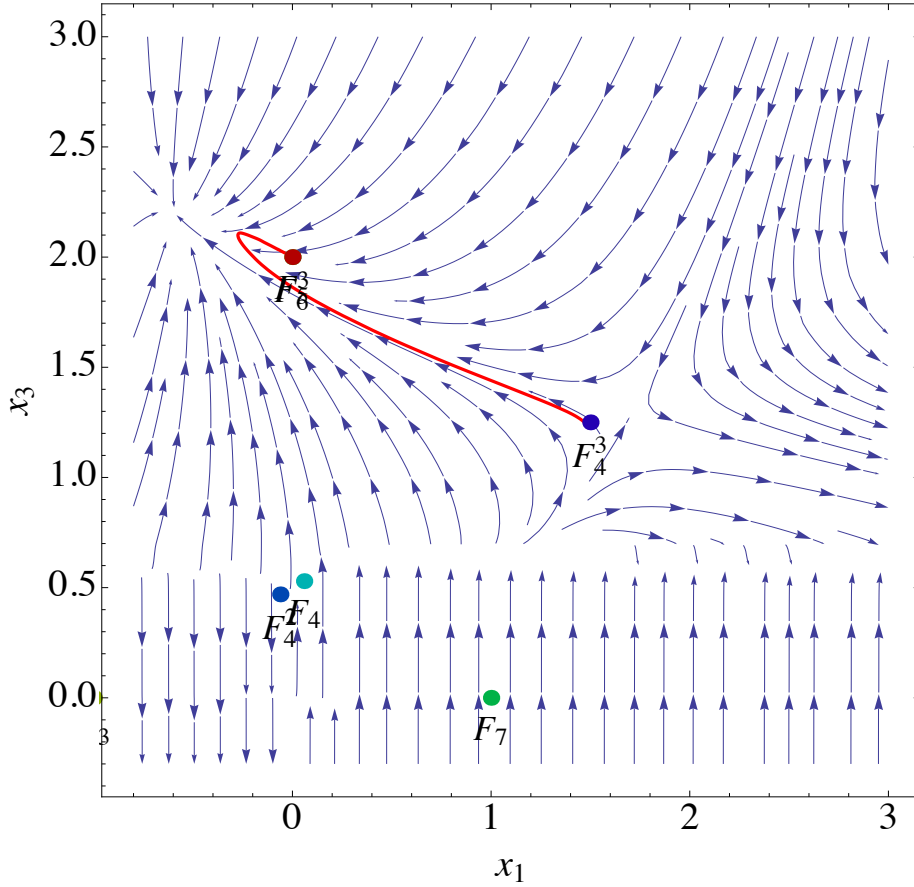
86

Figure 22: **Vector field and a trajectory of the type 4 models**. The vector field given by the system of Eqs. (4.8)–(4.12) in a rotation of the two dimensional section of (x_1, x_3) for models Eq. (4.39) with $\alpha\Lambda = 10^{-4}$. The red curve shows one possible cosmologically viable trajectory. By neglecting radiation for simplicity, initial conditions are chosen to be close to the matter fixed point F_4, $(x_1, x_2, x_3) = (0.04, -0.48, 0.51)$.

To obtain a viable expansion history, we need deviations from the equation of state given by ΛCDM to be small during the acceleration epoch. According to Eq. (3.22), this means that the value of the field, Rf_R, should be small compared to f. From Eq. (4.45)

$$f_R = -n\frac{c_1}{c_2^2}\left(\frac{M^2}{R}\right)^{n+1}\left[1 + \frac{1}{c_2}\left(\frac{M^2}{R}\right)^n\right]^{-2}, \qquad (4.48)$$

and thus we obtain the condition

$$\frac{Rf_R}{f} = \frac{n}{c_2}\left(\frac{M^2}{R}\right)^n\left[1 + \frac{1}{c_2}\left(\frac{M^2}{R}\right)^n\right]^{-1} \ll 1. \qquad (4.49)$$

But this is (up to a factor of n) equivalent to the condition Eq. (4.46). Note that, since the curvature is expected to only decrease with time, as long as Eq. (4.49),
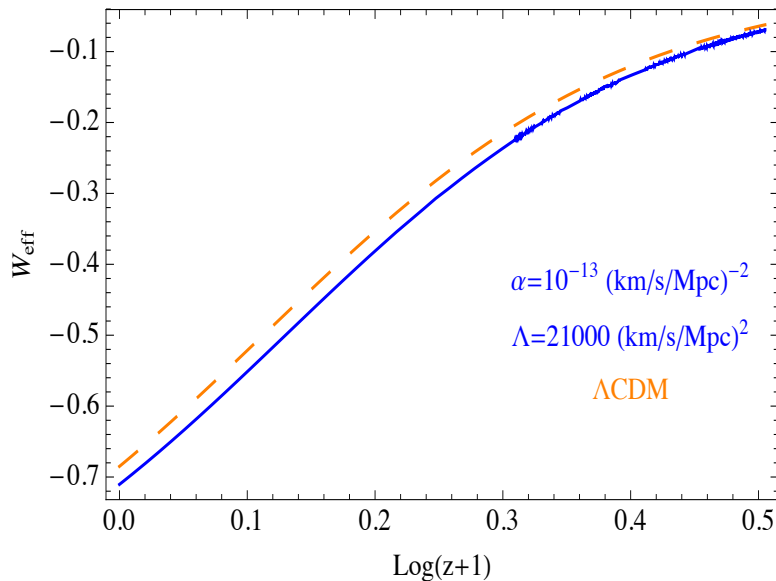
87

Figure 23: **Equation of state of type 4 models**. The blue line represents the w_{eff} of model Eq. (4.39) while the orange dashed line represents w_{eff} for the ΛCDM model with parameters $\Omega_{M0} = 0.3$, $\Omega_{R0} \approx 10^{-4}$. A very small value of α is required to reproduce an effective equation of state close to the one of the ΛCDM model.

or equivalently Eq. (4.46), hold for R_0, the scalar curvature today, these conditions and the approximation Eq. (4.47) holds for the entire past history. Furthermore, the second term in Eq. (4.47) could be neglected in the first approximation, leading to small deviation from a ΛCDM history.

Below we will work with a different parametrization of the model, which is more convenient for considerations of the general viability condition just discussed. First, following W. Hu and I. Sawicki [70], we fix the ratio of the model parameters c_1 and c_2, by setting

$$\frac{c_1}{c_2} = 6\frac{\tilde{\Omega}_\Lambda}{\tilde{\Omega}_M}, \tag{4.50}$$

where $\tilde{\Omega}_M$ and $\tilde{\Omega}_\Lambda = 1 - \tilde{\Omega}_M$ are the best-fit values of cosmological parameters of the standard ΛCDM model. With the ratio c_1/c_2 fixed by Eq. (4.50), the model has ΛCDM as a limiting case when $c_1/c_2^2 \to 0$, as explained above. Note that, while the physical value of $\Omega_M \equiv \frac{\kappa^2 \rho_0}{3H_0^2}$ is in general different from $\tilde{\Omega}_M$, in the limit $c_1/c_2^2 \to 0$ we do recover $\Omega_M = \tilde{\Omega}_M$.[††] Secondly, we reparametrize the amplitude c_1/c_2^2 in Eq. (4.47) in terms of the approximate value of the field today, $f_R(R_0)$. When Eq. (4.49) holds and the

---

[††]Similarly, since the Hubble parameter depends on the new scalar degree of freedom f_R, in general $H_0 \neq \tilde{H}_0$ (where $\tilde{H}_0$ is the best-fit value of the Hubble parameter in the standard ΛCDM). However, note that, as we have fixed the matter density to the ΛCDM value, we have $\Omega_M H_0^2 = \tilde{\Omega}_M \tilde{H}_0^2$ (i.e., $\rho_M = \tilde{\rho}_M$) irrespectively of the value of c_1/c_2^2.

model is close to the ΛCDM scenario, from Eq. (3.22), together with Eq. (4.47), we obtain

$$R \approx \kappa^2 \rho - 2f \approx \kappa^2 \rho + 2\frac{c_1}{c_2}M^2, \qquad (4.51)$$

with $2f$, nearly constant, playing the role of the energy density of a cosmological constant. Using Eq. (4.50) and $\kappa^2 \rho = \kappa^2 \bar{\rho}_0 a^{-3} = 3M^2 a^{-3}$, this becomes

$$R \approx 3M^2 \left(a^{-3} + 4\frac{\tilde{\Omega}_\Lambda}{\tilde{\Omega}_M} \right). \qquad (4.52)$$

At the present epoch, $a_0 = 1$, and using $\tilde{\Omega}_\Lambda = 1 - \tilde{\Omega}_M$, we obtain the following approximate expression for the scalar curvature today

$$R_0 \approx M^2 \left(\frac{12}{\tilde{\Omega}_M} - 9 \right). \qquad (4.53)$$

In the same regime, from Eq. (4.48) (or equivalently Eq. (4.47)), we also have

$$f_R \approx -n\frac{c_1}{c_2^2} \left(\frac{M^2}{R} \right)^{n+1}, \qquad (4.54)$$

which, after substituting Eq. (4.53) yields

$$f_R(R_0) \approx -n\frac{c_1}{c_2^2} \left(\frac{12}{\tilde{\Omega}_M} - 9 \right)^{-n-1}. \qquad (4.55)$$

Inspired by this *approximate* expression and using Eq. (4.50), we will reparametrize c_1 and c_2 in terms of a new parameter f_{R0} as follows

$$c_2 = -6\frac{\tilde{\Omega}_\Lambda}{\tilde{\Omega}_M}\frac{n}{f_{R0}} \left(\frac{12}{\tilde{\Omega}_M} - 9 \right)^{-n-1}; \qquad (4.56)$$

$$c_1 = 6\frac{\tilde{\Omega}_\Lambda}{\tilde{\Omega}_M}c_2, \qquad (4.57)$$

or equivalently

$$\frac{c_1}{c_2^2} = -\frac{f_{R0}}{n} \left(\frac{12}{\tilde{\Omega}_M} - 9 \right)^{n+1}. \qquad (4.58)$$

Note that, while by definition, we have the exact relationship

$$f_{R0} = -n\frac{c_1}{c_2^2} \left(\frac{12}{\tilde{\Omega}_M} - 9 \right)^{-n-1}, \qquad (4.59)$$

from Eq. (4.54), the value of the field today, $f_R(R_0)$, is given by f_{R0} only approximately, when Eq. (4.46) holds. From now on we will parametrize this type of models in terms of the two free parameters f_{R0} and n for our analysis in Chapter 5.

We now study more quantitatively for which parameter regions the approximation given by Eq. (4.46) holds. We will consider the slightly more stringent condition, Eq. (4.49). As noted above, it is sufficient if this condition is satisfied today, *i.e.*,

$$|c_2|(R_0/M^2)^n \gg n. \tag{4.60}$$

When this condition holds, so does the approximation Eq. (4.53), and it is thus self-consistent to use the latter as well, to rewrite Eq. (4.60) as

$$|c_2| \left(\frac{12}{\tilde{\Omega}_M} - 9 \right)^n \gg n \tag{4.61}$$

which using Eq. (4.56) we can express as a condition on f_{R0}[‡‡]

$$|f_{R0}| \ll 6 \frac{\tilde{\Omega}_\Lambda}{\tilde{\Omega}_M} \left(\frac{12}{\tilde{\Omega}_M} - 9 \right)^{-1}. \tag{4.63}$$

From Eq. (4.59) and Eq. (4.47), when $f_{R0} \to 0$, $f(R)$ turns into a cosmological constant. We do not consider $f_{R0} < -0.1$ (*i.e.*, $|f_{R0}| > 0.1$) in our analysis since such values are not allowed by solar system tests [70]. We do not consider $n < 1$ either, since, as we can see from the reparametrization Eqs. (4.56)-(4.57), in the limit $n \to 0$, $c_2 = c_1 = 0$, leads to $f(R) = 0$ which is not of our interest.

In the following we will see that studying the qualitative features of this model through the $m(r)$ function, is not as straightforward as it was for the previous models. However we can draw important conclusions. From Eq. (4.14) we obtain

$$r(B) = -\frac{c_2^2 B^{2n} + 2c_2 B^n - nc_1 B^{n-1} + 1}{[c_2 B^n - c_1 B^{n-1} + 1][c_2 B^n + 1]}, \tag{4.64}$$

where we have defined $B \equiv R/M^2$. Therefore we need to solve the equation

$$c_2^2(r+1)B^{2n} + 2c_2(r+2)B^n - c_1(n+r)B^{n-1} - c_1 c_2 r B^{2n-1} + r + 1 = 0 \tag{4.65}$$

for $B(r) \equiv R(r)/M^2$ in order to find $m(r)$, which from Eq. (4.13), is given by

$$m[B(r)] = \frac{nc_1 B^{n-1}[(1+n)c_2 B^n - n + 1]}{(c_2 B^n + 1)[(c_2 B^n + 1)^2 - nc_1 B^{n-1}]}. \tag{4.66}$$

Equation (4.65) cannot be solved exactly and for this type of model we would need to solve it for each value of n separately and analyze the different multibranched $m(r)$

[‡‡]If instead of Eq. (4.49) we had considered the weaker condition Eq. (4.46), we would have obtained

$$|f_{R0}| \ll 6 \frac{\tilde{\Omega}_\Lambda}{\tilde{\Omega}_M} \left(\frac{12}{\tilde{\Omega}_M} - 9 \right)^{-1} n. \tag{4.62}$$

functions obtained in each case one by one. An important qualitative feature can be guessed by looking at the limits of Eqs. (4.64)-(4.66): in both limits $B \to 0$ and $B \to \pm\infty$, $r(B) \to -1$ and $m(B) \to 0$, which guarantees the existence of a matter era, independently of the value of the parameters of the model.

In Fig. 24 we show the $m(r)$ curve of Eq. (4.45), which we have plotted parametrically from Eqs. (4.64) and (4.66) (blue curve). For comparison, we also show the $m(r)$ curve of Eq. (4.47) (dashed cyan curve), which from Eq. (4.14) and Eq. (4.13) is given by

$$r(R) = -\frac{1 - n\frac{c_1}{c_2^2}B^{-n-1}}{1 - \frac{c_1}{c_2}B^{-1} + \frac{c_1}{c_2^2}B^{-n-1}} \; ; \tag{4.67}$$

$$m(R) = \frac{n(n+1)\frac{c_1}{c_2^2}B^{-n-1}}{1 - n\frac{c_1}{c_2^2}B^{-n-1}} \; . \tag{4.68}$$

We have chosen positive values of the scalar curvature R, as it should be in the whole expansion history. The part of the blue curve approaching the 0-root from below (where $m < 0$), corresponds to values of $R < R_0$, while the part which approaches the 0-root from above (where $m > 0$), corresponds to values of $R \approx R_0$, which are the ones we are interested in. As we can observe, the dashed cyan curve coincides with the blue curve in the region of the $m(r)$ plane in which $R \approx R_0$. This shows that Eq. (4.47) is a good approximation of Eq. (4.45) in the curvature regime in which we are interested. We can observe that both curves pass close to the 0-root, which allows for a standard matter era, and directly after crossing one of the regions that allows for a final accelerated phase. In the left of Fig. 24, both curves for $n = 1$ and $f_{R0} = -0.01$, this final acceleration is given by the attractor F_5, placed in the de Sitter line. In the right of Fig. 24, for $n = 10$ and $f_{R0} = -0.1$, the accelerated expansion is given by the region IV of F_6. It is worth mentioning that for higher values of n and smaller values of f_{R0}, the curve freezes out and keeps crossing region IV after passing close to the 0-root. Similarly, for smaller values of n and higher values of f_{R0} (closer to zero since it should be negative), the curves just get closer to the axes $m = 0$. All the other possible combinations of n and f_{R0} are within these two asymptotic cases. This shows that the model of Eq. (4.45) with the reparametrization given by Eqs. (4.56)-(4.57) with $n > 0$ and $f_{R0} < 0$ and $|f_{R0}| << 1$, is cosmologically viable. By solving numerically the system of Eqs. (4.8)–(4.12) we also show in Fig (26) one of the possible trajectories of this model in which we have neglected radiation.

We obtain the effective equation of state w_{eff} of the model Eq. (4.45) using Eq. (2.25), by numerically solving Eq. (3.27). In Fig. 25 we show the w_{eff} of Eq. (4.45) (which we denote as w_{eff}^{HS}) for $n = 1$ and $n = 7$ respectively, for different values of f_{R0}. As we can see, the w_{eff} of this type of model gets closer to the one of ΛCDM as n and f_{R0} increase. By solving the system of Eqs. (4.8)–(4.12) we also show in Fig. 26 the vector field in a section of the three dimensional space (x_1, x_2, x_3), as well as one possible trajectory of this model. In this case we can appreciate damped oscillations around
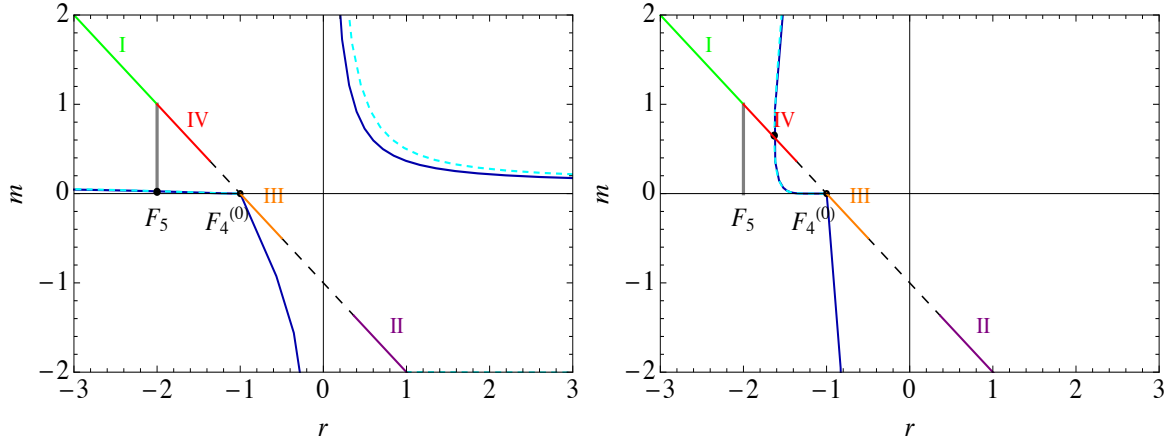
Figure 24: **The $m(r)$ curve of the type 5 models**. Parametric plot of $m(R)$ versus $r(R)$ with $n = 1$ and $f_{R0} = -0.01$ (left panel) and with $n = 10$ and $f_{R0} = -0.1$ (right panel) (and $\Omega_m = 0.315$). The solid line corresponds to Eq. (4.45) and the dashed line to the approximation Eq. (4.47).
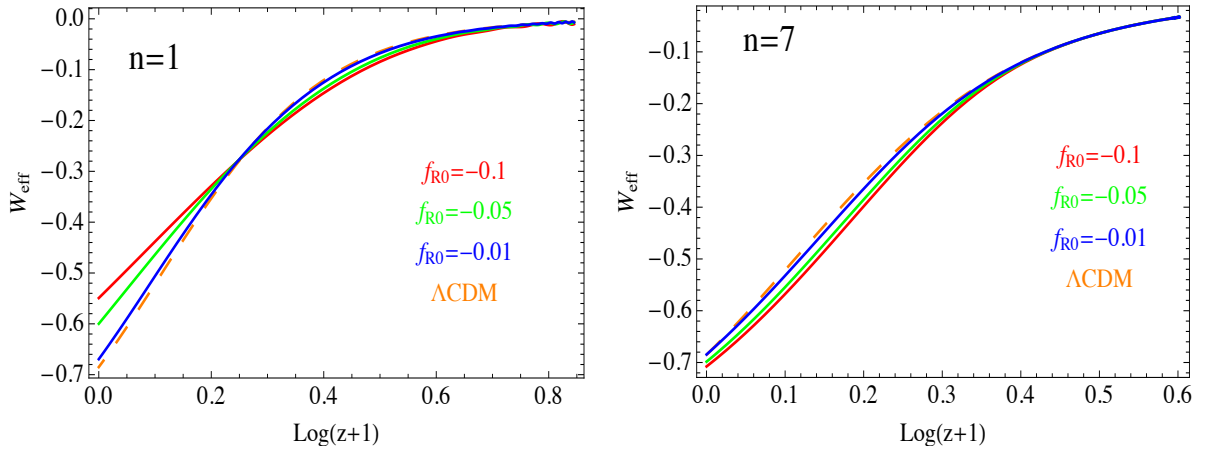

Figure 25: **Equation of state of type 5 models.** We depict w_{eff} given by Eq. (2.25) of the model given by Eq. (4.45) with $n = 1$ (left panel) and $n = 7$ (right panel) for various values of f_{R0}, together with the w_{eff} predicted in the ΛCDM model (with $\Omega_m = 0.315$).

the matter fixed point before landing in the accelerated attractor fixed point.

In the next chapter we analyze quantitatively the types of $f(R)$ models studied in this chapter by confronting their predictions to cosmological data. Furthermore we extend the analysis to first order in perturbations to combine geometrical probes with
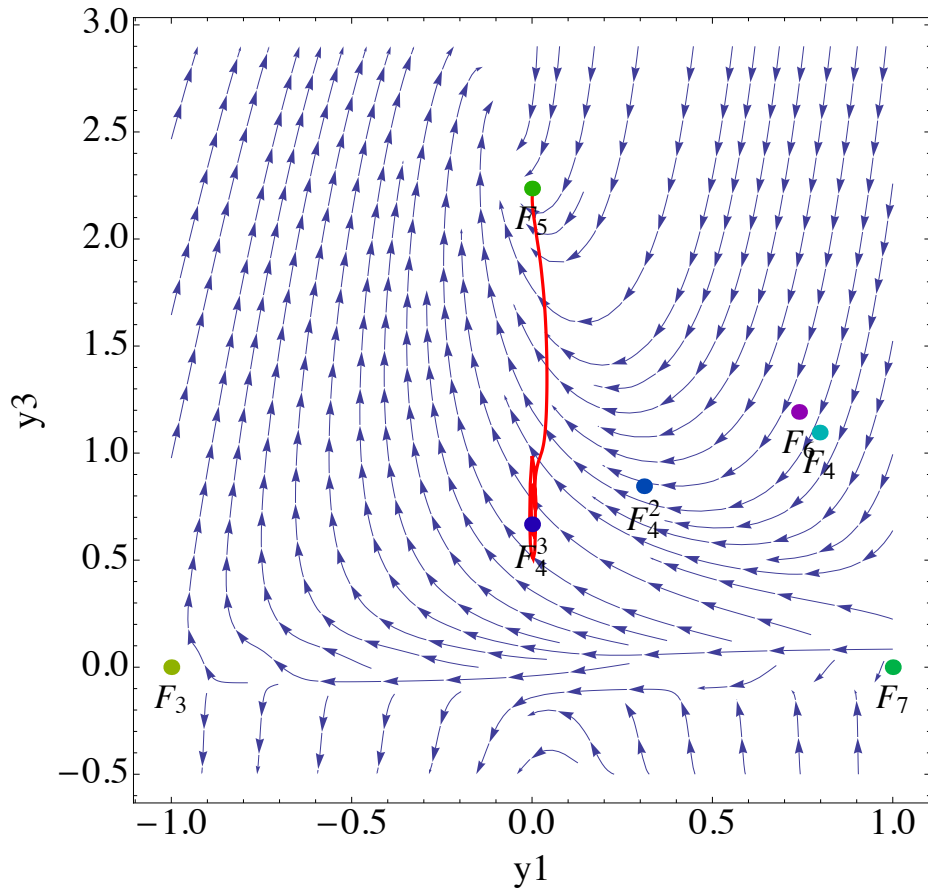
Figure 26: **Vector field and a trajectory of the type 5 models.** Vector field in a section of the space (x_1, x_2, x_3) and a possible trajectory with initial conditions close to $F_4^{(0)}$ and landing in F_5 for the model given by Eq. (4.45) with $n = 1$ and $f_{R0} = -0.08$. The axes (y_1, y_3) is a rotation of the subspace (x_1, x_3).

measurements of the growth of structure formation.

93

Chapter 5

Observational Tests of Viable $f(R)$ Models

In the previous chapter we have used a dynamical system approach to study the general conditions under which particular $f(R)$ models describe viable cosmological histories based on the qualitative features of the observed expansion history of the universe. We have shown five specific families of models that are cosmologically viable. In this chapter we extend the previous analysis to a quantitative study of the same families of $f(R)$ models by comparing their predictions to cosmological data. We also extend the analysis to first order in perturbations to combine geometrical probes, such as cosmic distances, with measurements of the growth of structure formation. We show in the following that the combination of cosmic distances data together with data of the growth of structure formation, constitutes a powerful tool to rule out modified gravity models which, according to the qualitative analyses of their homogeneous dynamics, are cosmologically viable. For the models that are allowed by cosmological data, this method can tightly constrain the free parameters of the models, allowing to test deviations from the standard ΛCDM scenario. In the following analysis we update the data sets used in [85] by considering the latest BAO [41, 86], CMB [87] and growth of structure measurements [29, 88–92]. We also use the latest constraints in the cosmological parameters given by Planck [2]. As we will see, in the following data analyses, we will rule out two more $f(R)$ families which, in principle, appeared acceptable by all the cosmological probes used in [85]. In Sec. 5.1 we describe the cosmological data sets that we use in our analysis, in Sec. 5.2 we introduce the χ^2 function as well as the maximum likelihood method, which we use for parameter estimation. In Secs. 5.4 and 5.5 we perform the quantitative analysis of the different types $f(R)$ models. In Sec. 5.4 we discuss the models which are ruled out by cosmological data and, in Sec. 5.5, the ones which are allowed by all data sets. In Sec. 5.3 we compute the χ^2 values of the standard ΛCDM model for the sake of comparison with $f(R)$ cosmologies. In the last section we explore the weak field limit of the types of models which we show to be consistent with cosmological probes.

5.1 Cosmological Data

The quantitative analysis of $f(R)$ models accomplished in this chapter is based on a combination of five different datasets, four of them are given by geometrical probes, namely standard candles, standard rulers and the Hubble parameter given by galaxy ages, while the fifth one is given by the growth of structure pattern. As we have described in Sec. 2.4.1, present SN Ia catalogs constitute the major dataset of standard candles available from observations, while the first acoustic peak of the CMB together with BAO data are the most powerful standard rulers. In the following we describe the datasets that we will use in the next section.

5.1.1 Supernova Ia

SN Ia measurements constitute a key probe to constrain the dark energy equation of state. Various groups have reported and refined different compilations since 1998 up to now, as more data have been collected. Some examples are the selection of SN Ia of Riess *et al.* [14], [93], Wood-Vasey *et al.* [94] and Davis *et al.* [95]. However, these catalogs combine measurements which were obtained with different analyses procedures and light-curve fitting functions. In 2008, Kowalski *et al.* [96], provided a consistent framework to analyze different SN Ia data sets and presented the world's data sets at the time as a compilation called Union SN Ia Compilation, consisting in 307 SN Ia after selection cuts. Since 2008, other groups have added a significant number of SN Ia to the Union SN Ia Compilation (Hicken *et al.* [97], Kessler *et al.* [98]). In a later work Amanullah *et al.* [99] have extended the sample and refined the analysis of Kowalski *et al.*. They have called this new compilation Union 2 Compilation and consists of 557 SN Ia ranging from a redshift z of 0.015 up to $z = 1.4$. Union 2 Compilation will be the dataset used in our analysis [99]. The data points are shown in Fig 27.

These observations provide the apparent magnitude $m_{obs}(z)$. As we have seen in Sec. 2.4.1, assuming that SN Ia have the same progenitor star, the absolute magnitude M is independent of the redshift. Equation (2.70) provides the observed distance moduli μ_{obs}, given $m_{obs}(z)$ and M. On the other hand μ is related to the luminosity distance (Eq. (2.70)), which is given by Eq. (2.45). We can compute the theoretical value of the distance moduli μ_{th}, given the Hubble expansion rate of any cosmological model, by integrating Eq. (2.45). The Hubble expansion rate of a particular $f(R)$ model depends, not just on the cosmological parameters but also on the free parameters of the $f(R)$ model which we seek to constrain throughout this chapter.
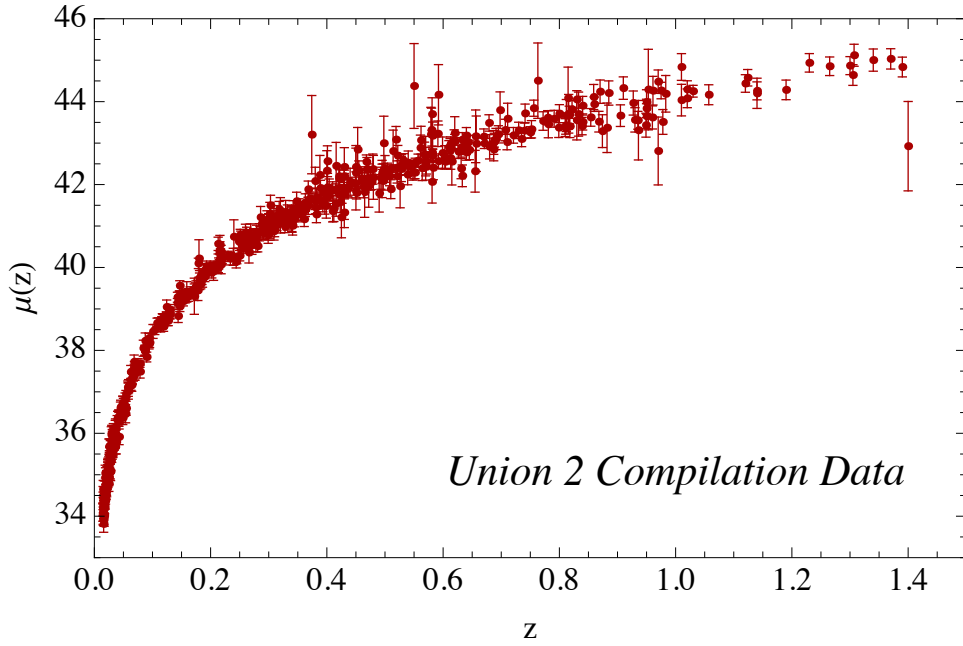
Figure 27: Union 2 Compilation data points from [99].

5.1.2 Galaxy Ages

Observational methods relying on the luminosity distance relation Eq. (2.45) for testing the value of the equation of state $w_{DE}(z)$ [*], face a theoretical limitation. Namely, the luminosity distance depends on $w_{DE}(z)$ through a multiple-integral relation as seen in Eq. (2.46). This smudges out the possibility of constraining accurately the value of $w_{DE}(z)$ and its time variation [100]. Motivated by this, the authors in [101] have proposed an alternative method that measures directly the integral in Eq. (2.45) by using spectroscopic dating of galaxy ages. Measuring the age difference Δt between two galaxies that formed at the same time but that are separated by a small redshift interval, Δz, it is possible to estimate dz/dt from the ratio $\Delta z/\Delta t$, which is directly related to $H(z)$,

$$H(z) = -\frac{1}{(1+z)}\frac{dz}{dt} \ . \tag{5.1}$$

In practice, the statistical significance of the measurements is improved by selecting a sample of galaxies at the two redshifts and comparing the upper cut-off in their age distribution. Early-type (elliptical) galaxies have generally a passive evolution, remaining undisturbed by mergers or interactions and devoid of ongoing star formation. They have typically a red color since their light is dominated by old stellar populations[†].

---

[*]As we have shown in Chapter 2, there is a mapping between $w_{DE}(z)$ and the extra terms that arise in the modified Einstein field equations in $f(R)$ models, see Eq. (3.34).

[†]Galaxies become redder as their brighter high mass (bluer) stars evolve into red giants.

Thus, the selected sample must be composed by red passively-evolving galaxies with similar metallicities [‡] and low start formation rate, in such a way that the average age of their stars is much larger than the age difference of the two galaxy samples. This method have been applied in [102] to a SDSS galaxy sample at $z \sim 0$ to determine H_0, showing that the result is in good agreement with other independent methods.

Due to the availability of new galaxy surveys, in [103] the *differential age method* has been used to determine $H(z)$ in the redshift range $0.1 < z < 1.8$. In this work the authors selected a sample of 32 galaxies from the Gemini Deep Deep Survey (GDDS) [104] and archival data [105–110]. In order to constrain the age of the oldest stars in these galaxies, information on the stellar ages must be extracted from the integrated light coming from each galaxy (it is not possible to study one by one all the stars belonging to galaxies outside the Local Group). The age of the dominant stellar population in each galaxy is obtained by fitting single stellar population models (a synthetic version of how many and what kind of stars are presented) to the observed spectrum. These models have two free parameters: age and metallicity, stellar ages are obtained by marginalizing the resulting likelihood over metallicity. From this data, they find an age-redshift relation: galaxies are older at lower redshifts (see Fig. 1 in Ref. [103]). To compute differential ages at different redshifts with the selected sample, they first group together all galaxies that are within a redshift interval $\Delta z = 0.3$ (small enough to avoid galaxies that have already evolved within the bin, but large enough to have more than one galaxy in most of the bins), discarding those that are more than 2σ away from the oldest galaxy in that bin. Then they compute age differences for those bins that are separated by more than $\Delta z = 0.1$ but not by more than $\Delta z = 1.5$, so that the age evolution between the two bins is larger than the error in the age determination of each bin. With this procedure they estimate dz/dt obtaining eight determinations of $H(z)$ from Eq. (5.1).

In our analyses, we shall use the value of H_0 obtained in [102] and the $H(z)$ data set obtained in [103], in total nine data points that are shown in Fig. 28.

5.1.3   CMB First Acoustic Peak

The angular scale of the sound horizon at the last scattering surface, θ_1, provides a deep geometrical probe of the standard cosmological paradigm since it constrains accurately the expansion history $H(z)$. The value of the angular scale is encrypted in the location of the first acoustic peak of the CMB temperature power spectrum, l_1, since $\theta_1 \sim 1/l_1$. From Eq. (2.48), the angular scale θ_1 can be written in terms of the comoving scale of the sound horizon at the last scattering surface, $r_s(z_{rec})$, and the angular diameter

---

[‡]The metallicity of a stellar object is the proportion of its matter made up elements other than hydrogen and helium, even if they are considered non-metals in chemistry. Thus, according to nucleosynthesis, older stars have lower metallicities than younger stars.
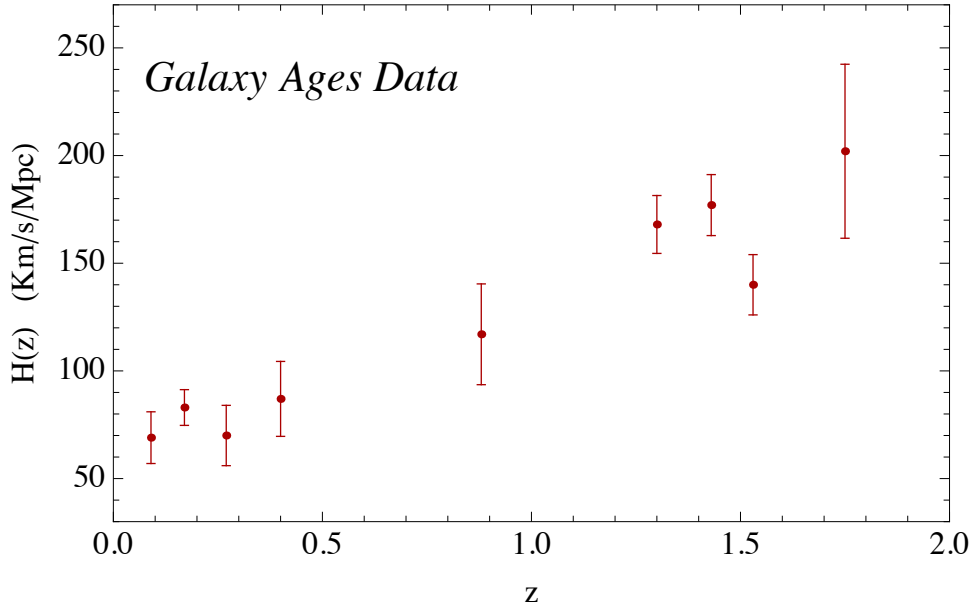
Figure 28: Galaxy ages data points from Refs. [102, 103].

distance at the time of decoupling, $d_A(z_{dec})$, as

$$\theta_1 = \frac{r_s(z_{dec})}{d_A(z_{dec})} \ , \tag{5.2}$$

where $z_{dec} = 1089$ is the redshift at decoupling. The comoving scale of the sound horizon at recombination is given by $r_s = \int_0^{\eta_{dec}} c_s d\eta$, where c_s is the sound speed of the baryon-photon fluid, which at decoupling is given by

$$c_s(z_{dec}) = \delta p/\delta \rho = 1/\sqrt{3\left(1 + \frac{3\Omega_b}{4\Omega_\gamma}\left(\frac{1}{1 + z_{dec}}\right)\right)}, \tag{5.3}$$

with Ω_b and Ω_γ the baryonic and photon densities respectively. In terms of the redshit, $r_s(z_{dec})$ is given by

$$r_s(z_{dec}) = \int_0^{z_{dec}} c_s \frac{dz}{H(z)} \ . \tag{5.4}$$

The angular diameter distance was defined in Eq. (2.50) and at decoupling (for a flat universe) it takes the form

$$d_A(z_{dec}) = \frac{1}{1 + z_{dec}} \int_0^{z_{dec}} \frac{dz}{H(z)} \ . \tag{5.5}$$

Thus, by measuring θ_1, Eq. (5.2) provides an accurate constraint on the integral of $H(z)$.

The shift parameter, R, is the least model dependent parameter that has been proposed in the literature to determine the angular scale θ_1 [111,112]. The shift parameter is defined as $R \equiv \theta_1^{ref}/\theta_1$ [113], where θ_1^{ref} is the angular scale of a reference model, which is a flat cold dark matter model without dark energy. From Eqs. (5.2) to (5.5), it is possible to show that, for a flat universe [114]

$$R = (\Omega_m H_0^2)^{1/2} \int_0^{z_{dec}} dz/H(z) . \tag{5.6}$$

In Ref. [115] it has been explicitly shown that the value of the shift parameter R is almost independent of the assumptions made about the dark energy component. We use here a CMB shift parameter value $R = 1.7407 \pm 0.0094$, as derived in Ref. [87].

5.1.4 Baryon Acoustic Oscillation

The acoustic peaks present in the temperature power spectrum of the CMB, are predicted to be also observed as *wiggles* in the matter power spectrum of galaxy surveys as a function of the scale. As we have discussed in Sec. 2.4.5, the position of these peaks serves as a *standard ruler* since it is sensitive to the Hubble parameter and the angular diameter distance. Thus, BAO measurements constitute a powerful independent geometrical probe of the standard cosmological model. The BAO signal has been already detected in the spatial distribution of galaxies by several galaxy surveys at a high significance [41,86,116]. Traditionally, the spherically correlation function is used

$$D_V(z) = \left(d_A^2(z) \frac{cz}{H(z)} \right)^{1/3} , \tag{5.7}$$

For a recent separate measurement of the Hubble parameter and the angular diameter distance, see [42]. Here we use the data sets reported in [86], where the BAO measurements are given in terms of the acoustic parameter A

$$A(z) \equiv D_V(z) \frac{\sqrt{\Omega_m H_0^2}}{zc} . \tag{5.8}$$

They report three measurements of the baryon acoustic peak at redshifts $z = 0.44, 0.6$ and 0.73 measured by the WiggleZ Dark Energy Survey together with a summary of another three measurements given by the 6-degree Field Galaxy Survey (6dFGS), at $z = 0.106$, and the Sloan Digital Sky Survey (SDSS), at $z = 0.2$ and $z = 0.35$. In addition we use the BAO measurement reported by the Baryon Oscillation Spectroscopic Survey (BOSS) at $z = 0.57$ [41]. All this data is summarized in Tab. 5.1 and shown in Fig. 29.

5.1.5 Linear Growth Rate

The galaxy distribution at large scales is mapped by galaxy surveys, which measure the redshift of galaxies, providing then a map of the galaxy distribution in redshift

z	$A(z)$	Reference
0.106	0.526 ± 0.028	[86]
0.2	0.488 ± 0.016	[86]
0.35	0.484 ± 0.016	[86]
0.44	0.474 ± 0.034	[86]
0.57	0.463 ± 0.017	[41]
0.60	0.442 ± 0.02	[86]
0.73	0.424 ± 0.021	[86]

Table 5.1: Current available data for the acoustic parameter $A(z)$.
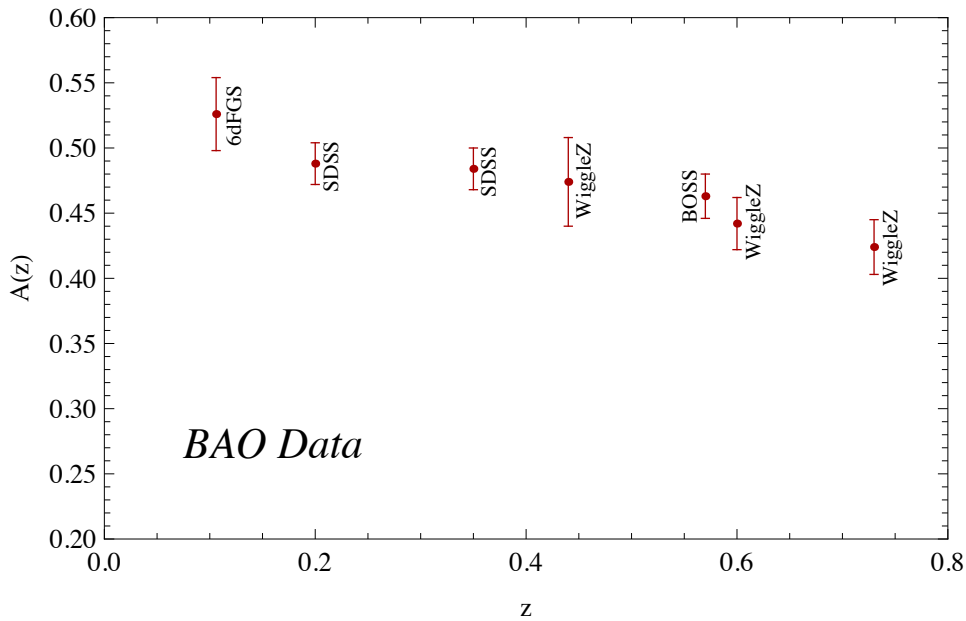
Figure 29: Data points of the acoustic parameter $A(z)$ given in Tab. 5.1.

space. The redshift of each galaxy provides a reasonable estimate of its radial distance (distance from us). However, the redshift is not a perfect distance indicator since the velocity of a galaxy is not only determined by the Hubble expansion: most galaxies have a non-negligible peculiar velocity, which is neglected in redshift space. In turn, the inferred galaxy distribution (and consequently the power spectrum) is distorted with respect to the true galaxy distribution. These are the so-called *redshift space distortions*.

In linear theory and with a local linear galaxy bias b, which is assumed to be scale independent, the relation between the true spectrum in real space and the spectrum

in redshift space is given by

$$P_{\text{redshift}}(\boldsymbol{k}) = \left(1 + \beta\mu_{\boldsymbol{k}}^2\right)^2 P(\boldsymbol{k}) \ , \tag{5.9}$$

where $\beta \equiv f/b$, with f the linear growth rate defined as (see Eq. (2.69))

$$f \equiv \frac{d\ln\delta}{d\ln a} \ , \tag{5.10}$$

and $\mu_{\boldsymbol{k}}$ is the cosine of the angle between the line of sight and the wavevector $\boldsymbol{k}$. Notice that perturbations with $\boldsymbol{k}$ perpendicular to the line of sight are not distorted. The relation among real space and redshift space overdensities given by Eq. (5.9) was first derived by Kaiser [117]. Since redshift space distortions relate peculiar velocities with the growth rate f, a measurement of $\beta \equiv f/b$ will provide information on the growth of structure formation if the galaxy bias, b, is known. It is possible to estimate the redshift distortion parameter β by using the ratio of the redshift space correlation function to the real space correlation function, which is obtained by averaging over all directions $\mu_{\boldsymbol{k}}$ in Eq. (5.9)

$$P_{\text{redshift}}(k) = \left(1 + \frac{2}{3}\beta + \frac{1}{5}\beta^2\right) P(k) \ , \tag{5.11}$$

and also by exploiting the ratio of the monopole and quadrupole harmonics of the redshift correlation function [118]:

$$Q_{\text{redshift}} = \frac{P_{\text{redshift}}^{(2)}(k)}{P_{\text{redshift}}^{(0)}(k)} = \frac{\frac{4}{3}\beta + \frac{4}{7}\beta^2}{1 + \frac{2}{3}\beta + \frac{1}{5}\beta^2} \ . \tag{5.12}$$

The continuity equation in $f(R)$ theories is exactly the same than in general relativity, see Eqs. (2.66), and therefore the relation between peculiar velocities and the matter overdensity is not modified in the $f(R)$ models studied here. Consequently, we use the available data on the growth rate f as an additional test for $f(R)$ models, to be added to the geometrical probes previously described. We quote the current available data on β, the galaxy bias b and the inferred growth rate in Tab. 5.2. These data points are shown in Fig.30.

5.2   Data analysis: estimating parameters

In the previous section we have described the data sets which we use in the data analysis of specific types of $f(R)$ models which have been proposed in the literature as viable models, alternative to dark energy. In the following we describe the methodology we will use in the next section to find the best-fit value of the parameters of each family of models. The Hubble expansion rate and the growth rate of structure formation of a particular $f(R)$ model depends, not just on the cosmological parameters described

z	β	b	f	References
0.15	0.49 ± 0.09	1.04 ± 0.11	0.51 ± 0.11	[90, 92]
0.22	0.72 ± 0.18	0.83 ± 0.16	0.60 ± 0.10	[88]
0.35	0.31 ± 0.04	2.25 ± 0.08	0.7 ± 0.18	[29]
0.41	0.77 ± 0.15	0.91 ± 0.15	0.70 ± 0.07	[88]
0.55	0.45 ± 0.05	1.66 ± 0.35	0.75 ± 0.18	[91]
0.60	0.66 ± 0.10	1.10 ± 0.13	0.73 ± 0.07	[88]
0.77	0.70 ± 0.26	1.30 ± 0.10	0.91 ± 0.36	[89]
0.78	0.58 ± 0.11	1.22 ± 0.18	0.70 ± 0.08	[88]

Table 5.2: Current available data for the redshift distortion parameter β, the bias b and the inferred growth factor, see Ref. [119].
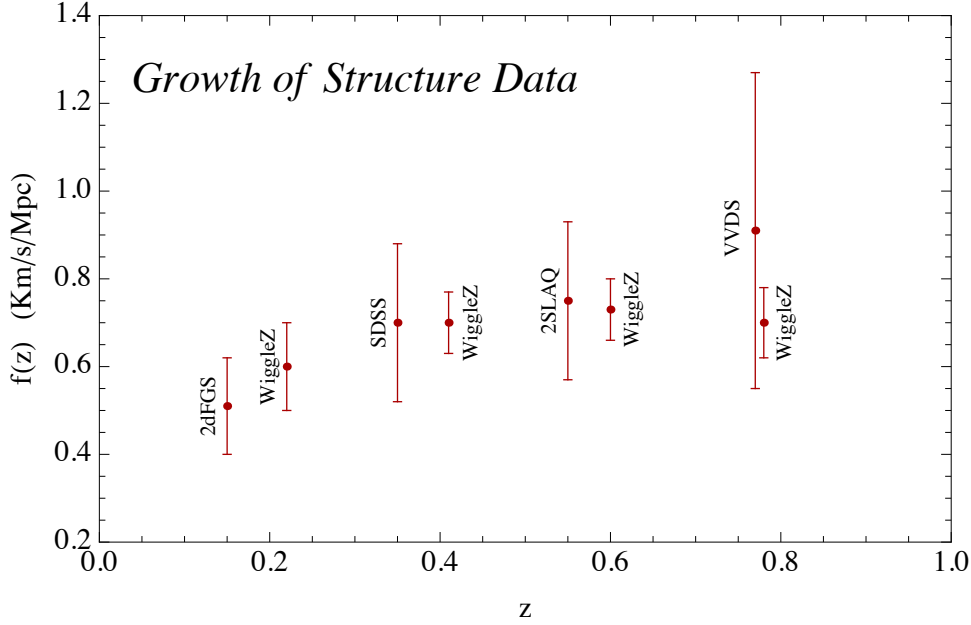
Figure 30: Data points of f, the logarithmic derivative of the linear growth factor, as a function of the redshift. See Tab. 5.2 for more details and references.

in Sec. 2.1.3, but also on the free parameters of the $f(R)$ model. We can estimate the value of these parameters in each particular case by means of the maximum likelihood principle. Consider a set of N measurements $\mathbf{d} = \{d_1, ..., d_N\}$ at points x_i of a random variable described by a joint probability density function (p.d.f.) $f(\mathbf{d}|\boldsymbol{\Theta})$, where $\boldsymbol{\Theta} = \{\theta_1, ..., \theta_p\}$ is a set of p unknown parameters. The *likelihood function* (LF) of the parameters given the data is described by the p.d.f. $f(\mathbf{d}|\boldsymbol{\Theta})$, but evaluated with the data $\mathbf{d}$ and viewed as a function of the parameters, *i.e.*, $L(\boldsymbol{\Theta}) = f(\mathbf{d}|\boldsymbol{\Theta})$. [§] If the

---

[§]The likelihood function is not a p.d.f. of the parameters.

measurements d_i are statistically independent and each follow the p.d.f. $f(\mathbf{d}|\mathbf{\Theta})$, the joint p.d.f. for $\mathbf{d}$ factorizes and the LF is

$$L(\mathbf{\Theta}) = \prod_{i=1}^{N} f(d_i|\mathbf{\Theta}) \,. \tag{5.13}$$

The estimated value of $\mathbf{\Theta}$ is given by the estimator $\hat{\mathbf{\Theta}}$. The method of maximum likelihood takes the estimator $\hat{\mathbf{\Theta}}$ to be the value of $\mathbf{\Theta}$ that maximizes $L(\mathbf{\Theta})$. Also $\ln L$ is maximized for the same value of the parameters $\mathbf{\Theta}$ and usually is easier to maximize $\ln L$ than L. If the measured quantities are independent and have a gaussian p.d.f. with mean $D(x_i, \mathbf{\Theta})$ and variance given by the experimental errors σ_i, the likelihood function is

$$L(\mathbf{\Theta}) = \frac{1}{(\sqrt{2\pi})^N} \exp\left(-\frac{1}{2} \sum_{i=1}^{N} \frac{(d_i - D(x_i, \mathbf{\Theta}))^2}{\sigma_i^2} \right), \tag{5.14}$$

and the method of maximum likelihood reduces to the method of least squares, since

$$\chi^2(\mathbf{\Theta}) = -2 \ln L(\mathbf{\Theta}) + cte = \sum_{i=1}^{N} \frac{(d_i - D(x_i, \mathbf{\Theta}))^2}{\sigma_i^2}. \tag{5.15}$$

In this case, maximizing $\ln L$ is equivalent to minimize the χ^2 function. If the measurements $\mathbf{d}$ are not independent but instead are correlated, the least square estimator $\hat{\mathbf{\Theta}}$ is determined by the minimum of

$$\chi^2(\mathbf{\Theta}) = (\mathbf{d} - D(\mathbf{\Theta}))^T C^{-1} (\mathbf{d} - D(\mathbf{\Theta})). \tag{5.16}$$

where $C_{i,j} = \text{cov}[d_i, d_j]$ is the covariance matrix.

By finding the estimator $\hat{\mathbf{\Theta}}$, the best-fit value of the parameters is obtained. We will also represent confidence regions in the p-dimensional parameter space around the best-fit value of the parameters. Confidence regions are delimited by confidence levels (CL) which are constant χ^2 boundaries representing a given percentage of the probability distribution. From the properties of the χ^2 distribution is possible to define confidence intervals in relation to $\Delta\chi^2$ such that $\chi^2 \leq \chi^2_{min} + \Delta\chi^2$ defines the confidence region in the parameter space. Table 5.2 shows the $\Delta\chi^2$ for 68.3%, 95.4% and 99.5% CL as a function of the number of parameters for the joint CL (in the case of Gaussian distributions these corresponds to the conventional 1, 2 and 3 σ CL).

In the following, we define the χ^2 function of the observables that we will use in the analysis. In the case of SNIa the observable is the distance moduli μ, measured as a function of the redshift z. The measurements are correlated in this case and the χ^2 function is defined as

$$\chi^2_{SNIa}(\theta_i) = \sum_{z,z'} \left(\mu_{obs}(z) - \mu_{th}(z, \theta_i) \right) C^{-1}_{z,z'} \left(\mu_{obs}(z') - \mu_{th}(z', \theta_i) \right), \tag{5.17}$$

CL(%)	$p = 1$	$p = 2$	$p = 3$
68.3%	1.00	2.30	3.53
95.4%	2.71	4.61	6.25
99.73%	9.00	11.8	14.2

Table 5.3: $\Delta\chi^2$ corresponding to 68.3%, 95.4% and 99.73% of the joint probability distribution as a function of the number of degrees of freedom.

the subscript th denotes the observable predicted by the theoretical model. The CMB observable is the shift parameter and the χ^2 function becomes

$$\chi^2_{CMB}(\theta_i) = \left(\frac{R_{obs} - R_{th}(\theta_i)}{\sigma_{R_{obs}}}\right)^2 . \tag{5.18}$$

The observable for BAO is given by the A parameter and the χ^2 function

$$\chi^2_{BAO}(\theta_i) = \sum_z \left(\frac{A_{obs} - A_{th}(\theta_i)}{\sigma_{A_{obs}}}\right)^2 . \tag{5.19}$$

The χ^2 function for the ages of galaxies is defined in terms of the Hubble parameter given by

$$\chi^2_{ages}(\theta_i) = \sum_z \left(\frac{H_{obs}(z) - H_{th}(z, \theta_i)}{\sigma_{H_{obs}}}\right)^2 . \tag{5.20}$$

Finally, the observable of the linear growth rate of structure is its logarithmic derivative $f(z)$, however the theoretical prediction of this observable is scale dependent, *i.e.*, $f(z, k, \mathbf{\Theta})$ and each experiment focuses in a particular range of k for redshift space distortion analyses. In order to compute the theoretical prediction for each $f(z_j, \theta_i)$ we average the function $f(z_j, k)$ over the k range indicated by each experiment (see references in Tab. 5.2). For $z = 0.15$, the k range we considered is $(0.03 - 0.125)h/\text{Mpc}$, for $z = 0.35$ we have used the $(0.01 - 0.09)h/\text{Mpc}$ range and for $z = 0.55$ we have focused in the $(0.01 - 0.5)h/\text{Mpc}$ range. Finally, for $z = 0.77$ the k range exploited here is $(0.05 - 0.5)h/\text{Mpc}$. The χ^2 function is defined as

$$\chi^2_{growth}(\theta_i) = \sum_z \left(\frac{f_{obs}(z) - f_{th}(z, \theta_i)}{\sigma_{f_{obs}}}\right)^2 . \tag{5.21}$$

Notice that the extraction of the $f(z)$ data has some model dependences associated to the derivation of the bias parameter b, since, in general, a ΛCDM cosmological scenario is assumed. We have tested the dependence of our results on the uncertainty in the bias parameter by enlarging the errors on the $f(z)$ data, as we shall comment.

The total χ^2 for all the geometrical probes is given by the sum of the individual χ^2 functions such that

$$\chi^2_{dis}(\theta_i) = \chi^2_{SNIa}(\theta_i) + \chi^2_{BAO}(\theta_i) + \chi^2_{CMB}(\theta_i) + \chi^2_{ages}(\theta_i), \tag{5.22}$$

ΛCDM	SNIa	BAO	CMB	Galaxy Ages	Growth	χ^2_{dis}	χ^2_{tot}
χ^2	543.2	6.7	3.4	10.6	4.7	564	569
d.o.f.	557	7	1	9	8	574	582
p-value	0.65	0.46	0.07	0.30	0.79	0.61	0.64

Table 5.4: χ^2 values for the different data sets of observables for the ΛCDM model for the best-fit of the cosmological parameters $H_0 = 67.3$ Km/s/Mpc, $\Omega_M = 0.315 \pm 0.017$ and $\Omega_\Lambda = 1 - \Omega_M$ [2].

and the global χ^2 is obtained after adding the growth rate of structure probe to the total distances χ^2,

$$\chi^2_{tot}(\theta_i) = \chi^2_{SNIa}(\theta_i) + \chi^2_{BAO}(\theta_i) + \chi^2_{CMB}(\theta_i) + \chi^2_{ages}(\theta_i) + \chi^2_{growth}(\theta_i). \qquad (5.23)$$

In the following sections we perform the data analysis of the specific families of $f(R)$ models which we have studied in the previous chapter as well as the analysis of the standard ΛCDM model for comparison.

5.3   The standard model: ΛCDM

In this section we compute the χ^2 value of each individual probe corresponding to the ΛCDM model. We will compare these values with the χ^2 values resulting from the analyses of the $f(R)$ models. We use the data sets described in the previous section and the latest constraints in the cosmological parameters from Planck [2], namely, $H_0 = 67.3 \pm 1.2$ Km/s/Mpc and $\Omega_M = 0.315 \pm 0.017$. Therefore, in the data analysis of all models we fix $H_0 = 67.3$ Km/s/Mpc and $\Omega_M = 0.315$ unless otherwise specified. Considering spatial flatness ($\Omega_k = 0$) and $\Omega_\Lambda = 1 - \Omega_M$, the ΛCDM model does not have any remaining parameters and the χ^2 in this case is a single number. The ΛCDM expansion history is given by Eq. (2.36), where we neglect radiation ($\Omega_R = 0$), and the growth of structure formation is given by Eq. (2.69). With this description is easy to compute the χ^2 value of each probe given by Eqs. (5.17)-(5.21) for the ΛCDM model. These values are shown in Tab. 5.3 together with the number of the degrees of freedom of each data set and the resulting p-value. With the best-fit value of H_0 and Ω_M given by Planck 2013 data, the p-value of the SNIa, BAO, galaxy ages and the growth χ^2 analysis is $p > 0.1$ while in the case of the CMB analysis is $p < 0.1$, however we should notice that the shift parameter measurement is very accurate with an error of order 10^{-3}, which leads to a large χ^2 value for this probe and moreover we have fixed all the parameters in the model. The total χ^2 of all distance measurements is given by Eq. (5.22) and the global χ^2 of all probes including the growth data is given by Eq. (5.23).

5.4 Ruled Out Models by Cosmological Data

In this section we find that, from the five different type of models studied in the previous chapter, three of them are ruled out by comparing the allowed regions by geometrical probes with the regions resulting from the fit to the growth of structure data in the parameter space. These results show that, testing modified gravity models against geometrical probes combined with growth of structure data, constitutes a robust method to rule out $f(R)$ models.

5.4.1 Type 1

We have shown in Chapter 3 that the model

$$f(R) = R^p \left[\log(\alpha R)\right]^q - R \,, \tag{5.24}$$

is cosmologically viable only for $p = 1$ and $q > 0$, therefore in the following analysis we set $p = 1$ and we consider two free parameters, q (positive) and α. We compute the best-fit value of these parameters by combining the different data sets described in Sec. 5.1. Figure 31 shows, in the 2-dimensional parameter space (α, q), that there is tension between the allowed regions by distance measurements (full color) and the allowed regions resulting from the fit to growth of structure data (red lines). The star represents the best-fit analysis given by distance measurements with a minimum $\chi^2_{dis} = 573.2$ for 572 d.o.f.. The best-fit value of the parameters given by distance measurements only is $q = 3.67$ and $\log \left[\alpha \left(\text{ in km/s/Mpc}\right)^{-2}\right] = -1.61$ (which gives $\alpha = 111(\bar{H}_0)^{-2}$, with $\bar{H}_0 = 67.3$ km/s/Mpc). The plus sign represents the best-fit to the growth data with a minimum $\chi^2_{growth} = 0.98$ for 6 d.o.f. corresponding to $q = 1.45$ and $\log \left[\alpha \left(\text{ in km/s/Mpc}\right)^{-2}\right] = -2.78$. Distance measurements prefer larger values of the power index q, while growth data prefer much smaller ones and there is no allowed region at more than 99.73% CL able to fit distances and growth data simultaneously. Errors in the inferred growth rate are still large (see Tab. 5.2), but sufficient to test this model. It is worth noticing that all the contours in Fig. 31 show a correlation between the parameters.

We compute the theoretical prediction of each observable with the best-fit value of the parameters q and α from distance measurements. Solving numerically Eq. (3.40) we compute the theoretical distance moduli curve $\mu(z)$ (Eq. (2.70)) predicted by this model (blue line), which is shown in Fig. 32 together with the Union Compilation 2 data points. We also show the curve given by the ΛCDM model for comparison (orange dashed line). Similarly, we calculate the theoretical acoustic parameter $A(z)$ (Eq. (5.8)) predicted by this model (blue line), which is shown in Fig. 33 together with the BAO data sets given in Tab. 5.1 and the ΛCDM model prediction. In Fig. 34 we show the Hubble parameter, $H(z)$, predicted by this model, together with the data set extracted from *differential* galaxy ages. The prediction of the CMB shift parameter (Eq. (5.6)) of this model is $R = 1.36$, while for a universe with a cosmological constant
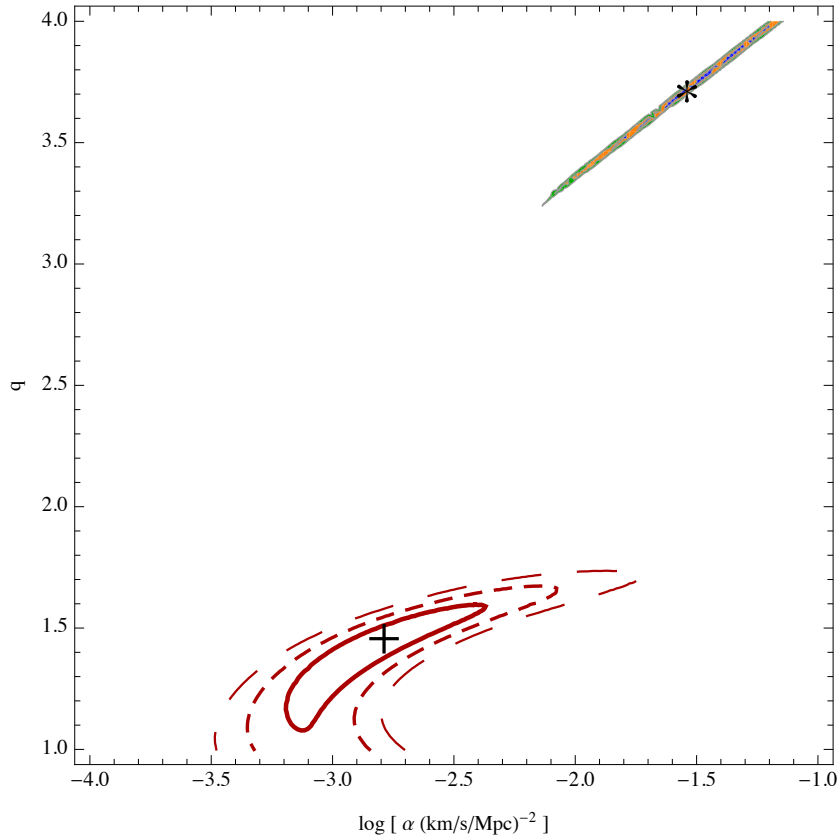
Figure 31: **Data analysis of type 1 model**. Full regions are bounded by the 68.3%, 95.4% and 99.7 % CL of the χ^2_{dis} analysis showing the allowed regions by distance measurements in the parameter space $(\alpha,\ q)$ of the model Eq. (5.24). The best-fit point of the analysis for distances-only is marked with a star. Red lines correspond to the 68.3% (solid), 95.4% (small dashed) and 99.7 % (large dashed) CL contours of the χ^2_{growth}. The best-fit point of the growth data analysis is marked with a plus sign.

(with $\Omega_M = 0.315$, $\Omega_\Lambda = 1 - \Omega_M$ and $H_0 = 67.3$ km/s/Mpc [2]), is $R_{\Lambda\text{CDM}} = 1.76$. We calculate the logarithmic derivative of the growth factor, f, as a function of the redshift for a typical scale $k_0 = 0.1h/\text{Mpc}$. The same choice of parameters as in the geometrical probes ensure an acceptable background cosmology but, as we have seen from Fig. 31, the best-fit value of the parameters to distance measurements is well outside the allowed regions by growth data. The $f(z)$ curve is shown in Fig. 35 together with the available data on $f(z)$ given in Tab. 5.2 and also the curve given by the ΛCDM model for comparison. We can see that the growth of matter perturbations predicted by this model in this range of parameters is highly suppressed compared to the one in a ΛCDM cosmology. In Fig. 9 we showed that, for parameters that reproduce correctly the expansion history the model Eq. (5.24), the linear growth does not depend on the scale, however is very much off the ΛCDM model. This statement holds independently

of the value of Ω_M chosen for the analysis, *i.e.*, we have computed the logarithmic derivative of the growth factor (f) varying Ω_M in the range $(0.1, 0.9)$, and f is always smaller than 10^{-2}. It was already expected that the model given by Eq. (5.24) provides a bad fit to the growth of structure data, see the discussion after Eq. (3.46) and Fig. 8. We find that, for parameters that reproduce the expansion history within the 99.7% CL, the $\chi^2_{growth} \geq 277$ for 6 d.o.f. giving a probability of the result being due to chance $p < 10^{-5}$. Statistically, we can safely reject the null hypothesis of this model being compatible with data.
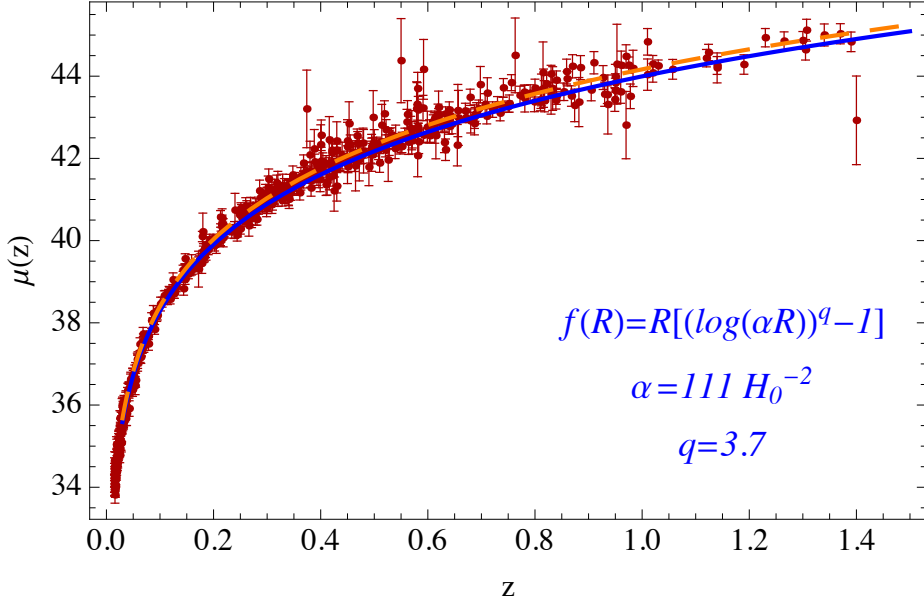
Figure 32: **Distance moduli of the** $f(R)$ **type 1 model**. The blue line shows the distance moduli of an expansion history described by the model of Eq. (5.24), with $q = 3.7$ and $\alpha = 111(\bar{H}_0)^{-2}$. The orange dashed line shows the distance moduli of the ΛCDM model (with $H_0 = 67.3$ km/sec/Mpc, $\Omega_M = 0.315$ and $\Omega_\Lambda = \Omega_M - 1$) for comparison. The data points are given by the Union Compilation 2 data set.
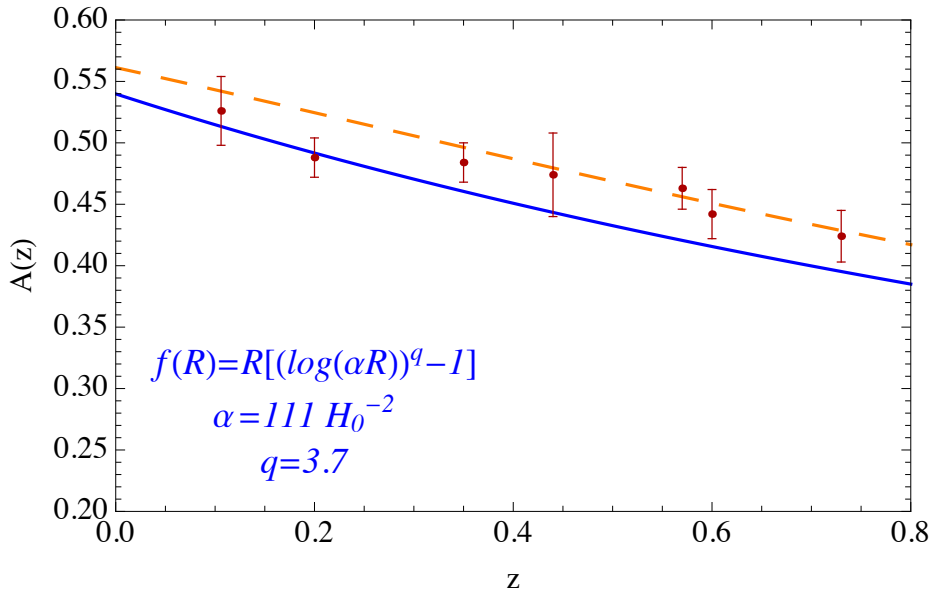
Figure 33: **Acoustic parameter of type 1 model**. The blue line shows the BAO parameter $A(z)$ of an expansion history described by the model of Eq. (5.24), with $q = 3.7$ and $\alpha = 111(\bar{H}_0)^{-2}$. The orange dashed line shows the $A(z)$ parameter, for a ΛCDM model (with $H_0 = 67.3$ km/sec/Mpc, $\Omega_M = 0.315$ and $\Omega_\Lambda = \Omega_M - 1$) for comparison. The data points are given by the data set given in Tab. 5.1.

5.4.2 Type 2

The family of exponential models

$$f(R) = R^p \exp(q/R) - R \,, \tag{5.25}$$

has an acceptable expansion history only when $p = 1$, as shown in the qualitative analysis of Chapter 3, and one free parameter remains, q. In this case, we also allow the current fraction of the energy density in the form of dark matter, Ω_M^0, to be an additional free parameter in the analysis of this type of model. This type of models contains the ΛCDM model as a limiting case; when q/R is small, $f(R) \to q$ and the parameter q plays the role of a cosmological constant. Therefore we expect the models of Eq. (5.25) to be allowed by all cosmological distance measurements, with a best-fit value of q close to the cosmological constant value. Figure 36 shows the results of the analysis of the model given by Eq. (5.25) in the parameter space (Ω_M, q). The star denotes the best-fit value of the parameters resulting from the fit to all the cosmological distance measurements described in Sec. 5.1. We obtain $q = -20960$ (km/s/Mpc)$^2 = -4.6\bar{H}_0^{\,2}$ (with $\bar{H}_0 = 67.3$ km/s/Mpc), and $\Omega_M^0 = 0.31$ with a minimum $\chi_{dis}^2 = 561.7$ for 572 d.o.f.. The full color regions represent the 68.3%, 95.4% and 99.7% CL allowed contours from the fit to cosmological distances and show that the parameters Ω_M and
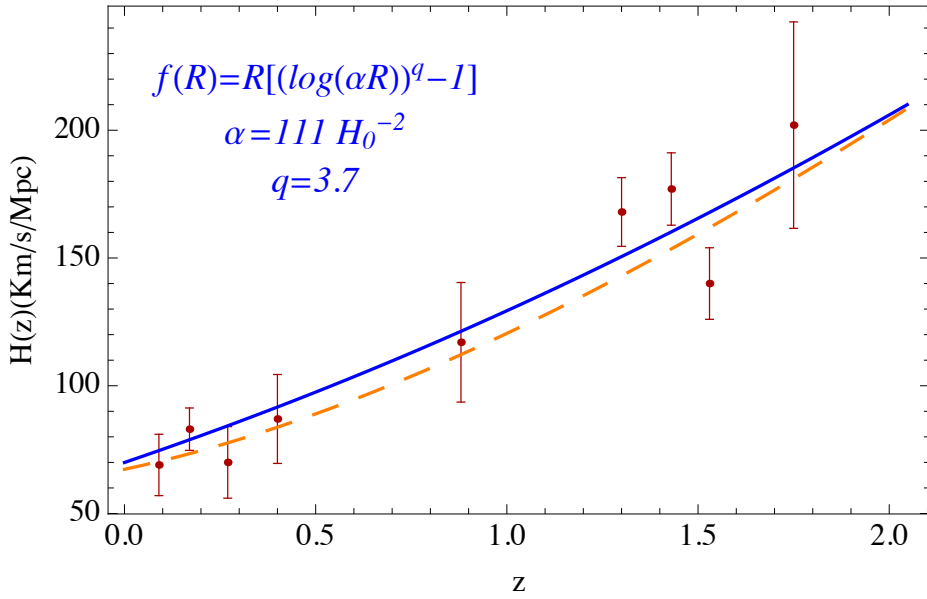
Figure 34: **Hubble parameter from galaxy ages of type 1 model**. The blue line shows the Hubble parameter, $H(z)$, for an expansion history described by the model of Eq. (5.24), for $q = 3.7$ and $\alpha = 111(\bar{H}_0)^{-2}$. The orange dashed line shows the Hubble parameter, $H(z)$, of the ΛCDM model (with $H_0 = 67.3$ km/sec/Mpc, $\Omega_M = 0.315$ and $\Omega_\Lambda = \Omega_M - 1$) for comparison. The data points are given by the data set extracted from *differential* galaxy ages.

q are correlated. The distances-only-data strongly constrain the value of the parameter q and, as we expected, its best-fit value is close to the cosmological constant value of a ΛCDM universe. The yellow dashed contour corresponds to the value $\chi^2_{\Lambda\text{CDM}} = 564$ (for 574 d.o.f.) resulting from the fit of the ΛCDM model to the cosmological distances data (see Tab. 5.3) and coincides with the 68.3% CL contour of the best-fit of the exponential family Eq. (5.25). The relevance of testing the model of Eq. (5.25) against cosmological data appears when comparing the allowed regions by geometrical probes to those coming from the growth of structure data. The latter prefers smaller values of Ω_M and q than the distances-only-data. The best-fit value to the growth of structure data is outside the parameter range plotted in Fig. 36 and far from the best-fit value to geometrical probes. The solid, small dashed and large dashed red lines denote the 68.3%, 95.4% and 99.7% CL allowed contours respectively, resulting from the fit to the growth of structure data. As we can see there is tension between both regions and there is no overlap at more than 3-σ between the two regions. As we mentioned in the introduction to this section, in this analysis we have updated the data sets used in [85]. With the data sets used in [85], this model was allowed by all data sets, since the allowed regions by growth of structure data used to overlap with the regions allowed by cosmic distances (see Fig. 5 of [85]). In the new analysis performed here, the
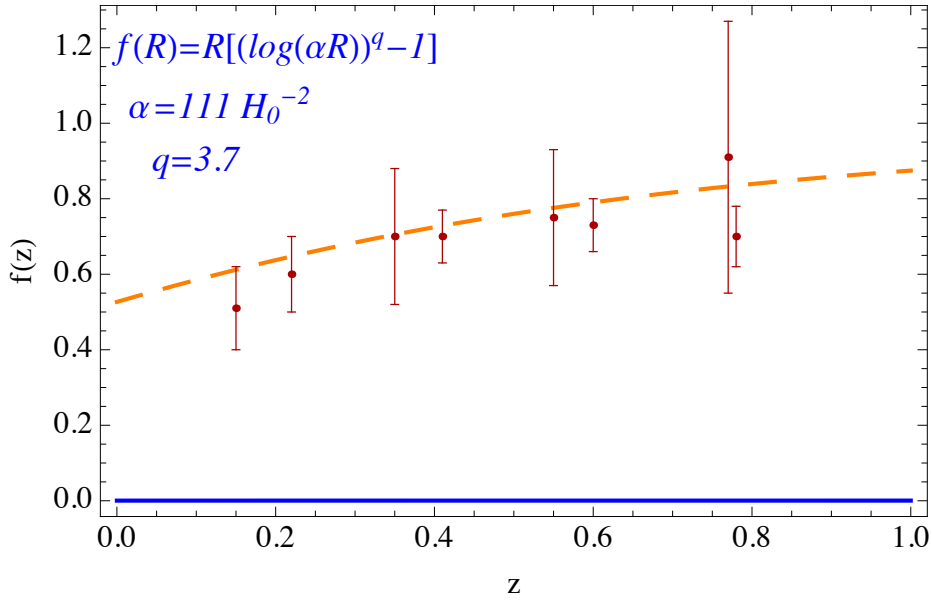
Figure 35: **Logarithmic derivative of the linear growth factor of type 1 model**. The blue curve denotes the predictions for the logarithmic derivative of the linear growth factor, $f(z)$, for $k_0 = 0.1h/\text{Mpc}$ of the model of Eq. (5.24). In this case the $f(z)$ function is almost constant in this redshift interval and equal to 0.012, and therefore, highly suppressed. We show the $f(z)$ function corresponding to the ΛCDM model for comparison (dashed, orange line). The current available data on $f(z)$ given in Tab (5.2) is also shown. The parameters are expressed in terms of $\bar{H}_0$, being $\bar{H}_0 = 67.3$ km/s/Mpc.

new CMB and BAO data points have pushed the contours resulting from the cosmic distances analysis towards larger values of q and Ω_M, while the new growth data points have pushed the growth contours towards smaller values of q and Ω_M. This effect has crucially generated enough tension between both regions to rule out the exponential family of models given by Eq. (5.25).

With the best-fit value of q and Ω_M^0 obtained from the fit to geometrical probes, we calculate the theoretical distance moduli $\mu(z)$ predicted by this model. This curve is shown in Fig. 37 together with the Union Compilation 2 data set points. In Fig. 38 we show the curve $A(z)$ predicted by this model for the same value of the parameters together with the BAO data set used in the analysis. In Fig. 39 we show the Hubble parameter, $H(z)$, predicted by this model together with the data set extracted from *differential* galaxy ages. Finally the value of the CMB shift parameter, R, for the same value of q and Ω_M^0, is $R = 1.48$ (while $R_{\Lambda\text{CDM}} = 1.76$). We calculate the logarithmic derivative of the growth factor, f, as a function of the redshift for a typical scale $k_0 = 0.1h/\text{Mpc}$. We chose the same value of the parameters as in the geometrical probes to assure an acceptable background cosmology. The curve is shown in Fig. 40
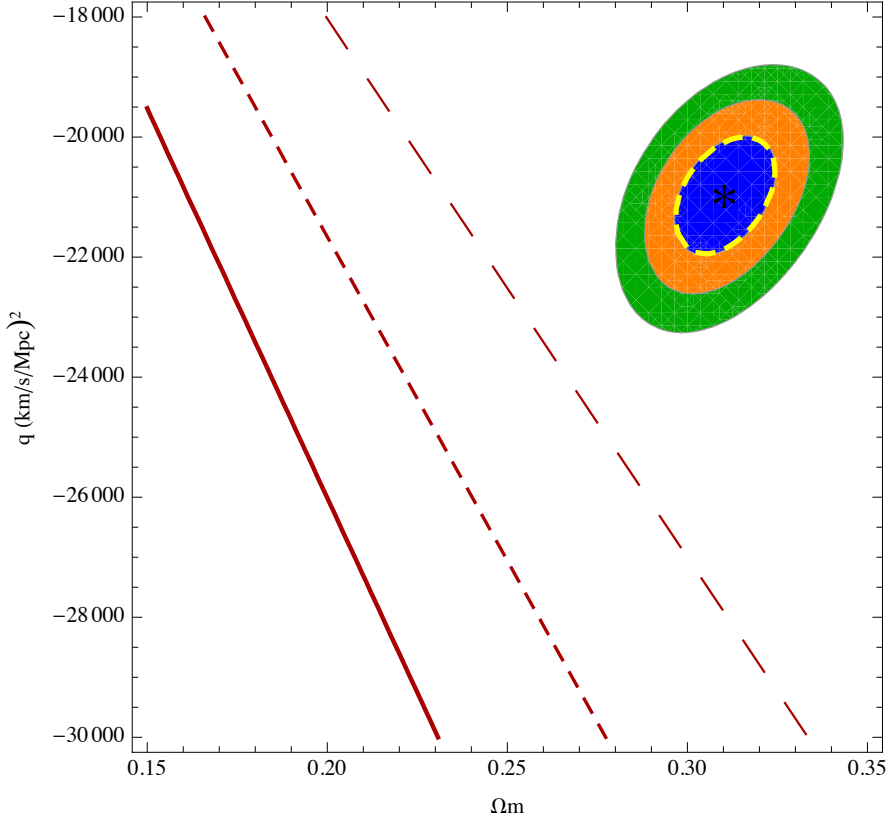
Figure 36: **Data analysis of model Type 2:** Full regions correspond to the 68.3%, 95.4% and 99.7 % CL of the χ^2_{dis} analysis in the parameter space (Ω^0_M, q) of the model of Eq. (5.25). The best-fit point of the geometrical probes analysis is marked with a star. Red lines correspond to the 68.3% (solid), 95.4% (small dashed) and 99.7 % (large dashed) CL upper limits of the growth data analysis.

together with the available data on $f(z)$ given in Tab. 5.2 and also the curve given by the ΛCDM model. In this figure we can appreciate again the tension between the best-fit value of the parameters obtained from distance measurements only and the allowed regions by growth of structure data. For values of the parameters that fit the distances data within the 99.7% CL, the $\chi^2_{growth} \geq 17$ for 6 d.o.f., giving a probability of the result being due to chance $p < 0.01$, this means that statistically we can reject the null hypothesis of this model being compatible with data. We should notice that the errors on $f(z)$ may be affected by the method used in the bias extraction, we estimate that, in order to accept this model with $p > 0.1$, the errors of $f(z)$ should be enlarged by a factor of $\sim 2 - 3$.
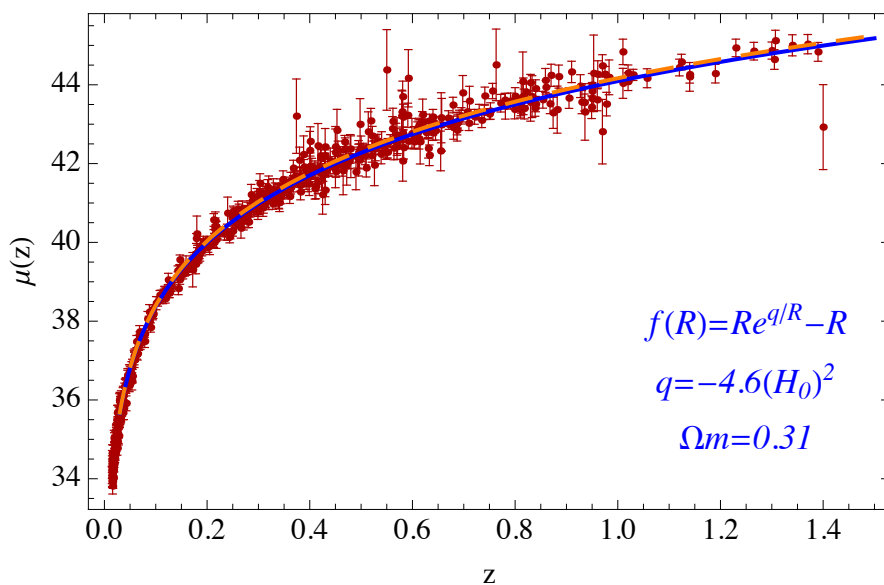
Figure 37: **Distance moduli of type 2 model**. The blue line shows the distance moduli of an expansion history described by the model Eq. (5.25), with $q = -4.6\bar{H}_0^2$ and $\Omega_M = 0.31$. The orange dashed line shows the distance moduli of the ΛCDM model (with $H_0 = 67.3$ km/sec/Mpc, $\Omega_M = 0.315$ and $\Omega_\Lambda = \Omega_M - 1$) for comparison. The data points are given by the Union Compilation 2 data set.

5.4.3 Type 3

There are two free parameters in the power law family

$$f(R) = \alpha R^n \,, \tag{5.26}$$

namely n and α. We have seen in Chapter 3 that, to satisfy the expansion history conditions these parameters are constrained to be in the range $\alpha < 0$, $0 < n < 1$. This family contains the ΛCDM universe as a limiting case, when $n \to 0$ then $f(R) \to \alpha$, thus, we expect this model to fit the cosmic distances data at least in the parameter space region where $n << 1$ and α close to the cosmological constant value. The results of the analyses of this model is shown in Fig. 41. Full colors correspond to the 68.3%, 95.4% and 99.7% CL contours resulting from a fit to the cosmological distances data exploited in this thesis and the star represents the best-fit value of the parameters, which corresponds to $n = 0.003$ and $\alpha = -19931$ (Km/s/Mpc)$^{2(1-n)} = -4.4\bar{H}_0^{2(1-n)}$ with a minimum $\chi^2_{dis} = 548.6$ for 572 d.o.f.. The dashed, yellow contour corresponds to the χ^2_{dis} value of the ΛCDM model given in Tab. 5.3. The solid, short dashed and large dashed lines correspond to the 68.3%, 95.4% and 99.7% CL contours respectively resulting from a fit to the growth of structure data. Growth of structure data prefers larger values of n than distances data. Still in both regions the power index n can be quite large and the normalization α can deviate from the cosmological constant present
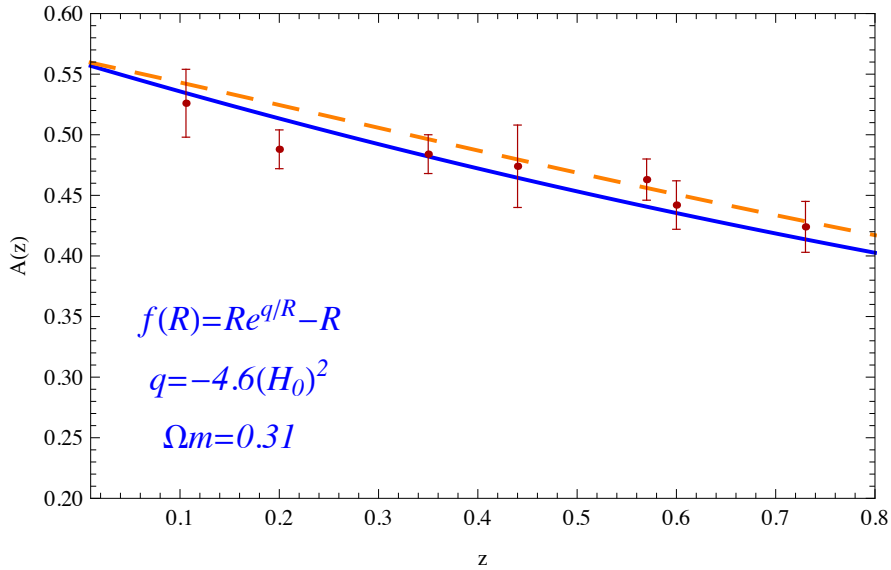
114

Figure 38: **Acoustic parameter of type 2 model**. The blue line shows the BAO parameter $A(z)$ of an expansion history described by the model of Eq. (5.25), with $q = -4.6\bar{H}_0^2$ and $\Omega_M = 0.31$. The orange dashed line shows $A(z)$, of the ΛCDM model (with $H_0 = 67.3$ km/sec/Mpc, $\Omega_M = 0.315$ and $\Omega_\Lambda = \Omega_M - 1$) for comparison. The data points are given by the data set given in Tab. 5.1.

in a ΛCDM universe, showing a clear correlation between both parameters. There is no overlap between the two regions at more than 3-σ and, for the parameter values that reproduce the expansion history within the 99.7% CL, the $\chi^2_{growth} \geq 19$ for 6 d.o.f. giving a probability of the result being due to chance $p < 0.004$. Statistically, we can reject the null hypothesis of this model being compatible with data. As it happens with models of type 2, this family was allowed by all data sets considered in the analysis of [85]. However, with the up-to-data data used in this thesis, we can ruled out the family of models belonging to type 3.

We calculate the theoretical prediction of the different observables according to this model using the best-fit value of the parameters obtained from distance measurements only. Figure 42 shows the theoretical distance moduli curve, $\mu(z)$, predicted by this model together with the Union Compilation 2 data set points. Figure 43 shows the curve $A(z)$ predicted by this model, together with the BAO data set used in the analysis and Fig. 44 shows the Hubble parameter, $H(z)$, predicted by this model together with the data set extracted from *differential* galaxy ages. In all the figures we also show the curve given by the ΛCDM model (with $\Omega_M = 0.315$ and $\Omega_\Lambda = \Omega_M - 1$) for comparison. The value of the shift parameter, R, is $R = 1.37$. The logarithmic derivative of the growth factor, f, as a function of the redshift for a typical scale $k_0 = 0.1h/$Mpc is shown in Fig. 45 together with the available data on $f(z)$ and given in Tab. 5.2. With the distances best-fit value of the parameters, which ensure a viable background
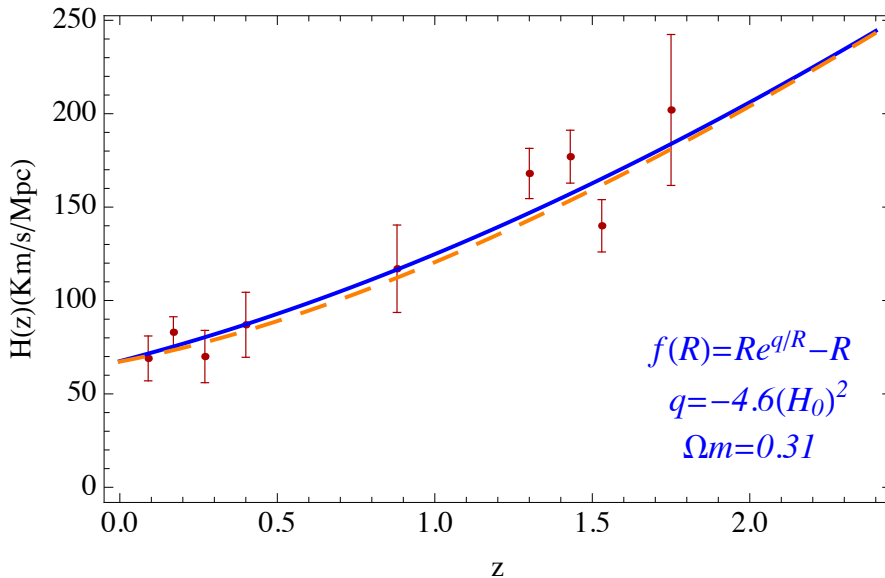
Figure 39: **Hubble parameter from galaxy ages of type 2 model**. The blue line shows the Hubble parameter, $H(z)$, of an expansion history described by the model of Eq. (5.25), with $q = -4.6\bar{H}_0^2$ and $\Omega_M = 0.31$. The orange dashed line shows the Hubble parameter, $H(z)$, of the ΛCDM model (with $H_0 = 67.3$ km/sec/Mpc, $\Omega_M = 0.315$ and $\Omega_\Lambda = \Omega_M - 1$) for comparison. The data points are given by the data set extracted from *differential* galaxy ages.

cosmology, we see that the logarithmic derivative of the growth factor for this model deviates from most of the data points, as expected from the tension observed in Fig. 41 between the allowed regions by cosmic distances and by the growth of structure data. As discussed in Sec. 5.1.5, the errors on $f(z)$ may be affected by the method used in the bias extraction. We find that, in order to accept this model with $p > 0.1$, the errors on $f(z)$ should be enlarged by a factor $\sim 2 - 3$.

5.5   Allowed Models by Cosmological Data

In this section we shall see that only models of type 4 and 5 are acceptable after the constraints of all the data sets used in this analysis. As we will next see, in these two cases the allowed regions by growth of structure data overlap with the allowed regions by geometrical probes and there is no tension between them as in the previous cases. In these cases we shall set tight constraints on the free parameters of each type of model.
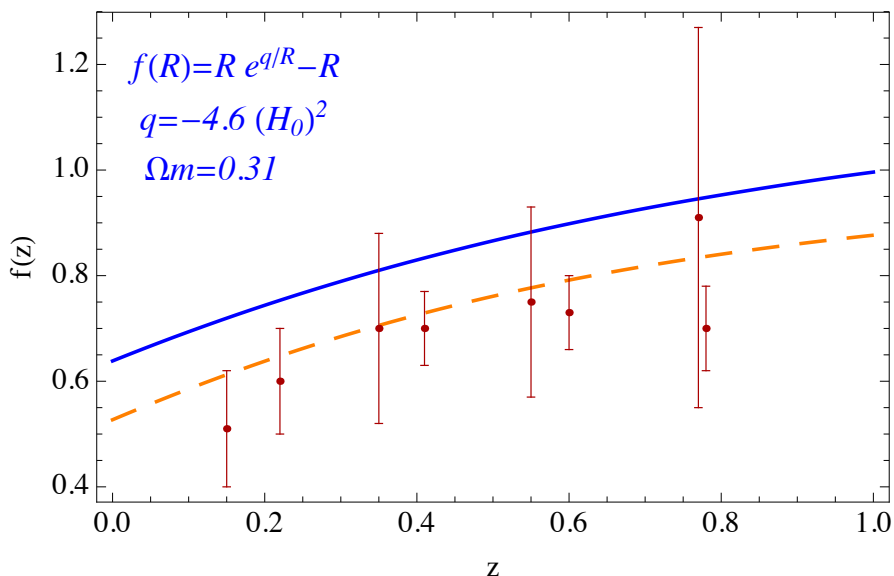
Figure 40: **Logarithmic derivative of the linear growth factor of type 2 model**. The blue curve denotes the predictions for the logarithmic derivative of the linear growth factor, $f(z)$, for $k_0 = 0.1h/\text{Mpc}$ of the Eq. (5.25) model together with the current available data on $f(z)$ given in Tab. 5.2. The $f(z)$ function corresponding to the ΛCDM model is also shown for comparison (dashed, orange line). The parameters are expressed in terms of $\bar{H}_0$, being $\bar{H}_0 = 67.3$ km/s/Mpc.

5.5.1   Type 4

The family of type 4,

$$f(R) = \alpha R^2 - \Lambda \,, \tag{5.27}$$

is described by two parameters, Λ and α. The condition for viability in this case is $\alpha\Lambda \ll 1$, as discuss in the previous chapter, and there exists a strong degeneracy among these two parameters. In the limit $\alpha \to 0$, $f(R) \to \Lambda$, a cosmological constant, and consequently this family contains the ΛCDM universe as a limiting case, implying that the model must be allowed by all geometrical probes in that parameter range. Notice that the Einstein Hilbert action contains the term $R - 2\bar{\Lambda}$, and therefore Λ, in the limit $\alpha \to 0$, is twice the usual cosmological constant $\bar{\Lambda}$. On the other hand, in the limit $\Lambda \to 0$, $f(R) = \alpha R^2$. Figure 46 shows the analysis of this model in the parameter space $(\log\alpha, \Lambda)$. As for the previous models, full color contours correspond to the 68.3%, 95.4% and 99.7% CL allowed regions resulting from the fit to all the distances measurements exploited in the analysis, the star, located at $\alpha = 1.6 \cdot 10^{-12}(\text{km/s/Mpc})^{-2} = 7 \cdot 10^{-9}\bar{H}_0^{-2}$ and $\Lambda = 20483$ $(\text{km/s/Mpc})^2 = 4.5\bar{H}_0^2$ (with $\bar{H}_0 = 67.3$ km/s/Mpc), is the best-fit value of distances-only, with a minimum $\chi^2_{dis} = 548.5$ for 572 d.o.f.. The solid, short dashed and large dashed lines correspond to the 68.3%, 95.4% and 99.7% CL contours resulting from the fit to growth
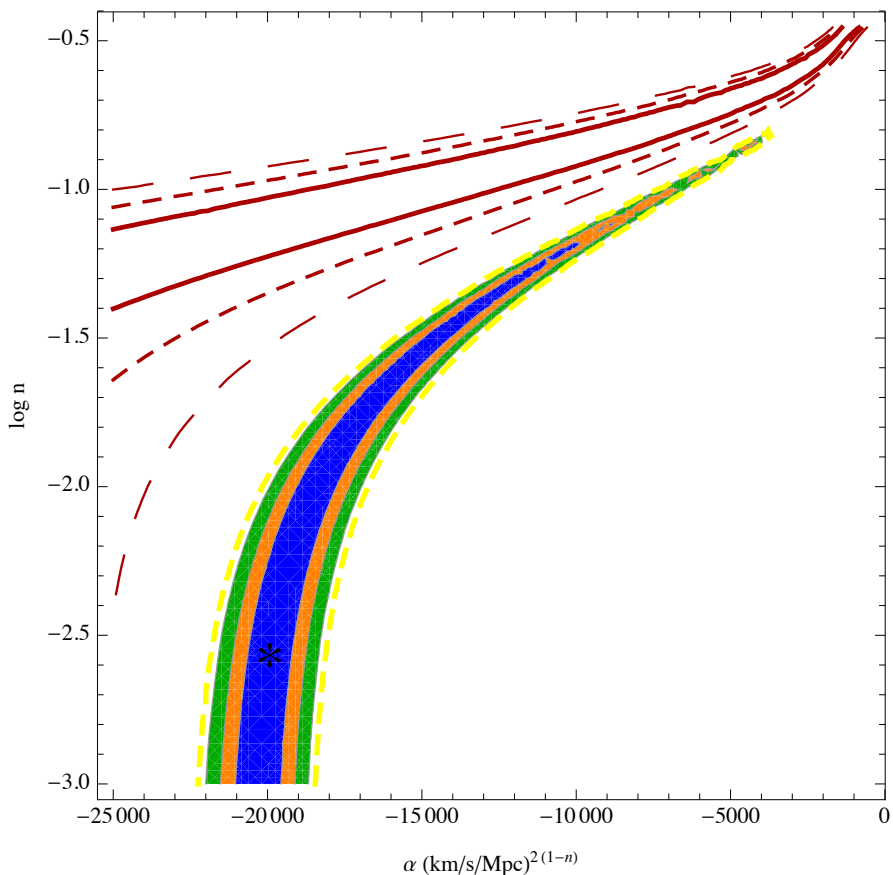
Figure 41: **Data analysis of type 3 model**. Full regions correspond to the 68.3%, 95.4% and 99.7 % CL of the χ^2_{dis} analysis in the (α, n) parameter space of the modified gravity model of Eq. (5.26). The best-fit point of the geometrical probes analysis is marked with a star. Red lines correspond to the 68.3% (solid), 95.4% (short dashed) and 99.7 % (large dashed) CL contours from the χ^2_{growth} analysis.

of structure data. The yellow dashed line corresponds to the χ^2_{dis} value of the ΛCDM model. As we expected, cosmic distances data constrain the value of Λ to be close to the cosmological constant value and the normalization α to be very small, with $\log[\alpha \text{ (in km/s/Mpc)}^{-2}] < -10$. These two parameters are anticorrelated, as α increases Λ decreases. Growth data prefers smaller values of α and larger values of Λ compared to the analysis resulting from the geometrical probes. However there is no tension between the regions preferred by geometrical probes and the ones preferred by the growth data, they overlap at the 1-σ level and the model is allowed by all the independent data sets. In this case we compute the global best-fit analysis, shown in Fig. 47. In this figure full colors correspond to the 68.3%, 95.4% and 99.7% CL contours resulting from the fit to all the cosmological data, χ^2_{tot}. As we observe, the allowed regions from the cosmic distances-only analysis in Fig. 46 almost coincides
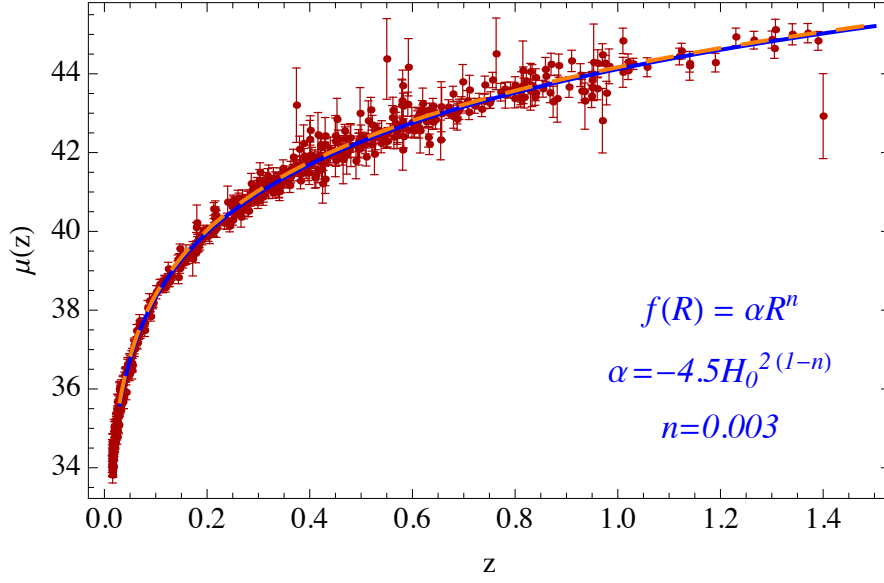
Figure 42: **Distance moduli of type 3 model**. The blue line shows the distance moduli of an expansion history described by the model of Eq. (5.26), for $\alpha = -4.5\bar{H}_0^{2(1-n)}$ and $n = 0.003$. The orange dashed line shows the distance moduli of the ΛCDM model (with $H_0 = 67.3$ km/sec/Mpc, $\Omega_M = 0.315$ and $\Omega_\Lambda = \Omega_M - 1$) for comparison. The data points are given by the Union Compilation 2 data set.

with the allowed regions by the global analysis. From the global analysis we obtain $\chi^2_{min} = 548.5$ for 580 d.o.f.. and the best-fit value of the parameters coincides with the best-fit value of geometrical probes only, which lead to a current effective dark energy equation of state $w_{\text{eff}}(z = 0) = -0.98$.

Using the best-fit value of α and Λ, we compute the theoretical distance moduli curve, $\mu(z)$, predicted by this model, which is shown in Fig. 48 together with the Union Compilation 2 data set. In Fig. 49 we show the curve $A(z)$ predicted by this model, together with the BAO data set used in the analysis. Fig. 50 depicts the Hubble parameter, $H(z)$, predicted by this model, together with the data set extracted from *differential* galaxy ages. We also show the curve given by the ΛCDM model (with $\Omega_M = 0.315$ and $\Omega_\Lambda = \Omega_M - 1$) for comparison. The best-fit values of Λ and α give a shift parameter $R = 1.36$. The logarithmic derivative of the growth factor, $f(z)$, is shown in Fig. 51 together with the data given in Tab. 5.2 (for a typical scale $k_0 = 0.1h$/Mpc as in the previous models). In this case, deviations of the growth of matter perturbations from the ΛCDM model are small, in agreement with the results of the best-fit analysis. Indeed, high precision future geometrical probes could reduce the model to a negligible perturbation of the ΛCDM model.
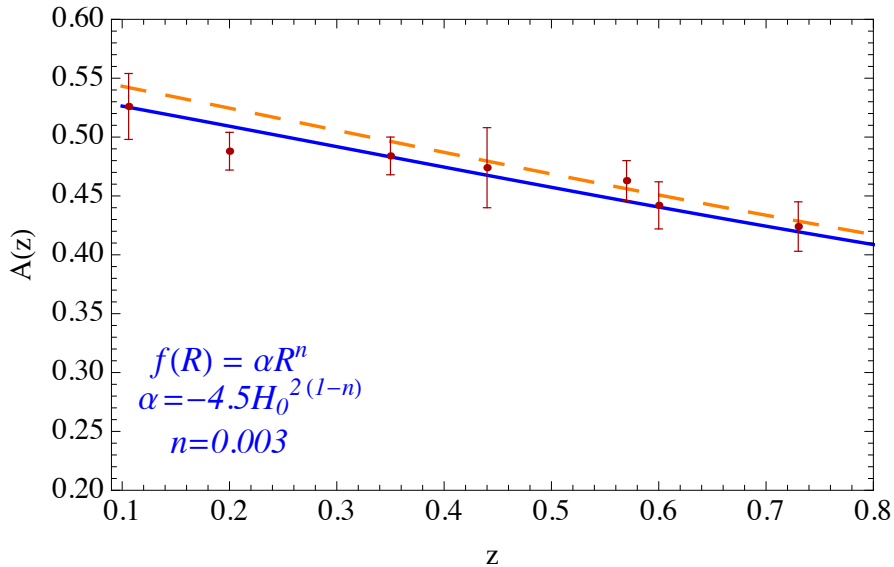
Figure 43: **Acoustic parameter of type 3 model**. The blue line shows the BAO parameter $A(z)$ of an expansion history described by the model of Eq. (5.26), with $\alpha = -4.5\bar{H}_0^{2(1-n)}$ and $n = 0.003$. The orange dashed line shows $A(z)$, of the ΛCDM model (with $H_0 = 67.3$ km/sec/Mpc, $\Omega_M = 0.315$ and $\Omega_\Lambda = \Omega_M - 1$) for comparison. The data points are given by the data set given in Tab. 5.1.

5.5.2   Type 5

As we have introduced in Sec. 4.2.5, it is convenient to parametrize the HS family of models,

$$f(R) = -M^2 \frac{c_1(\frac{R}{M^2})^n}{1 + c_2(\frac{R}{M^2})^n} , \qquad (5.28)$$

in terms of the parameters n and f_{R0} given by Eq. (4.59). The relation of these parameters with c_1 and c_2 is given by Eqs. (4.56)-(4.57). We have previously discussed that in the limit $f_{R0} \to 0$ the model of Eq. (4.45) converges to a cosmological constant. We have also mentioned that f_{R0} is constrained to be $| f_{R0} | < 0.1$ by solar system tests and we will not consider larger values of this parameter in our data analysis. We investigate the parameter region shown in Fig. 52 where we show the resulting CL contours for χ^2_{dis} (full colors) and χ^2_{growth} (red lines). Distances-only-data prefers smaller (more negative) values of f_{R0}, even smaller than those permitted by solar system tests. By contrast, the growth χ^2 prefers larger values of f_{R0} closer to 0. The dependence of χ^2_{dis} on n is relatively weak, while χ^2_{growth} prefers higher values of n. The best-fit value of the distances-only analysis is denoted by a star and corresponds to $n = 8.6$ and $f_{R0} = -0.1$ with $\chi^2_{min} = 544.33$ for 572 d.o.f.. The ΛCDM universe as a limiting case when $f_{R0} \to 0$ is consistent with the results shown in Fig. 52. For the best-fit ΛCDM we have $\chi^2_{dist}(\Lambda\text{CDM}) = 563.9$ (for 574 d.o.f.), and the χ^2_{dist} for the HS
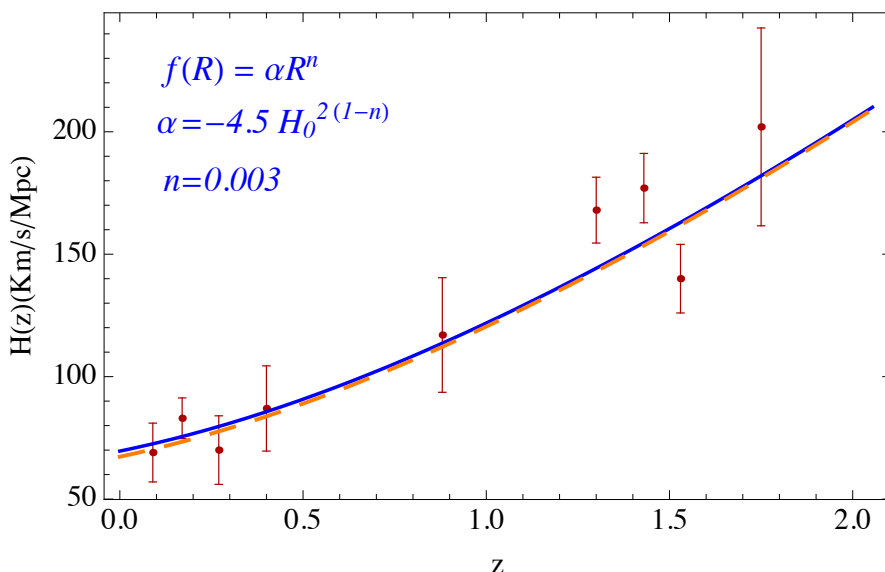
120

Figure 44: **Hubble parameter from galaxy ages of type 3 model**. The blue line shows the Hubble parameter, $H(z)$, of an expansion history described by the model of Eq. (5.26), for $\alpha = -4.5\bar{H}_0^{2(1-n)}$ and $n = 0.003$. The orange dashed line shows the Hubble parameter, $H(z)$, of the ΛCDM model (with $H_0 = 67.3$ km/sec/Mpc, $\Omega_M = 0.315$ and $\Omega_\Lambda = \Omega_M - 1$) for comparison. The data points are given by the data set extracted from *differential* galaxy ages.

model approaches this value as $f_{R0} \to 0$ (*e.g.* at $n = 6$ and $f_{R0} = -0.001$ it is 563.1). In the case of growth of structure, the convergence to a ΛCDM model is achieved for much smaller values of $|f_{R0}|$. While $\chi^2_{growth} \geq 14.92$ in the entire parameter region of Fig. 52 in which $f_{R0} \leq -0.001$ (*i.e.*, $|f_{R0}| \geq 0.001$), we have checked that, *e.g.*, for $f_{R0} = -10^{-7}$ (and $4 \leq n \leq 5$), $\chi^2_{growth} = 6.67$ which is very close to 6.65, the χ^2_{growth} value (for 8 d.o.f.) obtained from the ΛCDM equations (for both the background and the growth of structure) when starting from the same initial conditions used for the analysis of the HS model.

Figure 52 shows that the 99.7 % CL region of χ^2_{dis} overlaps with the 99.7 % CL region of χ^2_{growth}. Since there is no tension between the allowed regions by distances-only-data and the regions allowed by growth of structure data, we compute χ^2_{tot} given by Eq. (5.23), which is shown in Fig. 53. For comparison we also show the contour corresponding to the $\chi^2_{tot}(\Lambda\text{CDM})=570.84$ (for 582 d.o.f.) (see Tab. 5.3) (yellow dashed line), which is within the 95.4% contour of the χ^2_{tot} for the HS model. When considering all data sets, there are still parameter regions of the HS model (Eq. (4.45)), with f_{R0} significantly different from 0, which fits better the data than the ΛCDM model, as it happens with distances-only-data. However, the $\chi^2(\Lambda\text{CDM})$ value computed here has been obtained by fixing all the parameters of the model, *i.e.*, H_0 and Ω_M. The best-fit
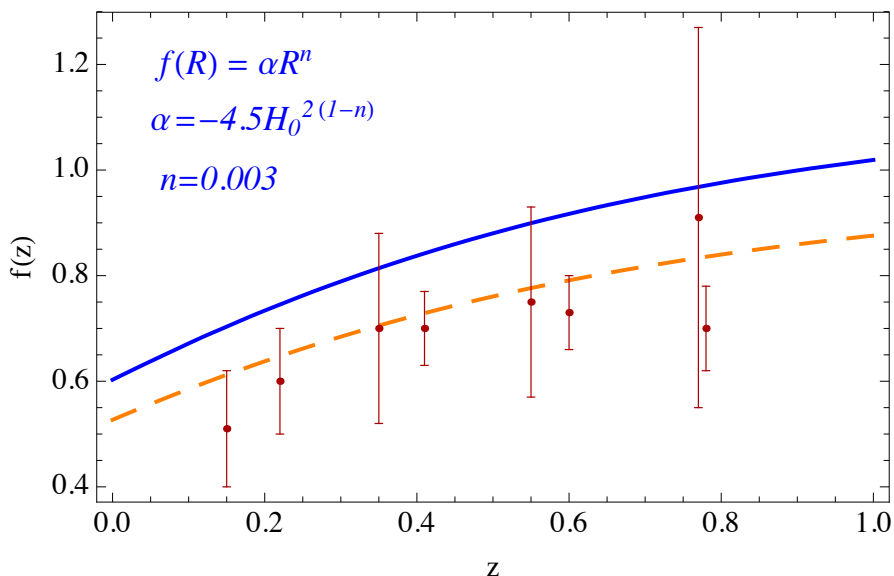
Figure 45: **Logarithmic derivative of the linear growth factor of type 3 model**. The blue curve denotes the predictions for the logarithmic derivative of the linear growth factor, $f(z)$, for $k_0 = 0.1h/\text{Mpc}$ of the Eq. (5.26) model together with the current available data on $f(z)$ given in Tab. 5.2. The $f(z)$ function corresponding to the ΛCDM model is also shown for comparison (dashed, orange line). The parameters are expressed in terms of $\bar{H}_0$, being $\bar{H}_0 = 72$ km/s/Mpc.

value of the parameters corresponding to the global analysis is $n = 10, f_{R0} = -0.1$ with $\chi^2_{min} = 565$ for 580 d.o.f.. We note that, since the minimum $\chi^2_{growth} = 14.92$ for 6 d.o.f., its p-value is $p < 0.1$, giving a bad fit to growth of structure data in the studied parameter region. As we have shown, growth of structure data prefers larger values of f_{R0}, closer to 0, while distances-only-data prefers smaller ones ($f_{R0} < -0.1$). This result suggests that future, more accurate data on the growth of structure could provide tighter bounds in the parameter regions allowed by growth data. If the model cannot fit simultaneously distances data and future growth of structure data it could potentially be ruled out.

With the best-fit value of the parameters obtained from the global analysis of the HS model, $n = 10$ and $f_{R0} = -0.1$, we now compute numerically the theoretical curves corresponding to each of the observables used in the analysis, namely, the distance moduli, $\mu(z)$ (Eq. (2.70)), the acoustic parameter, $A(z)$ (Eq. (5.8)), the Hubble parameter and the logarithmic derivative of the linear growth factor, f (Eq. (5.1.5)). In Figs. 54-57, we show these curves (blue lines) together with the data points in each case and the ΛCDM curve for comparison (orange lines). The shift parameter, R (Eq. (5.6)), is given by $R_{HS} = 1.750$ while $R_{\Lambda CDM} = 1.758$ (the measured value is $R = 1.7407 \pm 0.0094$). In particular, we can clearly appreciate from Fig. 55 that the HS
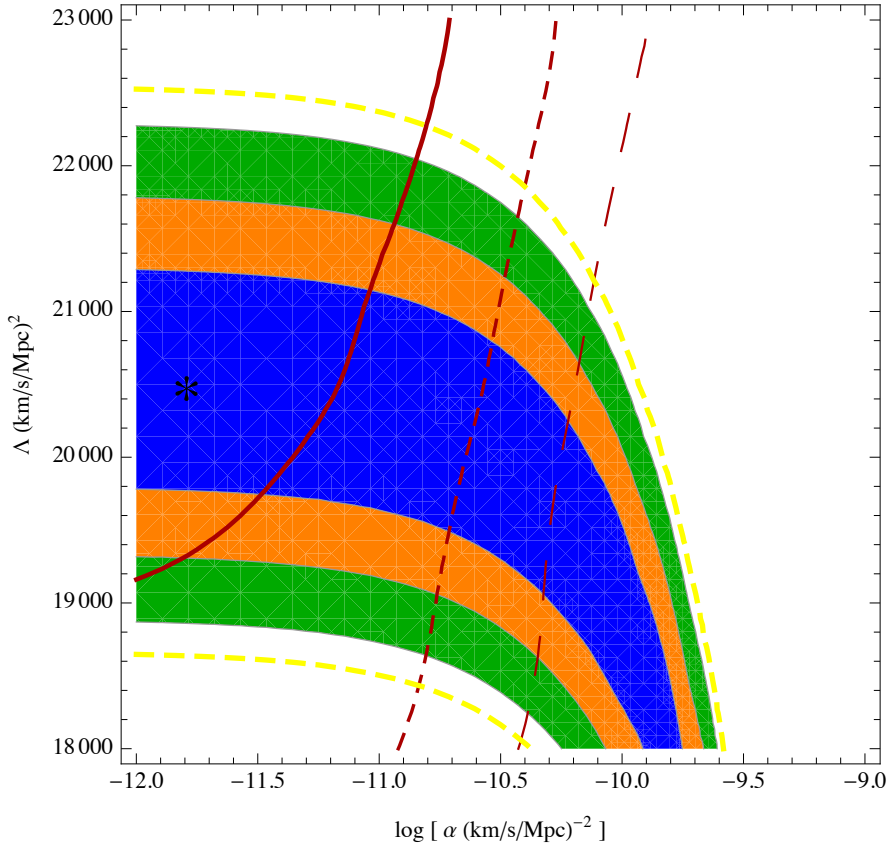
Figure 46: **Data analysis of type 4 model**. Full regions correspond to the 68.3%, 95.4% and 99.7 % CL of the χ^2_{dis} analysis in the (α, n) parameter space of the modified gravity model of Eq. (5.27) $(\alpha\Lambda \ll 1)$. The best-fit value of the geometrical probes analysis is marked with a star $(\log[\alpha \; (\mathrm{km/s/Mpc})^{-2}] = -11.8, \; \Lambda = 20483 \; (\mathrm{km/s/Mpc})^2)$. Red lines correspond to the 68.3% (solid), 95.4% (short dashed) and 99.7 % (large dashed) CL contours of the χ^2_{growth} analysis.

model with $n = 10$ and $f_{R0} = -0.1$ fits better the BAO data than the ΛCDM model, as expected from the χ^2 analysis. On the other hand, the ΛCDM model, even with all the parameters fixed, fits better the growth of structure data than the HS model for the best-fit value of the parameters, in agreement with the χ^2 analysis. To test the ΛCDM limit of the HS model as $f_{R0} \to 0$, we have checked the previous curves evaluated for different points on the upper line of the parameter grid, namely for $f_{R0} = -0.001$ and different values of n. For the distance moduli, the acoustic parameter and the Hubble parameter, these curves fully agree with the ΛCDM prediction, shown in Figs. 54-56 (orange lines); for the shift parameter we obtain $R = 1.758$, which also agree with the ΛCDM prediction. By contrast, in the case of the logarithmic derivative of the growth of structure, f (see Fig. 57), the curve obtained for parameters on the upper line (*i.e.*, for $f_{R0} = -0.001$) is not very different from the blue curve obtained for the best-fit HS
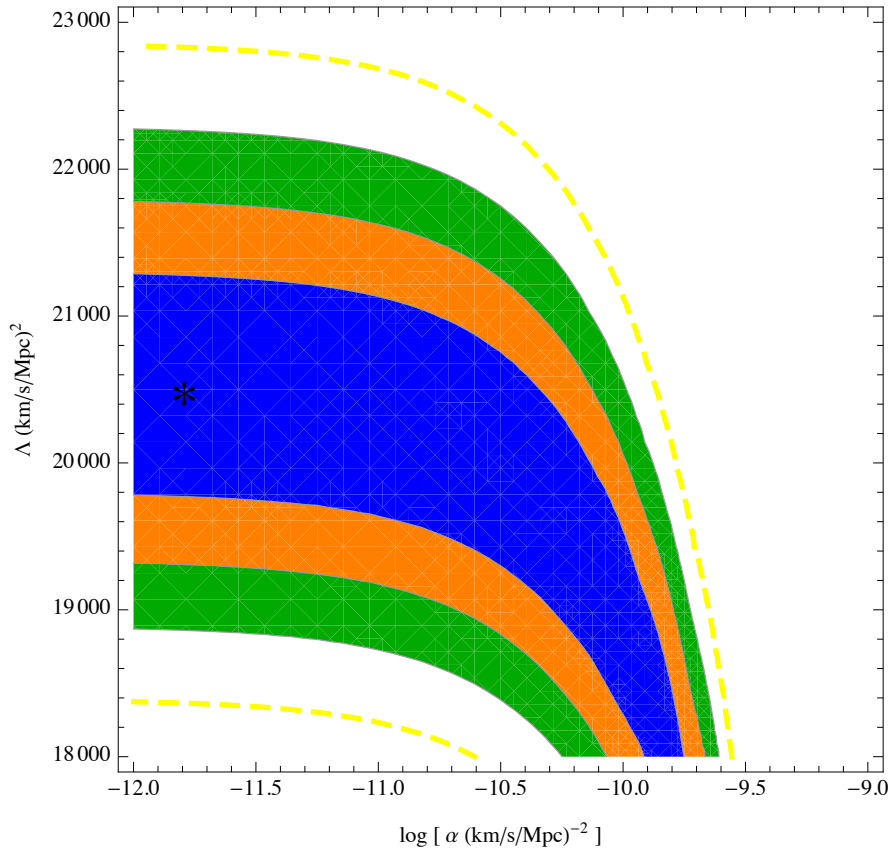
Figure 47: **Global data analysis of type 4 model**. Full regions correspond to the 68.3%, 95.4% and 99.7 % CL of the χ^2_{tot} analysis in the (α, n) parameter space of the modified gravity model of Eq. (5.27). The best-fit point of the global analysis is marked with a star.

model with $n = 10$ and $f_{R0} = -0.01$. This is because, in the case of the growth, the ΛCDM limit is recovered for much smaller values of $\mid f_{R0} \mid$, $\sim 10^{-7}$ (for such values, the curve indeed approximates well the ΛCDM curve).

5.6 Solar System Constraints

We have shown in the previous sections that only models of type 4 and 5 are allowed by the cosmological data considered here after combining measurements of several geometrical probes with linear growth data. In Chapter 3 we have described under which conditions $f(R)$ models pass solar system tests. In this section we study whether models of type 4 and 5 are allowed by solar systems constraints in the parameter region resulting from the cosmological data analyses.
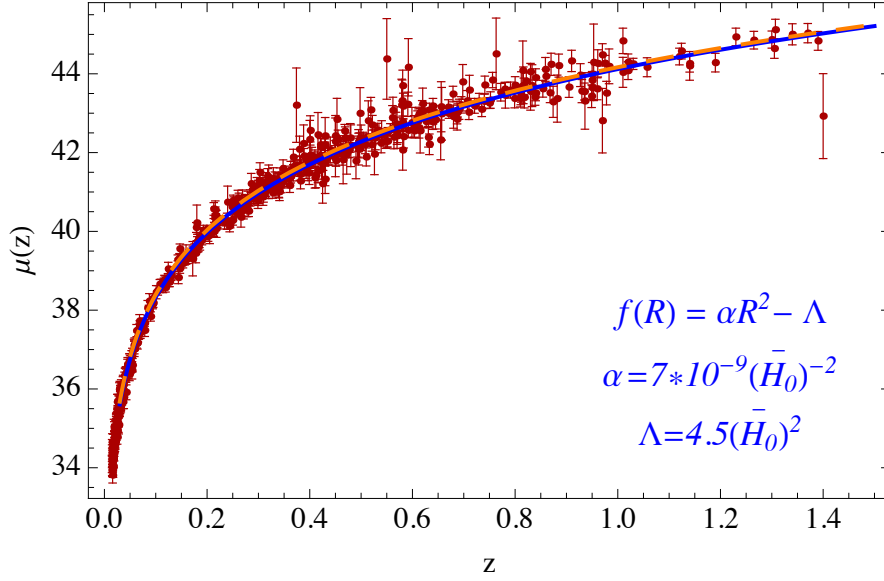
Figure 48: **Distance moduli of type 4 model**. The blue line shows the distance moduli of an expansion history described by the model of Eq. (5.27). The orange dashed line shows the distance moduli of the ΛCDM model (with $H_0 = 67.3$ km/sec/Mpc, $\Omega_M = 0.315$ and $\Omega_\Lambda = \Omega_M - 1$) for comparison. The data points are given by the Union Compilation 2 data set.

5.6.1 Type 4

For this model we have $f_R = 2\alpha R$ and Eq. (3.49) becomes

$$\nabla^2 f_R - \frac{1}{6\alpha} f_R = -\frac{\kappa^2 \rho + 2\Lambda}{3}, \qquad (5.29)$$

or equivalently

$$6\alpha \nabla^2 R - R + 2\Lambda = -\kappa^2 \rho. \qquad (5.30)$$

Taking into account the best-fit value of Λ from the previous chapter, we notice that Λ/κ^2 is of the order of the average matter density at cosmological scales, which is $\sim 10^{-30}$g/cm^3, while the value of the average matter density in our galaxy (and in the solar vicinity) is $\sim 10^{-24}$g/cm^3 (and much higher inside the Sun). Thus in the solar system, the term $\kappa^2 \rho$ in the r.h.s. of Eq. (5.29) is everywhere much larger than 2Λ (by at least $\sim 10^6$) , and we can safely ignore the latter. Thus, in the following we solve

$$6\alpha \nabla^2 R - R = -\kappa^2 \rho. \qquad (5.31)$$

which can be solved exactly, but before giving the full solution, we address the two limiting cases, the high curvature regime and the low one. Since $f_{RR} = 2\alpha$, the Compton wavelength of this model is given by $\lambda_{f_R} = \sqrt{6\alpha}$ (see Eq. (3.63)). We first
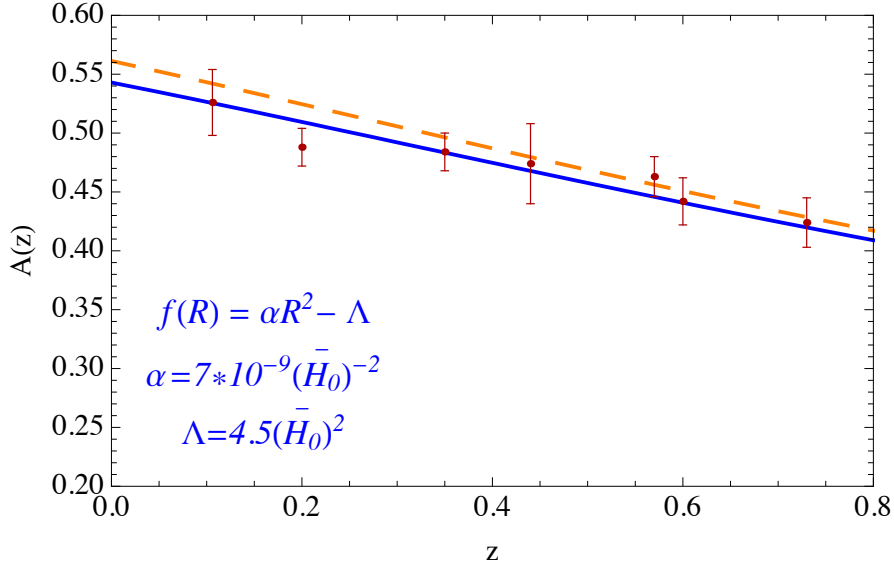
125

Figure 49: **Acoustic parameter of type 4 model**. The blue line shows the BAO parameter $A(z)$ of an expansion history described by the model of Eq. (5.27). The orange dashed line shows $A(z)$, of the ΛCDM model (with $H_0 = 67.3$ km/sec/Mpc, $\Omega_M = 0.315$ and $\Omega_\Lambda = \Omega_M - 1$) for comparison. The data points are given by the data set given in Tab. 5.1.

consider the limit in which the Compton wavelength is much smaller that the length at which the matter density changes, such that the Compton condition is satisfied. This corresponds to $\sqrt{6\alpha} \ll r_\odot$, and the solution to Eq. (5.31) is $R(r) \approx \kappa^2\rho(r)$, which is the GR solution. On the other hand, in the limit $\sqrt{6\alpha} \gg r_\odot$, the solution to Eq. (5.31) is given by

$$R(r) - R_\infty = \frac{\kappa^2 M_\odot}{4\pi r_\odot} \frac{1}{6\alpha} \begin{cases} \frac{1}{r} & r > r_\odot; \\ \frac{1}{2r_\odot}\left(3 - \frac{r^2}{r_\odot^2}\right) & r \leq r_\odot. \end{cases} \tag{5.32}$$

More generally, since Eq. (5.31) is linear, by assuming a step function for $\rho(r)$ (and ignoring the effect of ρ_g), the solution is given by the linear superposition of contributions from all point charges $\rho(\mathbf{x})d\mathbf{x}^3$, each contributing to the Yukawa kernel, leading to

$$R(\boldsymbol{r}) - R_\infty = \int \frac{e^{-|\tilde{\boldsymbol{r}} - \tilde{\mathbf{x}}|}}{|\tilde{\boldsymbol{r}} - \tilde{\mathbf{x}}|}\kappa^2(\rho(\tilde{\mathbf{x}}) - \rho_\infty)d\tilde{\mathbf{x}}^3, \tag{5.33}$$

where $\tilde{\boldsymbol{r}} = \boldsymbol{r}/\sqrt{6\alpha}$ and $\tilde{\mathbf{x}} = \mathbf{x}/\sqrt{6\alpha}$. Assuming a step-like profile for the density: $\rho(\mathbf{x}) = \rho_\odot$ for $|\mathbf{x}| \leq r_\odot$ and $\rho(\mathbf{x}) = \rho_\infty$ for $|\mathbf{x}| > r_\odot$, we obtain

$$R(r) - R_\infty = \kappa^2\rho_\odot \begin{cases} \frac{e^{-\tilde{r}}}{\tilde{r}}\left[\tilde{r}_\odot \cosh\tilde{r}_\odot - \sinh\tilde{r}_\odot\right] & r > r_\odot; \\ \left[1 - e^{-\tilde{r}_\odot}(1 + \tilde{r}_\odot)\frac{\sinh\tilde{r}}{\tilde{r}}\right] & r \leq r_\odot, \end{cases} \tag{5.34}$$
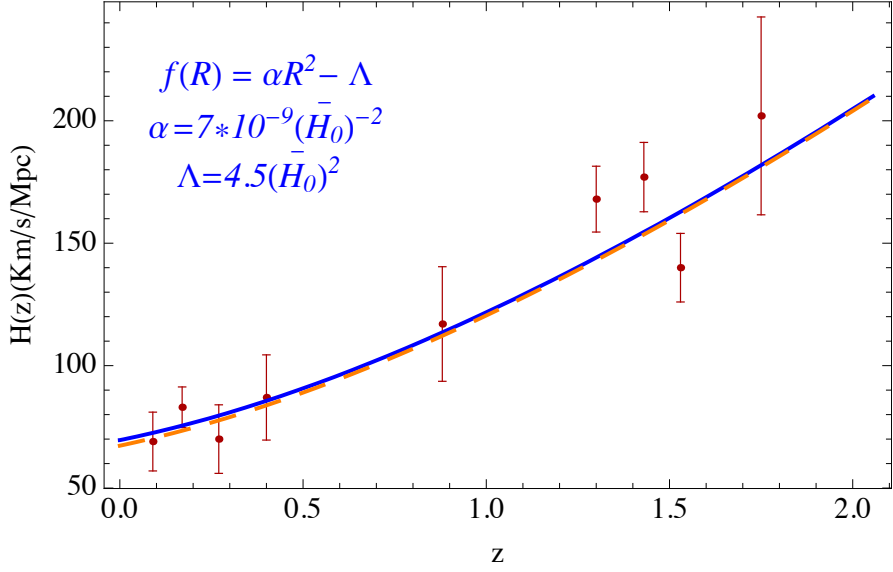
126

Figure 50: **Hubble parameter from galaxy ages of type 4 model**. The blue line shows the Hubble parameter, $H(z)$, of an expansion history described by the model of Eq. (5.27). The orange dashed line shows the Hubble parameter, $H(z)$, of the ΛCDM model (with $H_0 = 67.3$ km/sec/Mpc, $\Omega_M = 0.315$ and $\Omega_\Lambda = \Omega_M - 1$) for comparison. The data points are given by the data set extracted from *differential* galaxy ages.

where $\tilde{r} \equiv r/\sqrt{6\alpha}$ and $\tilde{r}_\odot \equiv r_\odot/\sqrt{6\alpha}$, and we have ignored ρ_∞ compared to $\rho_\odot$. Consider now Eq. (3.51) for this model,

$$\nabla^2 \mathcal{B} = -\frac{-\kappa^2 \rho + R(1 + \frac{9}{4}\alpha R) + \frac{\Lambda}{4}}{3(1 + 2\alpha R)} . \qquad (5.35)$$

First let us show that we can neglect all terms $\sim \alpha R$ in the r.h.s. of Eq. (5.35). From Eq. (5.34) is easy to see that the maximum of $R(r)$ always occurs at $r = 0$ (and $R(r) > 0$ everywhere), and is given by

$$R_{\max} = R(r = 0) = \kappa^2 \rho_\odot \left[1 - e^{-\tilde{r}_\odot} (1 + \tilde{r}_\odot) \right] , \qquad (5.36)$$

where we have ignored R_∞. Using

$$\kappa^2 \rho_\odot = \frac{8\pi G}{c^2} \frac{3M_\odot}{4\pi r_\odot^3} = \frac{GM_\odot}{c^2 r_\odot} \frac{6}{r_\odot^2}, \qquad (5.37)$$

we see that $\alpha R(r) \leq \frac{GM_\odot}{c^2 r_\odot} \frac{1}{\tilde{r}_\odot^2} \left[1 - e^{-\tilde{r}_\odot} (1 + \tilde{r}_\odot) \right]$. For any value of $\tilde{r}_\odot = r_\odot/\sqrt{6\alpha}$ we have $0 \leq \frac{1}{\tilde{r}_\odot^2} \left[1 - e^{-\tilde{r}_\odot} (1 + \tilde{r}_\odot) \right] \leq \frac{1}{2}$ and we obtain

$$2\alpha R(r) \leq \frac{GM_\odot}{c^2 r_\odot} = 2.12 \times 10^{-6} . \qquad (5.38)$$
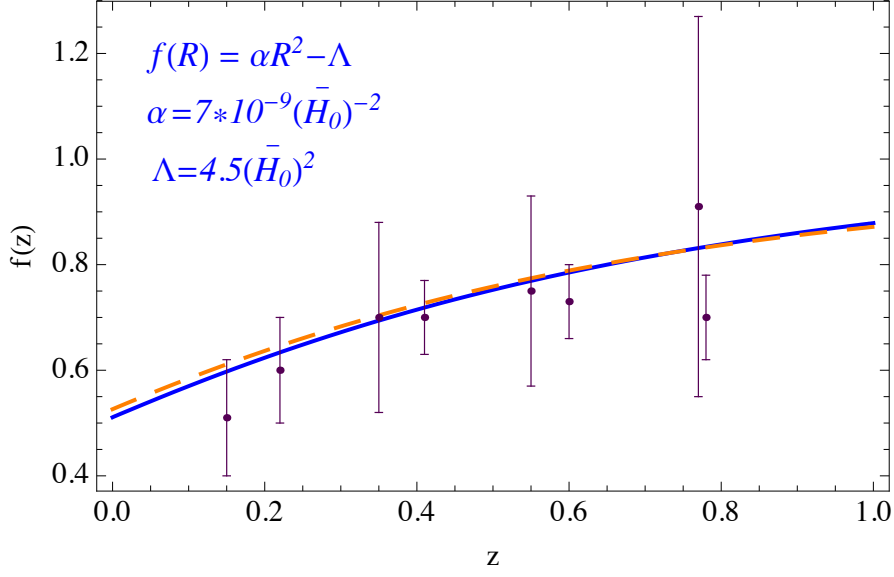
127

Figure 51: **Logarithmic derivative of the linear growth factor of type 4 model**. The blue curve denotes the predictions for the logarithmic derivative of the linear growth factor, $f(z)$, for $k_0 = 0.1h/\text{Mpc}$ of the model given by Eq. (5.27), together with the current available data on $f(z)$, see Tab. 5.2. The $f(z)$ function corresponding to the ΛCDM model is also shown for comparison (dashed, orange line). The parameters are expressed in terms of $\bar{H}_0$, being $\bar{H}_0 = 67.3$ km/s/Mpc.

Thus, we can ignore all terms $\sim \alpha R$ in the r.h.s. of Eq. (5.35) [¶]. With the boundary condition $\mathcal{B} \to 0$ as $r \to \infty$, we must subtract the constant asymptotic value of the r.h.s. of Eq. (5.35) and, ignoring Λ, we can rewrite this equation as

$$-3\nabla^2 \mathcal{B} \approx (R(r) - R_\infty) - \kappa^2(\rho(r) - \rho_\infty). \tag{5.39}$$

Comparing Eq. (5.39) and Eq. (5.31) we see that $\mathcal{B}$ and $-2\alpha(R - R_\infty)$ satisfy the same equation with the same boundary condition and they can be identified. Thus, using Eq. (5.34) and Eq. (5.37) for $r > r_\odot$, we obtain

$$\mathcal{B}(r)\left(\frac{2GM_\odot}{c^2 r_\odot}\right)^{-1} = -\frac{[\tilde{r}_\odot \cosh \tilde{r}_\odot - \sinh \tilde{r}_\odot]\, e^{-\tilde{r}}}{\tilde{r}_\odot^2}\frac{}{\tilde{r}}. \tag{5.40}$$

At $r = r_\odot$, where Eq. (5.40) is maximized, we obtain

$$\mathcal{B}(r_\odot)\left(\frac{GM_\odot}{c^2 r_\odot}\right)^{-1} = 2\frac{\tilde{r}_\odot \cosh \tilde{r}_\odot - \sinh \tilde{r}_\odot}{\tilde{r}_\odot^3}e^{-\tilde{r}_\odot} = \frac{\tilde{r}_\odot(1 + e^{-2\tilde{r}_\odot}) - 1 + e^{-2\tilde{r}_\odot}}{\tilde{r}_\odot^3}. \tag{5.41}$$

[¶]Notice that incorporating 2Λ or $\kappa^2\rho_0 = 3\Omega_m H_0^2$ does not modify this argument, since we know that $\alpha\Lambda \sim \alpha H_0^2 \ll 1$.
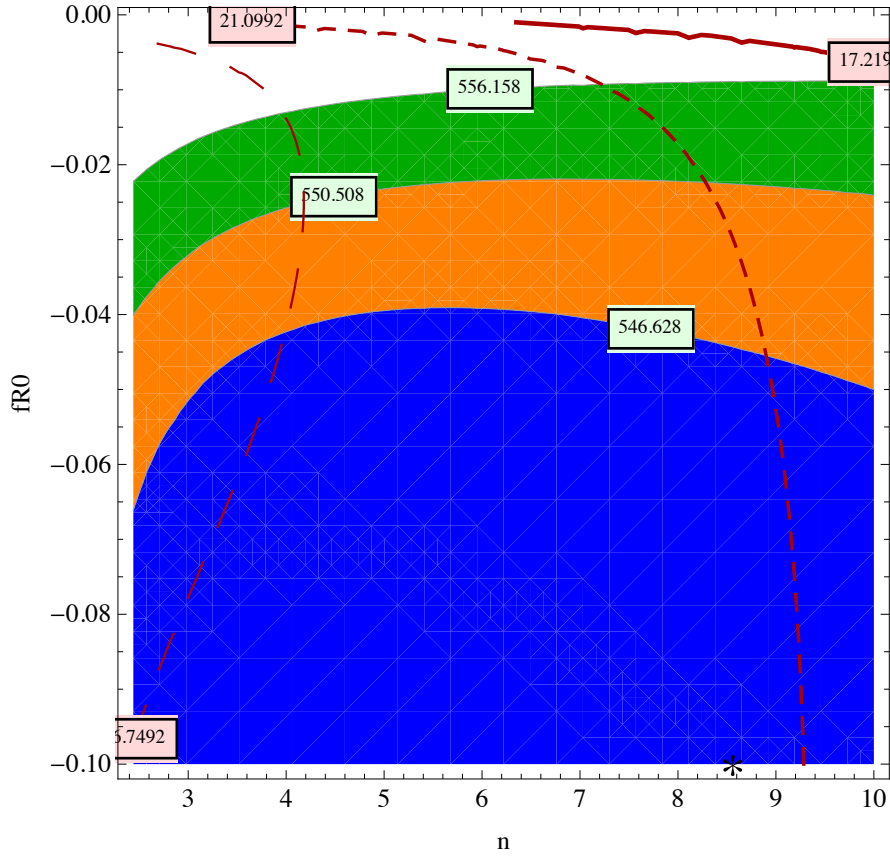
Figure 52: χ^2_{dis} **and** χ^2_{growth} **for the HS model**. Full regions correspond to the 68.3% (blue), 95.4% (orange) and 99.7 % (green) CL of χ^2_{dis} and red lines correspond to the 68.3% (solid), 95.4% (short dashed) and 99.7 % (long dashed) CL contours of χ^2_{growth} in the (n, f_{R0}) parameter space for the modified gravity model of Eq. (4.45). The best-fit value of the parameters given by distances-only is marked with a star and corresponds to $(8.56, -0.1)$ with $\chi^2_{dis} = 544.33$ for 572 d.o.f..

The r.h.s. of Eq. (5.41) is always smaller than 2/3 (value which happens for $\tilde{r}_\odot = 0$, *i.e.*, in the low-curvature regime where $\lambda_{f_R} \gg r_\odot$), however in order to satisfy the Cassini mission constraint, it must be smaller than 2.3×10^{-5}, the bound on $|\gamma - 1|$. The r.h.s. of Eq. (5.41) becomes small when $\tilde{r}_\odot \gg 1$, *i.e.*, when $r_\odot \gg \lambda_{f_R} = \sqrt{6\alpha}$ and the Compton condition is satisfied. In such limit the r.h.s. is well approximated by $\frac{1}{\tilde{r}_\odot^2}$. Thus, in order to satisfy the Cassini mission constraint we need

$$\frac{1}{\tilde{r}_\odot^2} \sim |\gamma - 1| < 2.3 \times 10^{-5}. \tag{5.42}$$

Since $\tilde{r}_\odot \equiv r_\odot/\sqrt{6\alpha}$, Eq. (5.42) leads to

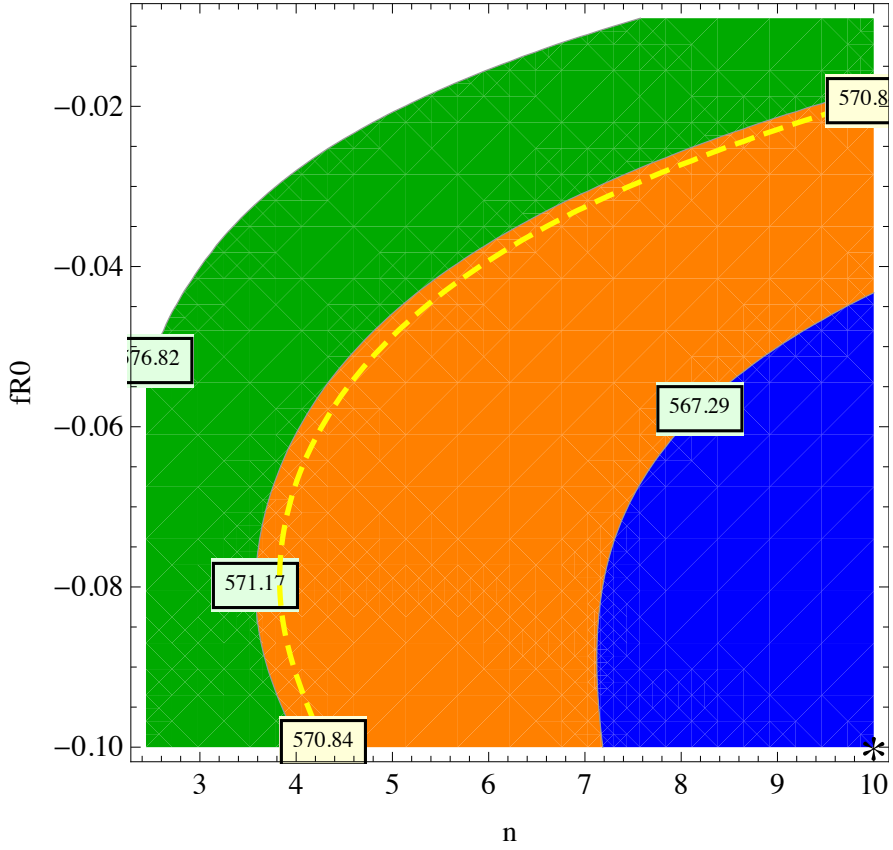$$\alpha < 3.83 \times 10^{-6} r_\odot^2. \tag{5.43}$$

129

Figure 53: **Global data analysis of the Hu and Sawicki model**. Full contours correspond to the 68.3% (blue), 95.4% (orange) and 99.7 % (green) allowed CL regions of χ^2_{tot} for the modified gravity model of Eq. (4.45). In the parameter space region considered in the analysis, the best-fit value of the parameters is marked with a star and corresponds to $(n = 10, f_{R0} = -0.1)$ with $\chi^2_{min} = 564.99$ for 580 d.o.f.. The dashed contour corresponds to best-fit ΛCDM value, $\chi^2_{tot}(\Lambda\text{CDM}) = 570.84$ for 582 d.o.f..

Converting Eq. (5.43) into units of H_0^{-2} with $r_\odot = 2.254 \times 10^{-14}$ Mpc and by using Eq. (2.14), we obtain

$$\alpha < 2.15h^2 \times 10^{-40} H_0^{-2} \approx 10^{-41} H_0^{-2} \tag{5.44}$$

which is about 32 orders of magnitude smaller than the cosmologically best-fit value of α obtained in the previous section. In conclusion, solar system constraints impose a strong bound on the size of α, effectively rendering unobservable any deviation from the ΛCDM model (at cosmological and local levels). This is ultimately due to the fact that this model does not have a chameleon mechanism: the field's Compton wavelength is not density-dependent. Therefore, the model would be compatible with solar system constraints only if the field's Compton wavelength was much smaller than the Sun's radius everywhere, in which case the field would become negligible at cosmological
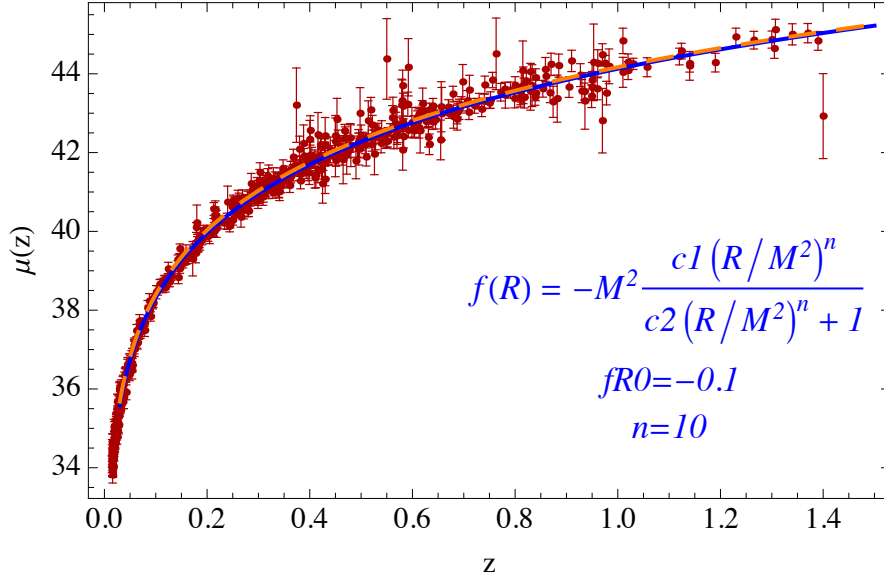
Figure 54: **Distance moduli of type 5 model**. The blue line shows the distance moduli of the expansion history described by the model of Eq. (5.28) for the best-fit value of the parameters obtained from the global analysis, $n = 10, f_{R0} = -0.1$. The orange dashed line shows the distance moduli of the ΛCDM model (with $H_0 = 67.3$ km/sec/Mpc, $\Omega_M = 0.315$ and $\Omega_\Lambda = \Omega_M - 1$) for comparison. The data points are given by the Union Compilation 2 data set.

scales.

5.6.2 Type 5

As we mentioned in the previous chapter, this type of models were proposed by W. Hu and I. Sawicki in [70], where they studied the solar system constraints on the model's free parameters. In this type of models, unlike in the previous one, the dynamical field equation Eq. (3.49) is non-linear and W. Hu and I. Sawicki have performed a numerical analysis to obtain approximated solutions. In the following we summarize the results presented in [70]. Let us rewrite the field equation, Eq. (4.54), in terms of R_0 and f_{R0}, given by Eqs. (4.53) and (4.59) respectively, such that

$$f_R = f_{R0} \left(\frac{R_0}{R} \right)^{n+1} . \tag{5.45}$$

Since

$$f_{RR} = -(n+1) \frac{f_{R0}}{R_0} \left(\frac{R_0}{R} \right)^{n+2} , \tag{5.46}$$
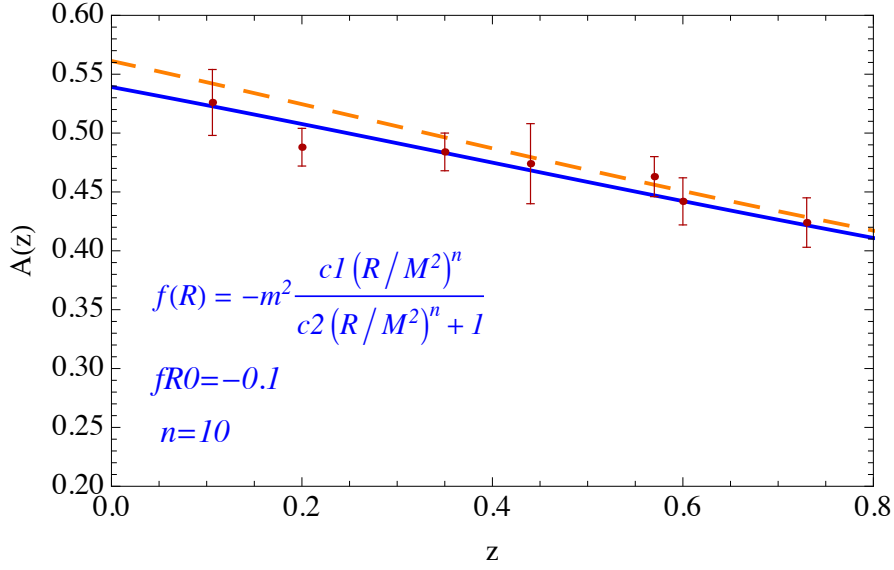
131

Figure 55: **Acoustic parameter of type 5 model**. The blue line shows the BAO parameter $A(z)$ of an expansion history described by the model of Eq. (5.28) for the best-fit value of the parameters obtained from the global analysis, $n = 10$, $f_{R0} = -0.1$. The orange dashed line shows $A(z)$, of the ΛCDM model (with $H_0 = 67.3$ km/sec/Mpc, $\Omega_M = 0.315$ and $\Omega_\Lambda = \Omega_M - 1$) for comparison. The data points are given by the data set given in Tab. 5.1.

the Compton wavelength for this model is given by (see Eq. (3.63))

$$\lambda_{f_R} = \left(3(n+1) \frac{|f_{R0}|}{R_0} \right)^{\frac{1}{2}} \left(\frac{R_0}{R} \right)^{\frac{n+2}{2}}, \tag{5.47}$$

which we can rewrite as

$$\lambda_{f_R} = \left(\frac{3(n+1) \mid f_{R0} \mid}{M^2} \right)^{\frac{1}{2}} \left(\frac{R_0}{M^2} \right)^{\frac{n+1}{2}} \left(\frac{M^2}{R} \right)^{\frac{n+2}{2}}. \tag{5.48}$$

The mass scale, M^2 is set to be

$$M^2 = \tilde{H}_0^2 \tilde{\Omega}_M \approx (8018 \times 10^6 \, \text{pc})^{-2} \left(\frac{h^2 \tilde{\Omega}_M}{0.14} \right), \tag{5.49}$$

and

$$\frac{\kappa^2 \rho}{M^2} \approx 1.14 \times 10^6 \left(\frac{\rho}{10^{-24} \text{gr cm}^{-3}} \right) \left(\frac{h^2 \tilde{\Omega}_M}{0.14} \right)^{-1}. \tag{5.50}$$
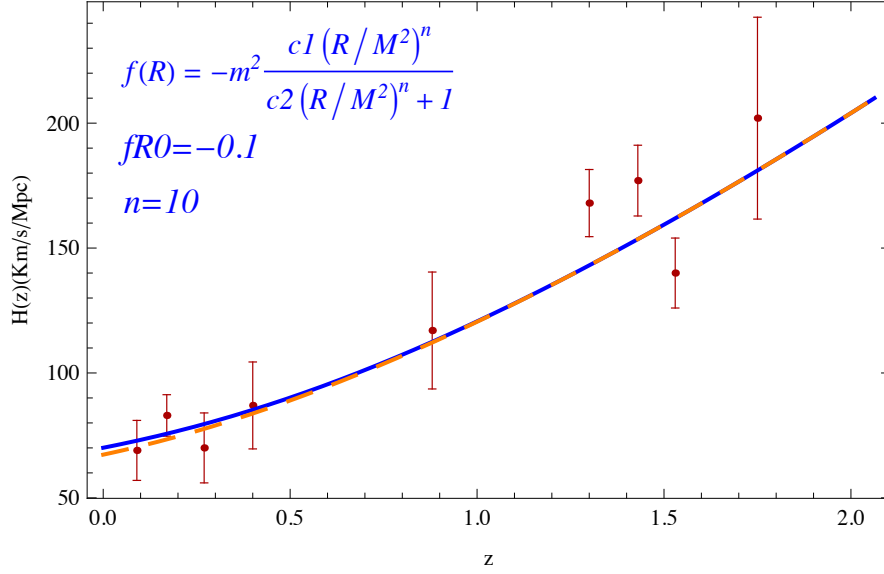
132

Figure 56: **Hubble parameter from galaxy ages of type 5 model**. The blue line shows the Hubble parameter, $H(z)$, of an expansion history described by the model of Eq. (5.28) for the best-fit value of the parameters obtained from the global analysis, $n = 10$, $f_{R0} = -0.1$. The orange dashed line shows the Hubble parameter, $H(z)$, of the ΛCDM model (with $H_0 = 67.3$ km/sec/Mpc, $\Omega_M = 0.315$ and $\Omega_\Lambda = \Omega_M - 1$) for comparison. The data points are given by the data set extracted from *differential* galaxy ages.

Thus, the Compton wavelength at $R = \kappa^2 \rho$ is given by

$$\lambda_{f_R} = \quad (11.4\text{pc}) \left(8.77 \times 10^{-7}\right)^{\frac{n-1}{2}} [(n+1) \mid f_{R0} \mid]^{\frac{1}{2}} \tag{5.51}$$

$$\left(\frac{R_0}{M^2} \frac{h^2 \, \tilde{\Omega}_M}{0.14}\right)^{\frac{n+1}{2}} \left(\frac{\rho}{10^{-24}\text{gr cm}^{-3}}\right)^{-\frac{n+2}{2}}. \tag{5.52}$$

Resulting from the simulation performed in [70], the authors find that, for standard values of the cosmological parameters, $h = .74$ and $\tilde{\Omega}_M = 0.24$, and for $n = 4$, the Compton condition is well satisfied in the whole solar density profile for an amplitude of $\mid f_{R0} \mid \leq 10^{-2}$ and the thin-shell condition is satisfied up to $\mid f_{R0} \mid \leq 10^{-1}$ in the solar corona. We note that the Compton wavelength given by Eq. (5.51) decreases rapidly as n increases while the dependence on the amplitude $\mid f_{R0} \mid$ is much weaker. For instance, in the solar corona where $\rho \approx 10^{-15}$ gr cm^{-3}, the Compton wavelength for the best-fit value of n obtained in the previous section, $n = 10$, is $\lambda_{f_R} \sim 10^{-63} \mid f_{R0} \mid^{1/2} r_\odot$ while for $n = 4$ is $\lambda_{f_R} \sim 10^{-23} \mid f_{R0} \mid^{1/2} r_\odot$. Thus, we expect the Compton condition to be well satisfied for the best-fit value of the parameters obtained in the previous section.

A constraint on the cosmological field value of this model is obtained from the
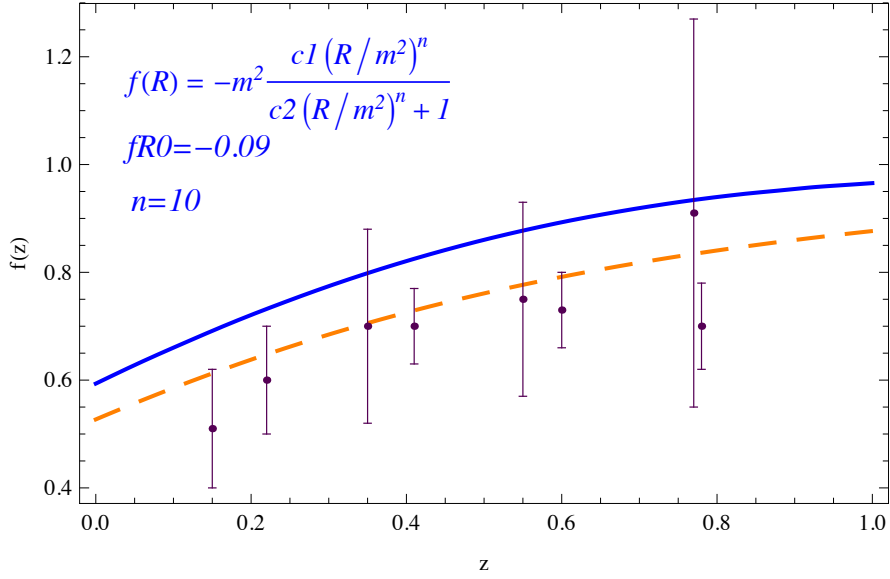
133

Figure 57: **Logarithmic derivative of the linear growth factor of type 5 model**.
The blue curve denotes the predictions for the logarithmic derivative of the linear
growth factor, $f(z)$, for $k_0 = 0.1h/\text{Mpc}$ of the Eq. (5.28) model or the best-fit value
of the parameters obtained from the global analysis, $n = 10$, $f_{R0} = -0.1$ together with
the current available data on $f(z)$ given in Tab. 5.2. The $f(z)$ function corresponding
to the ΛCDM model is also shown for comparison (dashed, orange line).

thin-shell condition given by Eq. (3.80) by assuming that the galaxy has enough mass
and extension to keep the field at the minimum of its effective potential. The relation
between the cosmological field, f_{R0} and the galactic field, f_{Rg}, is

$$\frac{f_{R0}}{f_{Rg}} = \left(\frac{R_g}{R_0}\right)^{n+1}. \tag{5.53}$$

Assuming $R_g = \kappa^2 \rho_g$ and using Eq. (5.50) we obtain

$$\frac{f_{R0}}{f_{Rg}} = \left(1.14 \times 10^6\right)^{n+1} \left(\frac{\rho_g}{10^{-24}\text{gr cm}^{-3}}\right)^{n+1} \left(\frac{R_0}{M^2}\frac{h^2\,\tilde{\Omega}_M}{0.14}\right)^{-(n+1)}. \tag{5.54}$$

Taking into account that the galactic density is $\rho_g \approx 10^{-24}\text{gr cm}^{-3}$ and using the
constraint on the galactic field given in Eq. (3.80), the cosmological field value is
constrained to be

$$|f_{R0}| < 64 \left(1.14 \times 10^6\right)^{n-1} \left(\frac{R_0}{M^2}\frac{h^2\,\tilde{\Omega}_M}{0.14}\right)^{-(n+1)}, \tag{5.55}$$

which is an extremely weak constraint.

Chapter 6

Summary and Conclusions

In this thesis we have analyzed phenomenological $f(R)$ modified gravity models, as one alternative explanation for the dark energy phenomena, *i.e.* for the observed late acceleration in the expansion of the universe. We have studied the empirical viability of various $f(R)$ models against the observed cosmological and solar system constraints. Different types of $f(R)$ models with a well-behaved expansion history have been confronted with different cosmological data sets, finding an enormous potential to rule out $f(R)$ models when the geometrical probes are combined with the linear growth of structure data.

In Chapter 2 we described the standard cosmological model and highlighted the observational evidence supporting the current accelerated expansion of the universe. In Chapter 3 we introduced the field equations of $f(R)$ modified gravity models. We derived the modified Friedmann equations, as well as the dynamical equations describing the evolution of small perturbations around the homogeneous cosmological background in these models. We have also computed numerically the expansion history and the growth of structure formation for the different $f(R)$ cosmologies that we analyze in later chapters. We also discussed in Chapter 3 the slow-motion weak-field limit of $f(R)$ models and summarized under which conditions these models can pass the stringent constraints given by solar system tests.

In Chapter 4 we reproduced the analysis presented in [69], for the class of $f(R)$ models that are shown to be cosmologically viable. In addition, we have analyzed the Hu-Sawicki (HS) model [70, 71]. This analysis consists of a powerful methodology to study qualitatively the dynamical behavior of a homogeneous universe in $f(R)$ cosmologies and allows to classify $f(R)$ models according to their cosmological viability. In this approach, the modified Friedmann equations are reformulated in the form of an autonomous system of first order differential equations in which the only dependence on the specific $f(R)$ model is encoded in one function $m(r)$, where $m \equiv Rf_{RR}/(1+f_R)$ and $r \equiv -R(1+f_R)/(R+f)$ (with $f_R \equiv df/dR$). The geometrical properties of the $m(r)$ curve on the (r, m) plane determine whether the specific class of $f(R)$ models

are cosmologically viable. Crucially, the fixed points of the dynamical system can be identified with the different epochs of the universe expansion history through the value of the observable cosmological parameters (Ω_i and the effective equation of state, w_{eff}) at each of the fixed points. Their stability depends on the function $m(r)$, which allows to generalize the conditions under which a general $m(r)$ function, and hence a general class of $f(R)$ models, can reproduce a viable cosmological history according to observations. We analyzed five different type of models shown to be cosmologically viable in the mentioned literature, finding the constraints in the free parameters of each type of model which allow for a qualitatively well-behaved expansion history. This has provided the key to identify the models that possess a late-time accelerated expansion, as well as a long enough matter dominated epoch.

In Chapter 5, we have updated the analyses performed in our previously published work [85,120], using the most recent data from Baryonic Acoustic Oscillations (BAO), Cosmic Microwave Background (CMB) and the growth of structure. The values of the cosmological parameters have been also updated using the results revealed by Planck [2], which we kept fixed in our numerical fits.

The key feature of $f(R)$ modified gravity models is that, unlike in General Relativity (GR), the linear growth of structure is scale-dependent. This key feature opens the possibility of rendering these theories distinguishable from GR at cosmological scales, even though they yield an indistinguishable expansion history. Thus, for models with a viable expansion history, we have extended the analysis to first order in perturbations to compute their linear growth rate of structure. With this information, we have performed a quantitative analysis by confronting the predicted expansion history and linear growth of structure against cosmological data. Specifically, focusing on models with a well-behaved expansion history (as shown in Chapter 4), we quantitatively confronted their expansion history with SNIa data, the CMB shift parameter R, the BAO acoustic parameter $A(z)$ measurements and the $H(z)$ data derived from galaxy ages. We furthermore fitted the linear growth of structure in these $f(R)$ models to the linear growth rate information derived from measurements of redshift space distortions, as a novel approach. The most important result found in these analyses is that the combination of cosmological data used here possess an enormous potential to rule out modified gravity models.

Models of type 1, $f(R) = R^p \left[\log(\alpha R) \right]^q - R$ with $p = 1$ and $q > 0$, were shown by the qualitative analysis of Chapter 4 to reproduce a viable expansion history. However, from the quantitative data analysis in Chapter 5, we have found that data on the linear growth prefers much smaller values of the power index q than the ones preferred by distance measurements. Thus, these models badly fail in reproducing an acceptable growth of structure for the same value of the parameters for which they can reproduce an acceptable expansion history. Consequently, we conclude that they are statistically rejected at 4-σ confidence level by present data.

Models of type 2, $f(R) = R^p \exp(q/R) - R$ with $p = 1$, have a well-behaved

qualitative expansion history. Since this model has only one free parameter, q, to ensure a viable expansion history, in the data analysis we have considered Ω_M as a free parameter as well. These models include the standard ΛCDM model as a limiting case, with q playing the role of the cosmological constant. As expected, these models show a good fit to distance measurements, reproducing the ΛCDM prediction. However, with the data sets and the cosmological parameter values used in this analysis, we find tension at more than the 3-σ level between the parameter regions reproducing an acceptable expansion history and the regions preferred by growth data. This result is very different from the one we obtained in [85], in which we had considered poorer growth and BAO data sets, a less accurate measurement of the CMB first acoustic peak and different cosmological parameter values (WMAP values [121] instead of the ones released by Planck [2]). In [85] we did not find significant tension between growth and distances measurements. This is a clear example of the great potential of more accurate cosmological data sets to rule out $f(R)$ models. We conclude that this class of models are not allowed by the entire set of cosmological data exploited in this analysis and are statistically rejected at 2-σ confidence level.

Models of type 3, $f(R) = \alpha R^n$ with constraints $\alpha < 0$ and $0 < n < 1$ posses a viable qualitative expansion history as well. These models also include a ΛCDM cosmology in the limit $n \to 0$, in which α mimics a cosmological constant. In the quantitative data analysis, we find that the power index n can be actually quite large while the value of α can deviate significantly from the cosmological constant value in ΛCDM, producing a strong correlation between these two parameters. However, the preferred parameter regions by growth data lie at more than 3-σ away from the allowed regions by distances data; growth data prefers larger values of n than the ones obtained from geometrical probes. As in models of type 2, we found this family to be allowed by all data sets used in [85]. Here, we have shown that by implementing newer data sets, we can reject this model at a high significance (3-σ confidence level).

Type 4 models, $f(R) = \alpha R^2 - \Lambda$ with the constraint $\alpha\Lambda \ll 1$, possess a cosmologically viable expansion history, as they clearly describe a ΛCDM cosmology when $\alpha \to 0$. As expected, the fit to distances data shows the preference of very small values of the amplitude α and values of Λ close to the best-fit value of cosmological constant for ΛCDM, showing also the expected anticorrelation of these two parameters. The growth data prefers larger values of Λ than the ones preferred by cosmic distances, but still the two regions overlap at the 1-σ level and therefore these models are allowed by all cosmological data sets exploited in this analysis. Observational techniques are currently developing very fast and the bounds obtained in this analysis can greatly improve with upcoming higher precision data of the growth of structure. If with higher precision measurements the regions preferred by growth data turn out to still overlap with the regions allowed by geometrical probes, probably it would not be possible to distinguish this type of models from the ΛCDM standard model since there are no regions allowed by geometrical probes that differ from from the ΛCDM model. We compute the total χ^2 of all cosmological probes exploited in the analysis

137

obtaining $\chi^2_{min} = 548.5$ for 580 d.o.f. and a best fit value of the parameters given by, $\alpha = 1.6 \cdot 10^{-12} (\text{km/s/Mpc})^{-2} = 7 \cdot 10^{-9} \bar{H}_0^{-2}$ and $\Lambda = 20483 \ (\text{km/s/Mpc})^2 = 4.5 \bar{H}_0^2$ (with $\bar{H}_0 = 67.3$ km/s/Mpc). These values lead to a current effective dark energy equation of state $w_{\text{eff}}(z = 0) = -0.98$.

Type 5 models, $f(R) = -M^2 c_1 (R/M^2)^n / [1 + c_2 (R/M^2)^n]$ with $n > 0$, are the models we referred to as the HS type [70], where $M^2 \equiv \kappa^2 \bar{\rho}_0 / 3$ is the mass scale (with $\bar{\rho}_0$ the average matter density today) and c_1 and c_2 are reparametrized as $c_1 = 6 c_2 (1 - \tilde{\Omega}_M) / \tilde{\Omega}_M$ and $c_2 = -6n / f_{R0} (1 - \tilde{\Omega}_m / \tilde{\Omega}_M)(12 / \tilde{\Omega}_M - 9)^{-n-1}$, where $f_{R0} \approx f_R(R_0)$ is the value of the scalar field today. Thus, the model is left with two free parameters, n and f_{R0}. From the analysis of Chapter 4, in the limit $f_{R0} \to 0$, the model converges to a ΛCDM universe. In Chapter 5 we have discussed this limit more quantitatively, finding that the constraint in the magnitude of f_{R0} such that the model's growth of structure becomes equivalent to the ΛCDM growth, is few orders of magnitude more stringent than the constraint on f_{R0} such that the model's expansion history becomes approximately equal to that of ΛCDM; the linear growth of structure in a HS universe becomes close to the ΛCDM growth when $|f_{R0}| \lesssim 10^{-6}$ while an amplitude of $|f_{R0}| \sim 10^{-3}$ is enough to recover the ΛCDM limit in the case of the background equations. From the data analysis we obtained that distances measurements prefer larger values of $|f_{R0}|$ than the growth data, which prefers $|f_{R0}|$ values closer to 0. Geometrical probes do not show a significant preference for the value of n, while the growth data prefers higher values of n. We find that there are parameter regions of the HS model, with f_{R0} significantly different from 0, which fit better the distances data than the ΛCDM model. The parameter regions preferred by growth data overlap at 2 and 3-σ with the regions reproducing an acceptable expansion history, while showing some tension at the 1-σ level in the parameter plane studied in this analysis. This feature suggests that upcoming higher precision measurements on the linear growth of structure can improve these bounds and potentially rule out this type of models at a high significance level. Nonetheless, models of type 5 are consistent with the cosmological datasets analyzed here, and are not ruled out by them. We compute the total χ^2 of all cosmological probes exploited in the analysis, obtaining a $\chi^2_{min} = 565$ for 580 d.o.f. and a best fit value of the parameters, in the parameter space studied here, of $n = 10$ and $f_{R0} = -0.1$ for this type of models.

Since we found that type 4 and type 5 models are compatible with all cosmological datasets considered, we analyzed the slow-motion, weak-field limit of these two types of models in the parameter range in which these models are viable at cosmological scales. For models of type 4, we have computed analytically the static, spherically symmetric solutions of the scalar field dynamical equation, relevant in the solar system. We have found that in order to pass solar system constraints, the parameter α of this type of model is bounded to be $\alpha < 10^{-41} H_0^{-2}$, which is about 32 orders of magnitude smaller that the best fit value of α obtained from the cosmological data analysis. We conclude that this strong bound on the amplitude parameter of this type of models coming from solar system scales renders any deviation from ΛCDM

at cosmological scales unobservable. This is due to the fact that this class of models do not allow for a chameleon mechanism, as according to them the field's Compton wavelength does not depend on the local matter density. Therefore the model can only pass solar system constraints by choosing parameters yielding a very small Compton wavelength everywhere (at solar system scales as well as at cosmological scales), at the price of rendering any contribution of the scalar field beyond that of ΛCDM negligible at cosmological scales.

The solar system constraints in models of type 5 were studied in [70]. For this type of models, unlike for models of type 4, the time-independent equation for the scalar field is nonlinear and to solve it a numerical analysis was performed in [70]. That reference showed that the Compton condition is well satisfied in the whole solar density profile for $n = 4$ and $|f_{R0}| \leq 10^{-2}$, while the thin-shell condition is satisfied for the same n up to $|f_{R0}| \leq 10^{-1}$ in the solar corona. The Compton wavelength rapidly decreases as n increases while the dependence on $|f_{R0}|$ is much weaker. Thus, we expect the Compton condition to be well satisfied for the best fit value of the parameters that we have obtained from the analysis at cosmological scales. From the thin-shell condition, by assuming that the galaxy has enough mass and extension to keep the field at the minimum of its effective potential in the galactic interior, a constraint on the cosmological field value was obtained in [70]. However this constraint turns out to be weak and not very significant. We conclude that the HS type of models are the only ones compatible with all cosmological the datasets consider in this analysis as well as with Solar system constraints.

By analyzing several $f(R)$ models, we have shown in this thesis that the combination of geometrical probes together with the dynamical probe coming from the growth of structure measurements, offers a powerful tool to rule out modified gravity scenarios (or else constrain deviations from ΛCDM) which are, in principle, cosmologically viable. We also find that $f(R)$ models whose dynamics in the slow-motion weak-field limit do not have a chameleon behavior (*i.e.*, those for which the scalar field's Compton wavelength does not depend significantly on the local matter density), are very unlikely to pass the solar system constraints while accelerating the expansion at cosmological scales. In particular, we found that the models $f(R) = R \left[\log(\alpha R) \right]^q - R$ (with $q > 0$), $f(R) = R \exp(q/R) - R$ and $f(R) = \alpha R^n$ (with $\alpha < 0$ and $0 < n < 1$), which are able to reproduce an acceptable background evolution according to observations, are statistically rejected by growth of structure data when studying their dynamics at first order in perturbations from homogeneity. Models of the type $f(R) = \alpha R^2 - \Lambda$ (with $\alpha \Lambda \ll 1$) are allowed by all the cosmological datasets exploited in the analysis. However, we also find that for the best fit parameters resulting from the cosmological data analysis, these models are not compatible with solar system tests, as they do not support a chameleon mechanism.

Among all the models analyzed in this thesis, the so-called Hu and Sawicki type of models, $f(R) = -M^2 c_1 (R/M^2)^n / [1 + c_2 (R/M^2)^n]$ (with $n > 0$), was shown to be the only one consistent with the combination of all datasets exploited in this work as well

139

as with solar system constraints. Precise measurements of the growth of structure are the most relevant upcoming data to further test cosmological $f(R)$ viable models.

Bibliography

[1] Edwin Hubble. A relation between distance and radial velocity among extra–galactic nebulae. *Proc. Nat. Acad. Sci.*, 15:168–173, 1929.

[2] P.A.R. Ade et al. Planck 2013 results. XVI. Cosmological parameters. 2013.

[3] K.A. Olive et al. Review of Particle Physics. *Chin.Phys.*, C38:090001, 2014.

[4] Alan H. Guth. The Inflationary Universe: A Possible Solution to the Horizon and Flatness Problems. *Phys. Rev.*, D23:347–356, 1981.

[5] Andrei D. Linde. A New Inflationary Universe Scenario: A Possible Solution of the Horizon, Flatness, Homogeneity, Isotropy and Primordial Monopole Problems. *Phys. Lett.*, B108:389–393, 1982.

[6] Andreas Albrecht and Paul J. Steinhardt. Cosmology for Grand Unified Theories with Radiatively Induced Symmetry Breaking. *Phys. Rev. Lett.*, 48:1220–1223, 1982.

[7] D. N. Spergel et al. Wilkinson Microwave Anisotropy Probe (WMAP) three year results: Implications for cosmology. *Astrophys. J. Suppl.*, 170:377, 2007.

[8] Hideo Kodama and Misao Sasaki. Cosmological Perturbation Theory. *Prog. Theor. Phys. Suppl.*, 78:1–166, 1984.

[9] James M. Bardeen. Gauge Invariant Cosmological Perturbations. *Phys.Rev.*, D22:1882–1905, 1980.

[10] Chung-Pei Ma and Edmund Bertschinger. Cosmological perturbation theory in the synchronous and conformal Newtonian gauges. *Astrophys. J.*, 455:7–25, 1995.

[11] Adam G. Riess et al. Observational Evidence from Supernovae for an Accelerating Universe and a Cosmological Constant. *Astron. J.*, 116:1009–1038, 1998.

[12] S. Perlmutter et al. Measurements of Omega and Lambda from 42 High-Redshift Supernovae. *Astrophys. J.*, 517:565–586, 1999.

[13] Subrahmanyan Chandrasekhar. The maximum mass of ideal white dwarfs. *Astrophys.J.*, 74:81–82, 1931.

[14] Adam G. Riess et al. Type Ia Supernova Discoveries at z¿1 From the Hubble Space Telescope: Evidence for Past Deceleration and Constraints on Dark Energy Evolution. *Astrophys. J.*, 607:665–687, 2004.

[15] T. Roy Choudhury and T. Padmanabhan. A theoretician's analysis of the supernova data and the limitations in determining the nature of dark energy II: Results for latest data. *Astron. Astrophys.*, 429:807, 2005.

[16] Raul Jimenez, Peter Thejll, Uffe G. Jorgensen, James MacDonald, and Bernard Pagel. Ages of Globular clusters: A new approach. *MNRAS*, 282:926, 1996. NORDITA-96-11-A.

[17] Harvey B. Richer et al. The Lower Main Sequence and Mass Function of the Globular Cluster Messier 4. *Astrophys. J.*, 574:L151–L154, 2002.

[18] Brad M. S. Hansen et al. The White Dwarf Cooling Sequence of the Globular Cluster Messier 4. *Astrophys. J.*, 574:L155–L158, 2002.

[19] Arno A. Penzias and Robert Woodrow Wilson. A Measurement of excess antenna temperature at 4080-Mc/s. *Astrophys.J.*, 142:419–421, 1965.

[20] D. J. Fixsen et al. The Cosmic Microwave Background Spectrum from the Full COBE/FIRAS Data Set. *Astrophys. J.*, 473:576, 1996.

[21] George F. Smoot et al. Structure in the COBE differential microwave radiometer first year maps. *Astrophys. J.*, 396:L1–L5, 1992.

[22] C.L. Bennett et al. Nine-Year Wilkinson Microwave Anisotropy Probe (WMAP) Observations: Final Maps and Results. *Astrophys.J.Suppl.*, 208:20, 2013.

[23] G. Hinshaw et al. Nine-Year Wilkinson Microwave Anisotropy Probe (WMAP) Observations: Cosmological Parameter Results. *Astrophys.J.Suppl.*, 208:19, 2013.

[24] P.A.R. Ade et al. Planck 2013 results. I. Overview of products and scientific results. 2013.

[25] Wendy L. Freedman, Barry F. Madore, Victoria Scowcroft, Chris Burns, Andy Monson, et al. Carnegie Hubble Program: A Mid-Infrared Calibration of the Hubble Constant. *Astrophys.J.*, 758:24, 2012.

[26] Max Tegmark et al. Cosmological parameters from SDSS and WMAP. *Phys. Rev.*, D69:103501, 2004.

[27] Max Tegmark et al. The 3D power spectrum of galaxies from the SDSS. *Astrophys. J.*, 606:702–740, 2004.

[28] Antony Lewis, Anthony Challinor, and Anthony Lasenby. Efficient computation of CMB anisotropies in closed FRW models. *Astrophys. J.*, 538:473–476, 2000.

[29] Max Tegmark et al. Cosmological Constraints from the SDSS Luminous Red Galaxies. *Phys. Rev.*, D74:123507, 2006.

[30] Antony Lewis and Sarah Bridle. Cosmological parameters from CMB and other data: a Monte- Carlo approach. *Phys. Rev.*, D66:103511, 2002.

[31] P. J. E. Peebles and J. T. Yu. Primeval adiabatic perturbation in an expanding universe. *Astrophys. J.*, 162:815–836, 1970.

[32] R. A. Sunyaev and Ya. B. Zeldovich. Small scale fluctuations of relic radiation. *Astrophys. Space Sci.*, 7:3–19, 1970.

[33] Daniel J. Eisenstein and Wayne Hu. Baryonic features in the matter transfer function. *Astrophys.J.*, 496:605, 1998.

[34] A. Meiksin, Martin J. White, and J. A. Peacock. Baryonic Signatures in Large-Scale Structure. *Mon. Not. Roy. Astron. Soc.*, 304:851–864, 1999.

[35] Martin J. White, 1. Baryon oscillations. *Astropart. Phys.*, 24:334–344, 2005.

[36] Volker Springel et al. Simulating the joint evolution of quasars, galaxies and their large-scale distribution. *Nature*, 435:629–636, 2005.

[37] Chris Blake and Karl Glazebrook. Probing dark energy using baryonic oscillations in the galaxy power spectrum as a cosmological ruler. *Astrophys. J.*, 594:665–673, 2003.

[38] Hee-Jong Seo and Daniel J. Eisenstein. Probing Dark Energy with Baryonic Acoustic Oscillations from Future Large Galaxy Redshift Surveys. *Astrophys. J.*, 598:720–740, 2003.

[39] Shaun Cole et al. The 2dF Galaxy Redshift Survey: Power-spectrum analysis of the final dataset and cosmological implications. *Mon. Not. Roy. Astron. Soc.*, 362:505–534, 2005.

[40] Daniel J. Eisenstein et al. Detection of the Baryon Acoustic Peak in the Large-Scale Correlation Function of SDSS Luminous Red Galaxies. *Astrophys. J.*, 633:560–574, 2005.

[41] Lauren Anderson, Eric Aubourg, Stephen Bailey, Dmitry Bizyaev, Michael Blanton, et al. The clustering of galaxies in the SDSS-III Baryon Oscillation Spectroscopic Survey: Baryon Acoustic Oscillations in the Data Release 9 Spectroscopic Galaxy Sample. *Mon.Not.Roy.Astron.Soc.*, 427(4):3435–3467, 2013.

143

[42] Lauren Anderson et al. The clustering of galaxies in the SDSS-III Baryon Oscillation Spectroscopic Survey: Baryon Acoustic Oscillations in the Data Release 10 and 11 galaxy samples. 2013.

[43] David Schlegel, Martin White, and Daniel Eisenstein. The Baryon Oscillation Spectroscopic Survey: Precision measurements of the absolute cosmic distance scale. 2009.

[44] Daniel J. Eisenstein et al. SDSS-III: Massive Spectroscopic Surveys of the Distant Universe, the Milky Way Galaxy, and Extra-Solar Planetary Systems. *Astron.J.*, 142:72, 2011.

[45] Will J. Percival et al. Baryon Acoustic Oscillations in the Sloan Digital Sky Survey Data Release 7 Galaxy Sample. *Mon.Not.Roy.Astron.Soc.*, 401:2148–2168, 2010.

[46] Beth A. Reid, Will J. Percival, Daniel J. Eisenstein, Licia Verde, David N. Spergel, et al. Cosmological Constraints from the Clustering of the Sloan Digital Sky Survey DR7 Luminous Red Galaxies. *Mon.Not.Roy.Astron.Soc.*, 404:60–85, 2010.

[47] Albert Einstein. Cosmological Considerations in the General Theory of Relativity. *Sitzungsber. Preuss. Akad. Wiss. Berlin (Math. Phys.)*, 1917:142–152, 1917.

[48] Steven Weinberg. The cosmological constant problem. *Rev. Mod. Phys.*, 61:1–23, 1989.

[49] P. D. B. Collins, Alan D. Martin, and E. J. Squires. PARTICLE PHYSICS AND COSMOLOGY. NEW YORK, USA: WILEY (1989) 496p.

[50] D. Bailin and A. Love. Supersymmetric gauge field theory and string theory. Bristol, UK: IOP (1994) 322 p. (Graduate student series in physics).

[51] J. David Brown and C. Teitelboim. Neutralization of the Cosmological Constant by Membrane Creation. *Nucl. Phys.*, B297:787–836, 1988.

[52] Andrei D. Linde. The Inflationary Universe. *Rept. Prog. Phys.*, 47:925–986, 1984.

[53] Jaume Garriga and Alexander Vilenkin. On likely values of the cosmological constant. *Phys. Rev.*, D61:083502, 2000.

[54] Hugo Martel, Paul R. Shapiro, and Steven Weinberg. Likely Values of the Cosmological Constant. *Astrophys. J.*, 492:29, 1998.

[55] Steven Weinberg. Anthropic Bound on the Cosmological Constant. *Phys. Rev. Lett.*, 59:2607, 1987.

[56] S. W. Hawking. The Cosmological Constant Is Probably Zero. *Phys. Lett.*, B134:403, 1984.

[57] Sidney R. Coleman. Why There Is Nothing Rather Than Something: A Theory of the Cosmological Constant. *Nucl. Phys.*, B310:643, 1988.

[58] Jun'ichi Yokoyama. Cosmological constant from degenerate vacua. *Phys. Rev. Lett.*, 88(15):151302, Mar 2002.

[59] Nima Arkani-Hamed, Savas Dimopoulos, Nemanja Kaloper, and Raman Sundrum. A small cosmological constant from a large extra dimension. *Phys. Lett.*, B480:193–199, 2000.

[60] Shamit Kachru, Michael B. Schulz, and Eva Silverstein. Self-tuning flat domain walls in 5d gravity and string theory. *Phys. Rev.*, D62:045021, 2000.

[61] Shamit Kachru, Renata Kallosh, Andrei D. Linde, and Sandip P. Trivedi. De Sitter vacua in string theory. *Phys. Rev.*, D68:046005, 2003.

[62] Raphael Bousso and Joseph Polchinski. Quantization of four-form fluxes and dynamical neutralization of the cosmological constant. *JHEP*, 06:006, 2000.

[63] T. Padmanabhan. Vacuum Fluctuations of Energy Density can lead to the observed Cosmological Constant. *Class. Quant. Grav.*, 22:L107–L110, 2005.

[64] C. Brans and R. H. Dicke. Mach's principle and a relativistic theory of gravitation. *Phys. Rev.*, 124(3):925–935, Nov 1961.

[65] Guido Magnano and Leszek M. Sokolowski. On physical equivalence between nonlinear gravity theories and a general relativistic selfgravitating scalar field. *Phys.Rev.*, D50:5039–5059, 1994.

[66] P. Teyssandier and Ph. Tourrenc. The Cauchy problem for the R+R**2 theories of gravity without torsion. *J.Math.Phys.*, 24:2793, 1983.

[67] Takeshi Chiba. 1/R gravity and scalar-tensor gravity. *Phys. Lett.*, B575:1–3, 2003.

[68] Justin Khoury and Amanda Weltman. Chameleon cosmology. *Phys. Rev.*, D69:044026, 2004.

[69] Luca Amendola, Radouane Gannouji, David Polarski, and Shinji Tsujikawa. Conditions for the cosmological viability of f(R) dark energy models. *Phys. Rev.*, D75:083504, 2007.

[70] Wayne Hu and Ignacy Sawicki. Models of f(R) Cosmic Acceleration that Evade Solar-System Tests. *Phys. Rev.*, D76:064004, 2007.

[71] Matteo Martinelli, Alessandro Melchiorri, and Luca Amendola. Cosmological constraints on the Hu-Sawicki modified gravity scenario. *Phys.Rev.*, D79:123516, 2009.

[72] Rachel Bean, David Bernat, Levon Pogosian, Alessandra Silvestri, and Mark Trodden. Dynamics of Linear Perturbations in f(R) Gravity. *Phys. Rev.*, D75:064020, 2007.

[73] Clifford M. Will. The confrontation between general relativity and experiment. *Living Rev. Rel.*, 9:3, 2005.

[74] Ignacy Sawicki and Wayne Hu. Stability of Cosmological Solution in f(R) Models of Gravity. *Phys.Rev.*, D75:127502, 2007.

[75] B. Bertotti, L. Iess, and P. Tortora. A test of general relativity using radio links with the Cassini spacecraft. *Nature*, 425:374, 2003.

[76] S.S. Shapiro, J.L. Davis, D.E. Lebach, and J.S. Gregory. Measurement of the Solar Gravitational Deflection of Radio Waves using Geodetic Very-Long-Baseline Interferometry Data, 1979-1999. *Phys.Rev.Lett.*, 92:121101, 2004.

[77] N. Ashby, D.F. Bartlett, and W. Wyss. General relativity and gravitation, 1989. Proceedings, 12th International Conference, Boulder, USA, July 2-8, 1989. 1990.

[78] Ignacio Navarro and Karel Van Acoleyen. On the Newtonian limit of Generalized Modified Gravity Models. *Phys. Lett.*, B622:1–5, 2005.

[79] Gonzalo J. Olmo. Post-Newtonian constraints on $f(R)$ cosmologies in metric and Palatini formalism. *Phys. Rev.*, D72:083505, 2005.

[80] Gonzalo J. Olmo. The gravity lagrangian according to solar system experiments. *Phys. Rev. Lett.*, 95:261102, 2005.

[81] S. Capozziello and Antonio Troisi. PPN-limit of fourth order gravity inspired by scalar- tensor gravity. *Phys. Rev.*, D72:044022, 2005.

[82] I. Navarro and K. Van Acoleyen. f(R) actions, cosmic acceleration and local tests of gravity. *JCAP*, 0702:022, 2007.

[83] Gonzalo J. Olmo. Limit to general relativity in f(R) theories of gravity. *Phys. Rev.*, D75:023511, 2007.

[84] S. Capozziello, A. Stabile, and A. Troisi. The Newtonian Limit of F(R) gravity. *Phys. Rev.*, D76:104019, 2007.

[85] Z. Girones, A. Marchetti, O. Mena, C. Pena-Garay, and N. Rius. Cosmological data analysis of f(R) gravity models. *JCAP*, 1011:004, 2010.

[86] Chris Blake, Eyal Kazin, Florian Beutler, Tamara Davis, David Parkinson, et al. The WiggleZ Dark Energy Survey: mapping the distance-redshift relation with baryon acoustic oscillations. *Mon.Not.Roy.Astron.Soc.*, 418:1707–1724, 2011.

[87] Yun Wang and Shuang Wang. Distance Priors from Planck and Dark Energy Constraints from Current Data. 2013.

[88] Chris Blake, Sarah Brough, Matthew Colless, Carlos Contreras, Warrick Couch, et al. The WiggleZ Dark Energy Survey: the growth rate of cosmic structure since redshift z=0.9. *Mon.Not.Roy.Astron.Soc.*, 415:2876, 2011.

[89] L. Guzzo et al. A test of the nature of cosmic acceleration using galaxy redshift distortions. *Nature*, 451:541–545, 2008.

[90] Licia Verde et al. The 2dF Galaxy Redshift Survey: The bias of galaxies and the density of the Universe. *Mon. Not. Roy. Astron. Soc.*, 335:432, 2002.

[91] Nicholas P. Ross et al. The 2dF-SDSS LRG and QSO Survey: The 2-Point Correlation Function and Redshift-Space Distortions. 2006.

[92] Ed Hawkins et al. The 2dF Galaxy Redshift Survey: correlation functions, peculiar velocities and the matter density of the Universe. *Mon. Not. Roy. Astron. Soc.*, 346:78, 2003.

[93] Adam G. Riess et al. New Hubble Space Telescope Discoveries of Type Ia Supernovae at $z > 1$: Narrowing Constraints on the Early Behavior of Dark Energy. *Astrophys. J.*, 659:98–121, 2007.

[94] W. Michael Wood-Vasey et al. Observational Constraints on the Nature of the Dark Energy: First Cosmological Results from the ESSENCE Supernova Survey. *Astrophys. J.*, 666:694–715, 2007.

[95] Tamara M. Davis et al. Scrutinizing exotic cosmological models using ESSENCE supernova data combined with other cosmological probes. *Astrophys. J.*, 666:716–725, 2007.

[96] M. Kowalski et al. Improved Cosmological Constraints from New, Old and Combined Supernova Datasets. *Astrophys. J.*, 686:749–778, 2008.

[97] Malcolm Hicken et al. Improved Dark Energy Constraints from 100 New CfA Supernova Type Ia Light Curves. *Astrophys. J.*, 700:1097–1140, 2009.

[98] Richard Kessler et al. First-year Sloan Digital Sky Survey-II (SDSS-II) Supernova Results: Hubble Diagram and Cosmological Parameters. *Astrophys. J. Suppl.*, 185:32–84, 2009.

[99] R. Amanullah et al. Spectra and Light Curves of Six Type Ia Supernovae at $0.511 < z < 1.12$ and the Union2 Compilation. *Astrophys. J.*, 716:712–738, 2010.

147

[100] Irit Maor, Ram Brustein, and Paul J. Steinhardt. Limitations in using luminosity distance to determine the equation of state of the universe. *Phys.Rev.Lett.*, 86:6, 2001.

[101] Raul Jimenez and Abraham Loeb. Constraining cosmological parameters based on relative galaxy ages. *Astrophys.J.*, 573:37–42, 2002.

[102] Raul Jimenez, Licia Verde, Tommaso Treu, and Daniel Stern. Constraints on the equation of state of dark energy and the Hubble constant from stellar ages and the CMB. *Astrophys.J.*, 593:622–629, 2003.

[103] Joan Simon, Licia Verde, and Raul Jimenez. Constraints on the redshift dependence of the dark energy potential. *Phys. Rev.*, D71:123001, 2005.

[104] Roberto G. Abraham, Karl Glazebrook, Patrick J. McCarthy, David Crampton, Richard Murowinski, et al. The Gemini Deep Deep Survey. 1. Introduction to the survey, catalogs and composite spectra. *Astron.J.*, 127:2455, 2004.

[105] T. Treu, M. Stiavelli, S. Casertano, P. Moller, and G. Bertin. The properties of field elliptical galaxies at intermediate redshift. I: empirical scaling laws. *Mon.Not.Roy.Astron.Soc.*, 308:1037–1052, 1999.

[106] T. Treu, M. Stiavelli, P. Moller, S. Casertano, and G. Bertin. The properties of field elliptical galaxies at intermediate redshift. 2. photometry and spectroscopy of an hst selected sample. *Mon.Not.Roy.Astron.Soc.*, 326:221, 2001.

[107] T. Treu, M. Stiavelli, S. Casertano, P. Moller, and G. Bertin. The evolution of field early-type galaxies to Z 0.7. *Astrophys.J.*, 564:L13, 2002.

[108] J. Dunlop, J. Peacock, H. Spinrad, A. Dey, Raul Jimenez, et al. A 3.5 - Gyr - old galaxy at redshift 1.55. *Nature*, 381:581, 1996.

[109] Hyron Spinrad, Arjun Dey, Daniel Stern, James Dunlop, John Peacock, et al. Lbds 53w091: an old red galaxy at z=1.552. *Astrophys.J.*, 484:581–601, 1997.

[110] Louisa A. Nolan, James S. Dunlop, Raul Jimenez, and Alan F. Heavens. F stars, metallicity, and the ages of red galaxies at $Z > 1$. *Mon.Not.Roy.Astron.Soc.*, 341:464, 2003.

[111] J.R. Bond, G. Efstathiou, and M. Tegmark. Forecasting cosmic parameter errors from microwave background anisotropy experiments. *Mon.Not.Roy.Astron.Soc.*, 291:L33–L41, 1997.

[112] G. Efstathiou and J.R. Bond. Cosmic confusion: Degeneracies among cosmological parameters derived from measurements of microwave background anisotropies. *Mon.Not.Roy.Astron.Soc.*, 304:75–97, 1999.

[113] Alessandro Melchiorri and Louise M. Griffiths. From anisotropy to Omega. *New Astron.Rev.*, 45:321–328, 2001.

[114] S. Nesseris and Leandros Perivolaropoulos. Crossing the Phantom Divide: Theoretical Implications and Observational Status. *JCAP*, 0701:018, 2007.

[115] Yun Wang and Pia Mukherjee. Robust Dark Energy Constraints from Supernovae, Galaxy Clustering, and Three-Year Wilkinson Microwave Anisotropy Probe Observations. *Astrophys. J.*, 650:1, 2006.

[116] D. Heath Jones, Mike A. Read, Will Saunders, Matthew Colless, Tom Jarrett, et al. The 6dF Galaxy Survey: Final Redshift Release (DR3) and Southern Large-Scale Structures. 2009.

[117] N. Kaiser. Clustering in real space and in redshift space. *Mon. Not. Roy. Astron. Soc.*, 227:1–27, 1987.

[118] A.J.S. Hamilton. Measuring Omega and the real correlation function from the redshift correlation function. *Astrophys.J.*, 385:L5–L8, 1992.

[119] S. Nesseris and Leandros Perivolaropoulos. Testing LCDM with the Growth Function $\delta(a)$: Current Constraints. *Phys. Rev.*, D77:023504, 2008.

[120] Matteo Martinelli, Alessandro Melchiorri, Olga Mena, Valentina Salvatelli, and Zahara Girones. Future constraints on the Hu-Sawicki modified gravity scenario. *Phys.Rev.*, D85:024006, 2012.

[121] E. Komatsu et al. Five-Year Wilkinson Microwave Anisotropy Probe (WMAP) Observations:Cosmological Interpretation. *Astrophys. J. Suppl.*, 180:330–376, 2009.